

# DISSERTATION

submitted to the

Combined Faculties of Physics and Electrical Engineering  
of the University of Bremen, Germany

for the degree of

Doctor of Natural Sciences

Put forward by

**Shokoufe Faraji**



Center of Applied Space Technology and Microgravity (ZARM)

# Physics of quadrupolar and accelerated compact astrophysical objects

A dissertation presented by

Shokoufe Faraji

## Referees

Dr. Eva Hackmann

*University of Bremen, Center of Applied  
Space Technology and Microgravity (ZARM)*

Prof. Hernando Quevedo

*National Autonomous University of Mexico  
Institute of Nuclear Sciences  
and*

*Sapienza University of Rome  
Department of Physics and ICRANet*

Date of defence: 26th July 2022

**Germany**





نہ کہیم  
عمر ہی دیکھتے تھے  
وقت نہ تھا کہ جو یہ  
نہر اپنی طرف سے  
گنہ گار تھے وہاں کہیم

Days and nights we were searching for him..  
who was with us and we were looking over the world for him..  
He was outside of the space and time..  
who we searched for in spaces and times...

Persian poet Saádi (13th century)



# Abstract

This thesis analyzes how the properties of space-times containing quadrupoles or acceleration parameters, depending on their values, can be distinguishable from the Schwarzschild or the Kerr solutions in the observational fingerprints or be a black hole mimicker. In fact, the recent window to the gravitational wave has shifted the debate about them from a purely theoretical issue to a phenomenological consideration.

To answer this question, this investigation takes place on two levels: first, constructing a solution containing two quadrupoles describing a non-isolated object to obtain a more realistic model. This metric is new generalization of the Schwarzschild solution containing a quadrupole. On the second level, space-times considered here are investigated in the eyes of the configurations and properties of accretion discs, collision of particles, quasi-periodic oscillations, geodesics, dynamics of uncharged and charged particles with or without a magnetic field, stability of the geodesics, and shadow.

In this work, the analytical and semi-analytical approaches are employed. Although the majority of astrophysical systems are studied via numerical methods and simulations, the analytical techniques always open a window and provide a systematic study as a stepping stone due to their large parameter space. For example, the Event Horizon Telescope findings that provided a new branch in studying characteristics of black holes and their accretion flows were predicted theoretically in 2000, the same for the famous Higgs boson in particle physics.

This study concludes that, first, the resulting generalized metric introduces novel analytical expressions to connect to the observable. For the accretion discs models new properties arose, in particular, enabling to connect the critical behavior of the observation of the quasi-periodic oscillations in observed microquasars to the metric parameters. Second, all space-times considered in this thesis are from the general family of the Weyl space-times including the Schwarzschild, the distorted Schwarzschild, the static and the stationary q-metric, characterizing with quadrupole, as the representative of the different classes of the solution in different ways. Thus, the complete discussion on astrophysical systems in these space-times provides the primary reference source for comparisons, particularly with the Kerr space-time. In the outlook, the various future works led by this thesis are listed.



## List of publications

1. *Thin accretion disk around the distorted Schwarzschild black hole*; Shokoufe Faraji, Eva Hackmann; **Phys. Rev. D** 101 023002 (2019).
2. *Effect of an external mass distribution on the magnetized accretion disk*; Shokoufe Faraji, Audrey Trova; **Phys. Rev. D** 104 083006 (2021).
3. *Magnetised tori in the background of a deformed compact object*; Shokoufe Faraji, Audrey Trova; **Astronomy & Astrophysics** 654 A100 (2021).
4. *Quasi-periodic oscillatory motion of particles orbiting a distorted, deformed compact object*; Shokoufe Faraji, Audrey Trova; **Universe**, 7(11), 447 (2021).
5. *Dynamics of charged particles and quasi-periodic oscillations in the vicinity of a distorted, deformed compact object embedded in a uniform magnetic field*; Shokoufe Faraji, Audrey Trova; **Mon. Notices of the Royal Astronomical Soc.** 882 (2022).
6. *Circular geodesics in a new generalization q-metric*; Shokoufe Faraji; **Universe Mathematical Physics** 8 (3), 195 (2022).
7. *Magnetised relativistic accretion disc around a spinning, electrically charged, accelerating black hole: case of C-metric*; Shokoufe Faraji, Valadimir Karas, Audrey Trova; **Phys. Rev. D** 105 (10), 103017 (2022).
8. *Thick accretion disk configurations in the Born-Infeld teleparallel gravity*; Sebastian Bahamonde, Shokoufe Faraji, Eva Hackmann, Christian Pfeifer; accepted in **Phys. Rev. D** (2022).
9. *Magnetized tori around a uniformly accelerating black hole*; Shokoufe Faraji, Audrey Trova; Contributed Proceedings of the Sixteenth Marcel Grossmann Meeting (2021).



10. *Properties of accretion disc models in the background with quadrupole*; Shokoufe Faraji; Contributed Proceedings of the Sixteenth Marcel Grossmann Meeting (2021).
11. *Summary of the parallel session Time in Physics and Philosophy*; Shokoufe Faraji; Contributed Proceedings of the Sixteenth Marcel Grossmann Meeting (2021).
12. *Thin accretion disc around the distorted deformed compact object*; Shokoufe Faraji; (2022) submitted to journal (uploaded to arXiv).
13. *Relativistic equilibrium fluid configurations around rotating deformed compact objects*; Shokoufe Faraji, Audrey Trova, Hernando Quevedo; (2022) submitted to journal (uploaded to arXiv).
14. *Axisymmetric oscillation modes of relativistic tori in the vicinity of a distorted deformed compact object*; Shokoufe Faraji, Audrey Trova; (2022) submitted to journal (uploaded to arXiv).





# Contents

<b>I</b>	<b>Prologue</b>	<b>xiii</b>
<b>1</b>	<b>Preface</b>	<b>xv</b>
1.1	General motivation . . . . .	xv
1.2	Aims . . . . .	xvii
1.3	Methodology . . . . .	xvii
1.4	Thesis outline . . . . .	xviii
<b>2</b>	<b>Analytical accretion disc models</b>	<b>3</b>
2.1	Thin accretion disc . . . . .	4
2.1.1	Assumption of the model . . . . .	4
2.1.2	Equations of the model . . . . .	6
2.2	Thick accretion disc . . . . .	11
2.2.1	Magnetized version . . . . .	13
2.2.2	Angular momentum distributions . . . . .	15
<b>3</b>	<b>Quasi-periodic oscillations</b>	<b>19</b>
3.1	Observations . . . . .	19
3.2	Theories . . . . .	20
3.3	Models of 3 : 2 quasi-periodic oscillation . . . . .	21
3.3.1	Resonance . . . . .	22
3.3.2	QPO Models . . . . .	23
3.4	Epicyclic oscillations: Local perturbation . . . . .	26
3.4.1	Test particle . . . . .	27
3.4.2	Perfect fluid disc . . . . .	27
<b>4</b>	<b>Shadow in the presence of plasma</b>	<b>31</b>
4.1	Equation of motion for light rays in plasma . . . . .	32
4.2	Radius of Shadow . . . . .	33
4.3	Low-density plasma . . . . .	34

<b>5</b>	<b>Stability analysis in the dynamical system</b>	<b>37</b>
5.1	Lyapunov stability . . . . .	37
5.2	Jacobi stability . . . . .	39
5.3	Kolmogorov entropy . . . . .	41
<b>6</b>	<b>Space-times</b>	<b>43</b>
6.1	Static and axisymmetric space-times . . . . .	43
6.2	Distorted Schwarzschild space-time . . . . .	46
6.3	Static q-metric space-time . . . . .	48
6.4	Stationary q-metric space-time . . . . .	50
6.5	C-metric space-time . . . . .	53
<b>II</b>	<b>Results</b>	<b>59</b>
<b>7</b>	<b>Generalized q-metric</b>	<b>61</b>
7.1	Construction of the metric . . . . .	61
7.2	Effective potential . . . . .	65
7.3	Circular geodesics . . . . .	66
7.3.1	The equatorial plane in Generalized q-metric . . . . .	67
7.3.2	Revisit the equatorial plane in q-metric . . . . .	76
7.4	Dynamics of charged particle in a uniform magnetic field . . .	80
7.5	Summary and conclusion . . . . .	82
<b>8</b>	<b>Extraction of energy: particle collision</b>	<b>87</b>
8.1	Particle collision . . . . .	88
8.2	Particle accelerator . . . . .	88
8.2.1	Distorted Schwarzschild . . . . .	89
8.2.2	q-metric . . . . .	90
8.3	Summary and conclusion . . . . .	91
<b>9</b>	<b>Cognitive study on the Stationary q-metric</b>	<b>93</b>
9.1	Ernst potential . . . . .	93
9.2	Effective potential . . . . .	96
9.3	Summary and conclusion . . . . .	99
<b>10</b>	<b>Thin accretion disc model in Generalized q-metric</b>	<b>101</b>
10.1	The valid region . . . . .	102
10.2	Properties of the Thin disc model . . . . .	103
10.3	Summary and conclusion . . . . .	108

<b>11 Thick accretion disc model</b>	<b>111</b>
11.1 Magnetized Thick disc in distorted Schwarzschild . . . . .	112
11.1.1 Discussion on the constant angular momentum . . . . .	112
11.1.2 Discussion on the power-law distribution . . . . .	117
11.1.3 Discussion on the trigonometric distribution . . . . .	121
11.1.4 Summary and conclusion . . . . .	122
11.2 Magnetized Thick disc in Static q-metric . . . . .	126
11.2.1 Discussion on the power-law angular momentum . . . . .	127
11.2.2 Discussion of the trigonometric angular momentum . . . . .	131
11.2.3 Summary and conclusion . . . . .	139
11.3 Thick disc in Stationary q-metric . . . . .	140
11.3.1 Discussion on the constant angular momentum . . . . .	140
11.3.2 Summary and conclusion . . . . .	143
11.4 Magnetized Thick disc in C-metric . . . . .	143
11.4.1 Von Zeipel radius . . . . .	143
11.4.2 Discussion on the constant angular momentum . . . . .	146
11.4.3 Summary and conclusion . . . . .	149
<b>12 QPOs in Generalized q-metric in the uniform magnetic field</b>	<b>153</b>
12.1 Epicyclic frequencies and stability of circular motion . . . . .	154
12.2 Different possibilities . . . . .	160
12.3 Comparison with the observations . . . . .	163
12.4 Summary and conclusion . . . . .	167
<b>13 Oscillations of tori in the background of Generalized q-metric</b>	<b>169</b>
13.1 The Thick disc model . . . . .	169
13.2 Radial epicyclic frequency . . . . .	171
13.3 Summary and conclusion . . . . .	174
<b>14 Shadow in the presence of cold plasma in the background of q-metric</b>	<b>177</b>
14.1 Photon sphere . . . . .	177
14.2 Radius of Shadow in the low density plasma . . . . .	179
14.3 Summary and conclusion . . . . .	181
<b>15 Stability analysis of circular geodesics in Generalized q-metric</b>	<b>185</b>
15.1 Existence of equilibrium points . . . . .	185
15.1.1 For time-like geodesics . . . . .	188
15.1.2 For light-like geodesics . . . . .	189

15.2 Lyapunov linear Stability . . . . .	190
15.3 Jacobi nonlinear stability . . . . .	191
15.4 Kolmogorov entropy . . . . .	192
15.5 Summary and conclusion . . . . .	193
 <b>III Epilogue</b>	 <b>195</b>
 <b>16 Summary</b>	 <b>197</b>
 <b>17 Outlook</b>	 <b>201</b>
 <b>Bibliography</b>	 <b>205</b>

## Acknowledgements

I want to express my sincere gratitude to Dr. Eva Hackmann, apart from the valuable scientific discussions which I gratefully appreciate. First, for providing me with this opportunity to study my PhD in the field that, without any doubt, I am willing to dedicate my life to! Second, I remember after initiating my first project and having some results; frankly, she let me choose to work on the related areas that I suggested. It helped me stay motivated, creative, and work with pleasure. I couldn't ask for a better... . Thank you!

I would like to thank Prof. Claus Laemmerzahl for his encouragement, positive attitude, and intriguing discussions that inspired me to enjoy working even more... . Thank you!

Dr. Audrey Trova stands out not only as my collaborator but also as my friend... . Together we always remember: focusing on the everyday goals, improving every day, and dreaming bigger. Thank you Audrey! For your trust, knowledge, and kindness... .

I have had the great pleasure and good fortune to learn with many wonderful scientists who made a significant contribution to my understanding of Mathematics, Physics and Astrophysics, also doing research, and I always remember gratefully include: Prof. Alexander Grigoryan, Prof. Michel Roeckner, Prof. Ramesh Narayan, Prof. Hernando Quevedo, Prof. Mehdi Golshani, Prof. Niayesh Afshordi, Prof. Vladimir Karas, Prof. Kamran Kaviani, Prof. Siavash Shahshahani, and Prof. Maryam Mirzakhani.

More important than the number of falls we take in life, is how fast and strong we get back on our feet. This is possible when surrounded by great people. Thank my amazing supporters: my family and my friends especially Elham, Asal, Taymaz, Sahar, and Parsa.

Special acknowledgement is due to those who demonstrated great support in different ways: Prof. Marc Avila, Mrs. Maria Petrogiannis, Mrs. Andrea Fischer, Mrs. Annette Leonhardt, Mrs. Sabine Vogelsang.

I offer additional acknowledgement to everyone who helped me grow with their judgments and criticisms.



# Part I

## Prologue





## CHAPTER 1

# Preface

### 1.1 General motivation

Gravity is responsible for enkindling various spectacularly astrophysical events. Einstein's theory of gravity so far provides the best description of gravitational interactions. In addition, this is also responsible for the existence of mysterious black holes.

Theoretical and observational efforts are being pursued to understand and test general relativity in many ways. The ideal regime for such surveying involves the strong gravitational fields in the vicinity of the astrophysical black holes and compact objects which are not directly accessible because of their nature. Hopefully, the situation is being better, thanks to great technological advancements. Nowadays, the significant efforts of astrophysicists and astronomers are devoted to improving the accuracy of astrophysical observations and fitting within the theoretical models. Large international collaborations like the Event Horizon Telescope, GRAVITY, the Advanced Telescope for High ENergy Astrophysics, the Fermi Gamma-ray Space Telescope, the Square Kilometers Array, the LIGO/Virgo and LISA focus on compact relativistic objects, among them very prominently the supermassive black hole at the center of our galaxy, Sagittarius A\*, and the one in the galaxy *M87*. In fact, our only source of information from the strong gravity produced by black holes and other compact objects comes from their fingerprint on the surrounding astrophysical environments, among them are accretion discs. Accretion discs can reach deeply into the vicinity of these objects.

An accretion disc generally consists of fluid orbiting around an astrophysical system. The matter orbiting in the gravitational field of the central mass loses its angular momentum and gradually spirals inward. Besides, the geometrical characteristics of the accretion discs depend on their back-

ground. Studying accretion discs is currently a topic of widespread interest in astrophysics that links different research areas from fundamental physics to high-energy astrophysics.

Furthermore, the existence of high-frequency peaks in the Fourier power spectra of X-ray radiation observational data from accreting compact sources connected to the so-far unexplained rapid variability known as high-frequency quasi-periodic oscillations. This important nowadays puzzle is usually supposed to originate from the orbital motion in the innermost parts of an accretion disc, which again shows the importance of studying accretion discs, as well as searching for different theoretical set-ups.

In addition, some stellar-mass black holes have received recoil velocity at their formations. There is a widespread agreement but not yet set exactly that the birth kicks of black holes are necessary to explain the large distances above the Galactic plane achieved by some binaries [1] and caused the black hole to accelerate within a local cosmological medium.

Moreover, the deformation of a compact object is a measurable effect on the physics of astrophysical systems like binaries, which play an important role in testing General Relativity. Most of them are caused by rotation; however, some intrinsic properties like quadrupole can lead to deformation. Although such an effect would be minimal, its influence can still manifest, for example, through the creation of gravitational waves or power density spectra, or as discussed in [2], in the case of extreme mass ratio inspiral (EMRI), one can extract the multipole moments from the gravitational wave signal, and any non-Kerr multipole moments should be encoded in the waves. Therefore, we can expect this metric to be applicable in studying gravitational waves generated in an EMRI.

Mostly, it is assumed that astrophysical black holes are described by the Kerr solution. However, besides these setup, others can also imitate a black hole's properties which makes it challenging to decide when one tries to link the models to the observation [3, 4, 5]. In fact, the black hole mimickers' issue is a topic currently of significant interest in the general relativity and astrophysics communities and has recently become quite popular. For instance, in the last case of recoil velocity, the author believes that considering the acceleration parameter in this setup instead of the Kerr solution may provide the first step towards a (semi-) analytical description of this behavior.

To sum up, astrophysical observations may not all well-fitted within the general theory of relativity by employing just a restricted family of Kerr space-time. It appears entirely natural to explore departures due to exercising relatively small parameters in the metric that can be taken as the additional physical degrees of freedom to the system and facilitate the link to the observational data that they can be interpreted as rotation or not.

These crucial issues are particularly challenging tasks yet to be overcome and require more study on the analytical models in the first place in parallel to developing new capabilities to check them in simulations.

## 1.2 Aims

This thesis main aims are:

- to Introduce a generalization of the static q-metric via considering the external distribution of matter characterized by the set of multipole moments.
- the Characterization of the impact of the external fields up to the quadrupole on the circular geodesics and the interplay of these two quadrupoles in the place of the Innermost Stable Circular Orbit (ISCO) where consider as the inner edge of the accretion discs in the equatorial plane.
- understanding of the effects of quadrupole and acceleration parameter (in C-metric) on the dynamics of matter, the morphology of the equilibrium configuration of the Thick discs, as well as properties of the Thin accretion discs and see if the space-times with quadrupole can act as black hole mimickers.
- the Characterization of the impact of the Generalized q-metric space-time and magnetic field parameters on the predicted quasi-periodic oscillations frequencies analytically and fit to the observational data and see if this metric can mimic the behavior of the Kerr metric.
- the comparison of the photon sphere position and radius of shadow in q-metric considering the space-time filled with cold plasma and see the similarities in the results with the Schwarzschild black hole.
- understanding the stability nature of the geodesics of Generalized q-metric and their chaos behavior.

## 1.3 Methodology

Realistic scenarios are usually models based on numerical methods and simulations. Nowadays, new analytic solutions continue to be produced and examine their ability to fit into data and serve in simulations. Of course, each method has its benefits and drawbacks. However, developing analytic

tools can provide a more complete understanding of the physical processes inside.

In fact, analytical studies are the underlying surface of numerical approaches and simulations. For example, the importance of the analytical methods can be seen especially in determining the last stable spherical and circular orbits, which are starting points for studying the accretion disc theories. In particular, the analytical approach offers a framework to test the accuracy and reliability of the mentioned methods. Furthermore, on the one hand, numerical simulations consider space parameters where the choice of the parameters is critically involved, and on the other hand, massive use of expensive numerical calculations leaves little room for a physical interpretation. However, analytical approaches demonstrate how exactly an effect depends on these parameters and they bring out the general features more clearly. In addition, they may serve as the systematical study of the characteristics of all observable in a given space-time which is the unique way of their understanding.

In this thesis, the analytical and semi-analytical approaches are hired to explore different alternatives that may open the door to a broader range of applications. However, in the quasi-oscillation study, we examine them by testing their ability to fit the observations.

## 1.4 Thesis outline

The thesis consists of three parts.

- Part I is thought of as an introduction to the main topics of research of the thesis. It is a brief review of the necessary background material, as seen from the point of view of the author and for the aims of this thesis, with references to the literature:

Chapter 2 introduces the analytical accretion disc models with particular care to their derivations. The Thin disc and the system of assumptions and equations are presented. Afterwards, the Thick disc model and its construction for both versions with and without a magnetic field are described. This information will be needed in the rest of the work in different parts.

Chapter 3 deals with the quasi-periodic oscillations and is devoted to describing the observation properties and the stable frequencies ratio observed in the high-frequency quasi-periodic oscillations, as well as theoretical models that serve to overcome this issue. In particular, resonance models, and oscillation of Thin and Thick disc models with

the test particle approach and the perfect fluid approach, respectively. In Chapter 4 the equation of motion for a light ray in a cold plasma is presented as well as the impact of the plasma on the radius of shadow. In Chapter 5 the mathematical tool to explore the linear Laypunov and non-linear stability analysis of the geodesics based on the Noether theorem is introduced. In addition, the Kolmogorov entropy which is a measurement in the study of chaotic behavior of the trajectories in a given space-time, is outlined. To conclude the background part, chapter 6 introduces the reader to different space-times considered in this thesis. They belong to the Weyl class of solutions. In particular, the C-metric belongs to the large class of Levi-Civita exact solutions, where also can be obtained from the Weyl metric by taking the limit of its Newtonian image source length tends to infinity.

- Part II consists of original contributions of the author to the literature:

Chapter 7 the construction of an alternative generalization of the static q-metric that describes a deformed compact object in the presence of external fields characterized by multipole moments is introduced. This metric gives an opportunity to study a non-isolated deformed compact object. Besides, this generalization is worth considering to have more vacuum metrics available, for example, to study the interplay of the vacuum solution with an external field. Therefore, it may be of some interest to investigate how the external field affects the geometry and geodesics of the q-metric. In addition, the effective potential, circular geodesics, and the stable circular orbits in the equatorial plane up to quadrupole are investigated. Since the properties of congruences of circular and quasi-circular orbits in an axisymmetric background seem vital to comprehend accretion processes in the vicinity of compact objects. The stable circular orbits, in particular, are important to study the accretion discs in the vicinity of a compact object. They encode information about the possibility of the existence of the discs and are considered as the inner boundary of the Thin accretion disc with a high accuracy [6]. Moreover, the radial and vertical epicyclic frequencies are the most important characteristics of these orbits that are crucial to understanding observational phenomena such as quasi-periodic oscillations, which is a quite profound puzzle in the x-ray observational data of accretion discs [7, 8, 9]. To have a comparison of the results with the q-metric the circular motion in this metric with a slightly different approach than the literature is presented. Moreover, the dynamics of a charged particle in this space-time in the presence of an asymptotically uniform magnetic field via the Hamiltonian approach are discussed,

and different bounded trajectories are studied.

Chapter 8 addresses the issue of examining the possible collision scenario in the background of the Generalized  $q$ -metric. In particular, this question is answered if the distorted Schwarzschild or  $q$ -metric background can act as an accelerator of particles that cause high energy in their vicinities. This study aims to have behavior of this solution to be able to have a comprehensible comparison with different space-times, especially with the Kerr solution at the end.

Chapter 9 explores some of the important features of the rather new exact analytical solution to Einstein's theory, the stationary  $q$ -metric described in Chapter 6. To this aim, the Ernst potential and effective potential of this metric in the equatorial plane are investigated. Besides, different types of trajectories are investigated semi-analytically. This investigation is needed to understand the existence and properties of bounded geodesics in the equatorial plane to construct Thick accretion discs in Chapter 11.

Chapter 10 deals with the Thin accretion disc properties in the background of Generalized  $q$ -metric. As this metric valid locally by its construction, in the first step the valid region is been investigated with respect to the parameter of the metric. In the second step, the properties of the model are presented that show new features that open up the possibility to fit this model to the observational data.

Chapter 11 presents an extensive study on the magnetized and unmagnetized Thick accretion discs in different space-times described in Chapter 6 with constant and non-constant angular momentum are discussed. In all cases, new features of equilibrium configurations of the disc structure are investigated. Among them is exploring this disc model around the  $C$ -metric. First, this study is applied to the question of whether the acceleration parameter in this space-time has a significant contribution to the properties of this model in comparison to the charge and rotation parameters.

Chapter 12 investigates one of the important observational phenomena related to epicyclic frequencies of circular motion with and without presenting a magnetic field in the background of the Generalized  $q$ -metric. In addition, explore the ability of this metric to fit into the observed frequencies of three microquasars XTE 1550 – 564, GRS 1915 + 105, and GRO 1655 – 40.

Chapter 13 presents the equipotential sequences of the Thick disc in the Generalized  $q$ -metric, also studies the oscillation of these discs via

the local perturbation approach. Subsequently, it highlights the importance of considering a perfect fluid model rather than a test particle one to study the radial epicyclic frequency of this oscillation.

Chapter 14 applies the method described in Chapter 4 to the q-metric and investigates the size of the radius of shadow in this space-time considering cold plasma. The result is compared with the shadow properties in the counterpart space-time; namely, the Schwarzschild solution.

Chapter 15 generalizes the method described in Chapter 5 to the Generalized q-metric. The conditions for having the equilibrium points are derived depending on the parameters of the metric. Then possible types of stable motion are classified. Finally, this method can apply to the off equatorial plane trajectories, which is future work in this direction. In addition, this study explores the conditions in terms of the quadrupoles in the metric that can be interpreted as the chaotic behavior of the solution via the Kolmogoroph entropy, which is linked to the physical entropy. Of course, the chaotic behavior can consider in the accretion disc models as an effort to present a new analytical model of accretion discs describing more realistic scenarios.

- The summary and outlook are presented in Part III.

Throughout this thesis, we use the signature  $(-, +, +, +)$  and geometrized unit system  $G = 1$ ,  $c = 1$ , and  $M = 1$ ; however, it stated otherwise. Latin indices run from 1 to 3, while Greek ones are from 0 to 3.





## CHAPTER 2

# Analytical accretion disc models

Accretion disc theory is classified in fundamental physics. Because accretion discs can reach deeply into the strong field regime in the vicinity of the black hole or a massive compact object. In addition, the accretion disc is one of the widespread interest phenomena in high-energy astrophysics from the protoplanet to gamma-ray bursts (GRBs), X-ray binaries, and the active galactic nuclei (AGN).

However, no unified theoretical accretion disc model could explain all the basic properties of these sources. In fact, the theory itself endure several phenomenological estimations and complexities like dynamics, equilibrium, stability under perturbations, and formation of jets. Each of the models has some properties that are the best fit for the observation. Investigation of such systems, either by analytical or numerical methods, may rely on the ability to construct suitable models based on physical assumptions. There are impressive studies in this area, analytically or by using simulation in a complementary fashion.

Analytic and semi-analytic models for accretion onto a compact object are generally stationary and axially symmetric. Among these successful theoretical models are the Thin accretion disc model, and the Thick disc model with a toroidal shape.

In this thesis, we consider both and study their properties and structure in different space-times 10, 11.1, 11.2, 11.3, and 11.4. In addition, the results compared with their counterpart Schwarzschild or Kerr solutions in all possible cases. In the next section, we study the Thin disc model and later the Thick disc model in section 2.2.

## 2.1 Thin accretion disc

Accretion discs establish when gaseous matter spirals onto a central object by gradually losing its initial angular momentum and forming a disc-like configuration in which angular momentum is transported outwards due to the differentially rotating fluid, which causes gas to be accreted onto the central object.

The standard Thin disc is a fascinating analytical model of accretion, was proposed and developed in the seminal works by Shakura & Sunyaev [10], Bardeen, Press & Teukolsky [11], Novikov & Thorne [12] in 1973, and Lynden-Bell & Pringle 1974 [13]. This model has been used to explain a variety of observations where the gas is cold and neutral in such a way that coupling between the magnetic field and the gas is negligible, e.g., [14, 15]. In general, observations provide the luminosity and the maximum temperature of the disc that enables us to fit the model to the data.

### 2.1.1 Assumption of the model

In the Thin standard accretion model, it is supposed that the disc can radiate a considerable fraction of its rest mass energy locally. This radiation is thermal black body-like radiation which is generated through the viscosity mechanism that we explain later. As a result, the Thin disc model is considered as the cold accretion disc. Since, depending on the mass of the central object, the gas temperature is in the order of 100 K which is considered cold regarding the virial temperature. For example, this model cannot produce a very high temperature ( $T > 10^{10}$  K) observed in the Galactic Center source Sgr A\* [16].

One of the crucial assumptions of the standard Thin disc is that it is taken to be razor thin and confined to the equatorial plane, meaning the ratio of the disc half-thickness  $H = H(r)$  over the radius  $r$  is very small,  $H/r \ll 1$ . As a result, the generated heat and radiation losses are in balanced  $Q^{\text{gen}} = Q^{\text{rad}}$ , and caused to have a negligible advection, since

$$Q^{\text{adv}} \sim \left(\frac{H}{r}\right)^2 Q^{\text{gen}}. \quad (2.1)$$

Consequently, it causes to luminosities be approximately below 30% of the Eddington luminosity,

$$L_{\text{Edd}} := 1.26 \times 10^{38} \left(\frac{M}{M_{\odot}}\right) \frac{\text{erg}}{\text{s}} \quad (2.2)$$

or the mass accretion rate  $\dot{M}$  be below the Eddington rate  $\dot{M}_{\text{Edd}}$ <sup>1</sup>. Above this limit, the gas becomes optically too thick and can not radiate all the dissipated energy locally [18, 19]. Therefore, one should justify applying the standard Thin model to discs with higher luminosity. Interestingly, also magnetized Thin accretion discs in X-ray binaries, at luminosities below 30% of Eddington, can be described by the Thin disc model successfully [20].

The solution to the Thin disc model can only be found by applying certain well-known assumptions that the model is based on. Following the approach of [10], one assumes that the specific internal energy density is negligible and the disc lies in the equatorial plane, implying  $u^\theta$  component of fluid four-velocity vanishes, also quasi-Keplerian circular orbits are assumed with a small radial drift velocity  $u^r$ , which is much smaller than the angular velocity. Near the central compact object,  $u^r$  is negative and gives rise to mass accretion. Also, no mass or angular momentum crosses the disc surfaces. Besides, the self-irradiation of the disc, and the loss of angular momentum due to wind and radiation are neglected. We consider the sub-Eddington accretion rate, which is the proper choice for the Thin disc model as it was discussed. The inner edge of a Thin accretion disc with sub-Eddington luminosities is the inner boundary of the region that most of the luminosity comes from, and this happens to be at the Innermost Stable Circular Orbit, ISCO.

In this model, the shear stress is supposed to be a form of viscosity responsible for transporting angular momentum and energy outward and accreting matter inward. Also, it heats the gas locally. This model introduces viscosity through a so-called  $\alpha$ -prescription without specifying the concept of the viscosity itself.

However, according to the very high Reynolds number, the viscosity in the accretion process can not be the same as molecular viscosity and may have a magnetic nature [21, 22].

Almost all the accretion disc models assume the dimensionless parameter  $\alpha$  to be a constant in this range  $0.01 - 0.1$  [23]. However, global magnetohydrodynamic simulations argued that  $\alpha$  is a function of  $r$ .

The standard  $\alpha_v$  viscosity prescription of the Shakura-Sunyaev model is assumed

$$S_{\hat{r}\hat{\phi}} = \alpha_v P, \quad (2.3)$$

where  $S_{\hat{r}\hat{\phi}}$  is the only non-vanishing component of viscous (internal) stress-energy tensor in the fluid frame, and  $P$  is pressure. In addition, there is

---

<sup>1</sup>There are other definitions of  $\dot{M}_{\text{Edd}}$  are used in the literature that one can see for example in [17]

another version of this prescription that is commonly used in terms of the vertically averaged sound speed and the vertical half-thickness of the disc, as

$$\nu \simeq \alpha_v c_s H, \quad (2.4)$$

which one should take it by cautious [24].

In an effort to modify the  $\alpha_v$ -prescription, in the literature in general, there are two ways, by considering  $\alpha_v$  as a function of radius, or keeping  $\alpha_v$  a constant and multiplying this by a factor e.g. [25, 26, 27].

Furthermore, in the first model, the authors assumed within the ISCO, the viscous torque vanishes, and material digs into the central object with the constant energy and angular momentum flux in its frame. This is called the zero-torque boundary condition. However, there has been debate on the validity of this assumption. Some theoretical works suggested that a non-zero-torque at the inner boundary can emerge due to a magnetic field, e.g., [28, 29]. However, Paczyński in 2000, based on the angular momentum conservation equation, and followed by the work of Abramowicz & Kato in 1989, argued that as long as the shear stress is smaller than the pressure, the Thin disc always satisfies the zero-torque condition. Later Afshordi & Paczyński [6] suggested that the torque at the ISCO is an increasing function of the disc thickness and at the inner edge is small. Further, the inner edge of the disc is almost identical to the place of ISCO. Besides, this result was satisfied by GRMHD simulations, e.g., [19, 20] and was shown that for a very Thin disc, inside the ISCO, the viscous dissipation is negligible, and the dissipation profile is identical to that predicted by the standard disc model. In [30] was argued that in the evolution of Thin discs, the vanishing stress boundary condition will be recovered.

Interestingly, this fact motivated the idea that one can estimate the spin of the black hole by measuring this radius. By the continuum fitting technique, this radius is determined from the temperature maximum of the soft X-ray flux [31].

### 2.1.2 Equations of the model

In this section, we introduce the structure of the Thin accretion disc and state the assumptions and equations in terms of  $(t, r, \theta, \phi)$  coordinate to be able to focus on the fundamental physics of the problem and to avoid being distracted by technical details. One could use the transformations (6.10) to rewrite them in prolate spheroidal coordinates easily.

We assume a steady axisymmetric fluid configuration. All physical quantities depend on the vertical distance from the equatorial plane and the radial

distance from the central object in these models. As a result of the geometrically thin assumption, the two-dimensional disc structure can be decoupled into two one-dimensional configurations: radial quasi-Keplerian flow and a vertical hydrostatic structure. In this model, usually, a vertically integrated approach is used. Namely, we integrate along with the height of the disc and neglect the  $z$ -dependences of the relevant quantities. However, when the accretion rate is significant, one should consider the  $z$ -dependence of fluid quantities [16].

Three fundamental equations govern the radial structure of the Thin disc model. First, the particle number conservation

$$(\rho u^\mu)_{;\mu} = 0, \quad (2.5)$$

where  $u^\mu$  is the four-velocity of the fluid and  $\rho$  is the rest mass density. The mass accretion rate is connected to this conservation law, meaning we expect the mass accretion rate to be constant; otherwise, we would see matter pile up at some certain region of the disc. The other equations are described by the radial component of conservation of energy-momentum tensor  $T^{\mu\nu}_{;\nu} = 0$ , parallel to the four-velocity

$$u_\mu T^{\mu\nu}_{;\nu} = 0. \quad (2.6)$$

And the radial component of projection of this conservation onto the surface normal to the four-velocity

$$h_{\mu\sigma}(T^{\sigma\nu})_{;\nu} = 0, \quad (2.7)$$

where  $h^{\mu\nu} = u^\mu u^\nu + g^{\mu\nu}$  is the projection tensor giving the induced metric normal to  $u_\mu$ . The stress-energy tensor  $T^{\sigma\nu}$  reads as

$$T^{\mu\nu} = \omega u^\mu u^\nu - p g^{\mu\nu} + q^\mu u^\nu + q^\nu u^\mu + S^{\mu\nu}, \quad (2.8)$$

where  $\omega$  is enthalpy density, which is the sum of internal energy per unit of proper volume and pressure over rest-mass density,  $p$  is the pressure,  $u^\mu$  is four-velocity of fluid,  $q^\nu$  is transverse energy flux, and  $S^{\mu\nu}$  is the viscous stress-energy tensor. In relativistic form, when we have no bulk viscosity, it is given by  $S^{\mu\nu} = -2\lambda\sigma^{\mu\nu}$ , where  $\lambda$  is the dynamical viscosity and  $\sigma^{\mu\nu}$  is the shear tensor, where the only non-vanishing component according to assumptions of the Thin disc model is

$$\sigma_{r\phi} = \frac{1}{2}(u_{r;\beta}h^\beta_\phi + u_{\phi;\beta}h^\beta_r) - \frac{1}{3}h_{r\phi}u^\beta_{;\beta}. \quad (2.9)$$

The shear rate is a measure of the rate of change of the angular velocity with the radius. However, the shear rate is the local measurement, and in the model, we should consider this component measured in the fluid frame  $\sigma_{\hat{r}\hat{\phi}}$ . Indeed, this frame is a proper frame to do minimal modifications to an inviscid flow and contains an orthogonal or nonholonomic basis concerning the chosen metric. This basis is with respect to the local Lorentz frame and used by a real observer versus the holonomic basis that represents the global space-time. Apart from the Cartesian one, they are not orthogonal. In general, one can obtain the nonholonomic basis from the holonomic one by applying the Gram-Schmidt process. The relation between  $\sigma_{\hat{r}\hat{\phi}}$  and  $\sigma_{r\phi}$  is given by

$$\sigma_{\hat{r}\hat{\phi}} = e^r_{\hat{r}} e^{\phi}_{\hat{\phi}} \sigma_{r\phi}, \quad (2.10)$$

where the basis  $e^{\nu}_{\hat{\nu}}$  contains orthonormal vectors. This basis is scaled by the coefficient in the original metric to obtain a unit vector.

By applying the assumptions of the Thin disc model on the basic equations (2.5)-(2.7) together with the relations describing radiative energy transport and vertical pressure gradient, we end up with a system of nonlinear algebraic equations governing this model [12], as follows.

The surface density  $\Sigma$  is obtained by vertical integration of the density,

$$\Sigma = \int_{-H}^{+H} \rho dz = 2\rho H, \quad (2.11)$$

where  $H$  is disc height or half of the thickness of the disc.

For steady accretion through the Thin discs, it is often assumed that the boundary conditions determine the mass accretion rate at a large distance from the central object. Considering this assumption and after vertical and radial integration of the continuity equation, the mass accretion rate is given by

$$\dot{M} = -2\pi\sqrt{-|g|}u^r\Sigma = \text{constant}, \quad (2.12)$$

where  $u^r$  is the radial velocity of inflow and  $|g|$  is the determinant of metric. However, under some circumstances, the expression for  $\dot{M}$  may not be that simple [32]. So, the radial velocity of the fluid which is responsible for accreting mass is obtained in terms of the mass accretion rate  $\dot{M}$

$$u^r = -\frac{\dot{M}}{2\pi\sqrt{-|g|}\Sigma}. \quad (2.13)$$

Although the motion is nearly circular in the disc, by passing the ISCO, the radial velocity increases rapidly.

Following the assumption of Thin disc models, the heat flow was assumed to be in the vertical direction, meaning  $q^z$ . Therefore, the time-averaged flux of radiant energy (energy per unit proper area and proper time) flowing out of upper and lower surfaces  $F$  relates to the heat flow as [33, 12]

$$q^z(r, z) = F(r) \frac{z}{H(r)}. \quad (2.14)$$

By using the fundamental equations (2.5), (2.7), (2.6) and usual manipulation with assumptions we obtain

$$\frac{(\Omega L - E)^2}{\Omega_{,r}} \frac{F\sqrt{-|g|}}{\dot{M}} = \int_{r_0}^r \frac{(\Omega L - E)}{4\pi} L_{,r} dr, \quad (2.15)$$

where  $E$  and  $L$  are the energy and angular momentum per unit mass of geodesic circular motion in the equatorial plane, and  $\Omega$  is the corresponding angular velocity [34].

The vertically integrated viscous stress  $W$ , whose obtained by vertical integration of the viscous stress  $S^{\hat{r}\hat{\phi}}$  equation (2.3) is given by

$$W = \int_{-H}^{+H} S^{\hat{r}\hat{\phi}} dz = 2\alpha_v P H. \quad (2.16)$$

The vertical integration generated energy flux via viscosity reads as

$$F = - \int_{-H}^{+H} \sigma_{\hat{r}\hat{\phi}} S^{\hat{r}\hat{\phi}} dz = -\sigma_{\hat{r}\hat{\phi}} W. \quad (2.17)$$

According to the models' assumptions, at each radius, the emission is like black body radiation. The energy transportation law is given by

$$aT^4 = \Sigma F \kappa, \quad (2.18)$$

here  $\kappa$  is the Rosseland-mean opacity,

$$\kappa = 0.40 + 0.64 \times 10^{23} \left( \frac{\rho}{\text{g}} \right) \left( \frac{T}{K} \right)^{-\frac{7}{2}} \text{cm}^2 \text{g}^{-1}, \quad (2.19)$$

where the first term is electron scattering opacity and the second one is free-free absorption opacity. And  $a$  is the radiation density constant given by

$$a = \frac{4\sigma}{c}, \quad (2.20)$$

where  $\sigma$  is the Stefan-Boltzmann's constant.

In general, for the vertical direction in the comoving frame of fluid, the force due to vertical pressure gradient is the balance with gravity, the centrifugal force, and vertically Euler force <sup>2</sup>. The pressure  $P$  is the sum of gas pressure from nuclei and the radiation pressure

$$P = \frac{\rho k T}{m_p} + \frac{a}{3} T^4, \quad (2.21)$$

where  $m_p$  is the rest mass of the proton,  $k$  is Boltzmann's constant,  $a$  is the radiation density constant, and  $T$  is the temperature. In fact, we ignore the mass difference between neutrons and protons in the first term for simplicity. In practice, the pressure equation in the vertical direction is given by

$$\frac{P}{\rho} = \frac{1}{2} \frac{(HL)^2}{r^4}, \quad (2.22)$$

which is derived from the relativistic Euler equation with no additional simplifications [35, equation 28].

By solving these eight equations (2.11), (2.13), (2.15), (2.16), (2.17), (2.18), (2.21) and (2.22), one obtains the radial profiles of the eight variables in the model, namely the half-thickness of the disc over radius  $\frac{H}{r} = h$ , surface density  $\Sigma$ , the central temperature  $T$ , pressure  $P$ , the radial velocity  $u^r$ , the radiation flux  $F$ , viscous stress  $W$  and  $\rho$  and from them one can calculate other physical quantities subsequently. All these parameters are functions of the distance from the central object. We utilize the Thin accretion disc model formalism in Chapter 10 and some of the related properties in the quasi-periodic oscillations in Chapter 12.

---

<sup>2</sup>Of course, in this frame, the Coriolis force vanishes.



## 2.2 Thick accretion disc

The Thick disc is the simplest analytic model of the hydrodynamical structure of an accretion disc with no accretion flow based on the Boyer's condition<sup>3</sup> was presented in these seminal works [36, 37, 38, 39, 40, 41, 42, 43]. Initially, the disc model presents a highly super-Eddington accretion, with low viscosity, rotating accretion flows that are optically thick, radiation pressure supported, cooled by advection, and radiatively very inefficient.

The Thick discs are believed to be present in quasars and other active galactic nuclei, some X-ray binaries, microquasars, and in the central engine of gamma-ray bursts. As numerical simulations show, such events often result in a black hole surrounded by a torus (see e.g. [44, 45, 46, 47]).

In this model, the equation of state is taken to be barotropic, and self-gravity is negligible. We briefly explain this model in the static case that we have studied. In general, the stationary metric, in the spherical coordinates, reads as

$$ds^2 = g_{tt}dt^2 + g_{t\phi}dtd\phi + g_{rr}dr^2 + g_{\theta\theta}d\theta^2 + g_{\phi\phi}d\phi^2. \quad (2.23)$$

where components of metric only depend on  $r$  and  $\theta$ . Also, rotation of perfect fluid is assumed to be in the azimuthal direction; therefore the four-velocity and a perfect fluid stress-energy tensor<sup>4</sup> simplifies to

$$u^\mu = (u^t, 0, 0, u^\phi), \quad (2.24)$$

$$T^\mu{}_\nu = (\epsilon + p)u_\nu u^\mu - \delta^\mu{}_\nu p, \quad (2.25)$$

here  $\epsilon$  is the proper energy density, and  $p$  is isotropic pressure as measured by an observer moving with the fluid. In fact, in this model, the time-scale of dynamic processes, involving pressure, centrifugal and gravitational forces, are considered to be smaller than thermal ones and therefore than the viscous time-scale. This implies that in  $T^\mu{}_\nu$  the dissipation due to the viscosity and the heat conduction be neglected. Adopting the definition of the specific angular momentum and the is the coordinate angular velocity as observed from infinity in the static case, we have

$$\ell = -\frac{u_\phi}{u_t}, \quad \Omega = \frac{u^\phi}{u^t}, \quad (2.26)$$

---

<sup>3</sup>Boyer's condition states the boundary of any stationary and barotropic perfect fluid body is an equipotential surface.

<sup>4</sup>The stress-energy tensor is stated here is the same as the one used in the description of the Thick disc in the literature.

It is worth mentioning that this is not the only definition for  $\ell$  and normally it is defined as a constant of geodesic motion in axially symmetric space-times as only the nominator  $u_\phi$ . However, for non-zero pressure, instead  $hu_\phi$  is a constant of motion, where  $h$  is specific enthalpy. For axially symmetric and stationary space-times the above relation (2.26) is a constant for both geodesic and perfect fluid motion. We also have their relationship as

$$\ell = -\frac{\Omega g_{\phi\phi} + g_{t\phi}}{\Omega g_{t\phi} + g_{tt}}, \quad \Omega = -\frac{\ell g_{tt} + g_{t\phi}}{\ell g_{t\phi} + g_{\phi\phi}}. \quad (2.27)$$

Besides, the corresponding redshift factor is given by

$$(u_t)^{-2} = -\frac{\ell^2 g_{tt} + 2\ell g_{t\phi} + g_{\phi\phi}}{g_{t\phi}^2 - g_{tt}g_{\phi\phi}}. \quad (2.28)$$

In this model, the motion of the fluid is described by the continuity equation

$$u^a \nabla_a \epsilon + (\epsilon + p) \nabla^a u_a = 0, \quad (2.29)$$

and the Euler equation

$$(\epsilon + p) u^a \nabla_a u^c + h^{bc} \nabla_b p = 0, \quad (2.30)$$

where  $h_{ab} = g_{ab} + u_a u_b$ . In general, by utilizing the conditions of hydrostatic equilibrium and axisymmetry simplifies the hydrodynamical equations and reduces them to Bernoulli-type equations [48],

$$\frac{1}{\epsilon + p} \nabla_i p = -\nabla_i \ln u_t + \frac{\Omega \nabla_i \ell}{1 - \Omega \ell} \quad (2.31)$$

where  $i$  is  $r$  or  $\theta$ . This leads to  $\Omega = \Omega(\ell)$ . Or equivalently

$$\frac{1}{\epsilon + p} \nabla_i p = \nabla_i \ln u^t - \frac{\ell \nabla_i \Omega}{1 - \Omega \ell} \quad (2.32)$$

where this gives  $\ell = \ell(\Omega)$  [49]. For a barytropic equation of state,  $p = p(\rho)$ , where  $\rho$  is the rest-mass density, this leads to

$$\int_{p_{\text{in}}}^p \frac{dp}{\epsilon + p} = -\ln |u_t| + \ln |(u_t)_{\text{in}}| + \int_{\ell_{\text{in}}}^\ell \frac{\Omega d\ell}{1 - \Omega \ell}, \quad (2.33)$$

where the subscript *in* refers to the inner edge of the disc. This relation implies  $\Omega = \Omega(\ell)$  and satisfies the general relativistic version of the von Zeipel theorem, which states for a toroidal magnetic field, the surfaces of constant  $p$  coincide with constant  $w$ , if and only if constant  $\Omega$  and constant  $\ell$  coincide [50, 51]. However, for the non magnetized version, the surface of equal  $\Omega$ ,  $\ell$ ,  $p$  and  $w$  all coincide [48]. Therefore, by specifying  $\Omega = \Omega(\ell)$ , one can construct the model via solving equation (2.27) for  $\Omega$  or  $\ell$ . Then from equation (2.33), one obtains  $W(r, \theta)$  and  $p(r, \theta)$ . This model can be adapted for either constant or a non-constant angular momentum distribution. We explore more about this while constructing the magnetized version.

### 2.2.1 Magnetized version

There is no doubt on the role of the magnetic fields in the study of astrophysical systems. In the processes occurring in the vicinity of compact objects, the magnetic fields can manifest their fingerprint in many ways, for example in the accretion process in MRI simulations [21].

The fully relativistic model was extended by Komissarov [52] by considering a purely azimuthal magnetic field. In the magnetized case, all previous assumptions are infeasible. Besides, following [52] the magnetic field is assumed to be purely azimuthal, i.e., the four-vector magnetic field has vanishing  $r$  and  $\theta$  components, and the flow is axially symmetric and stationary. In this method, we employ the strong toroidal magnetic field pressure compared to the gas pressure [53]. In what follows, the equations and assumptions of the magnetic Thick disc are reviewed.

### Equations of ideal relativistic MHD

Conservation laws that describe the covariant equations governing the evolution of the gas in the ideal relativistic Magnetohydrodynamics (MHD) are baryon conservation, stress-energy conservation, and induction equation [54, 55]

$$(\rho u^\nu)_{;\nu} = 0, \quad (2.34)$$

$$T^{\nu\mu}_{;\nu} = 0, \quad (2.35)$$

$${}^*F^{\nu\mu}_{;\nu} = 0, \quad (2.36)$$

where the subscript “;” refers to the covariant derivative,  $T^{\mu\nu}$  is the total stress-energy tensor of the fluid and the electromagnetic field together. By neglecting the dissipation due to the viscosity, and the heat conduction in the fluid frame  $T^{\mu\nu}$  reads as [55],

$$T^{\nu\mu} = (w + |b|^2) u^\nu u^\mu + \left( p + \frac{1}{2}|b|^2 \right) g^{\nu\mu} - b^\nu b^\mu, \quad (2.37)$$

where  $p$  is the gas pressure,  $|b|^2 = 2p_m$  where  $p_m$  is the magnetic pressure in the fluid [55], and  $*F^{\nu\mu}$  is the Hodge dual Faraday tensor

$$*F^{\nu\mu} = b^\nu u^\mu - b^\mu u^\nu, \quad (2.38)$$

where  $b^\mu$  is the four-vector magnetic field. We proceed here following [52], by the assumption of axially symmetric and stationary space-time

$$u^r = u^\theta = b^r = b^\theta = 0. \quad (2.39)$$

It is clear that considering these assumptions, the only nontrivial result follows from solving the stress-energy conservation. By choosing to have  $\Omega = \Omega(\ell)$  as the integrability condition, and projection of the conservation of stress-energy tensor into the plane normal to four-velocity, we obtain [36, 52]

$$\frac{1}{w} \nabla_i p = -\nabla_i \ln u_t + \frac{\Omega \nabla_i \ell}{1 - \Omega \ell} - \frac{\nabla_i \tilde{p}_m}{\tilde{w}}, \quad (2.40)$$

where  $\tilde{p}_m = \mathcal{L}p_m$ ,  $\tilde{w} = \mathcal{L}w$ , and in the static set-up  $\mathcal{L} = g_{t\phi}^2 - g_{tt}g_{\phi\phi}$ . Then this equation turns easily to

$$\int_0^p \frac{dp}{w} + \int_0^{\tilde{p}_m} \frac{d\tilde{p}_m}{\tilde{w}} = -\ln |u_t| + \ln |(u_t)_{\text{in}}| + \int_{\ell_{\text{in}}}^\ell \frac{\Omega d\ell}{1 - \Omega \ell}. \quad (2.41)$$

The constant of integration was chosen so that the pressures vanished on the surface of the disc and its inner edge i.e.,  $u_t = (u_t)_{\text{in}}$  and  $\ell = \ell_{\text{in}}$ .

Adopting [52], to be able to express the integrals of equation (2.41) in terms of elementary functions, we need to assume these extra relations

$$p = K w^\kappa, \quad \tilde{p}_m = K_m \tilde{w}^\eta, \quad (2.42)$$

where  $K$ ,  $\kappa$ ,  $K_m$  and  $\eta$  are constants. By this particular choice for equations of state, the Von Zeipel theorem is fulfilled. Therefore the equation (2.41) is fully integrated, and we obtain

$$W - W_{\text{in}} + \frac{\kappa}{\kappa - 1} \frac{p}{w} + \frac{\eta}{\eta - 1} \frac{p_m}{w} = \int_{\ell_{\text{in}}}^{\ell} \frac{\Omega d\ell}{1 - \Omega\ell}, \quad (2.43)$$

where  $W = \ln |u_t|$ . The model parameters to have a unique solution are  $\kappa > 0$ ,  $\eta$ ,  $W_{\text{in}}$ ,  $w_c$  enthalpy at the center, and the magnetization parameter  $\beta_c > 0$ , which is the ratio of the gas pressure to magnetic pressure, at the center. The positivity of  $\kappa$  and  $\beta_c$  is due to avoiding divergence in the equation (2.43). Also, one needs to specify  $\ell(r, \theta)$  to fix the geometry of the equipotential surfaces, where we consider different cases in what follows.

### 2.2.2 Angular momentum distributions

The first angular momentum case we have considered in this work has the constant distribution profile  $\ell = \ell_0$ . Therefore, the right-hand side of the equation (2.43) vanishes

$$W - W_{\text{in}} + \frac{\kappa}{\kappa - 1} \frac{p}{w} + \frac{\eta}{\eta - 1} \frac{p_m}{w} = 0. \quad (2.44)$$

The disc centre is found at the larger radius where  $\ell_0$  intersects with the local Keplerian angular momentum. In contrast,  $\ell_0$  is larger than the radius of the marginally stable Keplerian orbit  $\ell_{\text{ms}}$ . One can find the cusp point at the radius of the intersection of the specific angular momentum and the Keplerian one [36, 52]. Therefore, the disc surface is fully determined by choice of  $W_{\text{in}}$  independently of the magnetic field [56]. In this case, the total potential reads as

$$W(r, \theta) = \frac{1}{2} \ln \left| \frac{\mathcal{L}}{\mathcal{A}} \right|, \quad (2.45)$$

where  $\mathcal{A} = g_{\phi\phi} + 2\ell_0 g_{t\phi} + \ell_0^2 g_{tt}$  in the static case. Thus  $W$  satisfies this relation [48],

$$\begin{cases} W_{\text{in}} \leq W_{\text{cusp}} & \text{if } |\ell_{\text{ms}}| < |\ell_0| < |\ell_{\text{mb}}|, \\ W_{\text{in}} < 0 & \text{if } |\ell_0| \geq |\ell_{\text{mb}}|. \end{cases} \quad (2.46)$$

Besides, the gas pressure at the center  $p_c$  reads as

$$p_c = w_c (W_{\text{in}} - W_c) \left( \frac{\kappa}{\kappa - 1} + \frac{\eta}{\beta_{\text{mc}}(\eta - 1)} \right)^{-1}, \quad (2.47)$$

where the subscript  $c$  refers to the mentioned quantity at the center. Also,  $\beta_c = p_c/p_{mc}$  is the magnetization parameter at the center. The variables of model are then  $W$ ,  $w$ ,  $p$ ,  $p_m$ ,  $u^t$ ,  $u^\phi$ ,  $b^t$  and  $u^\phi$ . So by using equation of state, one can find  $K$  and  $K_m$ , then the solution is easily obtained utilizing (2.43) and (2.45) [52].

### Power-low angular momentum distribution

In the second case, we relax the condition of constant angular momentum. However, by considering pure rotation and a barotropic equation of state, angular velocity can state as a function of specific angular momentum  $\Omega = \Omega(\ell)$ . In this case, following [53] we consider

$$\Omega(\ell) = c\ell^n, \quad (2.48)$$

where  $c$  and  $n$  are constant parameters. Then the equation (2.43) can be written as [53],

$$\begin{aligned} W - W_{\text{in}} + \frac{\kappa}{\kappa - 1} \frac{p}{w} + \frac{\eta}{\eta - 1} \frac{p_m}{w} \\ = \frac{1}{n + 1} \ln \left( \frac{c\ell_{\text{in}}^{n+1} - 1}{c\ell^{n+1} - 1} \right). \end{aligned} \quad (2.49)$$

Of course, one needs to calculate  $c$  and  $n$  to obtain angular momentum distribution. It can be done using the center of the torus and the cusp of the disc. In the next step, by calculating  $\Omega(r_c)$ ,  $\Omega(r_{\text{cusp}})$ , and using the original definition of  $\Omega$  in equation (2.27), one obtains a system of equations that can be solved analytically to find parameters  $c$  and  $n$  and the distribution [53].

At this stage, we have all we need to build magnetized Thick discs. We can find the gas and magnetic distribution, the enthalpy distribution, and the rest-mass density distribution (2.42). The fluid enthalpy is giving by  $w = \rho h$ , where  $h = 1 + \epsilon + \frac{p}{\rho}$  is the specific enthalpy which in this case it can approximate by  $h \sim 1$ . This approximation is supported by the fact that the fluid is not relativistic from a thermodynamical point of view, and the internal energy and the pressure are very small compared to the rest-mass density. However, relaxing this assumption does not lead to noticeable differences in the models we considered. It is worth noticing that for a circular rotating perfect fluid, the shapes and location of the equipressure surface  $p(r, \theta) = \text{const.}$  are characterized by the assumed angular momentum distribution independently of the equation of state and the assumed entropy distribution [38].

### Trigonometric angular momentum distribution

The third case is also considered for non-constant angular momentum where presented in [57]. This is a reasonable assumption from a physical point of view to combine the constant profile with the Keplerian one. It has two important properties features of the angular momentum distribution in accretion discs. This distribution on the equatorial plane and far from the object is slightly sub-Keplerian, but closer it becomes slightly super-Keplerian and in the plunging region, it becomes again sub-Keplerian and almost constant. Following them, we have assumed an angular momentum distribution for the hydrodynamical case given by

$$\ell(r, \theta) = \begin{cases} \ell_0 \left( \frac{\ell_K(r)}{\ell_0} \right)^\alpha \sin^{2\delta}, & r \geq r_{\text{ms}}, \\ \ell_0 \zeta^{-\alpha} \sin^{2\delta}, & r < r_{\text{ms}}, \end{cases} \quad (2.50)$$

where  $\ell_0 = \zeta \ell_K(r_{\text{ms}})$ , and  $\ell_K$  is the Keplerian angular momentum in the equatorial plane, and

$$0 \leq \alpha \leq 1, \quad -1 \leq \delta \leq 1, \quad -1 \leq \zeta \leq \frac{\ell_K(x_{\text{mb}})}{\ell_K(x_{\text{ms}})}. \quad (2.51)$$

In this case, the equipressure surface which starts from the cusp is the marginally bound for  $\alpha = 0$ ,  $\delta = 0$ , and  $\zeta = \ell_K(x_{\text{mb}})/\ell_K(x_{\text{ms}})$ . Also, for the MHD case

$$\ell(r, \theta) = \begin{cases} \ell_0 \left( \frac{\ell_K(r)}{\ell_0} \right)^\alpha \sin^{2\delta}, & r \geq r_{\text{ms}}, \\ \ell_{\text{ms}}(r) \sin^{2\delta}, & r < r_{\text{ms}}, \end{cases} \quad (2.52)$$

where  $\ell_{\text{ms}}(r)$  is calculated on the equatorial plane via considering  $\Omega_{\text{ms}}$  simply by using equation (2.27). This means, aside from the constant case  $(\alpha, \delta) = (0, 0)$ , the angular momentum distribution in the equatorial plane behaves as follows. It starts with a constant value from the inner region to the marginally stable orbit, then monotonically increases from the marginally stable orbit to the outer part of the disc. In this case, the center is the inflection point of angular momentum behavior from the super-Keplerian to the sub-Keplerian. Also, increasing in  $\alpha$  tends to make angular momentum distribution closer to the distribution of the Keplerian one.

This procedure is described as follows. First, one should substitute  $i = r$  in equation (2.40), and after replace  $i = \theta$  in this equation. Second, divide the two equations to obtain [57],

$$\frac{\partial_r p}{\partial_\theta p} = \frac{\partial_r g^{tt} + \ell^2 \partial_r g^{\phi\phi}}{\partial_\theta g^{tt} + \ell^2 \partial_\theta g^{\phi\phi}} := -F(r, \theta) \quad (2.53)$$

Thus, for a given angular momentum distribution  $\ell$ , the function  $F$  is known. In addition, considering  $\theta = \theta(r)$  as the explicit equation for the equipressure surface leads to

$$\frac{d\theta}{dr} = F(r, \theta). \quad (2.54)$$

One can solve this equation for different initial conditions. Therefore one can obtain all the possible locations for the equipressure surfaces.

Throughout this thesis, we use this description in Chapters 11 and 13.



## Quasi-periodic oscillations

Nowadays, periodic and quasi-periodic variations are observed in several classes of astrophysical objects containing accretion discs. Although different models have been proposed for the interpretation of this rich phenomenology, it seems still there is not a widely accepted mechanism for most of the observed sources, for a review see e.g. [7, 58, 59].

The so-far unexplained rapid variability (so-called high-frequency quasi-periodic oscillations - HF QPOs) is usually supposed to originate from the orbital motion in the innermost parts of an accretion disc since the peaks of high frequencies are close to the orbital frequency of the marginally stable circular orbit where it represents the inner edge of Keplerian discs. The reasons are as follows; first, these quasi-periodic modulations are observed in the most luminous part of the source spectrum (and at high photon energies) implying its origin to be at the inner part of the accretion flow, since most of the gravitational potential energy of the accreting matter is released there. Second, a kHz modulation of unbeamed radiation should originate in a region not larger than almost 100 km<sup>1</sup>. Furthermore, this rapid variability arises across a large scale of mass of the compact sources including neutron stars, black hole low-mass X-ray binaries (LMXBs), as well as active galactic nuclei<sup>2</sup> [7, 60, 8, 61, 62, 63, 64, 65].

### 3.1 Observations

For the HF QPOs ( $> 100$  Hz) the oscillation frequencies are usually stable and often in a 3 : 2 ratio. The phenomenon is not universal, and more importantly, the HF QPOs are elusive with a low duty cycle. These occur

---

<sup>1</sup>Even with a sharper bound when the high degree of coherence of the observed modulation is considered.

<sup>2</sup>For BHBs:  $M_{\text{bh}} \sim 10M_{\odot}$ , and for AGN:  $M_{\text{bh}} \gtrsim 10^6 M_{\odot}$ .

only in certain states of luminosity and hardness. In the X-ray binaries, HF QPOs arise in the steep power-law state [66] or anomalous high-soft state [67, 68]. In fact, both of these correspond to a luminous state with a soft X-ray spectrum including a thermal disc component <sup>3</sup>. Surprisingly, the HF QPOs were observed only in 11 of almost 7000 observations of 22 stellar-mass black holes [67].

Since the time evolution of the viscous instabilities and accretion rate fluctuations is very long <sup>4</sup> compared to stellar-mass sources; therefore, in general, the QPOs in supermassive sources are not expected to vary over observational timescales. Furthermore, the impressive correlation between the frequency of QPOs and the black hole mass has been observed from stellar mass to supermassive black hole sources [70]. This is a piece of strong evidence to support the hypothesis of its scale-invariant and suggests the mechanism responsible for QPOs may be the same in both types of objects. This also may open a window to measure the supermassive black hole masses, particularly information on AGN light curves that can gather from like eROSITA, TESS, and future ground-based surveys.

Moreover, many microquasar and neutron star sources in LMXBs show QPOs in their observed X-ray fluxes in the Fourier variability peaks in the Power Density Spectra (PDS). In addition, the frequencies of some QPOs correspond to the orbital frequencies close to the central object. A special class of HF QPOs consists of twin peak QPOs with lower and upper frequencies of their pairs ( $\nu_U, \nu_L$ ) in PDS. These twin peak QPOs were reported also in the peculiar microquasar. In the LMXBs containing a black hole candidate in low-density discs, the X-ray luminosity is modulated quasi-periodically, giving rise to distinctive peaks in the PDS which have been found in sequences of small integers 2 : 3.

## 3.2 Theories

Despite the exciting possibilities raised by the observations, there is still no general agreement on the physical mechanism underlying HF QPOs. Most of the candidate theories consider resonant epicyclic or orbital frequencies caused by the gravitational field of the compact object. Because this is expected that the stable frequencies observed in HF QPOs should be governed by the fixed gravitational field of the central source, rather than be the properties of the accretion discs or the X-ray emitting corona, which are known to

---

<sup>3</sup>In the HF QPO frequency of GRS 1915+105 slight variability appears to depend on the spectral hardness [69].

<sup>4</sup>From tens to hundreds of years.

fluctuate. However, as mentioned none of the theorems have yet reproduced all of the observed phenomena successfully.

Among many models serving to explain QPOs in the past years is the Relativistic Precession Model (RPM). This model assumes that QPOs are produced by a local motion of accreted inhomogeneities like blobs, and relates the twin-peak QPOs to the Keplerian and periastron precession frequency on an orbit located in the inner part of the accretion disc as mentioned earlier [71, 72]. In this regard, the properties of the Keplerian and epicyclic frequencies of the orbital motion have been extensively studied in the context of particle motion underlying the presence of a uniform magnetic field in various space-times [73, 74, 75, 76, 77, 78, 79, 80, 81, 82, 83, 84, 85, 86] among many others.

Although, in general, the correlation between these frequencies is qualitatively fitted by the RPM prediction [87], the RPM suffers some theoretical difficulties to explain for example a relatively large observed HF QPO amplitudes which are often observed [88, 89]. During these years, this model was modified in many ways. In 2001, the orbital resonance model was introduced. In this model, it was supposed that HF QPOs arise from the resonances between oscillation modes of the accreted fluid [90, 91]. In fact, several studies within the HF QPOs framework consider fluid motion instead of a test particle motion. In this respect, a different class of models deals with the collective motion of accreted matter considering normal modes of thin accretion disc oscillations (so-called discoseismology) and thick disc (torus) oscillations e.g. [92, 93, 94, 95, 96, 97, 98, 99]. In some cases, the QPO frequencies predicted by a given model can still be expressed in the test particle motion for the epicyclic oscillations of slender accretion tori or with reasonable accuracy for the consideration of discoseismic modes. In principle, it is worth mentioning that it is a rather long way from the test particle motion examination to considering the more realistic case of non-slender tori oscillations that has severe impacts on the predicted QPO frequencies e.g. [100, 101].

### 3.3 Models of 3 : 2 quasi-periodic oscillation

In what follows we briefly introduce QPO models of the test particle, and in Chapter 12 we explore the properties of the Keplerian and epicyclic frequencies of a charged particle motion in the background of a distorted, deformed compact object 7 with a relatively weak uniform magnetic field. In the next step, in Section 3.4 we present an approach to consider a perfect fluid disc oscillation instead of a test particle approach.

### 3.3.1 Resonance

One of the popular models suggests that QPO arises in resonant interaction between the radial and vertical oscillation modes in the relativistic accretion flow. Many orbital resonance models are related to parametric resonance, forced resonance, or considering beat. Indeed, in these resonance models, epicyclic frequencies of the test particle circular motion play a crucial role [102]. In general, depending on internal conditions, it is possible to have more than one resonance excited in the disc simultaneously or at different times.

In fact, there are a variety of possibilities in the combination of resonances, where in the parametric and forced resonances, normally, people try to connect these combinations to the frequency ratio of oscillations; however, physical details vary [103]. This is worth mentioning here that in principle, for any case of the orbital resonance model, one can determine the mass and spin in the case of a rotating black hole. In fact, aside from detailed technical issues, the magnitude of the measured frequencies can determine the parameter  $M$  identifying as the mass of the source. While, on the other hand, the relation between the black hole spin and these frequency ratios is not unique. Namely, several values are possible for a given ratio set. Therefore, this is necessary to consider other spin measurement methods like spectral continuum fitting or profiled spectral lines [96, 104]. However, the different resonance models are linked to finding the desired combination of resonances that links them to the observations. In what follows, we explain the parametric (or internal) and forced resonances briefly.

#### Parametric resonance

This resonance is governed by the Mathieu equation. This equation is a linear second-order ODE, which differs from the one corresponding to a harmonic oscillator in the existence of a periodic and sinusoidal forcing of the stiffness coefficient as  $f(t) = f_0 + f_1 \cos(\omega_x^2 t)$ , and is given by

$$\frac{d^2 \xi^y}{dt^2} + \omega_y^2 [1 + \omega_y^2 h \cos(\omega_x^2 t)] \xi^y = 0. \quad (3.1)$$

where  $h = \frac{f_1}{f_0} \gg 0$  is the amplitude of the excitation (forcing) term,  $\nu_x = \frac{\omega_x}{2\pi}$  is its excited frequency, and  $\nu_y = \frac{\omega_y}{2\pi}$  is the natural, unexcited frequency.

It is well known that this set-up performs free oscillation around the stable equilibrium case. If the stiffness term contains the parametric excitation i.e.  $f_1 \neq 0$ , the motion can stay bounded which is referred to as stable, otherwise, the motion becomes unbounded and referred to as unstable.

Considering the vertical and radial epicyclic oscillations with the frequencies  $\nu_y = \frac{\omega_y}{2\pi}$  and  $\nu_x = \frac{\omega_x}{2\pi}$ , the Mathieu equation implies that a parametric resonance is excited strongly for the lowest possible value of integer numbers in the ratio of these two [103]. Such a parametric resonance [105] can occur if

$$\frac{\omega_x}{\omega_y} = \frac{\nu_x}{\nu_y} = \frac{2}{n}, \quad n = 1, 2, 3, \dots \quad (3.2)$$

and is strongest for the smallest possible value of  $n$ . In the case of a black hole, because in its vicinity  $\nu_x < \nu_y$  satisfies, one can say that this lowest possible value is  $n = 3$ , which means that  $3\nu_x = 2\nu_y$ . This can explain most of the observed 3 : 2 ratio in HF QPOs.

### Forced resonance

In a more realistic physical model, we should consider small deviations from the planar circular motion. The related models are based on the forced non-linear oscillator. The equations governing the behavior of these fundamental frequencies read as

$$\frac{d^2\xi^y}{dt^2} + \omega_y^2\xi^y + [\text{non-linear terms in } \xi^y] = h_1 \cos(\omega_0^2 t), \quad (3.3)$$

$$\frac{d^2\xi^x}{dt^2} + \omega_x^2\xi^x + [\text{non-linear terms in } \xi^x] = h_2 \cos(\omega_0^2 t), \quad (3.4)$$

where  $\omega_0$  is the frequency of the external force. In this case also, the resonance occurs if the frequencies are in the ratio of small natural numbers

$$\frac{\omega_x}{\omega_y} = \frac{k}{l}, \quad k, l = 1, 2, 3, \dots \quad (3.5)$$

The non-linear terms are responsible for beat frequencies in the resonant for  $\xi_y(t)$  and  $\xi_x(t)$ . Indeed, because of the nature of non-linearity in these equations, they are related to the dissipative processes and the change in their amplitude the contrary to the Mathieu equation [103]. However, since the details of dissipative processes in accretion discs are not known one can not find the corresponding  $h_1$  and  $h_2$  exactly in this more realistic model. One of the possibilities is to solve them mathematically and try to find the best match between them and observed QPOs [102].

### 3.3.2 QPO Models

A class of models, so-called orbital models which assume a relation between the QPO frequencies and the frequencies related to the motion of accreted

matter orbiting in the vicinity of a compact object is considered here. These models focus on hot-spot or disc-oscillation to describe QPOs.

Among these various models of accretion disc oscillations, we consider the whole group of QPO models in [106] related to the test particle motion and examine them in Chapter 12. For a detailed discussion on these models see also [102, 96, 107, 108]. As we see in the following, the prescription of these models relies on the formulae for epicyclic frequencies of a particle motion [106] which are shared the primary motivation with some cases for example models based on the dynamic of fluid [101]. In fact, in a given model, the predicted QPOs can be expressed in the test particle motion with reasonable accuracy even for the consideration of discoseismic modes. In the following, the two kinematic models are RP and TD, and the resonant models are WD, Ep, Kp, RP1 and RP2. In fact, they consider different possibilities in the combination of disc-oscillation modes.

### RPM

The Relativistic Precession Model (RP) is one of the first attempts to model QPOs, proposed in [72, 109]. In RPM the upper frequency is defined as the Keplerian frequency  $\nu_U = \Omega$  and the lower frequency is defined as the periastron frequency i.e.  $\nu_p := \nu_L = \Omega - \nu_x$ . Their correlations are obtained by varying the radius of the associated circular orbit. Within this framework, it is usually assumed that the variable component of the observed X-ray arises from the motion of “hot-spots” or biting inside the accretion disc on a slightly eccentric orbit. Therefore, due to the relativistic effects, the observed radiation is supposed to be periodically modulated. In this model, frequencies predicted are scaled as  $1/M$  for a fixed spin value; therefore, the expected frequency ratio is mass independent. As weakness of this model is the lack of a generic explanation for the observed 3 : 2 frequency ratio.

### TDM

Another kinematic model is the Tidal Disruption Model (TD) presented in [110, 111]. This follows also a very similar approach as the RPM. In this model, the QPOs are assumed as a result of tidal disruption of large accreting inhomogeneities. In other words, when blobs orbiting the central compact object can be stretched by tidal forces forming the ring section. However, in this case also, the frequency ratio is not reliably constrained. In TD the frequencies are identified with the frequencies of the orbital motion; namely, the upper frequency is defined as  $\nu_U = \Omega + \omega_x$  and the lower frequency is defined as  $\nu_L = \Omega$ .

Table 3.1: Frequency relations corresponding to individual QPO models

Model	$\nu_U$	$\nu_L$
RP	$\Omega$	$\Omega - \omega_x$
Kp	$\Omega$	$\omega_x$
Ep	$\omega_y$	$\omega_x$
TD	$\Omega + \omega_x$	$\Omega$
WD	$2\Omega - \omega_x$	$2\Omega - 2\omega_x$
RP1	$\omega_y$	$\Omega - \omega_x$
RP2	$2\Omega - \omega_y$	$\Omega - \omega_x$

### WDM

The Warped disc Model (WD) introduced in [112], which is related to non-axisymmetric modes in a warped accretion disc. In WD the upper frequency is defined as  $\nu_U = 2\Omega - \omega_x$  and the lower frequency is  $\nu_L = 2\Omega - 2\omega_x$ . In more realistic versions of this model, the higher harmonic oscillations are also considered up to the third order, then frequencies like  $3\Omega - \omega_x$  are possible to consider. On the contrary with the two last models, the ratio of the frequencies is crucial for the model. However, this model suffers from the fact that it considers a somehow exotic disc geometry that causes a doubling of the observed lower QPO frequency.

### EpM-KpM

The Epicyclic resonance Model (Ep) [102] is the simplest variant. It is about considering radial and vertical epicyclic oscillations and relates them to the resonance of axisymmetric disc-oscillation modes. The Keplerian resonance Model (Kp) considers a resonance between the orbital Keplerian and the radial epicyclic oscillations. In Ep the upper frequency is defined as  $\nu_U = \omega_y$  and the lower frequency is  $\nu_L = \omega_x$ . In Kp the upper frequency is defined as  $\nu_U = \Omega$  and the lower frequency is  $\nu_L = \omega_x$ .

### RP1M-RP2M

The RP1 model by Bursa in 2005 and the RP2 model [76], both consider different combinations of non-axisymmetric disc-oscillation modes. In RP1M the upper frequency is defined as the Keplerian frequency  $\nu_U = \omega_y$ , and the lower frequency is  $\nu_L = \Omega - \omega_x$ . In RP2M the upper frequency is defined as  $\nu_U = 2\Omega - \omega_y$  and the lower frequency is  $\nu_L = \Omega - \omega_x$ . In the case of slow

rotation, their outcome frequencies of oscillation modes almost coincide with the frequencies predicted by the RP.

In Chapter 12 we study these models in the Generalized q-metric background 7, and also attempt to fit them to the data. However, such an investigation is worth studying and we can have a good agreement with the observation, some other observational outcomes in different situations trigger the idea that considering the effect of perfect fluid than just a test particle can improve the fitting <sup>5</sup>. There are different approaches to dealing with this scenario. In the next section, we state the vertically integrated quantities approach to study the radial epicyclic frequencies in a perfect fluid disc and present the results in Chapter 13.

### 3.4 Epicyclic oscillations: Local perturbation

As mentioned in the previous section 3, there is not a great agreement on interpretation of the accepted mechanism of the observed QPOs. In this regard, studying axisymmetric modes of the relativistic geometrically Thick discs seems to be a systematic investigation of the oscillation properties of accretion discs. In fact, the oscillations of these discs are important since they can produce intense gravitational radiation, also these oscillations may explain the high-frequency QPOs observed in LMXBs containing a black hole candidate in low-density discs.

As a standard approach, the oscillation modes of geometrically Thick discs can be studied through local perturbative analyses when the perturbations of the space-time are neglected. In this regard, the current approach tends to extend the relativistic discoseismology analysis carried out for Thin discs to systems having a non-negligible contribution of pressure gradients. Besides, this allows us to investigate the possible connections between the oscillation modes of relativistic Thick disc model and the X-ray observed in QPOs. Furthermore, the axisymmetric oscillations of Thick discs may provide a criterion in the study of the runaway instability e.g. [113].

In a series of papers [114, 115, 116] it has been shown that the Thick accretion discs show a long-term oscillatory behavior with the duration of tens of orbital periods including the vertical integration analytical approach. In this way, this chapter aims to investigate if and how the dynamics of such objects change when the influence of quadrupoles is taken into account. In the following, we discuss briefly the local perturbation approach for the

---

<sup>5</sup>For example, to interpret the observed QPOs in some sources like a neutron star X-ray binaries, the mass of the neutron star which is needed to fit to the observations is larger ( $\sim 2M_{\odot}$ ) than the observed value of neutron star mass ( $\sim 1.4M_{\odot}$ ).



circular orbiting test particle and a perfect fluid.

### 3.4.1 Test particle

For a test particle moving in a circular orbit in a stationary and axisymmetric background, we can consider its four-velocity as  $u^\mu = u^t(1, 0, \Omega, 0)$ . The particle motion obeys the energy and momentum conservation laws, and in particular, it moves along geodesics. Using this information the equation of motion for this particle can take this form

$$(v^\mu{}_{;\nu} + v^\mu \partial_\nu \ln u^t) v^\nu = 0, \quad (3.6)$$

where “ $;$ ” represents the covariant derivative and  $v^\mu$  is the physical velocity of the particle that relates to the four-velocity as  $v^\mu = \frac{u^\mu}{u^t}$ . In the standard perturbation approach, one can assume the perturbed physical velocity of this type

$$v^\mu = (1, \delta v^r, \Omega + \delta v^\phi, 0). \quad (3.7)$$

Considering this relation in the equation (3.6), and terms up to the first order, one can obtain the radial epicyclic frequency  $\kappa_r$  e.g. [117]. For example, as a special case, in Schwarzschild space-time, one obtains the familiar formula

$$\kappa_r^2 = \frac{M(r - 6M)}{r^2}. \quad (3.8)$$

Or in Kerr space-time we have [117]

$$\kappa_r^2 = \frac{M(r^2 - 6Mr + 8a\sqrt{Mr} - 3a^2)}{r^2(\sqrt{r^3} + a\sqrt{M})}. \quad (3.9)$$

This is worth mentioning that we only derive the epicyclic frequency referring to the prograde orbits. Since there is a maximum of this frequency at a radius outside the ISCO, which would be linked to the oscillation modes trapped in the inner part of the accretion discs.

### 3.4.2 Perfect fluid disc

In this part we are interested to study this space-time in the vicinity of the equatorial plane (i.e.  $|y - 0| \ll 1$ ). In addition, we concentrate on a simple

model for the torus which can be treated analytically. The main simplification in the models is that the vertical structure of the tori is accounted for by integrating the relevant quantities along the direction perpendicular to the equatorial plane. Therefore, the tori were built with vertically integrated and vertically averaged quantities. The point here is that this vertically averaging corresponds to collapsing the vertical structure of the torus onto the equatorial plane, and not just studying the equatorial slice of the vertically extended torus.

The general approach is the same in Newtonian and in General relativity. Here we explain this method briefly. We consider an extended perfect fluid configuration orbiting a central object and we neglect self-gravitating. We can introduce the vertically integrated pressure  $\mathcal{P}$ , corresponding rest-mass density  $\mathcal{S}$ , velocity components  $\mathcal{U}$  and  $\mathcal{W}$  respectively as

$$\mathcal{P}(r) := \int_{-H}^H p dz, \quad (3.10)$$

$$\mathcal{S}(r) := \int_{-H}^H \rho dz, \quad (3.11)$$

$$\mathcal{U}(r) := \frac{1}{2H} \int_{-H}^H v^r dz, \quad (3.12)$$

$$\mathcal{W}(r) := \frac{1}{2H} \int_{-H}^H v^\phi dz, \quad (3.13)$$

where  $H = H(r)$  is the local thickness of the torus and  $v^i$  are the three-velocity components of the fluid. Considering two first equations the general polytropic equation of state  $p = K\rho^\gamma$ , becomes  $\mathcal{P} = \mathcal{K}\mathcal{S}^\Gamma$ , where  $\mathcal{K}$  and  $\Gamma \frac{d \ln \mathcal{P}}{d \ln \mathcal{S}}$  are the corresponding polytropic constant and the adiabatic index respectively. We also need to modify the equation of state in a consistent way since  $P$  does not represent a vertically integrated polytropic equation of state if  $\Gamma \neq 1$ . In addition, to get rid of the height dependence of  $\Gamma = \Gamma(r, z)$  for simplicity one can assume  $p$  and  $\rho$  have a weak dependence on height, so that they can be stated in terms of their values at the equatorial plane. Therefore, we can use this modified expression for the equation of state

$$P = K\mathcal{S}^\gamma. \quad (3.14)$$

With these quantities the dynamics of the torus is fully determined once we choose the parameters of the model [118, 115]. Now we introduce harmonic Eulerian perturbations of this type

$$\begin{pmatrix} \delta\mathcal{U} \\ \delta\mathcal{W} \\ \delta Q \end{pmatrix} \sim e^{-i\sigma t + ikr}, \quad (3.15)$$

where

$$\delta Q = \frac{\delta\mathcal{P}}{\mathcal{S}} \quad (3.16)$$

since we also included the fluid pressure. In fact, the harmonic spatial dependence in this relations as the signature of the local perturbation is valid for when the wavelength of the perturbations is smaller than the radial variations in the equilibrium configuration, the Wenzel–Kramers–Brillouin (WKB) approximation. By applying the perturbations (3.15) in the equilibrium tori model and considering only up to the first-order terms and neglecting the time derivatives, we derive the perturbation equations [115]. This linear system of differential equations has a non-trivial solution by searching for the zeros of determinants of coefficients matrix, which simply leads to the dispersion relation

$$\sigma^2 = \kappa_r^2 + f(r)k^2c_s^2, \quad (3.17)$$

where  $f(r)$  in Newtonian set-up is 1, and in general is obtain from the metric in Schwarzschild space-time [115, equation 42], or in the Kerr space-time [116, equation 17]. Besides,  $k_r$  is the epicyclic frequency in the radial direction, and  $c_s$  is the local sound velocity in the vertically integrated disc. Moreover, it is assumed that the perturbation wavelength is much smaller than the radius of the disc, and the imaginary part of the epicyclic frequency is also neglected [115].

In fact, the first term in the dispersion relation is the radial oscillation of a fluid element when due to a restoring centrifugal force, it is infinitesimally displaced from its equilibrium with no change in the angular momentum that produces inertial oscillations. This produces inertial oscillations with the frequency  $\kappa_r$ . However, there exist also a vertical epicyclic frequency with an amplitude much smaller than the radial one [119], therefore we neglected here. The second term, the frequency  $kc_s$  is due to pressure gradients in compressible fluids that leads to the acoustic oscillations <sup>6</sup>.

---

<sup>6</sup>Both of these terms are collectively referred to as inertial–acoustic waves.

The important key here is in general theory of relativity  $\kappa_r$  does not increase as we go closer and closer to the central object, but instead have a maximum at a few gravitational radii before the ISCO where consider as a very good estimation of the inner edge of the disc, and it is zero at the ISCO. Therefore, oscillations in this part of the disc may trap and lead to the periodic flux variations which we can observe [120]. However, this is not the case in the Newtonian gravity.

To study the radial epicyclic oscillation in this approach, one can consider different angular momentum distributions. However, for the Keplerian angular momentum distribution where  $\Omega \propto r^{-\frac{3}{2}}$  the radial epicyclic frequency is equal to the orbital frequency  $\kappa_r^2 = \Omega^2$ . Besides, the radial epicyclic frequency vanishes for the constant specific angular momentum dictating by the corresponding equations [115, 116]. So, one can conclude that a constant angular momentum distribution provides a limit for the properties of p-mode oscillations. In Chapter 13 we study the radial epicyclic frequency in the background of Generalized q-metric.

## CHAPTER 4

# Shadow in the presence of plasma

The Event Horizon Telescope Collaboration et al. [121, 122, 123, 124, 125, 126, 127, 128] reveal the characteristics of black holes and their accretion flows that are optically thin at millimeter wavelengths [129] by the first images of a supermassive black hole at event horizon scale resolution. In fact, such a flow is transparent to synchrotron emission and characterized by a bright ring of emission which is called the shadow of the black hole. Therefore, the shadow encodes information about underlying space-time which makes it a powerful tool to study the strong gravity field regime.

On the other hand, there are methods to compute the shape and the size of the shadow analytically. However, in presenting the actual scenario, one should take into account, for example, the surrounding accretion disc of a compact object like the numerical methods [130]. Since the light ray is influenced by matter. Analytical results as a complementary part of numerical simulations can formulate the dependence of shadow on the underlying parameters. In this regard, and as a first step, we consider the surrounding matter to be a cold plasma that is non-magnetized and pressure-less plasma and present the analytical results on the size of the shadow [131] in spherically symmetric set-up.

However, before starting, it is worth stating the definition of shadow that we employ here. If we consider light rays sent from an observer <sup>1</sup> at radius coordinate into the past and it goes towards the horizon of the black hole, also we assume no light sources between the observer and the black hole, initial directions of the light ray corresponds to the darkness on the observer's sky. This dark circular disc on the observer's sky is called the shadow of the black hole. In fact, the boundary of this shadow is determined by the initial directions of light rays that asymptotically spiral towards the

---

<sup>1</sup>The observer is assumed to be static somewhere between the outermost photon sphere and infinity.

outermost photon sphere. Notably, the light rays in the photon sphere are unstable with respect to radial perturbations since they may serve as limit curves. For this reason, we can not use this construction straightforward in the distorted space-times (distorted Schwarzschild or Generalized q-metric) since their structures contain stable photon orbit 6.2 and 7.3.

In what follows, we briefly explain the properties of shadow in the presence of the cold plasma.

#### 4.1 Equation of motion for light rays in plasma

We consider a spherically symmetric space-time is filled with cold plasma with the frequency of

$$\omega_p(r)^2 = \frac{4\pi e^2}{m_e} N(r), \quad (4.1)$$

where  $\omega_p$  is the plasma frequency,  $e$  is the charge of the electron,  $m_e$  is the mass of an electron, and  $N$  is the electron number density. In addition, the fraction index is given by

$$n(r, \omega)^2 = 1 - \frac{\omega_p(r)^2}{\omega(r)^2}, \quad (4.2)$$

where  $\omega$  is the frequency of photon measured by a static observer. Light propagation in this medium is only possible if  $\omega \geq \omega_p$ . Furthermore, the Hamiltonian of the system with plasma is

$$H = \frac{1}{2}(g^{\mu\nu} p_\mu p_\nu + \omega_p^2). \quad (4.3)$$

Having vanishing Hamiltonian for light rays and utilizing Hamiltonian equations, it turns out easily that  $p_t$  and  $p_\phi$  are constants of motion. For asymptotically flat space-times frequency  $\omega$  measured by a static observer related to the gravitational redshift as follows

$$\omega^2 = -\frac{p_t}{g_{tt}}. \quad (4.4)$$

Besides, one obtains [131]

$$\left(\frac{dr}{d\phi}\right)^2 = \frac{g_{\phi\phi}}{g_{rr}} \left( \frac{p_t^2}{p_\phi^2} h^2 - 1 \right), \quad (4.5)$$

where

$$h^2 = -\frac{g_{\phi\phi}}{g_{tt}} \left( 1 + g_{tt} \frac{\omega_p^2}{p_t^2} \right) \quad (4.6)$$

A light ray that comes in from infinity and reaches the minimum at a radius  $R$ , meaning  $\frac{dr}{d\phi}|_R = 0$  and again goes out to infinity. The integration over the orbit gives the formula for the bending angle  $\delta$  [131] as follows

$$\pi + \delta = 2 \int_R^\infty \sqrt{\frac{g_{rr}}{g_{\phi\phi}}} \left( \frac{h^2(r)}{h^2(R)} - 1 \right)^{-\frac{1}{2}} dr, \quad (4.7)$$

where

$$h^2(R) = \frac{p_\phi^2}{p_t^2}, \quad (4.8)$$

where by this equation  $R$  has been related to the constants of motion.

## 4.2 Radius of Shadow

Considering approximations we used the equation for the radius of a circular light orbit [131] is given by

$$\frac{d}{dr} h^2(r) = 0. \quad (4.9)$$

This means any solution of this equation gives rise to a photon sphere. If a light ray starts tangentially it stays on a circular orbit at  $r = r_{ph}$ . If the space-time is asymptotically flat, and if  $\omega_p(r) \rightarrow 0$  for  $r \rightarrow \infty$ , the outermost photon sphere is always unstable with respect to radial perturbations. Therefore, this radius is the critical value of the minimal radius  $R$  mentioned above. If a light ray comes in from infinity that  $R > r_{ph}$  it will go out to infinity again. The case  $R = r_{ph}$  corresponds to a light ray that spirals asymptotically towards

a circular photon orbit in the sphere of radius  $r_{ph}$ . All other rays cross the photon sphere and we exclude the case that they can come back, where this is the case when there is a second photon sphere.

We consider a light ray sent by the observer at  $r_O$  into the past under angle  $\alpha$  with respect to the radial direction. Then  $\alpha$  easily reads as

$$\cot \alpha = \left( \sqrt{\frac{g_{rr}}{g_{\phi\phi}}} \frac{dr}{d\phi} \right) \Big|_{r=r_o}, \quad (4.10)$$

where by using (4.5) we obtain

$$\sin \alpha = \frac{h(R)}{h(r_o)}. \quad (4.11)$$

The boundary of the shadow,  $\alpha_{bd}$ , is determined by light rays that spiral asymptotically towards a circular light orbit at radius  $r_ph$

$$\sin \alpha_{bd} = \frac{h(r_{ph})}{h(r_o)}. \quad (4.12)$$

This is convenient to assume that the observer is in a region where the plasma density is negligibly small,  $N(r_o) \ll N(r_{ph})$ , and neglect the corresponding terms we obtain

$$\sin^2 \alpha_{bd} = \frac{g_{\phi\phi}(r_{ph})g_{tt}(r_o)}{g_{\phi\phi}(r_o)g_{tt}(r_{ph})} \left( 1 + \frac{g_{tt}(r_{ph})\omega_p(r_{ph})^2}{p_t^2} \right). \quad (4.13)$$

Therefore, considering the signature of metric <sup>2</sup> in this situation the plasma always has a decreasing effect on the size of the shadow.

### 4.3 Low-density plasma

In this case, by writing the linearized  $h(r)^2$  around the corresponding values for vacuum light rays we have

$$h^2(r) = -\frac{g_{\phi\phi}}{g_{tt}} \left( 1 + \epsilon \frac{g_{tt}\omega_p^2}{p_t^2} \right). \quad (4.14)$$

---

<sup>2</sup>Signature of the metric is  $(-, +, +, +)$ .



And the equation (4.9) is written as

$$\left(\frac{g_{\phi\phi}}{g_{tt}}\right)' \left(1 + \epsilon \frac{g_{tt}\omega_p^2}{p_t^2}\right) + \epsilon \frac{g_{\phi\phi}}{g_{tt}} \left(\frac{g_{tt}\omega_p^2}{p_t^2}\right)' = 0, \quad (4.15)$$

where obviously for  $\omega_p = 0$  we have just  $\left(\frac{g_{\phi\phi}}{g_{tt}}\right)' \Big|_{r=r_{ph}} = 0$  and in this case we show the photon sphere by  $r_{ph}^0$ . Therefore, the solution to the equation (4.15) can be written in the following form

$$r_{ph} = r_{ph}^0 + \epsilon r_{ph}^1 + \dots, \quad (4.16)$$

where  $\epsilon$  is a linearization parameter, and

$$r_{ph}^1 = \frac{\left(\frac{g_{\phi\phi}}{g_{tt}}\right) \left(\frac{g_{tt}\omega_p^2}{p_t^2}\right)' \Big|_{r=r_{ph}^0}}{\left(\frac{g_{\phi\phi}}{g_{tt}}\right)'' \Big|_{r=r_{ph}^0}}. \quad (4.17)$$

Hence, the effect of plasma manifests through the signs of derivative terms that can shift the photon sphere inwards or outwards. By neglecting higher orders in  $\epsilon$ , and assume  $\omega_p \ll \omega$  we have [131]

$$\sin^2 \alpha_{bd} = \frac{g_{\phi\phi}(r_{ph}^0)g_{tt}(r_o)}{g_{\phi\phi}(r_o)g_{tt}(r_{ph}^0)} \left(1 - \left(\frac{g_{tt}(r_{ph}^0)\omega_p^2(r_{ph}^0)}{p_t^2(r_{ph}^0)}\right) + \left(\frac{g_{tt}(r_o)\omega_p^2(r_o)}{p_t^2(r_o)}\right)\right). \quad (4.18)$$

Then in the low-density plasma, depending on the second and the third term in the parenthesis plasma can have a decreasing effect on the shadow.

We use this construction to study the shadow in the background of q-metric, as the first step approximation, in Chapter 14. The second step is considering the axisymmetric space-time that we studied in [132].



## Stability analysis in the dynamical system

In the dynamical system approach to studying nonlinear systems, one can consider the linearization of such a system around its equilibria. Without loss generality, let us consider one-dimensional ordinary differential equation as

$$\dot{x} = f(x), \quad (5.1)$$

where  $x \in \mathbb{R}^n$ , and  $f$  is a differentiable function. This function  $f$  is called a vector field. Having linear or nonlinear system of ODEs depends on the linearity of  $f$ , respectively. A point  $x^*$  is called a *fixed point* or an *equilibrium point* if it satisfies  $f(x^*) = 0$ . In the follow we describe briefly the linear Lyapunov and Jacobi stabilities.

### 5.1 Lyapunov stability

Let us consider the two-dimensional system of ODEs where describe by

$$\begin{cases} \dot{u} = f(u, v), \\ \dot{v} = g(u, v). \end{cases} \quad (5.2)$$

At the equilibrium point, both functions are zero. The jacobian matrix of this system is

$$J = \begin{pmatrix} f_{,u} & f_{,v} \\ g_{,u} & g_{,v} \end{pmatrix}. \quad (5.3)$$

It is common that show this matrix at the fixed point  $(u^*, v^*)$  by  $A$

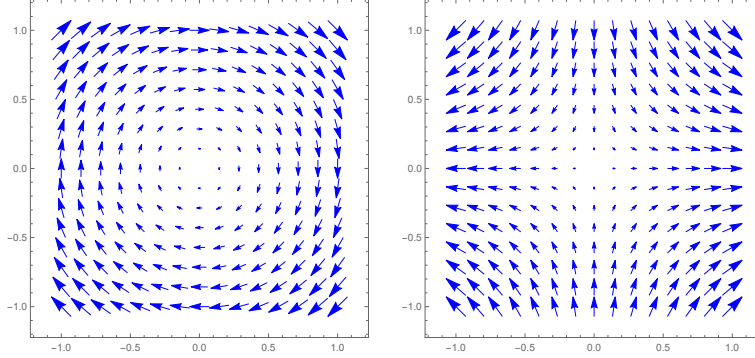


**Figure 5.1:** Left plot shows Center map, and the right one Saddle point singularity.

$$A := J \quad \text{at} \quad (u^*, v^*). \quad (5.4)$$

Then the characteristic equation reads as

$$\lambda^2 - \text{tr}A\lambda + \det A = 0, \quad (5.5)$$

where  $\lambda$  is eigenvalue of matrix  $A$ , "tr" is the trace of  $A$ , and "det" is the determinant of the  $A$ . The sign of the trace, determinant and  $\Delta$ , where  $\Delta = (\text{tr})^2 - 4 \det A$ , give the linear stability of the fixed points. In fact, the linear stability of the fixed point means it is a local attractor, or physically means the trajectories are converging.

There is a standard classification of the fixed points e.g. [133], where here we state the ones that are more relevant to this work:

1. If  $\lambda_+, \lambda_- \in \mathbb{R}^+$ : The fixed point is an unstable point or a saddle point singularity.
2. If  $\lambda_+, \lambda_- \in \mathbb{I} (= i\mathbb{R})$ : The fixed point is a center and to understand its stability behavior one needs to investigate the higher-order derivatives (see Figure 5.1).

The physical meaning of the center is that all solutions are periodic and the corresponding oscillations have fixed amplitude. We will apply this linear stability analysis in Chapter 15 to study the geodesics of Generalized q-metric.

## 5.2 Jacobi stability

Jacobi stability is a natural generalization of the stability of the geodesic flow on a differentiable manifold describing the evolution of dynamical systems. The Jacobi stability of a dynamical system is considered as the robustness of the system to the small perturbations of the whole trajectory [134]. This stability is related to a powerful mathematical theory proposed by Kosambi–Cartan–Chern (KCC). This theorem relates the stability of the system to intrinsic properties of geometry with five invariants, where the Jacobi stability is the second one. To explain this theorem let's start with by the general form of the Euler–Lagrange equations for the Lagrangian of the system  $\mathcal{L}$  as

$$\frac{d}{dt} \frac{\partial \mathcal{L}}{\partial \dot{x}^i} - \frac{\partial \mathcal{L}}{\partial x^i} = F_i, \quad i = 1, 2, \dots, n, \quad (5.6)$$

where  $F_i$  are the external forces. However, solving this equation, for a regular Lagrangian is equivalent to solving a second-order differential equation as

$$\frac{d^2 x^i}{dt^2} + 2G^i(x, y) = 0, \quad i \in \mathbb{N} \quad (5.7)$$

where  $G$  is a smooth function defined in local coordinates system  $x = (x^1, x^2, \dots, x^n)$  and  $y = (y^1, y^2, \dots, y^n)$ . The equivalent vector field of this equation is given by

$$S := y^i \frac{\partial}{\partial x^i} - 2G^i(x^j, y^j, t) \frac{\partial}{\partial y^i}. \quad (5.8)$$

This determines a nonlinear connection on the tangent bundle of real, and smooth  $n$ -dimensional manifold  $M$ ,  $TM$ , with local coefficients as

$$N_j^i = \frac{\partial G^i}{\partial y^j}. \quad (5.9)$$

Now, the KCC covariant differential defines by

$$\frac{Dy^i}{dt} = \frac{dy^i}{dt} + N_j^i y^j. \quad (5.10)$$

By applying this derivative for  $y^i = \dot{x}^i$  we obtain

$$\frac{D\dot{x}^i}{dt} = \frac{d\dot{x}^i}{dt} + N_j^i \dot{x}^j, \quad (5.11)$$

and by using equation (5.7)

$$\frac{D\dot{x}^i}{dt} = -2G^i + N_j^i \dot{x}^j. \quad (5.12)$$

This contravariant vector field is called the first KCC invariant. Now to derive the second invariant KCC, we use a small perturbation via a diffeomorphism

$$x^i(t) = \tilde{x}^i(t) + \delta\zeta^i(t), \quad (5.13)$$

where  $\zeta^i(t)$  are components of a contravariant vector field defined along the path  $\tilde{x}^i$  that we can choose as  $\dot{x}^i$ .

In this theory, the properties of any dynamical system are described in terms of five geometrical invariants, with the second one giving the Jacobi stability of the system. Consider a system of second-order differential equation

$$\frac{d^2x^i}{dt^2} + 2G^i(X, Y) = 0, \quad i \in \mathbb{N} \quad (5.14)$$

where  $G^i(X, Y)$  are smooth functions defined in a local system of coordinates on TM with  $X = (x^1, x^2, \dots, x^n)$ ,  $Y = (y^1, y^2, \dots, y^n)$ . The second KCC invariant which is also known as a deviation curvature tensor of the system of the second-order differential equation, gives the Jacobi stability of the system and is given by

$$P_j^i = -2\frac{\partial G^i}{\partial x^j} - 2G^l G_{jl}^i + y^l \frac{\partial N_j^i}{\partial x^l} + N_l^i N_j^l, \quad (5.15)$$

where  $G_{jl}^i = \frac{\partial N_l^i}{\partial y^j}$  is called the Berwald connection, and  $N_j^i = \frac{\partial G^i}{\partial y^j}$  defines the coefficient of a nonlinear connection  $N$  on the tangent bundle TM.

The trajectories of a given system of second-order differential equations are Jacobi stable if and only if the real parts of the eigenvalues of the deviation curvature tensor  $P_j^i$  are strictly negative everywhere, and Jacobi unstable otherwise. Geometrically, the trajectories of the system are bunching together if they are Jacobi stable and dispersing if they are Jacobi unstable. We use this information in the study of the behavior of trajectories in the Generalized q-metric solution in Chapter 15.

### 5.3 Kolmogorov entropy

The Lyapunov exponents describe how the nearby trajectories diverge exponentially in a phase space [133, 135]. An important quantity which is related to the Lyapunov exponents is the so-called Kolmogorov-Sinai entropy ( $h_{ks}$ ), which gives a measure of the amount of information lost or gained by a chaotic orbit as it evolves [135]. In other words, it tells us how the nearby trajectories diverge in a chaotic system as it evolves. This quantity allows to analyze the random behavior of system. Following Pesin's Theorem [136, 137] it is equal to the sum of the positive Lyapunov exponents  $n$

$$h_{ks} = \sum_{i=1}^n \lambda_i. \quad (5.16)$$

The relation between this entropy and the physical entropy first was discussed in [138, 139]. Alternatively, it determines how a system is chaotic or disorder when  $h_{ks} > 0$  and non-chaotic for  $h_{ks} = 0$ . In general, Lyapunov exponents describe how nearby trajectories diverge exponentially in the phase space, and regarding the Kolmogorov entropy measures the complexity of a system and the positivity of this entropy means the existence of chaos.

We will consider this stability analysis and entropy in Chapter 15 to study the geodesics of the Generalized q-metric.





## CHAPTER 6

# Space-times

The black hole uniqueness theorems in general relativity are one of the most intriguing results in this theory. In general, for Einstein-Maxwell theory in the static space-times, the theorem guarantees that the Reissner–Nordström space-time is the unique black hole solution with a regular event horizon and asymptotically flat. However, there are some interesting situations where the hypotheses of this theorem do not hold. For example, in the case of considering matter other than Maxwell fields coupled to the gravity, or black holes can have Yang-Mills "hair", therefore there is no such uniqueness theorem for Einstein-Yang-Mills theory. Besides, on the one hand, there are solutions in Einstein-Maxwell theory which are asymptotically flat but do not have a regular event horizon like the C-metric or q-metric solutions. On the other hand, there are static solutions which have a regular event horizon but are not asymptotically flat like distorted Schwarzschild space-time. Apart from the mathematics beauty of this solution, it may also have a physical and astrophysical interest in describing the near horizon geometry of an isolated black hole which is distorted by the presence of far away matter. The matter could be a magnetic field in which the black hole is immersed.

In this chapter, we briefly explain the space-times considering in this thesis. We start with the wide class of Weyl solutions and represent three special classes of this metric; namely, distorted Schwarzschild, static and stationary q-metric. Finally, we close this chapter by explaining generalized C-metric families.

## 6.1 Static and axisymmetric space-times

In the static space-time, the time evolution is a symmetry transformation. This means that it admits a time-like Killing vector field which provides a one-parameter group of isometries corresponding to the time translation, such

that this parameter can be taken as a time coordinate. Besides, the static Killing vector  $\zeta$  is orthogonal to a space-like hypersurface. This condition is formulated as follows [140]

$$\zeta_{[\mu}\Delta_{\nu}\zeta_{\lambda]} = 0, \quad (6.1)$$

where  $\zeta$  is a time-like Killing vector field.

Because of the time independency, we can consider a three-dimension manifold  $N$  of trajectories of the time-like Killing vector field  $\zeta$ . This is the space-like hypersurface orthogonal to  $\zeta$ . In the general case, the relation between tensor fields on this manifold  $N$ , and the space-time was investigated in detail by Geroch [141]. In addition, we consider the axisymmetric space-times. This condition provides the existence of a space-like Killing vector field  $\eta$ , with closed integral curves. Both conditions together easily lead to this relation

$$\eta^\mu \nabla_\mu (\zeta^\nu \nabla_\nu f) = \zeta^\mu \nabla_\mu (\eta^\nu \nabla_\nu f), \quad (6.2)$$

where  $f \in C^\infty$ . In this case, we can define coordinates  $t$  and  $\phi$  in such a way that

$$\zeta^\nu = \partial_t^\nu, \quad (6.3)$$

$$\eta^\nu = \partial_\phi^\nu. \quad (6.4)$$

In general, the class of static and axisymmetric solutions of Einstein's field equation is described by the Weyl metric.

Weyl derived the family of solutions to the static Einstein vacuum equations in 1917. From that time, an interest in the Weyl metrics developed, particularly in providing exterior solutions to astrophysical problems via modelling the exterior gravitational field of compact axially symmetric bodies. Since the Weyl coordinates are valid only in a region where the Killing vector  $\zeta$  is timelike, these coordinates cover only the exterior region. In addition to their astrophysical relevance, mathematically they are also of some interest since they present the opportunity of explicitly determining and investigating a large class of relativistic solutions to the Einstein equation. Using cylindrical coordinates  $(\rho, z, \phi)$  the Weyl metric is given by

$$ds^2 = -e^{2\psi} dt^2 + e^{2(\gamma-\psi)} (d\rho^2 + dz^2) + e^{-2\psi} \rho^2 d\phi^2, \quad (6.5)$$

where  $\psi = \psi(\rho, z)$  and  $\gamma = \gamma(\rho, z)$  are the metric functions, and  $\psi$  plays the role of the gravitational potential. If we consider a three-dimensional manifold  $N$ , orthogonal to the static Killing vector field, then this metric induces the flat metric on  $N$ . Besides, the metric function  $\psi$  with respect to this flat metric obeys the Laplace equation

$$\psi_{,\rho\rho} + \frac{1}{\rho}\psi_{,\rho} + \psi_{,zz} = 0, \quad (6.6)$$

The metric function  $\gamma$  is obtained from the metric function  $\psi$  [142]

$$\begin{aligned} \gamma_{,\rho} &= \rho(\psi_{,\rho}^2 - \psi_{,z}^2), \\ \gamma_{,z} &= 2\rho\psi_{,\rho}\psi_{,z}, \end{aligned} \quad (6.7)$$

where equation (6.6) is the integrability condition for the metric function  $\gamma$ . This approach provides a straightforward technique for obtaining static, axisymmetric, vacuum and general relativistic fields.

The relation between Schwarzschild coordinates and Weyl coordinates is given by

$$\rho = \sqrt{r(r - 2M)} \sin \theta, \quad z = (r - M) \cos \theta, \quad (6.8)$$

where  $M$  is a parameter that is identified with the mass of the compact object. Later, in 1959, Erez and Rosen pointed out that the multipole structure of a static axially symmetric solution has a simpler form in the prolate spheroidal coordinates <sup>1</sup> rather than the cylindrical coordinates of Weyl via this transformation relation [143, 144]

$$\begin{aligned} x &= \frac{1}{2M}(\sqrt{\rho^2 + (z + M)^2} + \sqrt{\rho^2 + (z - M)^2}), \\ y &= \frac{1}{2M}(\sqrt{\rho^2 + (z + M)^2} - \sqrt{\rho^2 + (z - M)^2}). \end{aligned} \quad (6.9)$$

Equivalently,  $\rho = M\sqrt{(x^2 - 1)(1 - y^2)}$  and  $z = Mxy$ . The relation to Schwarzschild coordinates is given by

$$x = \frac{r}{M} - 1, \quad (6.10)$$

$$y = \cos \theta. \quad (6.11)$$

---

<sup>1</sup>Prolate spheroidal coordinates are three-dimensional orthogonal coordinates that result from rotating the two-dimensional elliptic coordinates about the focal axis of the ellipse.

As mentioned, the Weyl metric is the most general static and axisymmetric solution which contains an infinite number of parameters, representing all the multipole moments. Indeed, such a metric with infinite parameters is not applicable to realistic sources like compact astrophysical objects. For this reason and using analytical approaches, in what follows we consider solutions containing only two independent parameters that can be interpreted as mass and quadrupole and treated (semi-) analytically.

## 6.2 Distorted Schwarzschild space-time

The Schwarzschild space-time is the unique static solution of Einstein's vacuum equation which is asymptotically flat. However, there is another class of static, vacuum solution describing non-asymptotically flat space-time, which is obtained by assuming the existence of a static and axially symmetric external distribution of matter. This space-time is a local solution of the Einstein field equation [145]. In 1965, Doroshkevich and his colleagues considered an external gravitational field up to a quadrupole in the Schwarzschild space-time. They also showed that by adding quadrupole correction to the Schwarzschild space-time, the horizon remains regular [146]. Later, in 1982 a detailed analysis of the global properties of the distorted Schwarzschild space-time was introduced by Geroch and Hartle [147]. In 1997, the explicit form of the metric was presented [148].

In brief, since in vacuum, static axisymmetric space-times, Einstein's equations reduce to the linear Laplace's equation on the flat space, the distorted black hole can be obtained by adding an appropriate distortion function to the Schwarzschild solution. We will see more about this construction in the Result chapter. However, for example, this technique cannot be extended to Einstein-Maxwell theory because the result will be a non-linear set of coupled partial differential equations.

The resulting class is not asymptotically flat. Therefore, the uniqueness theorem fails in this case. Furthermore, it is not possible to introduce the notion of null infinity and consequently, the standard concept of an event horizon in this case. Nevertheless, this class of solutions can be interpreted as black holes with locally defined isolated horizons, or alternatively, considering the matter far away from the isolated horizon and extending the solution as asymptotically flat space-time. The latter allows us to identify the isolated horizon with an event horizon. ‘

The distorted Schwarzschild space-time in the prolate spheroidal coordinates is described by

$$ds^2 = - \left( \frac{x-1}{x+1} \right) e^{2\hat{\psi}} dt^2 + M^2 (x+1)^2 e^{-2\hat{\psi}} \left[ e^{2\hat{\gamma}} \left( \frac{dx^2}{x^2-1} + \frac{dy^2}{1-y^2} \right) + (1-y^2) d\phi^2 \right], \quad (6.12)$$

where  $t \in (-\infty, +\infty)$ ,  $x \in (1, +\infty)$ ,  $y \in [-1, 1]$ , and  $\phi \in [0, 2\pi]$ .  $\hat{\psi}$  and  $\hat{\gamma}$  are distortion function related to external source. If this is assumed that the distortion field is generated by material satisfying the strong energy condition then the explicit general form of  $\hat{\psi}$  should be negative [147]. In this metric, the location of the horizon and the singularity are at  $x = 1$  and  $x = -1$ , respectively. And the distortion functions can be expressed in terms of Legendre polynomials of the first kind and up to quadrupole are given by

$$\hat{\psi} = \sum_{n=1} q_n R^n P_n\left(\frac{xy}{R}\right), \quad (6.13)$$

$$\begin{aligned} \hat{\gamma} = & + \sum_{n=1} q_n \sum_{l=0}^{n-1} [(-1)^{n-l+1} (x+y) - x+y] R^l P_l \\ & + \sum_{k,n=1} \frac{nkq_nq_k}{(n+k)} R^{n+k} [P_n P_k - P_{n-1} P_{k-1}], \end{aligned} \quad (6.14)$$

where

$$P_n := P_n\left(\frac{xy}{R}\right), \quad R = \sqrt{x^2 + y^2 - 1}. \quad (6.15)$$

Up to quadrupole these functions reduce to

$$\begin{aligned} \hat{\psi} = & -\frac{q}{2} [-3x^2y^2 + x^2 + y^2 - 1], \\ \hat{\gamma} = & -2xq(1-y^2) \\ & + \frac{q^2}{4} (x^2-1)(1-y^2)(-9x^2y^2 + x^2 + y^2 - 1). \end{aligned} \quad (6.16)$$

where  $q_2 := q$  is the quadrupole link to the external source. To have some intuitive picture about the role of  $q$  here, let us consider Newtonian gravity (we show quadrupole in Newtonian picture by  $q_N$ ). In Newtonian theory, it is rather familiar piece of knowledge that the multipole expansion dominated by a quadrupole moment  $\beta_N$  can be modelled by two equal point-like masses  $m$  located on some axis, say  $z$ , and at some distance from the center, also

an infinitesimally thin ring of the mass  $M$  and radius  $R$  located at the plane perpendicular to this axis. If the contribution of the point-like masses to the gravitational field is greater than the ring, then  $q < 0$ , and if for ring is greater we have  $q_N > 0$ . If  $q < 0$ , then there exist a net force directed toward the  $z$ -axis. This force creates a potential barrier. If  $q > 0$ , there is a net force directed to the ring, outward from the central object. This force balances the gravitational of the central source and the external fields.

We will investigate this space-time via different tools throughout this thesis.

### 6.3 Static q-metric space-time

Around four decades after introducing a wide class of static and axisymmetric solutions to the vacuum Einstein field equations by Weyl, in 1959 Erez and Rosen published the first static solution with quadrupole moment by using the Weyl method which includes the Schwarzschild metric as special case [143]. This quadrupolar solution was generalized to include an infinite number of multipole moments by Quevedo [144]. In the 1960s, Zipoy [149] and Voorhees [150] found a transformation which allows us to generate new static solutions called  $\gamma$ -metric or  $\delta$ -metric from known solutions and was interpreted as the simplest static solution which generalizes the Schwarzschild metric by including a quadrupole moment, and later on, by using a transformation is known as q-metric [151]. Later, Gutsunaev and Manko suggested another exact solution with monopole and quadrupole moments to have the same quadrupole as in the Erez–Rosen metric, but different in higher relativistic multipole moments [152]. In 1990, Manko introduced a quadrupolar metric which can be interpreted as the nonlinear combination of the Schwarzschild monopole solution with the quadrupolar term of the Weyl metric [153]. In 1994, Hernández-Pastora and Martín derived two exact solutions with different monopole–quadrupole structures [154], and this is an interesting ongoing area of study. In the present work, we are interested to study q-metric in the different astrophysical settings via accretion discs and their properties.

As mentioned, q-metric describes static, axially symmetric, and asymptotically flat solutions to the Einstein equation with quadrupole moment generalizing the Schwarzschild family. The metric represents the exterior gravitational field of an isolated static axisymmetric mass distribution. It can be used to investigate the exterior fields of slightly deformed astrophysical objects in the strong-field regime [155]. In fact, the presence of a quadrupole,

independent of its value, changes the geometric properties of space-time drastically. The metric is presented as follows [144]

$$ds^2 = \left(1 - \frac{2M}{r}\right)^{1+q} dt^2 - \left(1 - \frac{2M}{r}\right)^{-q} \left[ \left(1 + \frac{M^2 \sin^2 \theta}{r^2 - 2Mr}\right)^{-q(2+q)} \left( \frac{dr^2}{1 - \frac{2M}{r}} + r^2 d\theta^2 \right) + r^2 \sin^2 \theta d\phi^2 \right]. \quad (6.17)$$

In the prolate spheroidal coordinates this metric is written as

$$ds^2 = - \left( \frac{x-1}{x+1} \right)^{(1+q)} dt^2 + M^2 (x^2 - 1) \left( \frac{x+1}{x-1} \right)^{(1+q)} \left[ \left( \frac{x^2 - 1}{x^2 - y^2} \right)^{q(2+q)} \left( \frac{dx^2}{x^2 - 1} + \frac{dy^2}{1 - y^2} \right) + (1 - y^2) d\phi^2 \right], \quad (6.18)$$

where  $t \in (-\infty, +\infty)$ ,  $x \in (1, +\infty)$ ,  $y \in [-1, 1]$ ,  $\phi \in [0, 2\pi)$ , and  $q \in (-1, \infty)$  is the quadrupole parameter.

This metric has a central curvature singularity at  $x = -1$ , where it occurs for all real values of  $q$ . Moreover, for non-vanishing  $q$  an additional singularity appears at  $x = 1$ , and the norm of the time-like Killing vector at this radius vanishes. Also, outside this hypersurface, there exists no additional horizon. However, considering a relatively small quadrupole moment, this hypersurface is located very close to the origin of coordinates so that a physically reasonable interior solution could be used to cover them [155]. Besides, out of this region, there is no more singularity, and the metric is asymptotically flat. It is worth mentioning that there are different definitions of multipole moments; however, in the lower order, all are equivalent and link to the parameter  $q$ . In fact, the quadrupole can present how the mass is stretched-out along some, for example, a sphere has zero quadrupole. The sign of quadrupole determines the shape of the source, which can be either prolate or oblate, corresponding to different gravitational fields.

This solution for any finite values of parameters  $q$  and  $M$  is asymptotically flat, and for  $q = 0$  the obtaining result is the Schwarzschild solution. In addition, in the limiting case  $M = 0$  independently of the parameter  $\alpha$ , via coordinate transformations that transform the Minkowski space-time is recovered. This means that the parameter  $q$  is related to a genuine mass

distribution. In another word, by using the invariant definition of Geroch [156], the lowest independent multipole moments, monopole, for this metric reads as

$$m_0 = M(1 + q), \quad (6.19)$$

where  $m_0$  is being positive to avoid having a negative mass distribution, is equivalent to restricting quadrupole at most to this domain  $\alpha \in (-1, \infty)$ <sup>2</sup>. The second multipole moment is also given by

$$m_2 = -\frac{M^3}{3}q(1 + q)(2 + q), \quad (6.20)$$

where describe the deformation from the spherical case, which is positive for prolate mass distribution and negative for an oblate one. It turns out that all higher multipole moments can be written in terms of  $m_0$  and  $m_2$  [155]. This means, equivalently, the only independent parameters are mass  $M$  and the quadrupole moment  $\alpha$ . Besides, all odd multipole moments vanish because of reflection symmetry with respect to the equatorial plane.

The properties of this metric have been studied in the literature, for example [157, 151, 158]. In the result part 7, we revisit some of its circular geodesics on the equatorial plane, with a slightly different approach. Through this thesis, this metric is explored via different implements.

## 6.4 Stationary q-metric space-time

A stationary generalization of the static Zipoy-Vorhees space-time was first presented in [159]. However, the physical meaning of the quadrupole parameter, in this case, was first investigated in [151]. In 2018, the explicit form of the metric was calculated [160]. The rotating q-metric has three independent parameters: mass, rotation parameter and quadrupole and may represent deformed rotating objects. In prolate spheroidal coordinates  $(t, x, y, \phi)$  reads as

$$\begin{aligned} ds^2 = & -f(dt - \omega d\phi)^2 \\ & + \frac{\sigma_0^2}{f} \left[ e^{2\gamma}(x^2 - y^2) \left( \frac{dx^2}{x^2 - 1} + \frac{dy^2}{1 - y^2} \right) \right. \\ & \left. + (x^2 - 1)(1 - y^2)d\phi^2 \right], \end{aligned} \quad (6.21)$$

---

<sup>2</sup>In fact, the Arnowitt-Deser-Misner mass which characterizes the physical properties of the exact solution also has the same expression and should be positive [157, App.], also for stationary space-time it is equivalent to the Komar mass.



where  $\sigma_0$  is a constant

$$\sigma_0 := \frac{M(1 - \tau_0^2)}{(1 + \tau^2)}, \quad (6.22)$$

$$(6.23)$$

where  $\tau$  is a constant. The relations between rotation parameter  $a$ ,  $\tau$  and  $\sigma_0$  are as follows

$$a := \frac{-2\sigma_0\tau}{(1 - \tau^2)}, \quad (6.24)$$

$$\sigma^2 = M^2 - a^2. \quad (6.25)$$

There is a freedom to either consider  $\sigma_0$  and  $\tau$  as the independent parameters or  $M$  and  $a$ . However, it turns out that it is more convenient to work with  $M$  and  $a$ . The other metric functions are given by

$$\begin{aligned} f &= \frac{A}{B}, \\ \omega &= -2(a + \sigma_0 \frac{C}{A}), \\ e^{2\gamma} &= \frac{1}{4} \left(1 + \frac{m}{\sigma_0}\right)^2 \frac{A}{(x^2 - 1)^{1+q}} \left[ \frac{x^2 - 1}{x^2 - y^2} \right]^{(1+q)^2}. \end{aligned} \quad (6.26)$$

Besides

$$A = a_+ a_- + b_+ b_-, \quad (6.27)$$

$$B = a_+^2 + b_+^2,$$

$$C = (x + 1)^q [x(1 - y^2)(\lambda + \eta)a_+ + y(x^2 - 1)(1 - \lambda\eta)b_+].$$

And

$$a_{\pm} = (x \pm 1)^q [x(1 - \lambda\eta) \pm (1 + \lambda\eta)],$$

$$b_{\pm} = (x \pm 1)^q [y(\lambda + \eta) \mp (\lambda - \eta)],$$

$$\lambda = \tau(x^2 - 1)^{-q}(x + y)^{2q},$$

$$\eta = \tau(x^2 - 1)^{-q}(x - y)^{2q},$$

$$\tau a = \sigma_0 - M.$$

The functions  $f$  and  $\omega$  are related to the twist scalar  $\Omega$  through

$$f^2 \nabla \omega = \rho \phi \times \nabla \Omega \quad (6.28)$$

And the transformation relation to the Schwarzschild like coordinates is given by

$$x = \frac{1}{\sigma_0}(r - M), \quad (6.29)$$

$$y = \cos \theta. \quad (6.30)$$

In the limiting cases,  $M = 0$  and  $q = -1$ , the Minkowski metric is recovered as expected. In general, the stationary  $q$ -metric is asymptotically flat and free of curvature singularities outside the hypersurface  $r = 2M$ . This implies that we can use it safely to describe the gravitational field of relativistic compact objects for which  $r > 2M$ . In addition, the physical meaning of the parameters entering the metric can be clarified by calculating the relativistic multipole moments [156, 160, 161, 162] as

$$m_2 = M \left[ -M^2 + \sigma_0^2(1 - \tau^2) + \sigma_0 \tau \left( \frac{7}{3} \frac{\sigma_0^2}{M} - 3M \right) - \frac{1}{3} \tau^3 \frac{\sigma_0^3}{M} \right], \quad (6.31)$$

$$m_0 = M + \sigma_0 \tau, \quad (6.32)$$

$$J_1 = Ma + 2a\sigma_0\tau. \quad (6.33)$$

As the static case, all the higher moments can be expressed in terms of  $m_0$ ,  $m_2$  and  $J_1$ , and all the odd mass moments  $m_{2k+1}$  and even angular momentum moments  $J_{2k}$  vanish, since we have the reflection symmetry with respect to the equatorial plane. An analysis shows that for negative values of  $q$  we have  $m_2 > 0$  and vice versa. Beside  $m_2$  is symmetric with respect to  $a$ . This means the gravitational field does not depend on the direction of rotation that we expected. We study the Ernst potential, the effective potential and circular trajectories on the equatorial plane in this metric in Chapter 9 and the Thick accretion disc in Section 11.3.

## 6.5 C-metric space-time

Within the first few years of the field equations being known, a few mathematical solutions were discovered whose physical meanings were unknown. Among them were solutions discovered by Levi-Civita in 1918 [163]. The C-metric family originally belongs to this class. However, this metric again was discovered in the early 1960s probably following the work by Newman and Tamburino [164], Robinson and Trautman [165] and Ehlers and Kundt [166]. The latter classified invariantly the degenerate static vacuum fields to A, B, and C type metrics, where the standard C-metric today is the axisymmetric vacuum solution which inherited its name from this classification. At that time, the physical interpretation of C-metric was not clear. In 1970, Kinnersley and Walker provided the interpretation of this solution as an accelerated black hole [167]. Later, in 1976 the Plebanski-Demianski (PD) family of solutions was introduced to describing a new class of stationary and axisymmetric solutions to the Einstein-Maxwell- $\Lambda$  field equations [168]. From this metric, via using a series of different coordinate transformations, one could obtain many of the known black hole solutions like Kerr solution and C-metric. Additionally, the solution contains a parameter that can be identified as the NUT charge within certain limits.

However, at this stage, it is impossible to write the C-metric in pseudo-spherical coordinates since we cannot factorize the metric functions for further transformation. Without going to the details, this problem causes by existence of high order polynomials in the metric. Around three decades later, Hong and Teo succeeded in expressing these polynomials in a factorized form with simple roots [169, 170]. The new version of the metric is not only more convenient, but it is also possible to entirely written in Boyer-Lindquist coordinates. The most characteristic of this family of solutions is its acceleration nature. In order to realize the accelerating feature of this solution intuitively, it is helpful to compare this metric with Rindler coordinates. In short, to do so, it is required to work from its flat-space limit. Then by using a nontrivial coordinate transformation, we are able to recover the Rindler metric in  $3 + 1$ -dimensional cylindrical coordinates. Thus, this comparison requires interpreting one of the parameters in the metric as the acceleration parameter.

Mathematically, the acceleration is supported by the existence of a conical deficit corresponding to the effect of a cosmic string attached to the horizon. In fact, the cosmic string has  $\delta$ -function stress energy tensor. This causes the existence of an angular deficit around the cosmic string. More precisely, in the asymptotically flat space, the C-metric describes a configuration of two black holes that each of them has unequal conical deficits extending from the

north and south poles of each event horizon to either acceleration horizon or the boundary that separates them. They are accelerating in opposite directions. The conical deficit  $\delta = 2\pi - \Delta\phi$ , where  $\phi$  is a generic azimuthal coordinate, is related to the tension of a cosmic string  $\mu = \delta/8\pi$ . To make it more familiar, one may also introduce such defects to the Schwarzschild metric by replacing the azimuthal coordinate with

$$g_{\phi\phi} = r^2 \sin^2 \theta K^{-2}, \quad (6.34)$$

where  $K > 1$ . This  $g_{\phi\phi}$  defines a string running through the core to the black hole. In this case, the deficit along both the  $\theta = 0$  and  $\theta = \pi$  axes is the same and  $\mu = \frac{1}{4}(1 - K^{-1})$  [171]. However, in the C-metric situation is different. This metric has unequal deficits where the deficit along both axes are not the same, this imbalanced tension is the origin of the driven acceleration. As we will see in the following, the conical defect in the C-metric is controlled through the parameter  $K$  by regulating the distribution of tensions along either axis and allows  $\phi$  to be  $2\pi$ -periodic. It is also worth mentioning that a negative deficit is also possible; however, theoretically, this would be sourced by a negative energy object. The spinning charged C-metric in Boyer-Lindquist type coordinates reads as [170]

$$ds^2 = \frac{1}{\Omega^2} \left( -\frac{f}{\Sigma} \left[ dt - a \sin^2 \theta \frac{d\phi}{K} \right]^2 + \frac{\Sigma}{f} dr^2 + \Sigma r^2 \frac{d\theta^2}{g} + \frac{g \sin^2 \theta}{\Sigma r^2} \left[ a dt - (r^2 + a^2) \frac{d\phi}{K} \right]^2 \right), \quad (6.35)$$

with the metric functions

$$\Omega = 1 + \alpha r \cos \theta, \quad (6.36)$$

$$f(r) = (1 - \alpha^2 r^2) \left( 1 - \frac{2m}{r} + \frac{e^2 + a^2}{r^2} \right), \quad (6.37)$$

$$g(\theta) = (e^2 + a^2) \alpha^2 \cos^2 \theta + 2m\alpha \cos \theta + 1, \quad (6.38)$$

$$\Sigma(r, \theta) = \frac{a^2}{r^2} \cos^2 \theta + 1, \quad (6.39)$$

$$\xi = \alpha^2 (e^2 + a^2) + 1, \quad (6.40)$$

$$K = \xi + 2m\alpha. \quad (6.41)$$

The metric has four independent parameters: the mass  $m$ , the electric charge  $e$ , the rotation  $a$ , and the acceleration parameter  $\alpha$  that usually are taken to

be positive. As mentioned also there is a conical singularity on the  $\theta$  axis. In fact, the regularity condition at the poles  $\theta_+ = 0$  and  $\theta_- = \pi$  provided  $K_{\pm} = g(\theta_{\pm})$  where  $K$  can regularize only one pole that need to choose from the beginning. By choosing  $K = K_+$  in equation (6.41) we only have a string at the south pole.

Almost all analyses considering the family of C-metric are revolved around the coordinate ranges, which are dictated by the metric functions and their root configurations. First of all, the conformal factor  $\Omega$  determines the location of the boundary

$$r_b = -\frac{1}{\alpha \cos \theta}. \quad (6.42)$$

In addition, the roots of metric function  $f(r)$  correspond to horizons. Thus, obviously  $f(r)$  should have at least one root for  $r \in (0, \frac{1}{\alpha})$  to have a black hole in the space-time. In general, mostly with charge, generic configurations have different distinct horizons in a pair of inner and outer horizons. Like the regular Reissner-Nordström solution, they typically approach one another and vanish for a relatively high charge. Furthermore, the pairs of horizons separated the space-time into different regions with the same signature. In addition, when the acceleration horizon is present, there is also a second outer acceleration horizon where both intersect with the boundary. The astrophysics point of view is more interested in the outer communication region between the outer horizon and the acceleration horizon. To have a better inside, in Figure 6.1 the place of the inner and outer horizons have been presented for the chosen parameters. As we see, by increasing  $a$  the place of horizons become closer to each other, and to the black hole. However, since the accelerating horizon depends on  $\alpha$ , the valid region becomes wider. The same behavior expected for increasing  $e$ , as the metric function  $f(r)$  is symmetric in both parameters  $e$  and  $a$ .

In addition, from the analyzing the  $\theta$ -coordinate, the metric function  $g(\theta)$  should have positive roots in  $[0, \pi)$ . Therefore it requires to have

$$e^2 + a^2 \leq m^2, \quad (6.43)$$

and for a slowly accelerating black hole the following condition should be fulfilled

$$2m\alpha \leq \begin{cases} 2\sqrt{\xi-1} & \xi > 2, \\ \xi & 0 < \xi \leq 2. \end{cases} \quad (6.44)$$

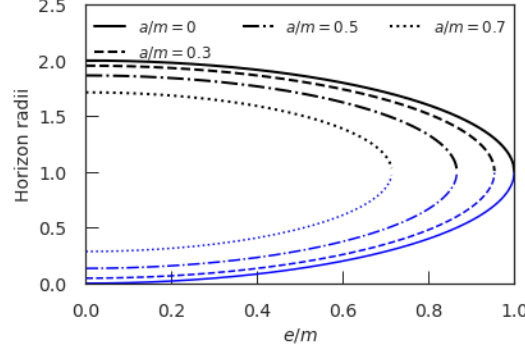


**Figure 6.1:** Place of horizons as a function of charge parameter  $e$ , for different rotation parameter  $a$ .

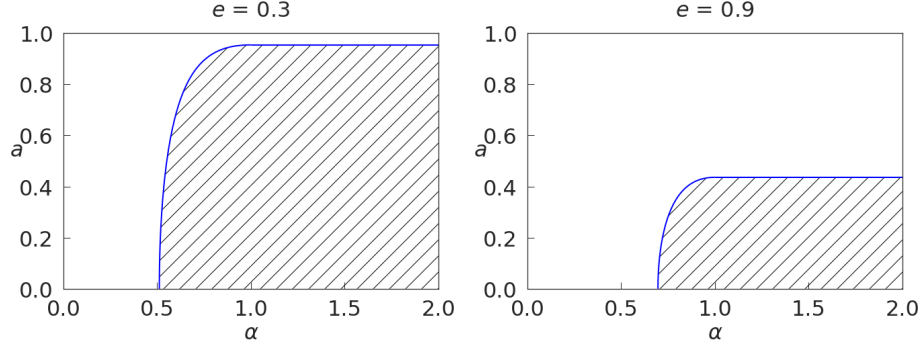


**Figure 6.2:** Allowed parametric regions for the spinning charged C-metric as a function of  $a$ . The regions marked out with hatching correspond to the forbidden regions. The axes scaled with  $m$ .

Figure 6.2 shows different parametric set-ups. The hatched parts are the excluded regions by the equation (6.44) for chosen parameters. We see that this condition acts as an upper bound on the rotation or the acceleration for relatively small parameters. The plots also would have the same pattern as a function of  $e$ , because of the symmetry in the equation. Figure 6.3 shows the metric function  $g(\theta)$  for chosen parameters. As it has shown, the forbidden region is the hatched part, which shrinks as  $a$  and  $e$  increase since  $g(\theta)$  is also symmetric with respect to  $a$  and  $e$ . In Section 11.4 we study the Thick disc configuration and its properties in this space-time.

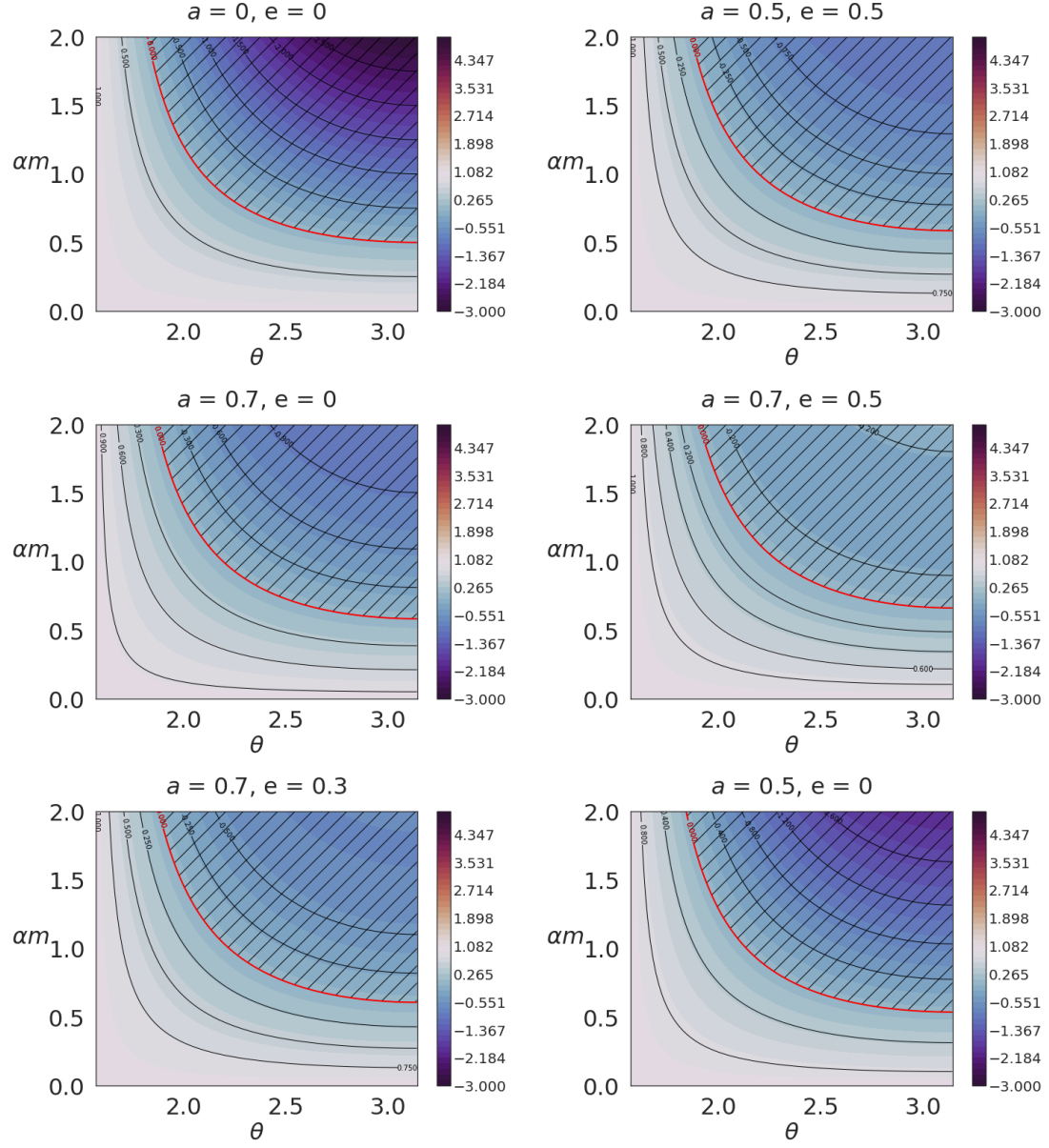


**Figure 6.3:** Plots of metric function  $g(\theta)$ . The red line corresponds to  $g(\theta) = 0$ , and the hatched areas correspond to the forbidden regions.





# Part II

## Results



## CHAPTER 7

# Generalized q-metric

As mentioned, the q-metric has the Minkowski space as the limiting case. While this seems natural, the question of how an external distribution of mass may distort compact objects described by this metric led us to introduce its generalization by considering an external matter distribution up to quadrupoles, similar to adding a magnetic environment to the black hole solution [172]. Of course, solutions of the static Einstein vacuum equations obtained by Weyl's method for a long time have played a relatively important role in the describing exterior gravitational field of axially symmetric compact objects. To do so we utilized the Weyl's method we used the q-metric as a background metric to present a family of solutions, given as an expansion in terms of Legendre polynomials, that may describe for instance the exterior gravitational field of a non-spherically symmetric body embedded in an external gravitational field. This generalization preserves the main virtues of the seed metric aside from asymptotical flatness by its construction.

In the second part of this chapter, we consider this metric up to quadrupole to carry out the characterization of the impact of both quadrupole parameters on the circular geodesics in the equatorial plane. Of course, the effect of other multipole moments is negligible compared to quadrupole moments. Undoubtedly, there is a number of studies on geodesics in the background with quadrupoles, for example [173, 174, 175, 176, 177, 178, 179, 180, 181, 182, 183] among many others. Throughout this thesis, we investigate various properties of this generalized metric in different astrophysical scenarios.

## 7.1 Construction of the metric

We start with the Weyl metric described briefly in Section 6.1. As mentioned, in the Weyl metric (6.5) the function  $\psi$  obeys the Laplace equation with

respect to the flat metric

$$\psi_{,\rho\rho} + \frac{1}{\rho}\psi_{,\rho} + \psi_{,zz} = 0, \quad (7.1)$$

where ", " is used for partial derivatives. This linear equation is the key factor in the Weyl technique of generating solutions. The metric function  $\gamma$  is obtained by the explicit form of the function  $\psi$ , and the equation (7.1) is the integrability condition for this solution

$$\nabla\gamma\nabla\rho = \rho(\nabla\psi)^2, \quad (7.2)$$

where  $\nabla := \partial_z + i\partial_\rho$ , or equivalently as mentioned

$$\begin{aligned} \gamma_{,\rho} &= \rho(\psi_{,\rho}^2 - \psi_{,z}^2), \\ \gamma_{,z} &= 2\rho\psi_{,\rho}\psi_{,z}. \end{aligned} \quad (7.3)$$

Before proceeding with the q-metric, we write field equations in the more symmetric form in the prolate spheroidal coordinates  $(t, x, y, \phi)$ . The relation of the cylindrical coordinates of Weyl to the prolate spheroidal coordinates is given by

$$\begin{aligned} x &= \frac{1}{2M}(\sqrt{\rho^2 + (z + M)^2} + \sqrt{\rho^2 + (z - M)^2}), \\ y &= \frac{1}{2M}(\sqrt{\rho^2 + (z + M)^2} - \sqrt{\rho^2 + (z - M)^2}). \end{aligned} \quad (7.4)$$

In this coordinates system the field equation for  $\psi$  (7.1) reads as

$$[(x^2 - 1)\psi_{,x}]_{,x} + [(1 - y^2)\psi_{,y}]_{,y} = 0, \quad (7.5)$$

And for  $\gamma$  (6.7) is given by

$$\begin{aligned} \gamma_{,x} &= \frac{1 - y^2}{x^2 - y^2} [x(x^2 - 1)\psi_{,x}^2 - x(1 - y^2)\psi_{,y}^2 - 2y(x^2 - 1)\psi_{,x}\psi_{,y}], \\ \gamma_{,y} &= \frac{1 - y^2}{x^2 - y^2} [y(x^2 - 1)\psi_{,x}^2 - y(1 - y^2)\psi_{,y}^2 + 2x(1 - y^2)\psi_{,x}\psi_{,y}]. \end{aligned} \quad (7.6)$$

We can see from the form of equation (7.5), that it allows separable solutions. Therefore,  $\psi$  can be written in terms of multiplication of two functions, say

$\psi = \mathcal{X}(x)\mathcal{Y}(y)$ . By using the separation of variable methods in differential equations, it is easy to see that one can write the  $y$  part in terms of Legendre polynomial. Then, the  $x$  dependence part also fulfills the Legendre's equation [184]

$$[(x^2 - 1)\mathcal{X}_{,x}]_{,x} - n(n+1)\mathcal{X} = 0. \quad (7.7)$$

In brief,  $\mathcal{X}$  can be expressed in terms of Legendre polynomials of the first kind and second kind. However, by relaxing the assumption of asymptotic flatness, the second kind's coefficient should vanish. In addition, by the requirement of elementary flatness<sup>1</sup> in the neighborhood of the symmetry axis, the general solution for  $\psi$  is obtained as

$$\psi = \sum_{n=0} \beta_n R^n P_n\left(\frac{xy}{R}\right), \quad R = \sqrt{x^2 + y^2 - 1}, \quad (7.8)$$

where  $P_n$  is Legendre polynomial of order  $n$ , and  $\beta_n \in \mathbb{R}$ . Note that, since  $\psi$  is the solution of linear Laplace equation any superposition of solutions is still a solution of this equation. Regarding our static metric should represent the q-metric in the presence of the external field, so we shall choose a field in this form

$$\psi = \frac{(1 + \alpha)}{2} \ln \left( \frac{x-1}{x+1} \right) + \sum_{n=1} \beta_n R^n P_n\left(\frac{xy}{R}\right). \quad (7.9)$$

To obtain the field function  $\gamma$  corresponding to this potential  $\psi$  (7.9) explicitly, one needs to solve equations (7.6), where determines  $\gamma$  up to some constant. However, the requirement of elementary flatness in the neighborhood of the symmetry axis fixes the constant, and it should be set equal to zero. For the resulting function, we obtain this expression

$$\begin{aligned} \gamma = & \frac{(1 + \alpha)^2}{2} \ln \left( \frac{x^2 - 1}{x^2 - y^2} \right) + \sum_{n=1} \beta_n (1 + \alpha) \sum_{l=0}^{n-1} [(-1)^{n-l+1} (x + y) - x + y] R^l P_l \\ & + \sum_{k,n=1} \frac{nk\beta_n\beta_k}{(n+k)} R^{n+k} [P_n P_k - P_{n-1} P_{k-1}], \end{aligned} \quad (7.10)$$

---

<sup>1</sup>In general, these fields should be regular at the symmetry axis. Sometimes this condition is referred to as the elementary flatness condition.

where

$$P_n := P_n\left(\frac{xy}{R}\right), \quad R = \sqrt{x^2 + y^2 - 1}. \quad (7.11)$$

Where the first term in (7.10) is the  $\gamma$  function of the q-metric. For simplicity and emphasis on the external contributions by noting them as  $\hat{\psi}$  and  $\hat{\gamma}$ , we can show the equations (7.9) and (7.10) by

$$\begin{aligned} \psi &= \psi_q + \hat{\psi}, \\ \gamma &= \gamma_q + \hat{\gamma}, \end{aligned} \quad (7.12)$$

where  $\psi_q$  and  $\gamma_q$  are fields for q-metric; namely, one preserves the q-metric fields by taking  $\hat{\gamma} = \hat{\psi} = 0$ , equivalently no external field. It can easily be checked that in the limits  $\hat{\psi} = 0$ ,  $\hat{\gamma} = 0$ , and  $\alpha = 0$  we recover the Schwarzschild fields. Ultimately, the metric is then given by

$$\begin{aligned} ds^2 &= - \left( \frac{x-1}{x+1} \right)^{(1+\alpha)} e^{2\hat{\psi}} dt^2 + M^2(x^2-1) e^{-2\hat{\psi}} \\ &\quad \left( \frac{x+1}{x-1} \right)^{(1+\alpha)} \left[ \left( \frac{x^2-1}{x^2-y^2} \right)^{\alpha(2+\alpha)} e^{2\hat{\gamma}} \right. \\ &\quad \left. \left( \frac{dx^2}{x^2-1} + \frac{dy^2}{1-y^2} \right) + (1-y^2)d\phi^2 \right], \end{aligned} \quad (7.13)$$

where  $t \in (-\infty, +\infty)$ ,  $x \in (1, +\infty)$ ,  $y \in [-1, 1]$ , and  $\phi \in [0, 2\pi)$ . Again for  $\hat{\psi} = 0$ ,  $\hat{\gamma} = 0$  the q-metric (6.18) is recovered. If also  $\alpha = 0$ , the Schwarzschild metric is obtained. Of course, by replacing  $\alpha$  with parameter of ZV space-time via  $\delta := 1 + \alpha$ , one can consider this metric as the generalization of ZV space-time, as well. Up to the quadrupole  $\beta := \beta_2$ , the external field terms read as follows

$$\begin{aligned} \hat{\psi} &= -\frac{\beta}{2} [-3x^2y^2 + x^2 + y^2 - 1], \\ \hat{\gamma} &= -2x\beta(1+\alpha)(1-y^2) \\ &\quad + \frac{\beta^2}{4}(x^2-1)(1-y^2)(-9x^2y^2 + x^2 + y^2 - 1). \end{aligned} \quad (7.14)$$

Therefore, if we consider the external fields up to quadrupole, this metric contains three free parameters: the total mass, the deformation parameter

$\alpha$ , and the distortion  $\beta$ , which are taken to be relatively small and connected to the compact object's deformation and the external mass distribution, respectively. Moreover, further analysis shows that these parameters are not independent of each other, as we will see in the following parts. The result is locally valid by its construction and can be considered as the distorted q-metric. From the physics perspective, this solution is similar to the q-metric solution with an additional external gravitational field, like adding a magnetic surrounding [172].

## 7.2 Effective potential

To elucidate some aspects of the influence of the parameters, we consider the effective potential of geodesic motion in this space-time. Regarding the symmetries in the metric, there are two constants of geodesic motion

$$\begin{aligned} E = -g_{tt}\dot{t} &= \left(\frac{x-1}{x+1}\right)^{(1+\alpha)} e^{2\hat{\psi}} \dot{t}, \\ L = g_{\phi\phi}\dot{\phi} &= M^2(x^2-1)(1-y^2) \left(\frac{x+1}{x-1}\right)^{(1+\alpha)} e^{-2\hat{\psi}} \dot{\phi}, \end{aligned} \quad (7.15)$$

where "over-dot" notation is used for partial derivatives with respect to the proper time. By using these relations and the normalization condition  $g_{\rho\nu}\dot{x}^\rho\dot{x}^\nu = -\epsilon$ , where  $\epsilon$  can take values  $-1$ ,  $0$  and  $1$ , for the space-like, light-like and for the time-like trajectories, respectively; the geodesic equation is obtained as

$$\left(\frac{x^2-1}{x^2-y^2}\right)^{\alpha(2+\alpha)} M^2 e^{2\hat{\gamma}} \dot{x}^2 + V^2 = E^2, \quad (7.16)$$

where

$$\begin{aligned} V^2 &= \frac{x^2-1}{1-y^2} \left(\frac{x^2-1}{x^2-y^2}\right)^{\alpha(2+\alpha)} M^2 e^{2\hat{\gamma}} \dot{y}^2 \\ &+ \left(\frac{x-1}{x+1}\right)^{(2\alpha+1)} \frac{L^2 e^{4\hat{\psi}}}{M^2(1-y^2)(x+1)^2} \\ &+ \left(\frac{x-1}{x+1}\right)^{(\alpha+1)} e^{2\hat{\psi}} \epsilon. \end{aligned} \quad (7.17)$$

One can interpret (7.16) as the motion along the  $x$  coordinate in terms of  $V^2$  so-called potential. However, due to the appearance of  $\dot{y}$  in this expression, in fact, it is not a potential. In the next subsection, we rewrite  $V^2$  in the equatorial plane ( $\dot{y} = 0$ ). Then, it will have the meaning of related effective potential, and we rename it to  $V_{\text{eff}}$ , accordingly.

In what follows we study the circular geodesics in this set-up.

### 7.3 Circular geodesics

The geodesic equation in an arbitrary space-time is described by

$$\ddot{x}^\mu + \Gamma_{\nu\rho}^\mu \dot{x}^\nu \dot{x}^\rho = 0, \quad (7.18)$$

where derivatives are with respect to the affine parameter,  $\dot{x}^\mu$  is the four-velocity, and  $\Gamma_{\beta\gamma}^\alpha$  are the Christoffel symbols, which in this space-time read as follows

$$\begin{aligned} \Gamma_{tx}^t &= \frac{(1+\alpha)}{x^2-1} + \hat{\psi}_{,x}, \\ \Gamma_{ty}^t &= \hat{\psi}_{,y}, \\ \Gamma_{tt}^x &= \frac{e^{4\hat{\psi}-2\hat{\gamma}}}{M^2} \left( \frac{x-1}{x+1} \right)^{2\alpha+1} \left( \frac{x^2-y^2}{x^2-1} \right)^{\alpha(\alpha+2)} \left[ \frac{1+\alpha}{(x+1)^2} + \left( \frac{x-1}{x+1} \right) \hat{\psi}_{,x} \right], \\ \Gamma_{xx}^x &= -\frac{1+\alpha}{x^2-1} + \frac{\alpha(\alpha+2)(y^2-1)(1+2x)}{(x^2-1)(x^2-y^2)} + \hat{\gamma}_{,x} - \hat{\psi}_{,x}, \\ \Gamma_{xy}^x &= -\frac{y\alpha(\alpha+2)}{x^2-y^2} + \hat{\gamma}_{,y} - \hat{\psi}_{,y}, \\ \Gamma_{yy}^x &= \left( \frac{1-x}{1-y^2} \right) \left[ 1 - \frac{\alpha}{x-1} + (\hat{\gamma}_{,x} - \hat{\psi}_{,x})(x+1) \right] - \frac{x}{(x^2-y^2)} \alpha(\alpha+2), \\ \Gamma_{\phi\phi}^x &= e^{-2\hat{\gamma}}(1-y^2) \left( \frac{x^2-y^2}{x^2-1} \right)^{\alpha(\alpha+2)} \left[ 1 + \alpha - x + \hat{\psi}_{,x}(x^2-1) \right], \\ \Gamma_{tt}^y &= \frac{e^{4\hat{\psi}-2\hat{\gamma}}}{M^2} \left( \frac{1-y^2}{x^2-1} \right) \left( \frac{x^2-y^2}{x^2-1} \right)^{\alpha(\alpha+2)} \hat{\psi}_{,y}, \end{aligned}$$



$$\begin{aligned}
\Gamma_{xx}^y &= \frac{y^2 - 1}{x^2 - 1} \left[ \frac{y\alpha(\alpha + 2)}{x^2 - y^2} + \hat{\gamma}_{,y} - \hat{\psi}_{,y} \right], \\
\Gamma_{xy}^y &= \frac{x - 1 - \alpha}{x^2 - 1} + \left( \frac{1 - y^2}{x^2 - y^2} \right) x\alpha(2 + \alpha) + \hat{\gamma}_{,x} - \hat{\psi}_{,x}, \\
\Gamma_{yy}^y &= \frac{y}{1 - y^2} + \frac{y\alpha(\alpha + 2)}{x^2 - y^2} + \hat{\gamma}_{,y} - \hat{\psi}_{,y}, \\
\Gamma_{\phi\phi}^y &= \left( \frac{x^2 - y^2}{x^2 - 1} \right)^{\alpha(2+\alpha)} (1 - y^2) e^{-2\hat{\gamma}} \left[ y + \hat{\psi}_{,y}(1 - y^2) \right] \Gamma_{\phi x}^\phi = \frac{x - 1 - \alpha}{x^2 - 1} - \hat{\psi}_{,x}, \\
\Gamma_{\phi y}^\phi &= \frac{y}{y^2 - 1} - \hat{\psi}_{,y}.
\end{aligned}$$

### 7.3.1 The equatorial plane in Generalized q-metric

In this part, we consider the metric functions up to quadrupole to analyse the circular motion and the place of ISCO in the equatorial plane. In the equatorial plane  $y = 0$ , the distortion functions (6.16) up to the quadrupole simplify to

$$\begin{aligned}
\hat{\psi} &= -\frac{\beta}{2}(x^2 - 1), \\
\hat{\gamma} &= -2\beta(1 + \alpha)x + \frac{\beta^2}{4}(x^2 - 1)^2.
\end{aligned} \tag{7.20}$$

The metric in the equatorial plane is given by

$$\begin{aligned}
ds^2 &= - \left( \frac{x - 1}{x + 1} \right)^{(1+\alpha)} e^{2\hat{\psi}} dt^2 + M^2(x^2 - 1) e^{-2\hat{\psi}} \\
&\quad \left( \frac{x + 1}{x - 1} \right)^{(1+\alpha)} \left[ \left( \frac{x^2 - 1}{x^2} \right)^{\alpha(2+\alpha)} e^{2\hat{\gamma}} \right. \\
&\quad \left. \left( \frac{dx^2}{x^2 - 1} + dy^2 \right) + d\phi^2 \right].
\end{aligned} \tag{7.21}$$

Further, the relation (7.16) is reduced to

$$\left( \frac{x^2 - 1}{x^2} \right)^{\alpha(2+\alpha)} M^2 e^{2\hat{\gamma}} \dot{x}^2 + V_{\text{eff}} = E^2, \tag{7.22}$$

where

$$V_{\text{eff}} = \left( \frac{x-1}{x+1} \right)^{(\alpha+1)} e^{2\hat{\psi}} \left[ \epsilon + \frac{L^2 e^{2\hat{\psi}}}{M^2 (x+1)^2} \left( \frac{x-1}{x+1} \right)^\alpha \right]. \quad (7.23)$$

As mentioned earlier, in the equatorial plane, we point out  $V^2$  by  $V_{\text{eff}}$  to emphasise that the contrary to the general form in (7.17), on the equatorial plane it has the meaning of potential. In addition, the effective potential  $V_{\text{eff}}$  for  $\beta = 0$ , reduce to the effective potential for q-metric, and  $\alpha = 0$  corresponds to the effective potential for distorted Schwarzschild metric, and in the case of  $\alpha = \beta = 0$  the one for Schwarzschild space-time.

By analyzing the effective potential one can investigate the general properties of the particle dynamics, in particular, in the equatorial plane. In fact, this motion is determined by the energy's boundaries given by  $E^2 = V_{\text{eff}}$ . In general, depending on the parameters  $\epsilon$ ,  $E$ ,  $L$ ,  $\alpha$  and  $\beta$ , one obtains different trajectories. The analytical exploration depends on the number of positive real zeros and the sign of  $E^2 - \epsilon$ . In fact, for each valid pair of parameters, one can distinguish different trajectories in this background. In general in this background, depending on initial values and parameters, particles can fall onto the central object, escape from it, or trap in some region and form a toroidal shape around the central object. As in this work, we analyze also the accretion discs and oscillations in Sections 10, 13 and 12 in this background where related to the bounded geodesics, the analysis of the effective potential allows us to examine the regions where these orbits are possible to study the disc configuration. We can interpret this as indicating the existence of accretion discs around the gravitational source. Figure 7.1 shows specifically when particles trapped via the existence of both initial conditions on inner and outer boundaries. As one can see in the plots, only by a slight change in the initial values one can obtain different trajectories for a chosen pair of parameters. In addition, the bounded orbits in the presence of magnetic field are presented in the following part 7.4.

### The timelike trajectories

In the circular motion, there is no change in the  $x$  direction  $\dot{x} = 0$ , so one can study the motion of test particles in the effective potential (7.23) equivalently.

In Figure 7.2,  $V_{\text{eff}}$  is plotted for different values of  $\alpha$  and  $\beta$ . As we see, the Schwarzschild effective potential lies in between the one with a negative

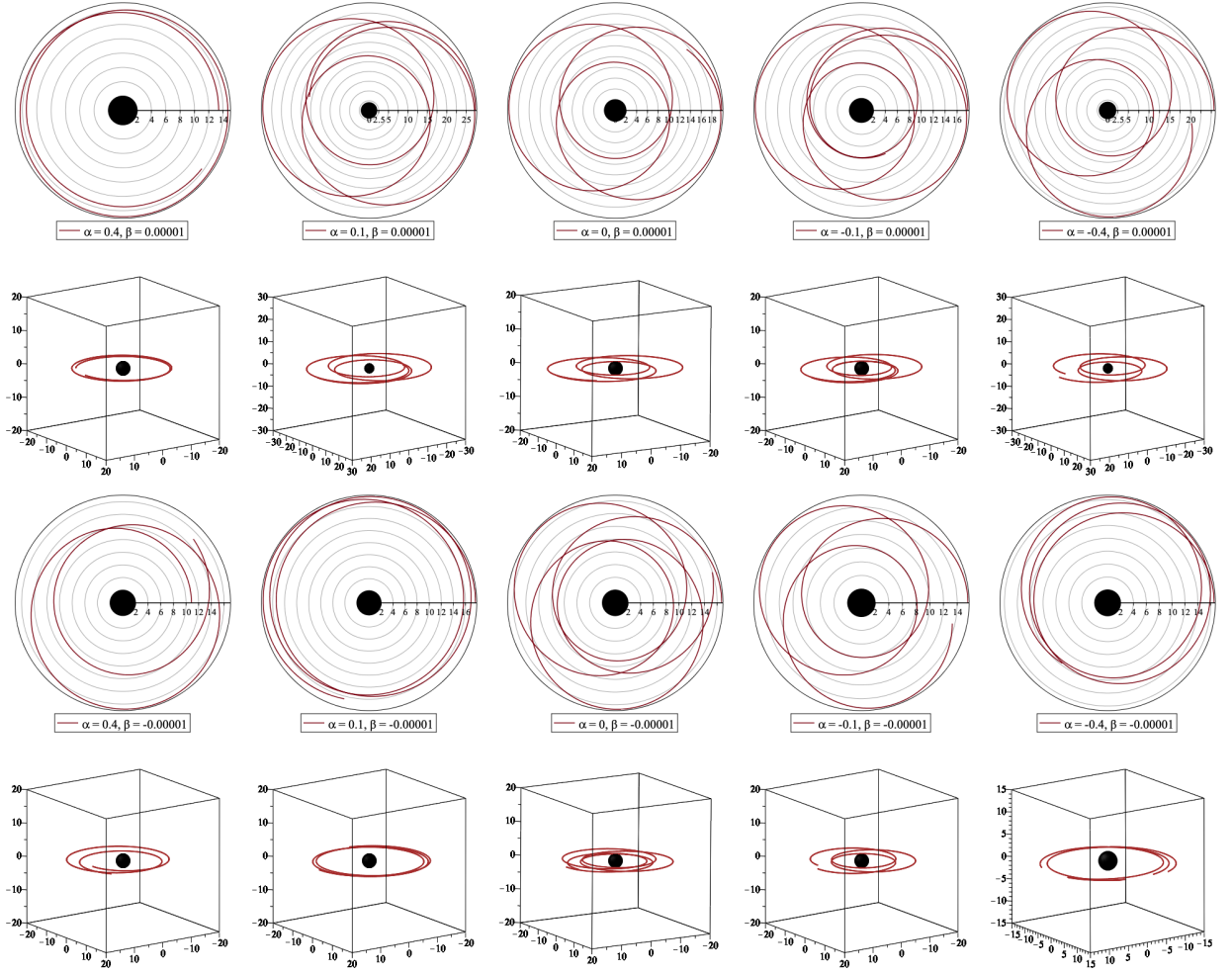


**Figure 7.1:** Timelike geodesic for different pairs of  $(\alpha, \beta)$ . The trajectories in the  $(r, \phi)$  section and in the complete 3D are plotted. In the first column, both configurations  $\mathcal{E} = 0.90$  and  $\mathcal{L} = 25$ . In the second column, both configurations have  $\mathcal{E} = 0.94$  and  $\mathcal{L} = 22$ . In the central column, both configurations have  $\mathcal{E} = 0.93$  and  $\mathcal{L} = 12$ . In the fourth column, both configurations have  $\mathcal{E} = 0.93$  and  $\mathcal{L} = 15$ . In the last one, both configurations have  $\mathcal{E} = 0.96$  and  $\mathcal{L} = 9$ .

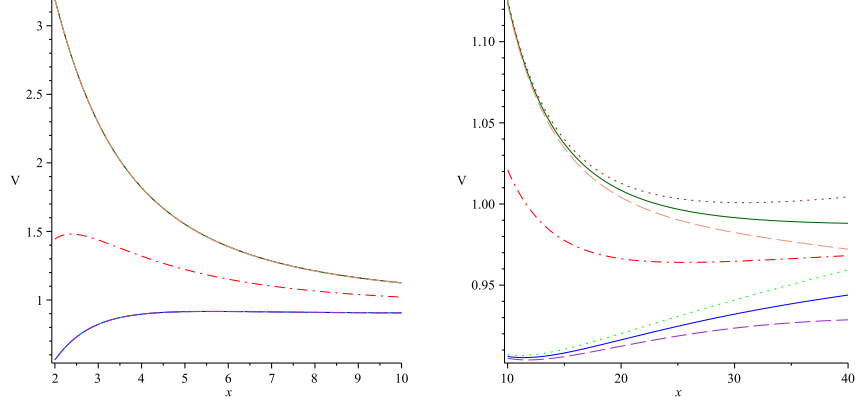


**Figure 7.2:** Plots of  $V_{\text{eff}}$  for different values of  $\alpha$  and  $\beta$ . In both plots, the dot-dashed line in the middle is Schwarzschild ( $\alpha = \beta = 0$ ), the solid line under the Schwarzschild corresponds to values ( $\alpha = 0.5, \beta = 0$ ), and the solid line above the Schwarzschild corresponds to ( $\alpha = -0.4, \beta = 0$ ). The dotted line under the Schwarzschild is for the values ( $\alpha = 0.5, \beta = -0.00001$ ), and the dotted line above the Schwarzschild is plotted for ( $\alpha = -0.4, \beta = -0.00001$ ). The dashed line under the Schwarzschild is for values ( $\alpha = 0.5, \beta = 0.00001$ ), and the dashed line above the Schwarzschild is plotted for ( $\alpha = -0.4, \beta = 0.00001$ ).

value of  $\alpha$  and the positive value of  $\alpha$ . Also, for each fixed value of  $\alpha$ , the effective potential for a negative  $\beta$  is higher than the effective potential for the same  $\alpha$  but vanishing  $\beta$ . The opposite is also true for positive  $\beta$  at each  $x$ . As Figure 7.2 shows, further away from the central object, they are more diverged.

Typically, the place of ISCO, the last innermost stable orbit, is the place of the extrema of  $V_{\text{eff}}$  and  $(V_{\text{eff}})'$  simultaneously. However, finding extrema of  $V_{\text{eff}}$ , equivalents to analysis the extrema of  $L^2$  for massive particle, and it is given by

$$L^2 = \frac{M^2(x+1)^{\alpha+2} [-\beta x^3 + \beta x + \alpha + 1]}{(x-1)^\alpha [2\beta x^3 + (1-2\beta)x - 2\alpha - 2]} e^{-2\psi}. \quad (7.24)$$

The vertical asymptote of this function for  $x > 1$  is

$$2\beta x^3 + (1-2\beta)x - 2\alpha - 2 = 0, \quad (7.25)$$

which leads to this relation for  $\beta$

$$l_1 := \frac{-x + 2(\alpha + 1)}{2x(x^2 - 1)}. \quad (7.26)$$

In the space-time with the quadrupole (in general with multipole moments), there is an interesting possibility that there exists a curve in which  $L^2$  may vanish along with it. This means that particles are at rest along this curve with respect to the central object. Of course, this is not the case in Schwarzschild or in the q-metric space-times. In this way, the external matter manifests its existence by neutralizing the central object's gravitational effect at the region determined by this curve. In this case, this happens along  $-\beta x^3 + \beta x + \alpha + 1 = 0$ , which can be written also as

$$l_2 := \frac{\alpha + 1}{x(x^2 - 1)}. \quad (7.27)$$

However, it is worth mentioning that, there is just one position for each chosen value of  $\beta$ . In general, the region between curves  $l_1$  (7.26) and  $l_2$  (7.27) defines the valid range for the distortion parameter  $\beta$ , due to the fact that  $L^2$  is a positive function. A straightforward calculation of  $\frac{d}{dx}L^2 = 0$  leads to

$$\begin{aligned} & 4x^3(x^2 - 1)^3\beta^3 \\ & + 6x^2(-2(x^2 - 1)^2\alpha + x^5 - 2x^4 - 2x^3 + 4x^2 + x - 2)\beta^2 \\ & + 4x(x^2 - 1)(3\alpha^2 + 3(2 - x)\alpha + x^2 - 3x + 3)\beta \\ & - (\alpha + 1)x^2 + 6(\alpha + 1)^2x - 4\alpha^3 - 12\alpha^2 - 13\alpha - 5 \\ & = 0. \end{aligned} \quad (7.28)$$

Which gives the solution for  $\beta$  as

$$\beta = \frac{1}{2x(x^2 - 1)} \left( \frac{\sqrt[3]{D^2} - 3x^2}{3\sqrt[3]{D}} + 2 - x + 2\alpha \right), \quad (7.29)$$

where

$$D = 27x^3 - 81x^2(\alpha + 1) + 27(\alpha + 1) + 3\sqrt{\Delta}, \quad (7.30)$$

and

$$\begin{aligned} \Delta &= 84x^6 - 486x^5(\alpha + 1) + 729x^4(\alpha + 1)^2 \\ &+ 162x^3(\alpha + 1) - 486x^2(\alpha + 1)^2 + 81(\alpha + 1)^2. \end{aligned} \quad (7.31)$$

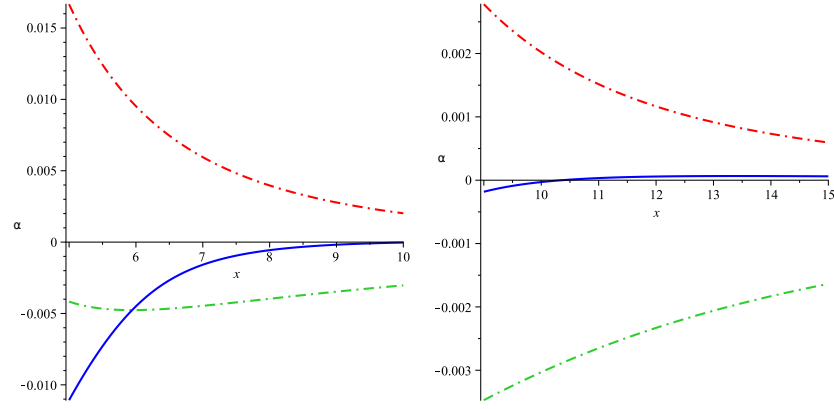


**Figure 7.3:** The dashed lines are  $l_1$  (7.26) and  $l_2$  (7.27). The solid lines are the plots of  $\beta$  (7.29) for  $\alpha = 1$ , noted as  $\beta^{\alpha=1}$ . Minimum of  $\beta^{\alpha=1}$  is  $-0.0047632$  at  $x = 5.94338$ , and maximum of  $\beta^{\alpha=1}$  is  $0.0000659$  at  $x = 13.38972$ . Moreover,  $\beta = 0$  at  $x = 10.35890$ , so this is the place of ISCO for  $\alpha = 1$  with vanishing  $\beta$  in the q-metric.

An analysis shows that for any value of  $\alpha$  chosen in this domain  $[-0.5, \infty)$ , the minimum of  $\beta$  is obtained at the intersection of the curve  $\beta$  (7.29) with  $l_1$  (7.26). Besides, the maximum of the curve  $\beta$  in the valid region is determined by the maximum of  $\beta$  for this chosen  $\alpha$ . For instance, in Figure 7.3, 7.4 and 7.5,  $\beta$  and the valid region for one positive and two negative values  $\alpha = 1$ ,  $\alpha = -0.4$ , and  $\alpha = -0.5$  are plotted. In the later, the minimum of  $\beta$  is obtained by its intersection with  $l_1$  (7.26), placed at the very close to outer singularity.

For the values of  $\alpha$  in this domain  $[-1 + \frac{\sqrt{5}}{5}, -0.5)$ , where  $-1 + \frac{\sqrt{5}}{5} \sim -0.553$ , the curve  $\beta$  behaves differently, and it always lies in the valid region, so the minimum and maximum of  $\beta$  are determined by its extrema. In Figure 7.6, the minimum for  $\alpha = -0.526$  was shown, where its minimum is obtained by the minimum of a curve  $\beta$  itself.

It turns out that the maximum value of  $\beta$  is a monotonically decreasing function of  $\alpha$ . However, the place of ISCO for a maximum of  $\beta$  is a monotonically increasing function of  $\alpha$  (see Figure 7.7). In addition, the minimum of  $\beta$  is a decreasing function of  $\alpha$  from  $\alpha \sim -0.5528$  to  $\alpha = -0.5$ , and from this value, it monotonically increases.

To summarize, the minimum of  $\beta$  is obtained in the case  $\alpha = -0.5$ , and the maximum of  $\beta$  is reached for  $\alpha \sim -0.5528$ . In Table 7.1, the values of minimum and maximum of  $\beta$  for various chosen values of  $\alpha$  are presented<sup>2</sup>. Besides, the places of ISCO in the cases of maximum, minimum, and

<sup>2</sup>Note that in the third row it is calculated for some  $\alpha$  very close to  $-0.5$ .

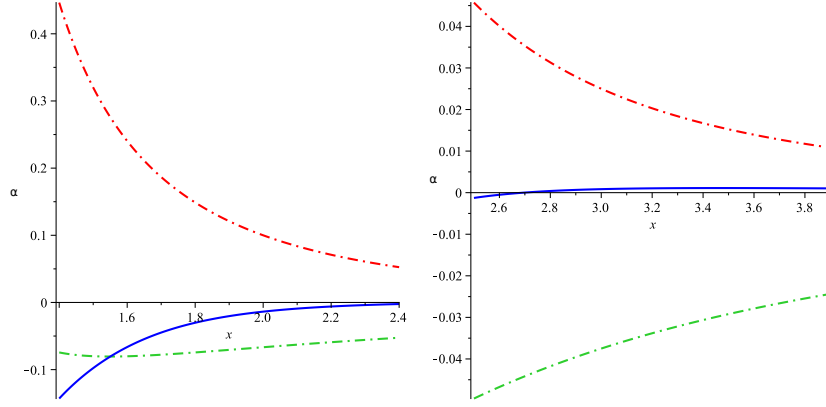


**Figure 7.4:** The dot-dashed lines depict  $l_1$  (7.26) and  $l_2$  (7.27). The solid lines present plots of  $\beta$  (7.29) for  $\alpha = -0.4$ , noted as  $\beta^{\alpha=-0.4}$ . Minimum of  $\beta^{\alpha=-0.4}$  is  $-0.0805014$  at  $x = 1.55038$ , and maximum of  $\beta^{\alpha=-0.4}$  is  $0.0011090$  at  $x = 3.47165$ . Also,  $\beta = 0$  at  $x = 2.69443$ , so this  $x$  shows the value of ISCO for  $\alpha = -0.4$  with  $\beta = 0$  in the q-metric.

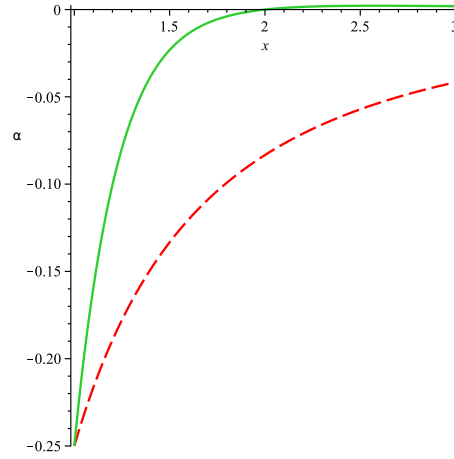


**Figure 7.5:** Around  $\alpha = -0.5$  curve  $\beta$  begins to intersect with curve 1 (7.26). Before this value, the minimum is determined by the minimum of  $\beta$  itself, and after that, the minimum of  $\beta$  is obtained by the intersection of these two curves.

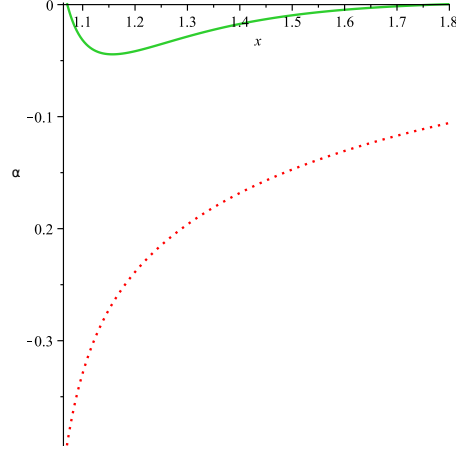


**Figure 7.6:** The dotted line is  $l_1$  (7.26), and solid line is  $\beta$  (7.29) for  $\alpha = -0.526$ . In this interval  $[-0.5528, -0.5)$  the minimum is determined by the minimum of the curve  $\beta$  (7.29) itself.

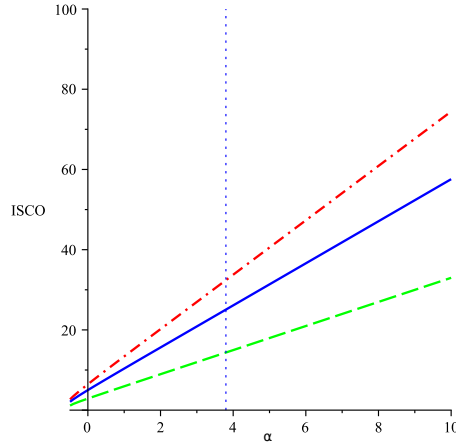


**Figure 7.7:** The vertical axis presents the  $x$  value at the ISCO. For any chosen value for parameter  $\alpha$ , the solid line is ISCO for  $\beta = 0$ , the dot-dashed line is ISCO for  $\beta_{\max}$ , and the dashed line is ISCO for  $\beta_{\min}$ . In all cases, ISCO is a monotonically increasing function of  $\alpha$ . Besides, one can see that the place of ISCO is also a monotonic increasing function of  $\beta$ . For example, if we look at the plot for any fixed value of  $\alpha$ , like the vertical dotted line, the intersections of this line with all lines show the place of ISCO for a fixed  $\alpha$ , but different values of  $\beta$ . Therefore, one can see the place of ISCO for the negative value of  $\beta$  (green line), is less than  $\beta = 0$  (the blue one), and it is also less than a positive value (red line). Thus, the ISCO is also a monotonically increasing function of  $\beta$ .



vanishing external quadrupole distortion parameter  $\beta$  are shown. We have seen for  $\alpha = \beta = 0$ , the place of ISCO for Schwarzschild is recovered at  $x = 5$ . We should mention that  $\beta$  is a parameter chosen for the entire space-time; however, when  $\beta$  is outside of the bounds, there will be no circular orbits at the given  $x$  (similar to  $r < 3M$  in Schwarzschild space-time).

### The light-like trajectory

In this case,  $\epsilon = 0$ , and the effective potential (7.23) for light-like geodesics is reduced to

$$V_{\text{eff}} = \left( \frac{x-1}{x+1} \right)^{(\alpha+1)} e^{2\hat{\psi}} \left[ \frac{L^2 e^{2\hat{\psi}}}{M^2 (x+1)^2} \left( \frac{x-1}{x+1} \right)^\alpha \right]. \quad (7.32)$$

In fact, a straightforward analysis of the effective potential shows that its first derivative vanishes for

$$\alpha = \frac{1}{2}(2\beta x^3 - 2\beta x + x - 2), \quad (7.33)$$

where for  $\alpha = \beta = 0$ , it reduces to the Schwarzschild value  $x = 2$  equivalently to  $r = 3M$  in the standard Schwarzschild coordinates (6.10). Furthermore, the relation (7.33) is the limiting curve for time-like circular geodesics, curve  $l_1$  (7.26), which is written in terms of  $\alpha$ . By inserting the relation (7.33) for  $\alpha$ , into the second derivative of the effective potential  $(V_{\text{eff}})''$ , we obtain a very interesting result. The second derivative vanishes along

$$\beta = -\frac{1}{2(3x^2 - 1)}. \quad (7.34)$$

This expression is also the minimum of the curve (7.33). Surprisingly, this means that for some negative values of  $\beta$ , we have a bound photon orbit in the equatorial plane in this space-time, which is neither the case in Schwarzschild space-time, nor in q-metric. In fact, this arises due to the existence of quadrupoles related to the external source. From this relation (7.34) one can find the negative values of quadrupole which lead to having ISCO for light-like geodesics

$$\beta \in \left(-\frac{1}{4}, 0\right). \quad (7.35)$$

There is no surprise that the minimum value of  $\beta$  in the case of light-like trajectories coincides with the minimum value of  $\beta$  in the case of time-like trajectories, which occurs for the choice of  $\alpha = -0.5$ , see Table 7.1.

### 7.3.2 Revisit the equatorial plane in q-metric

In this part, following the discussion above to have a comparison, we briefly revisit circular motion on the equatorial plane in the q-metric with this slightly different approach from the studies in the literature for example [157].

#### Time-like geodesics in q-metric

In this case, the specific angular momentum (7.24) is reduced to

$$L^2 = \frac{M^2(x+1)^{\alpha+2}(1+\alpha)}{(x-1)^\alpha [x-2(1+\alpha)]}. \quad (7.36)$$

An analysis of  $\frac{d}{dx}L^2$ , like the previous case, shows the vertical asymptote to this function for  $x > 1$  is

$$k_1 := \frac{x}{2} - 1. \quad (7.37)$$

Also,  $L^2$  vanishes along this curve

$$k_2 := -1. \quad (7.38)$$

This value is the infimum value for  $\alpha$ , since regarding the domain of  $\alpha = (-1, \infty)$ , for  $\alpha = -1$  the space-time will be flat as mentioned before. The region between curves  $k_1$  (7.37) and  $k_2$  (7.38), defines the valid range for  $\alpha$ , considering  $L^2$  is a positive function. A direct calculation for the extrema of  $L^2$ , leads to

$$\alpha \pm = \frac{3}{4}x - 1 \pm \frac{1}{4}\sqrt{5x^2 - 4}. \quad (7.39)$$

Since for the domain of our interest  $x > 1$ , this relation  $5x^2 - 4 > 0$  satisfies, therefore we always have two curves  $\alpha_-$  and  $\alpha_+$ . In fact,  $\alpha_+$  lies out of the valid region between  $k_1$  and  $k_2$ , for all  $x > 1$ . However,  $\alpha_-$  intersect with  $k_1$  and enter to the region at  $x = 1$ , where  $\alpha_-(1) = -\frac{1}{2}$ , and always remain inside this region (see Figure 7.8).

One can show that  $\alpha_-$  has a minimum inside this region at  $x = 3\frac{\sqrt{5}}{5} \approx 1.342$ , where  $\alpha_-^{\min} = -1 + \frac{\sqrt{5}}{5} \approx -0.5528$ , and after this point,  $\alpha_-$  is a

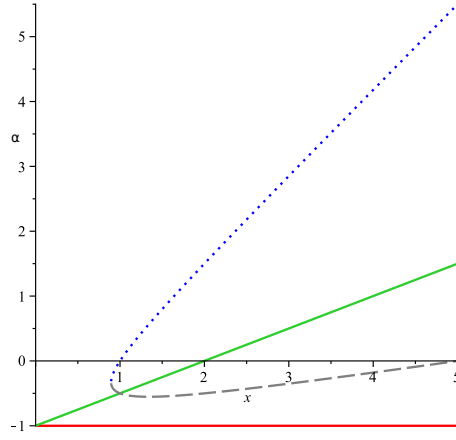


**Figure 7.8:** Solid lines  $\alpha_2$  and  $\alpha_1$  show the valid region, where dashed line  $\alpha_-$  always lies in this region and dotted line  $\alpha_+$  is out of this region for any choice of  $\alpha$ .

monotonically increasing function. So in this case, the domain of  $\alpha$  is  $[-1 + \frac{\sqrt{5}}{5}, \infty)$ .

For obtaining ISCOs, we rewrite equation  $L_{,x}^2 = 0$  in terms of  $x$ ,

$$x_{\pm} = 3 + 3\alpha \pm \sqrt{\Delta}, \quad \Delta = 5\alpha^2 + 10\alpha + 4. \quad (7.40)$$

By using the above analysis for  $\alpha_{\pm}$ , from (7.37) and (7.38) we obtain

$$x_1 = 2\alpha + 1, \quad (7.41)$$

$$x_2 = 0. \quad (7.42)$$

If we plot them with  $x_+$  and  $x_-$  (7.40) together, we see that the corresponding valid ISCOs are obtained by  $x_+(=x_{\text{ISCO}})$  (see Figure 7.9). Furthermore, this relation (7.40) shows that  $\Delta \geq 0$  is equivalent to  $\alpha \in [-\infty, -1 - \frac{\sqrt{5}}{5}] \cup [-1 + \frac{\sqrt{5}}{5}, +\infty)$ , where only the second part, meaning  $[-1 + \frac{\sqrt{5}}{5}, \infty)$ , lies in the valid region. Consequently, this gives us no new information on the domain of  $\alpha$  more than what we have obtained before.

Again, we can see how ISCOs positions evolve as  $\alpha$  increases by plotting  $x_+(=x_{\text{ISCO}})$ . the place of ISCO in Schwarzschild is at  $x = 5$  (equivalent to  $r = 6M$ ). For a negative  $\alpha$ , ISCO is closer to the horizon  $x = 1$ , and for a positive  $\alpha$  the place of ISCO is going farther, see Figure 7.10.

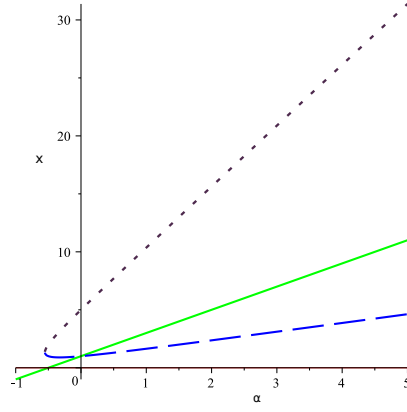


**Figure 7.9:** The green line  $x_1 = 2\alpha + 1$  and  $x_2 = 0$ , show the valid region, where the dashed line is the place of ISCO  $x_+$ , and dots line  $x_-$  is outside, for any choice of  $\alpha$ .

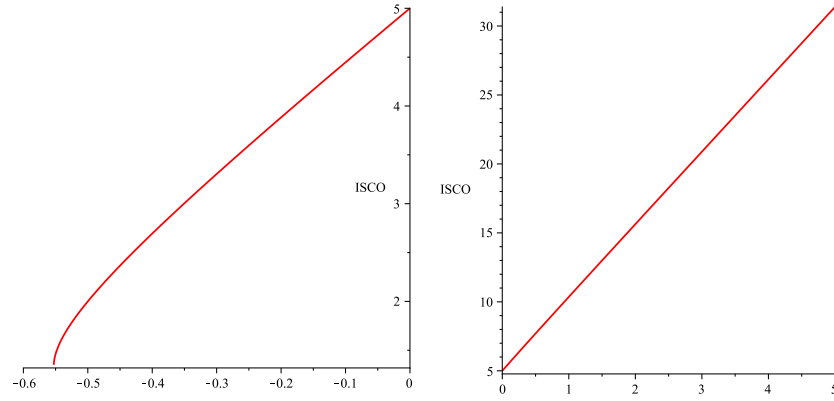


**Figure 7.10:** The vertical axis presents the  $x$  value at the ISCO. The plots show the evolution of ISCO with  $\alpha$ , where the domain of  $\alpha$  is  $[-0.5528, +\infty)$ . The value of ISCO at  $\alpha = -0.5528$  is 1.3416. The place of ISCO for  $\alpha < 0$  is below the Schwarzschild value  $x = 5$  and for  $\alpha > 0$  is upper.

Table 7.1: The minimum and the maximum of  $\beta$  and the place of ISCO for different values of  $\alpha$ . The letter  $\alpha$  appearing as the upper index in  $\beta$  and  $x$  means that these quantities are calculated at a fixed value of  $\alpha$  in the left column.

$\alpha$	$\beta_{\min}^{\alpha}$	$x_{\beta-\min}^{\alpha}$	$\beta_{\max}^{\alpha}$	$x_{\beta-\max}^{\alpha}$	$x_{\beta=0}^{\alpha}$
-0.5528	-0.0006262	1.333070	0.0040976	1.93984	1.40333
-0.526	-0.0443754	1.15685	0.0028270	2.30093	1.77325
-0.5	-0.2499996	1.000001	0.00217281	2.58141	2.00000
-0.49	-0.1757730	1.13203	0.0019932	2.68029	2.07818
-0.4	-0.0805014	1.55038	0.0011090	3.47165	2.69443
0	-0.0209443	2.87940	0.0002927	6.45602	5.00000
0.5	-0.0086651	4.42340	0.0001202	9.95281	7.70156
1	-0.0047632	5.94338	0.0000659	13.38972	10.35890
10	-0.0001533	32.98501	0.0000021	74.44744	57.57641

### Light-like geodesics in q-metric

In this case, the effective potential (7.32) is reduced to

$$V_{\text{eff}} = \left( \frac{x-1}{x+1} \right)^{(\alpha+1)} \left[ \frac{L^2}{M^2(x+1)^2} \left( \frac{x-1}{x+1} \right)^{\alpha} \right], \quad (7.43)$$

and the straightforward calculation shows that its first derivative vanishes along

$$x = 2 + 2\alpha. \quad (7.44)$$

So for any chosen value of  $\alpha$ , one obtains a value for  $x$ . Of course, in the case of  $\alpha = 0$ , Schwarzschild metric, we obtain  $x = 2$  or equivalently  $r = 3M$  with the transformation law (6.10). Moreover, the sign of the second derivative of the effective potential for this value of  $x$ , and any chosen value for  $\alpha$ , unlike the previous case indicates this circular motion is unstable.

## 7.4 Dynamics of charged particle in a uniform magnetic field

In this part, we study the dynamics of charged particles in this background in the presence of an asymptotic uniform magnetic field in this background that we use this result in the study of QPOs in Chapter 12. In this set-up, it is assumed that the external weak magnetic field has no influence on the underlying space-time. Explicitly, we are interested in the dynamics that occur when a static, axisymmetric central compact object is embedded in an asymptotic uniform magnetic field of strength  $B$  aligned with the central body's symmetry axis, and nonsingular throughout the exterior region [185]. In general, by comparing the compact object's size with the typical length of varying the strength's electric and magnetic fields, we can define a test particle. In fact, by using the fundamental variability plane, the magnitude of the magnetic field in the vicinity of a black hole is estimated as

$$B \sim \begin{cases} 10^8 G & , \quad M \sim M_\odot, \\ 10^4 G & , \quad M \sim 10^9 M_\odot. \end{cases} \quad (7.45)$$

Furthermore, the motion of neutral test particles that is not influenced by magnetic fields satisfying

$$B_G \sim 10^{19} G \left( \frac{M_\odot}{M} \right). \quad (7.46)$$

However, the charged test particles' motion could be strongly influenced even by relatively weak test magnetic fields [81]. This is also satisfied in the vicinity of magnetars. This condition comes from comparing the central body's gravitational effect and the strength of the magnetic field  $B$  on its vicinity, and for most astrophysical black holes is perfectly satisfied [186]. In addition, the relative strength of the Lorentz and gravitational forces acting on a charged particle can be characterized by the order of

$$b \sim 4.7 \times 10^7 \left( \frac{q}{e} \right) \left( \frac{m_p}{m} \right) \left( \frac{B}{10^8} \right) \left( \frac{M}{10 M_\odot} \right), \quad (7.47)$$

where  $m_p$  is the mass of a proton and  $q$  is the charge of the particle. The ratios in this quantity suggest that this characterization is relevant and cannot be neglected for the astrophysical scales. The standard electric-magnetic tensor is given by

$$F_{\mu\eta} = \partial_\mu A_\eta - \partial_\eta A_\mu. \quad (7.48)$$

As mentioned, following [185] the external asymptotically homogeneous magnetic field is chosen to be along the polar axis. The  $\phi$ -component of the vector potential in this metric is described by

$$A_\phi = \frac{1}{2}B(x^2 - 1)e^{-2\hat{\psi}} \left( \frac{x+1}{x-1} \right)^{(1+\alpha)}. \quad (7.49)$$

The Lorentz equation that describes the charged test particle motion is given by

$$m \frac{du^\mu}{ds} = q F^\mu{}_\nu u^\nu, \quad (7.50)$$

where  $u^\mu = \frac{d}{ds}$  is the four-velocity of the particle with the mass  $m$  and charge  $q$ .

### Hamiltonian formalism

Now we use the general Hamiltonian formalism to describe the effective potential and dynamics of a charged particle in the vicinity of a distorted, deformed compact object embedded in the external uniform magnetic field. The Hamiltonian for the charged particle motion is written as

$$H = \frac{1}{2} [(\pi^\mu - qA^\mu)(\pi_\mu - qA_\mu) + m^2], \quad (7.51)$$

where  $\pi^\mu$  is the generalized canonical four-momentum

$$\pi^\mu = p^\mu + qA^\mu. \quad (7.52)$$

Considering the metric is static and axisymmetric immersed in an external asymptotically homogeneous magnetic field, the conserved quantity specific angular momentum  $L$  of the particle (7.15) is modified as follows

$$L = \pi_\phi = M^2(x^2 - 1)(1 - y^2)e^{-2\hat{\psi}} \left( \frac{x+1}{x-1} \right)^{(1+\alpha)} \left( \frac{d\phi}{ds} + Q \right), \quad (7.53)$$

where  $Q := \frac{qB}{2m}$  is magnetic parameter. In addition, the generalized effective potential, in this case, is obtained as

$$V^2 = \left(\frac{x-1}{x+1}\right)^{(\alpha+1)} e^{2\hat{\psi}} [\epsilon + e^{-2\hat{\psi}} \left(\frac{x+1}{x-1}\right)^\alpha (1-y^2) \left(\frac{Le^{2\hat{\psi}}}{(x+1)(1-y^2)} \left(\frac{x-1}{x+1}\right)^\alpha - Q(x+1)\right)^2] \quad (7.54)$$

The second term corresponds to the central force potential related to  $L$ , and electromagnetic potential energy related to  $B$ . In Figure 7.11, the effective potential in the equatorial plane  $V^2 := V_{\text{eff}}$  presented for different values of parameters  $\alpha$  and  $\beta$ . In general, we can discuss four different situations in terms of signs of  $L$  and  $Q$ . However, because of the even power in the second term, it is sufficient to consider only two situations:

1.  $LQ > 0$ , the Lorentz force pushes the particle away in the outward direction with respect to the central object.
2.  $LQ < 0$ , the Lorentz force pushes the particle in the direction of the z-axis towards the central object.

Again we study the bounded orbits in this set-up while considering the external magnetic field. There is no surprise that test particles' motion can be chaotic in this metric for some combinations of parameters  $Q$ ,  $\alpha$  and  $\beta$ . In particular, as we see in Figures 7.12-7.14, apart from the effect of other parameters, the value for  $\alpha$  makes a profound difference in the trajectories. Further analysis reveals that aside from the magnitude, the influence of the signs of magnetic parameter  $Q$  along with the sign of  $\alpha$  together, have a significant impact on the results.

## 7.5 Summary and conclusion

This chapter has presented a Generalized q-metric for the relatively small quadrupole moment via Weyl's procedure. This metric explains the exterior of a deformed body locally in the presence of an external distribution of matter up to the quadrupole. It contains three free parameters: the total mass, deformation parameter  $\alpha$ , and the distortion parameter  $\beta$ , referring to the central object's quadrupoles and its surrounding mass distribution, where in the case of the circular motion these two quadrupole parameters are not independent.

In fact, due to its mathematics form, it is possible to study this metric via the analytical and semi-analytical models of astrophysical relevance, like



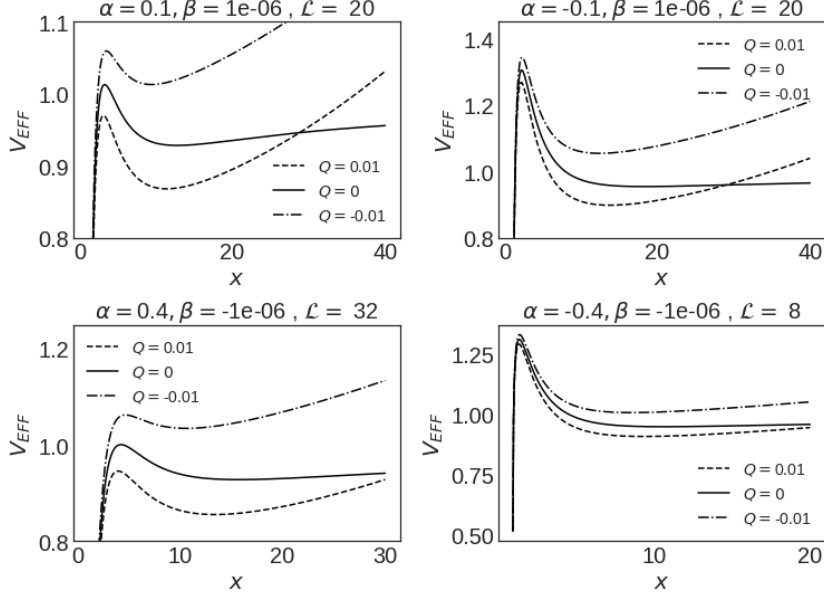


**Figure 7.11:** Effective potential for various combinations of the model's parameters; the distortion  $\beta$ , the deformation  $\alpha$  and the magnetic parameter  $Q$ .

the stability analysis of geodesic motion 15, accretion disc models 10, quasi-periodic oscillations 12 and 13 that we investigate through this thesis.

Furthermore, we carried out a characterization of quadrupole parameters' impact via studying the circular geodesics on the equatorial plane with and without a magnetic field, as well as the region of the parameters for which circular orbits can exist. Some of the examples are listed in Table 7.1. In consequence, we found out for each choice of  $\alpha$  there are ISCOs for time-like geodesics for  $\beta \in [\beta_{\min}^{\alpha}, \beta_{\max}^{\alpha}]$  such that in general  $\beta_{\min} \approx -2.5 \times 10^{-1}$  at  $\alpha = -0.5$  and  $\beta_{\max} \approx 4.1 \times 10^{-3}$  at  $\alpha = -0.5528$ . Besides, the place of ISCO is closer to the horizon for negative quadrupole moments contrary to positive quadrupole moments.

An interesting result is that there is a bound orbit for light-like geodesics on the equatorial plane, which is not the case neither in Schwarzschild nor in q-metric. This bound orbit's existence when we have a negative quadrupole in the external matter and provides the range for  $\beta \in (-0.25, 0)$  in this case. The result of this chapter is presented in [187].

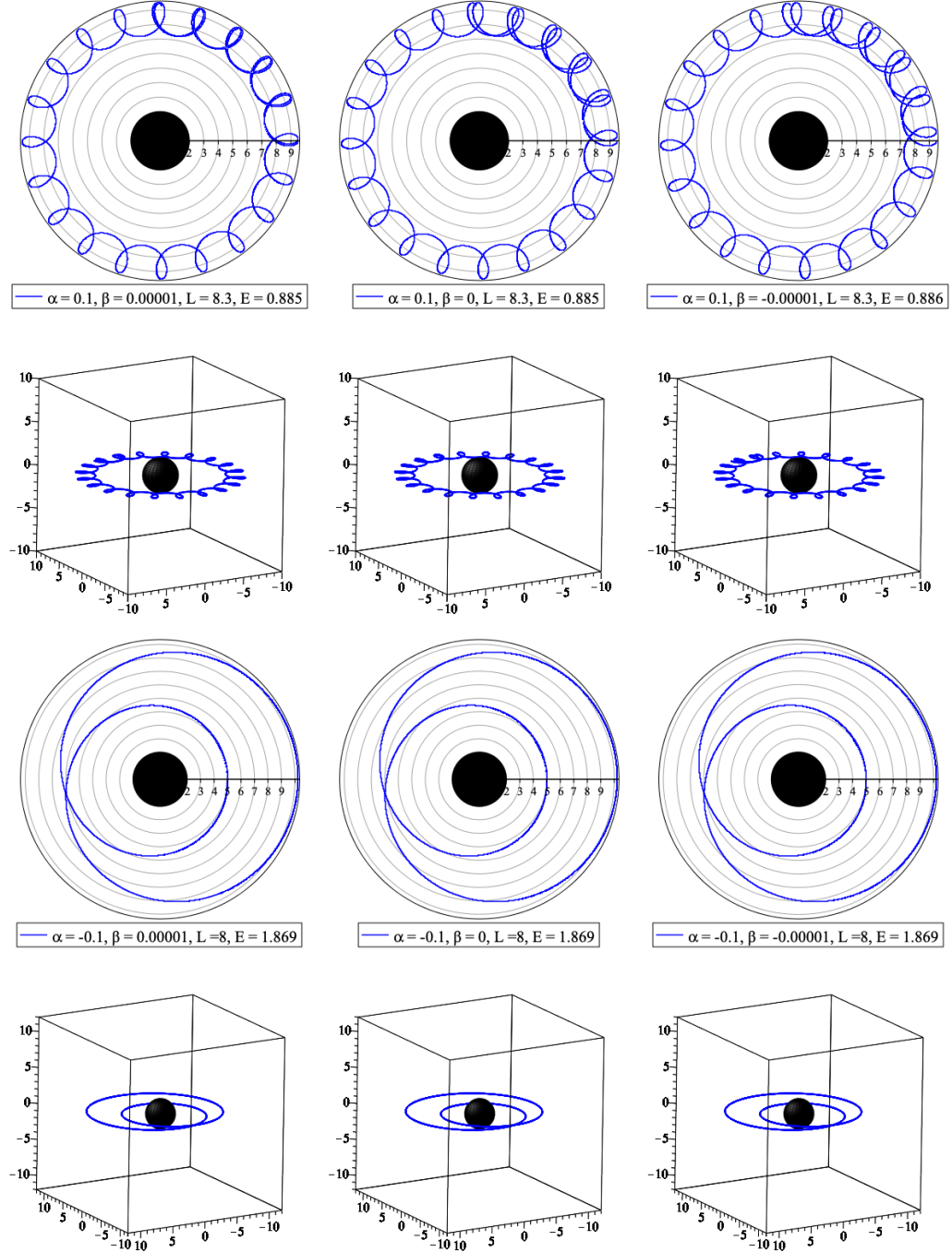


**Figure 7.12:** Trajectories of particles for some choices of the parameters. In the first row  $Q > 0$  and  $\alpha > 0$ , and the initial radius is set to be  $r_0 = 9.5$ . In the second one  $Q < 0$  and  $\alpha < 0$ , and the initial radius is set to be  $r_0 = 8$ .

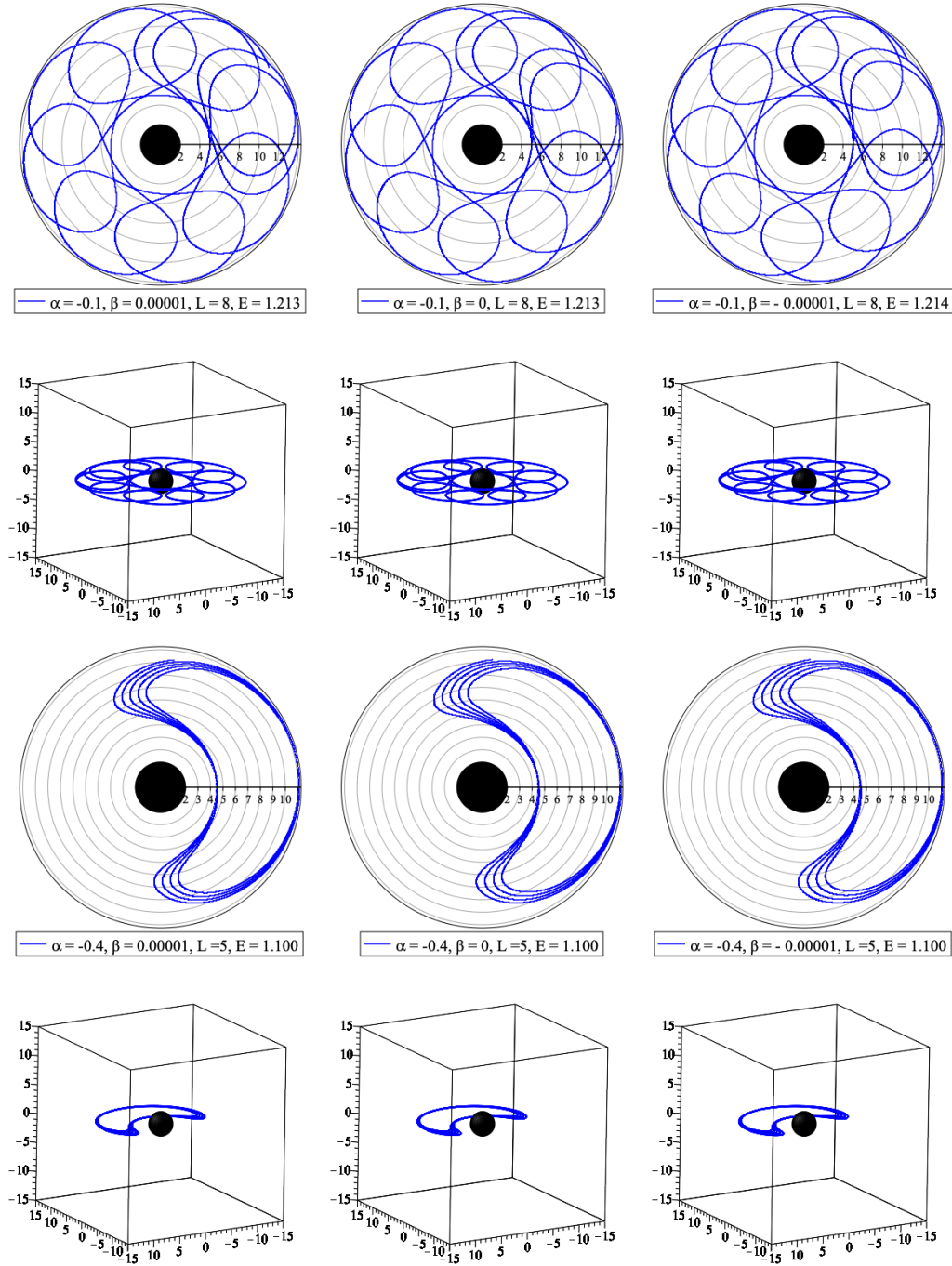


**Figure 7.13:** Trajectories of particles for some choices of the parameters. In all plots  $Q > 0$  and  $\alpha < 0$ . In the first row, the initial radius is set to be  $r_0 = 5$ , and in the second one is  $r_0 = 4.5$ .

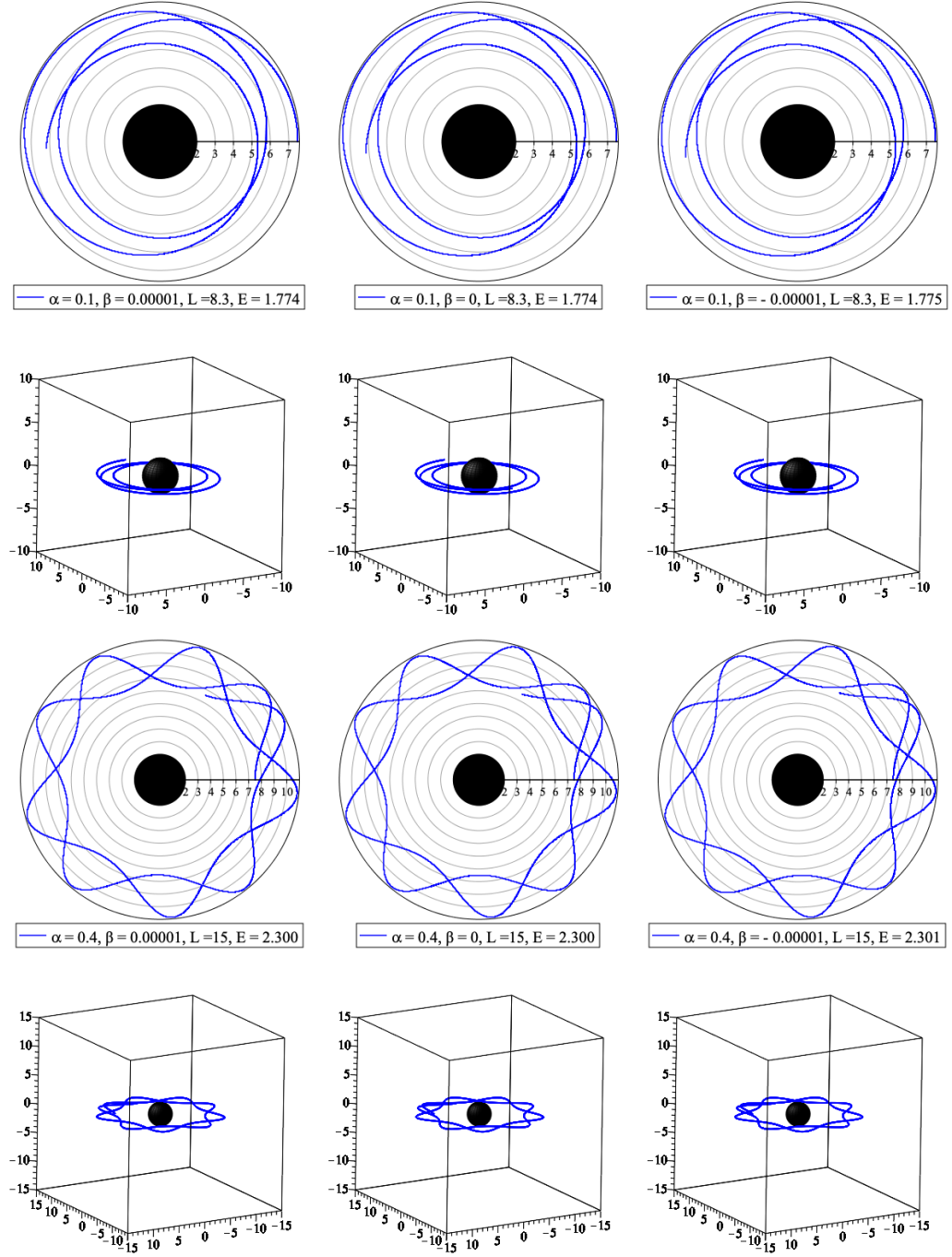


**Figure 7.14:** Trajectories of particles for some choices of the parameters. In all plots  $Q < 0$  and  $\alpha > 0$ . In the plots, the initial radius is set to be  $r_0 = 7.5$ .

## CHAPTER 8

### Extraction of energy: particle collision

In this chapter, in the following section we briefly examine the possible collision scenario in the background of the Generalized q-metric, which in principle may lead to chaotic behavior. Of course, in the end, by choosing to have only one quadrupole, the result is valid in both cases: the distorted Schwarzschild black hole and the q-metric. However, the main focus of this chapter is on the possibility of having the high energy collisions near distorted Schwarzschild black hole and the q-metric.

In addition, Bañados et.al. [188] showed that particles falling freely from rest in the vicinity of a Kerr black hole can collide with an arbitrarily high center of mass-energy for some spin parameters. Such processes are connected with the Penrose effect which has been studied a long time ago [189, 190, 191]. In this view, this situation might be related to the high energy collisions, for example, dark matter particles. In an idealized set-up, this energy can be even higher than Planck energy, therefore this allows us to have a possible interpretation of a black hole as a super high energy collider.

This type of effect even within the test-particle regime is an interesting theoretical issue and its investigation has continued in many different ways. For example, the BSW effect for non-equatorial particles in different spacetimes studied in [192, 193, 194]. In addition, within equatorial motion this notion is generalized to the arbitrary rotating black holes [195]; moreover [196] presented some restrictions on the model. For a quick literature review see e.g. [197, 195, 198, 199, 200, 201, 202, 203, 204]. In the next sections, we investigate this situation in the distorted Schwarzschild and the q-metric solutions to see if we can have the results in Kerr solution for some quadrupole parameters.

## 8.1 Particle collision

The collision may occur in this vicinity of Generalized q-metric. For example, consider the collision of a particle moving in the ISCO with another particle coming initially at rest. After the collision energy of the particle may change. For simplicity, we assume during the collision, the azimuthal angular momentum and the initial radial velocity remains invariant. Therefore, the orbit of the particle changes slightly; otherwise, the particle can move away from the original path completely. After the collision, the particle gains the escape velocity  $v$  in the vertical direction [205]. Thus, its angular momentum and energy become

$$L_e^2 = (x_0 + 1)^2 v^2 + L^2, \quad (8.1)$$

$$E_e^2 = \left( \frac{x-1}{x+1} \right)^{1+\alpha} e^{2\hat{\psi}} v^2 + E^2, \quad (8.2)$$

where  $v = -(x+1)\dot{y}$  is the particles' initial velocity in the  $y$  direction. Then particle gains greater angular momentum and energy. Therefore, for an unbounded motion, the particle requires  $E \geq 1$ , then the necessary condition is

$$v \geq e^{-2\psi} \sqrt{\left( \frac{x+1}{x-1} \right)^{1+\alpha} e^{2\psi} - \frac{x-S}{x-2S}}. \quad (8.3)$$

where

$$S := 1 + \alpha + \beta x - \beta x^3. \quad (8.4)$$

Of course, this brief analysis is also valid for both the distorted Schwarzschild and q-metric cases by substituting  $\alpha = 0$  and  $\beta = 0$  respectively.

## 8.2 Particle accelerator

Now we restrict attention here to orbits in the equatorial plane. Given the energy, and the unit four-velocity normalization, one can compute the limiting energy for a pair of collisions of two particles colliding in the vicinity of the distorted Schwarzschild black hole the q-metric. We assume the collision energy comes only from gravitational acceleration.

$$E_{cm}^2 = -g_{\mu\nu}(p_1^\mu + p_2^\mu)(p_1^\nu + p_2^\nu) = m_1^2 + m_2^2 - 2g_{\mu\nu}p_1^\mu p_2^\nu \quad (8.5)$$

where  $p^i$  is the four momentum of particles. In fact, this relation for  $E_{cm}$  is valid both in flat and in curved space-times. In the following subsections, we examine this scenario in the distorted Schwarzschild and the q-metric.

### 8.2.1 Distorted Schwarzschild

In this part, we study the center of mass energy of particle collisions in the vicinity of the distorted Schwarzschild black hole (6.12). In this background we assume two particles approaching the black hole with different angular momentum and colliding at some distance  $x$ . The center of mass relation (8.5) is obtained as follows

$$\begin{aligned} \frac{E_{cm}^2}{2m_1m_2} &= \frac{(m_1 - m_2)^2}{2m_1m_2} + 1 - \frac{L_1L_2}{(x+1)^2} \\ &+ \left( \frac{x+1}{x-1} \right) e^{-2\psi} \left[ E_1E_2 - \sqrt{(E_1^2 - V_{1\text{eff}}^2)(E_2^2 - V_{2\text{eff}}^2)} \right]. \end{aligned}$$

To see the center of mass energy behavior in the vicinity of the horizon  $x = 1$ , we need to study the limiting case. However, in the limit  $x \rightarrow 1$  the last term seems challenging since this term approaches the horizon as  $\infty \times 0$ . However, by writing this term as  $\frac{0}{0}$ , we can evaluate the limit via L'Hopital's rule easily.

$$\begin{aligned} \lim_{x \rightarrow 1} \frac{E_{cm}^2}{2m_1m_2} &= \frac{(m_1 - m_2)^2}{2m_1m_2} + 1 - \frac{L_1L_2}{4} \\ &+ \frac{E_1}{2E_2} \left( 1 + \frac{L_2^2}{4} \right) + \frac{E_2}{2E_1} \left( 1 + \frac{L_1^2}{4} \right). \end{aligned} \quad (8.6)$$

For equal mass  $m_1 = m_2 := m$  this reduces to

$$\lim_{x \rightarrow 1} \frac{E_{cm}^2}{2m^2} = 1 - \frac{L_1L_2}{4} \quad (8.7)$$

$$+ \frac{E_1}{2E_2} \left( 1 + \frac{L_2^2}{4} \right) + \frac{E_2}{2E_1} \left( 1 + \frac{L_1^2}{4} \right). \quad (8.8)$$

In the case of  $E_1 = E_2 := E$  we have

$$\lim_{x \rightarrow 1} \frac{E_{cm}^2}{2m^2} = \frac{(L_1 - L_2)^2}{8} + 2 \quad (8.9)$$

Of course, the maximum center of mass-energy happens when  $L_1$  and  $L_2$  have their maximum allowed values with an opposite sign for geodesics falling into

the black hole. If  $L_1 = L_2$  we have  $E_{\text{cm}} = 2m$  as it should be. A finite limit of center of mass-energy comes from the fact that all particles proceed toward the horizon with the same incident angle; therefore their relative velocities limits are zero.

### 8.2.2 q-metric

In the second case, we investigate the limit of the center of mass energy of particle collisions in the vicinity of q-metric (6.18). The center of mass relation (8.5) becomes

$$\begin{aligned} \frac{E_{\text{cm}}^2}{2m_1m_2} = & \frac{(m_1 - m_2)^2}{2m_1m_2} + \\ & 1 - \left(\frac{x-1}{x+1}\right)^\alpha \frac{L_1L_2}{(x+1)^2} \\ & \left(\frac{x+1}{x-1}\right)^{(\alpha+1)} \left[ E_1E_2 - \sqrt{(E_1^2 - V_{\text{1eff}}^2)(E_2^2 - V_{\text{2eff}}^2)} \right]. \end{aligned} \quad (8.10)$$

Here again, to see the center of mass energy behavior close to  $x = 1$ , we need to study the limiting case via utilizing L'Hopital's rule. It turned out that for  $\alpha > 0$  and our technical assumptions we obtain <sup>1</sup>

$$\lim_{x \rightarrow 1} \frac{E_{\text{cm}}^2}{2m_1m_2} = \frac{(m_1 - m_2)^2}{2m_1m_2} + 1 + \left( \frac{E_1^2 + E_2^2}{E_1E_2} \right). \quad (8.11)$$

For equal mass  $m_1 = m_2 := m$  this reduces to

$$\lim_{x \rightarrow 1} \frac{E_{\text{cm}}^2}{2m^2} = 1 + \left( \frac{E_1^2 + E_2^2}{E_1E_2} \right). \quad (8.12)$$

An analysis reveals that, in general, for  $\alpha > 0$  we have the limit considering our assumption. However, for  $\alpha < 0$  this limit can blow up. The calculation is long and complicated where not presented here. This result for  $\alpha < 0$  can link to the fact that particles approach  $x = 1$  with different incident angles, so they have tangential velocities relatively which allows the large center of mass collision where considering this sign is related to a prolate shape this is consistent with other findings. Therefore, the q-metric for some parameter  $\alpha$  can be a particle accelerator like the Kerr solution and can mimic its behavior.

---

<sup>1</sup>The Schwarzschild solution is excluded (i.e  $\alpha \neq 0$ ).



### 8.3 Summary and conclusion

In this chapter, we study the possibility of study collision in the background of Generalized q-metric. In addition, we investigated if the distorted Schwarzschild solution or q-metric can act as a particle accelerator or not. It turns out that like Kerr space-time for some range of parameters in these metrics there is a possibility to reach the high energy in the vicinity of the compact object described with these two solutions.



## Cognitive study on the Stationary q-metric

As this the Stationary q-metric is quite new, in this chapter, we investigate some of the most important properties of the metric in the equatorial plane including the behavior of effective potential and circular geodesics, to explore the possibility of construction the Thick accretion disc model in this background. The metric and its general properties are described briefly in Section 6.4.

### 9.1 Ernst potential

The first tool, we utilize to investigate more about this metric following [206], is the complex Ernst potential

$$E = f + i\Omega. \quad (9.1)$$

where  $f$  and  $\omega$  are the metric functions equation (6.21). It means that if the potential  $E$  is given, one can find the metric function  $f$  with an algebraic manipulation, and the metric function  $\omega$  is obtained by solving

$$\sigma_0(x^2 - 1)\Omega_x = f^2\omega_y, \quad (9.2)$$

$$\sigma_0(1 - y^2)\Omega_y = -f^2\omega_x. \quad (9.3)$$

Moreover, by having  $E$  the function  $\gamma$  in the metric equation (6.21) is determined by a system of differential equations. It means all necessary information of the metric, interestingly, is contained in the Ernst potential. In addition, analyzing the behavior of the Ernst potential leads to the fact that the stationary q-metric is also asymptotically flat like the static case. The

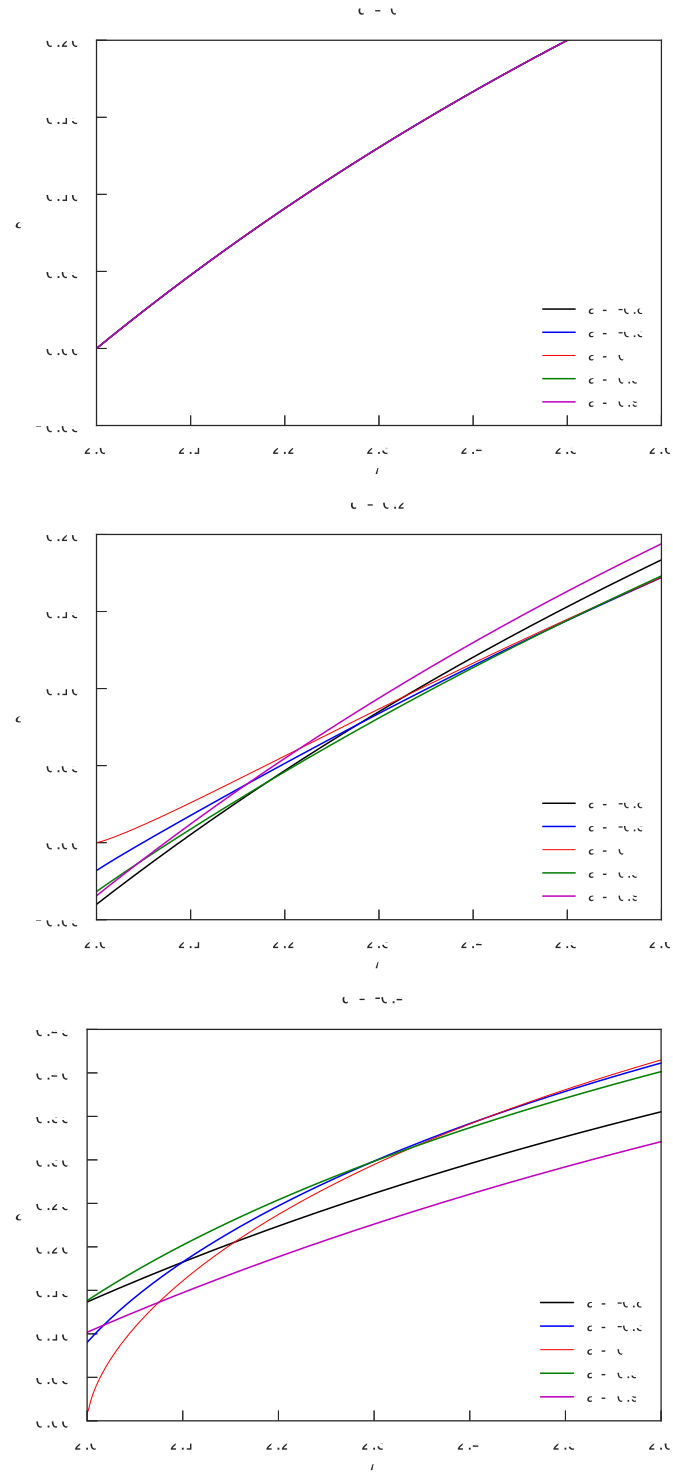


**Figure 9.1:** The Ernst potential,  $\mathcal{E}$ , is depicted for various values of  $q$  and  $a$

Ernst potential for this metric by utilizing the solution generating techniques [207] is calculated [208] as follows

$$\mathcal{E} = \left( \frac{x-1}{x+1} \right)^q \left[ \frac{x-1 + (x^2-1)^{-q} d_+}{x+1 + (x^2-1)^{-q} d_-} \right], \quad (9.4)$$

where

$$\begin{aligned} d_{\pm} = & -\alpha^2(x \pm 1)h_+h_-(x^2-1)^{-q} \\ & + i\alpha[y(h_+ + h_-) \pm (h_+ - h_-)], \end{aligned} \quad (9.5)$$

and

$$h_{\pm} = (x \pm y)^{2q}. \quad (9.6)$$

Additionally, in the case of  $q = 0$ , we obtain

$$\mathcal{E} = \frac{a^2(x-1) - (\sigma_0 - m)^2(x+1)}{a^2(x+1) - (\sigma_0 - m)^2(x-1)}, \quad (9.7)$$

since  $|a| \in [0, 1)$  then its power two is smaller, also the coefficients of  $a^2$  in the nominator and denominator of the equation (9.7) are of the same order and comparable, the results for different values of  $a$  are very close to each other and not distinguishable. In Figure 9.1 we studied the behavior of the Ernst potential on the equatorial plane outside the curvature singularity  $r = 2m$ . We presented these results for different values of  $a$  and  $q$  that we use later to construct the Thick disc model in Section 11.3. In this Figure, we see that for each value of  $a$  the Ernst potential is a continuous function of  $r$  that approaches monotonically to a constant at infinity. There are certain points at which the Ernst potential for different values of  $a$  coincide. Since the Ernst potential contains all the information about the gravitational field, this means that at the intersection points the corresponding space-times are identical. This can be one interpretation, While another can consider them as a signal to put some restriction on the chosen values of metric parameters. To illustrate more the nature of these intersections, the Kretschmann scalar  $\mathcal{K}$  is investigated in the equatorial plane [209]. This scalar reads as

$$\mathcal{K} = R_{\nu\mu\tau\theta}R^{\nu\mu\tau\theta}, \quad (9.8)$$

where  $R_{\nu\mu\tau\theta}$  is the Riemann tensor. This analysis shows that the singularities are always happened to be inside  $r = 2M$  (for  $r \neq a$ ) for the chosen values of the parameters. Since, in principle the considered values of  $q$  are relatively small, say smaller than 1, we expect to have similar behavior for all quadrupole values  $q$  within this range. Therefore, the corresponding intersections in the Ernst potential are inside the latest singularity and we can neglect them as we are interested to study the exterior of the stationary  $q$ -metric. Furthermore, we see that the place of singularities is a decreasing function of  $a$ ; namely, as  $|a|$  increases the singularities are concentrated closer to the central curvature singularity.

## 9.2 Effective potential

In the next step of the study of this metric, we analyze the effective potential of this space-time. We will use this discussion here in Section 11.3 to construct the Thick accretion disc model. The exact relation for  $V_{\text{eff}}$  in this space-time is too complicated that we prefer to state its general form in the stationary and axisymmetric space-time in terms of the metric components as

$$V_{\text{eff}} = -1 + \frac{E^2 g_{\phi\phi} + ELg_{t\phi} - L^2 g_{tt}}{g_{t\phi}^2 + g_{tt}g_{\phi\phi}}, \quad (9.9)$$

where  $E$  is a specific energy, and  $L$  is the specific angular momentum that we investigate  $L$  more in Section 11.3 since this has a key role in constructing the Thick accretion disc model. In Figure 9.2 we plotted  $E$  for different values of  $a$  and  $q$ . In particular, we consider cases with  $a = 0 = q$  to have the Schwarzschild case to compare with, as well as static  $q$ -metric in each case. We can see very different behavior for  $a > 0$  and  $a < 0$ . We see that for negative parameters, in general, the curves can reach more to the strong gravity field while for positive values the minimums are farther away from the central object. Interestingly, if we compare these plots with  $E$  for Kerr in Figure 9.3 we see the situation is completely opposite, which indicates there are obvious differences between these two solutions regarding observational data.

Figure 9.4 shows the effective potential of the stationary  $q$ -metric for different values of  $q$  and  $a$ . In Figure 9.4 we see that the amplitudes for the extreme cases where  $a = -0.8$  and  $a = 0.9$  are much higher; however, there is not a unique pattern to formulate the behavior of its extrema as a function of  $a$ . Again, in general, the amplitudes are higher for negative values of parameters as we expected from the behavior of the class of  $q$ -metric in

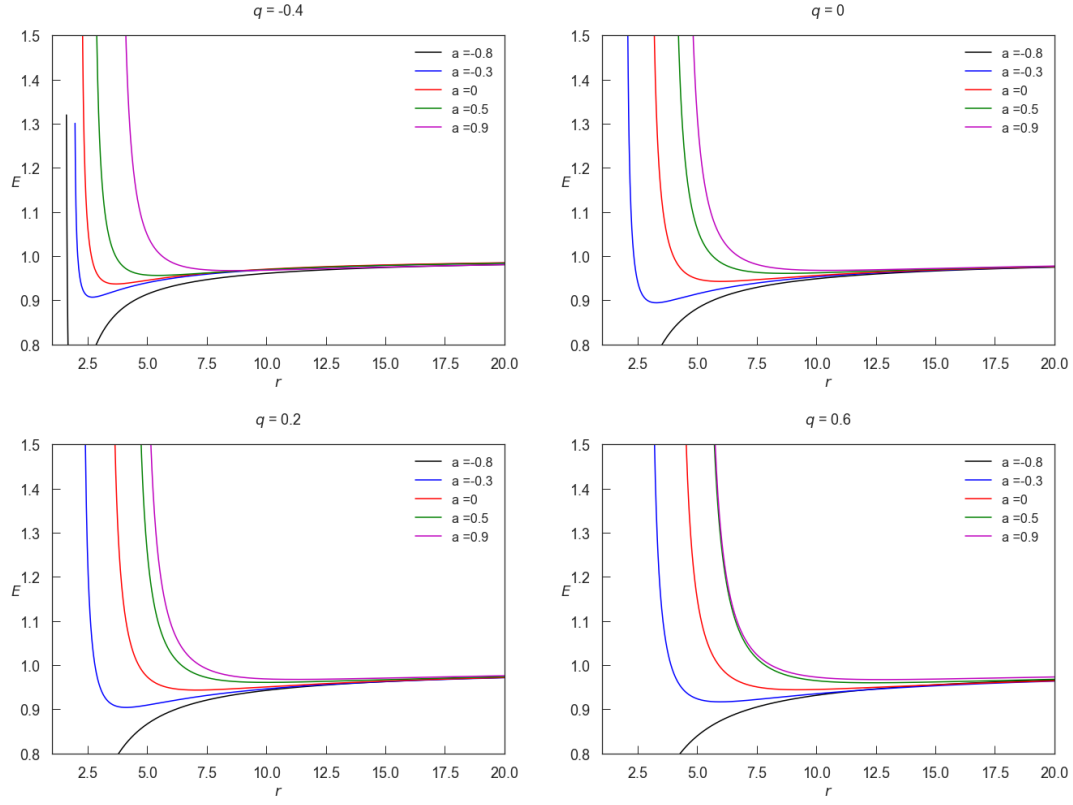


**Figure 9.2:** Plots of  $E$  for different values of  $a$  and  $q$  in the equatorial plane of stationary  $q$ -metric.

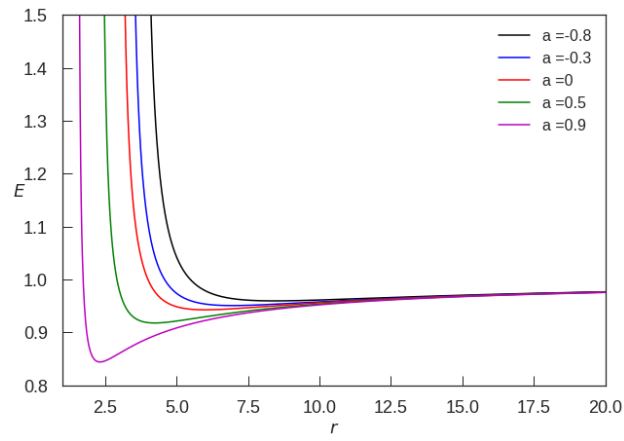


**Figure 9.3:** Plots of  $E$  for different values of  $a$  in the equatorial plane of Kerr metric.

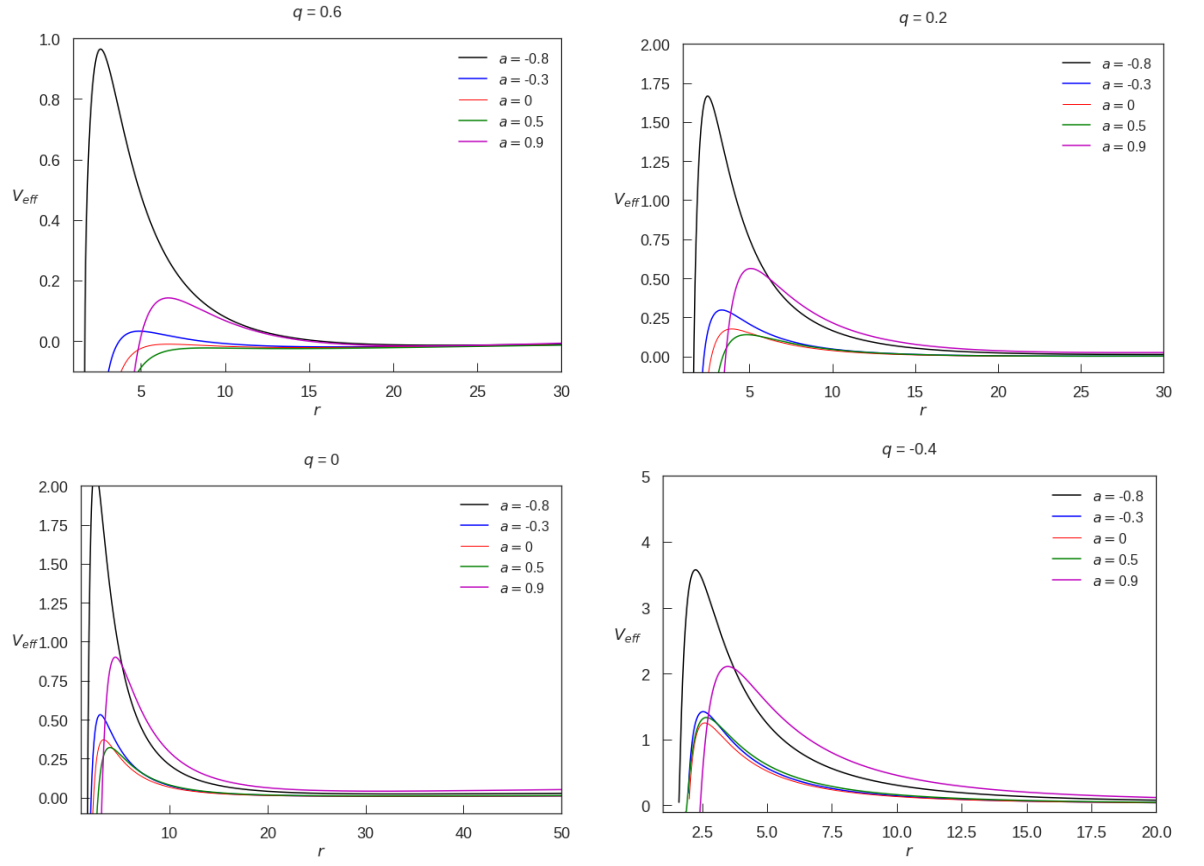


**Figure 9.4:** Effective potential  $V_{\text{eff}}$  for different chosen values of  $a$  and  $q$ .



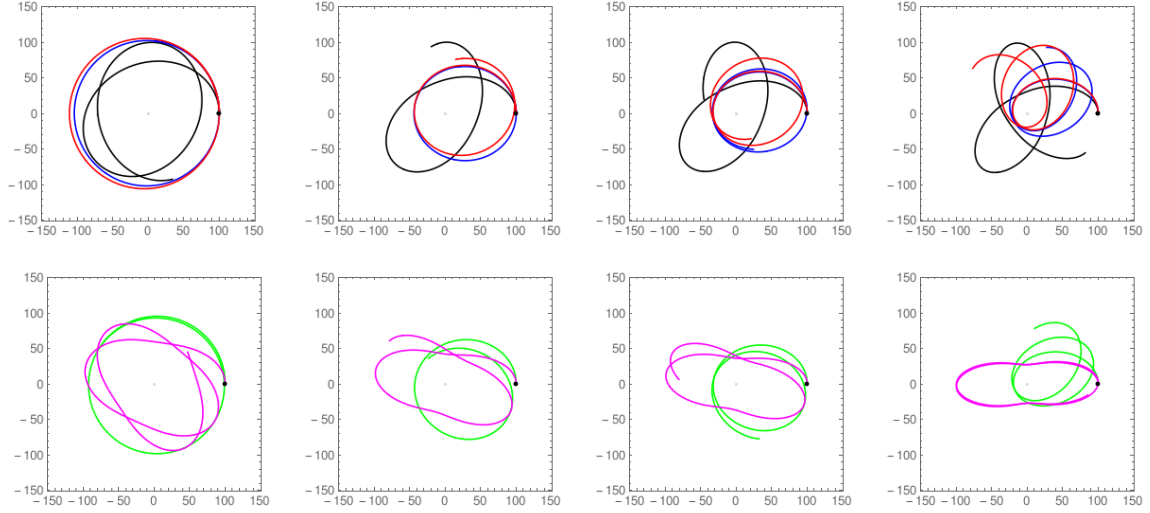


**Figure 9.5:** Bounded trajectories for various combinations of  $a$  and  $q$ . The first row is dedicated to  $a \leq 0$  and the second one to  $a > 0$ . The colors refers to the values of  $a$  the same as others e.g. Figure 9.4. From the left to the right  $q = -0.4$ ,  $q = 0$ ,  $q = 0.2$  and  $q = 0.6$ . All along the plots the following parameters remain constant: The angular momentum  $L = 8$ , the initial point  $r(0) = 100$ ,  $\phi(0) = 0$ .

general. As a standard approach, by analyzing  $V_{\text{eff}}$  we can investigate the particle dynamics. In general, different types of trajectories are obtained by the energy's boundaries  $E^2 = V_{\text{eff}}$ , depending on the parameters of the model. In Figures 9.5 and 9.6, for each valid choice of parameters, we see that it is possible to determine different trajectories.

### 9.3 Summary and conclusion

In this chapter, we studied the main properties of the stationary q-metric that mostly are needed to know about the existence and construction of the Thick accretion disc model in this background. This metric is asymptotically flat and free of curvature singularities outside the hypersurface  $r = 2M$ . This implies that we can use it safely to describe the gravitational field of relativistic compact objects for which  $r > 2M$ . Besides, there are properties which can be distinguishable in the observational data from the Kerr solution.

In particular, we analyzed the main properties of the Ernst potential and the effective potential of the stationary q-metric on the equatorial plane. Interestingly, it turns out that there are certain points on the equatorial plane at which the Ernst potential has the same value for different values of  $a$ . However, an analysis of the Kretschmann scalar showed that the intersection

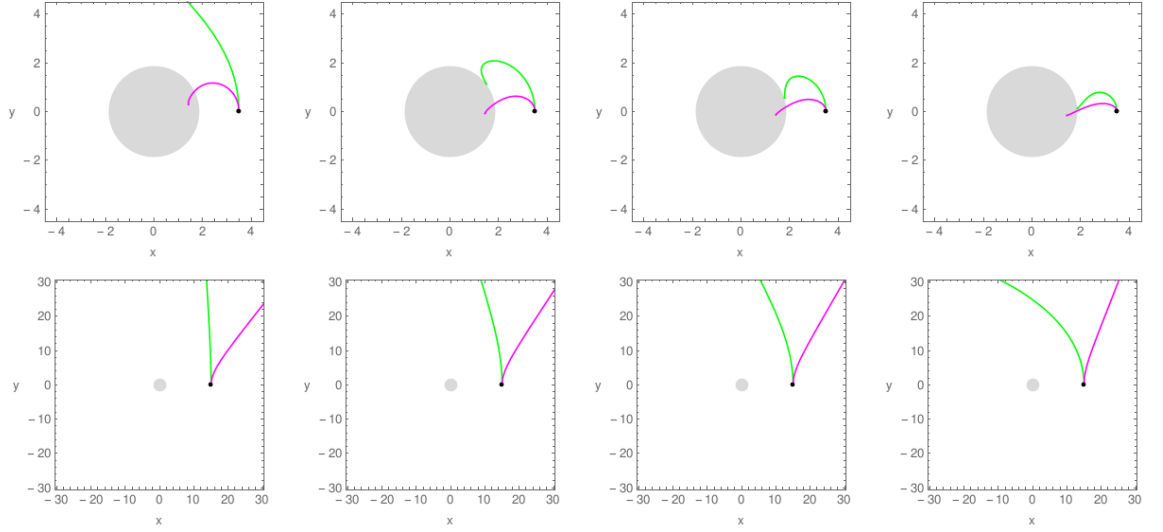


**Figure 9.6:** Fall-in and fly-by trajectories for various combinations of  $a > 0$  and  $q$ . The colours refer to the values of  $a$  the same as others e.g. Figure 9.4. From the left to the right  $q = -0.4$ ,  $q = 0$ ,  $q = 0.2$  and  $q = 0.6$ . All along with the plots, the following parameter remains constant: The angular momentum  $L = 8$ , the initial point  $r(0) = 3.5$ ,  $\phi(0) = 0$ .

points are located in a neighborhood of the curvature singularity and around the hypersurface  $r = 2M$ . This means that degeneracy does not affect the study of different astrophysical scenarios since they are located far away from this surface. The main results of this chapter are presented in [209]. In Section 11.3 we will explore the Thick disc configuration and its properties in this background.

## CHAPTER 10

# Thin accretion disc model in Generalized q-metric

In this chapter, we investigate the properties of the Thin accretion disc model discussed in Section 2.1 in the background of Generalized q-metric up to quadrupole. First of all, we need to write the metric (7.13), in the equatorial plane (7.21), where  $y = 0$  (or equivalently  $\theta = \frac{\pi}{2}$ ). We state the metric and functions again here to be easier to follow

$$\begin{aligned}
 ds^2 = & - \left( \frac{x-1}{x+1} \right)^{(1+\alpha)} e^{2\hat{\psi}} dt^2 + M^2 (x^2 - 1) e^{-2\hat{\psi}} \\
 & \left( \frac{x+1}{x-1} \right)^{(1+\alpha)} \left[ \left( \frac{x^2-1}{x^2} \right)^{\alpha(2+\alpha)} e^{2\hat{\gamma}} \right. \\
 & \left. \left( \frac{dx^2}{x^2-1} + dy^2 \right) + d\phi^2 \right].
 \end{aligned} \tag{10.1}$$

And the distortion functions up to the quadrupole moment in the equatorial plane are simplified to

$$\begin{aligned}
 \hat{\psi} &= -\frac{\beta}{2}(x^2 - 1), \\
 \hat{\gamma} &= -2\beta(1 + \alpha)x + \frac{\beta^2}{4}(x^2 - 1)^2.
 \end{aligned} \tag{10.2}$$

The second step is to determine the inner edge of the disc. As mentioned earlier, the inner edge of the standard Thin disc model is assumed to be at the Innermost Stable Circular Orbit, ISCO. So, we need to analyze the location of the ISCO in this solution that we had in Section 7.3.1. It has been

shown that there is a valid range for  $\beta$ , quadrupole moment of source, for each choice of  $\alpha$ , quadrupole of the central object, for time-like trajectories. First the domain of the central object quadrupole is  $\alpha \in [-1 + \frac{\sqrt{5}}{5}, \infty)$ . Further, for each choice of  $\alpha$ , there exist ISCOs for time-like geodesics for some range of quadrupole of external matter  $\beta \in [\beta_{min}, \beta_{max}]$ , such that in general,  $\beta_{min} \approx -2.5 \times 10^{-1}$  at  $\alpha = -0.5$  and  $\beta_{max} \approx 4.1 \times 10^{-3}$  at the minimum of  $\alpha$ , meaning  $\alpha = -0.5528$ . In addition, from  $\alpha = -0.5$ ,  $|\beta|$  is a monotonically decreasing function of  $\alpha$  and approaches zero. Some of the examples are listed in Table 7.1. Also, the place of ISCO, in general, is closer to the horizon for negative quadrupoles, and it is farther away from it for positive quadrupoles in both cases, see Figure 7.7. Therefore, from an ISCO analysis, we restricted choosing the quadrupole values in the model.

## 10.1 The valid region

Furthermore, one can derive the various physical quantities appearing in the equations of the Thin disc model described earlier in Section 2.1. As mentioned earlier in Chapter 7, by its definition the distorted metric is only valid locally. We can see this in the analysis of the behavior of physical quantities like  $E = -u_t$ ,  $L = u_\phi$  and  $\Omega = \frac{u^\phi}{u^t}$  in this space-time, and consider the valid region where they are real-valued, for a given value of quadrupoles. Interestingly, the angular velocity - which is supposed to be a monotonically decreasing function for vanishing quadrupoles - in this space-time may possess an extremum at some  $x$ . A likely explanation is that the effect due to the external matter starts to reveal from this point. So, one can take this as the signature of external matter indicating that from this distance  $x$ , the local solution is no longer valid.

Further analysis shows that, although angular velocity gives us an upper bound for the valid region, one can find a better estimate on the valid region by analyzing the shear rate (2.9), in the local rest frame  $\sigma_{\hat{x}\hat{\phi}}$ . An analysis shows that for positive values of  $\beta$ , these two estimations are in good agreement. Consequently, for asymptotically flat solutions, meaning  $\beta = 0$ , always  $\sigma_{\hat{x}\hat{\phi}}$  is negative for this space-time; therefore, there is no restriction for any chosen value of  $\alpha$ . However, the place of ISCO, the inner edge, will be different, as was discussed earlier. Besides, for positive values of  $\beta$ , meaning  $(\beta > 0, \alpha)$  always  $\sigma_{\hat{x}\hat{\phi}}$  is negative; however, it is restricted to some region. For negative  $\beta$ , meaning  $(\beta < 0, \alpha)$  at some point say  $x_0$ , shear rate  $\sigma_{\hat{x}\hat{\phi}}$  changes the sign, which means the valid region is restricted to  $x_0$ . However, in this case, it depends on the value of  $\alpha$ , the behavior of the  $\sigma_{\hat{x}\hat{\phi}}$  in the valid region is different. Since  $\sigma_{\hat{x}\hat{\phi}}$  is the major contributing factor mostly in vertical

structure, we expect to have some effects, especially in this direction. Nevertheless, this effect becomes more strong for larger values of  $\alpha$ . We should mention that as the absolute value of the quadrupole  $|\beta|$  approaches zero, we arrive at a wider valid range for  $x$ , as it is expected from the  $(\beta = 0, \alpha)$  limit for each choice of  $\alpha$ .

The final result is obtained by summing up the results from the analysis of physical quantities being real-valued, and the upper bound given by  $\sigma_{\hat{x}\hat{\phi}}$  analysis. This gives us some restrictions on the range of the  $x$  coordinate for any chosen value of  $\alpha$  and  $\beta$ .

As the last step, before solving the system of equations stated in Section 2.1.2, one needs to rewrite equations and quantities in the prolate spheroidal coordinates  $(t, x, y, \phi)$  simply via the transformation (6.10) to obtain the system of algebraic equations that can be treated analytically. In fact, this system of equations admits a unique solution for considering positive temperature and pressure. The results are described and plotted in the next Section.

## 10.2 Properties of the Thin disc model

In fact, as the distorted solutions are only valid locally, we only consider the inner part of the disc in this space-time. As discussed earlier, the upper limit of the solution depends on the choice of both the quadrupoles  $\alpha$  and  $\beta$ . The results were produced by Mathematica, and the physical constants and parameters that were used are as follows

$$\begin{aligned} G &= 6.67 \times 10^{-8} \text{ cm}^3 \text{g}^{-1} \text{sec}^{-2}, \\ c &= 3 \times 10^{10} \text{ cm sec}^{-1}, \\ \kappa_{es} &= 0.40 \text{ cm}^2 \text{g}^{-1}, \\ M &= 10^{34} \text{ g}, \end{aligned} \tag{10.3}$$

$$\begin{aligned} \dot{M} &= 0.25 \dot{M}_{\text{Edd}} (= 10 \frac{L_{\text{Edd}}}{c^2}) \text{ g sec}^{-1}, \\ \alpha &= 0.02. \end{aligned} \tag{10.4}$$

Apart from the height scale  $h$ , which is dimensionless, the results are represented in the cgs units.

First, in Figure 10.1 the flux, temperature, pressure and height scale are plotted over the distance for different value of  $\alpha$  when  $\beta = 0$ . We see that, for any negative value of  $\alpha$ , plots start at a place closer to the horizon, and they get further away as  $\alpha$  increases. This is due to the fact that the inner edge of

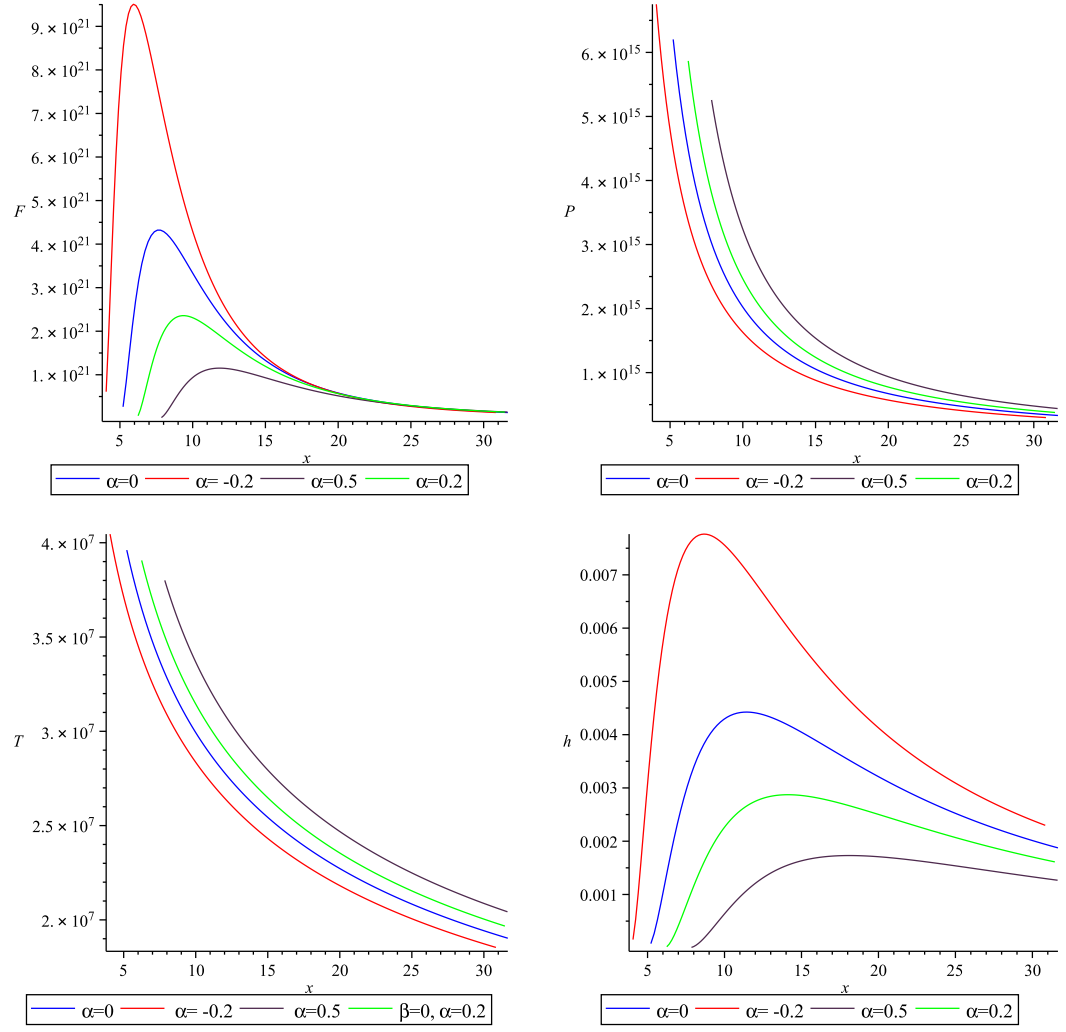


**Figure 10.1:** Radiation flux  $F$ , pressure  $P$ , temperature  $T$  and The height scale of the disc  $h$  for different values of quadrupole  $\alpha$ .

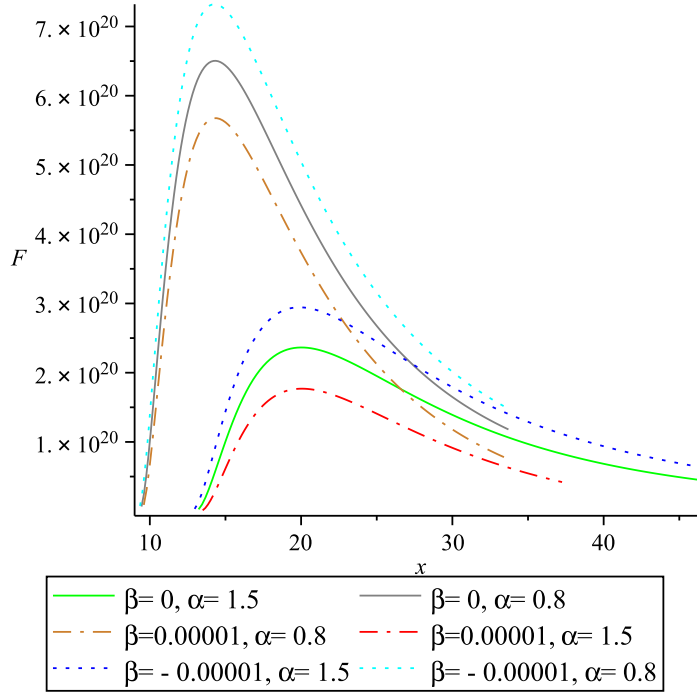


**Figure 10.2:** Radiation flux  $F$  for different values of parameters.

the disc, ISCO, for the negative quadrupoles is closer to the compact object and the opposite for positive ones, Figure 7.7. Furthermore, the maximum of plots is much higher for the negative quadrupoles  $\alpha$ , compared to the Schwarzschild case  $\alpha = 0$ , and for the positive quadrupoles  $\alpha$ . In addition, in the case of negative quadrupoles  $\alpha$ , there is a sharper ascent and descent rather than for positive quadrupoles  $\alpha$ . In this regard, the place of the pick of each plot is a monotonically decreasing function in  $\alpha$ . Therefore, for some values of quadrupoles there are distinguishable differences between the properties of a standard Thin disc around q-metric and the Schwarzschild case. This behavior repeats in other quantities that in the following we discuss them with non-vanishing  $\beta$ . This is worth mentioning that after intersection the order of curves will change which is not the case in Kerr space-time.

The radiation flux  $F$  is plotted over distance in Figure 10.2 for different values of  $\alpha$  and  $\beta$ . Without loss generality, we chose positive  $\alpha$ , since we already see the impact of  $\alpha$  on the properties in Figure 10.1. By comparing the black line and the green one, we see that as  $\alpha$  becomes larger the intensity of the flux reduces and the position of its maximum shifts away from the central object; therefore, this is not a surprise that its amplitude decreases.

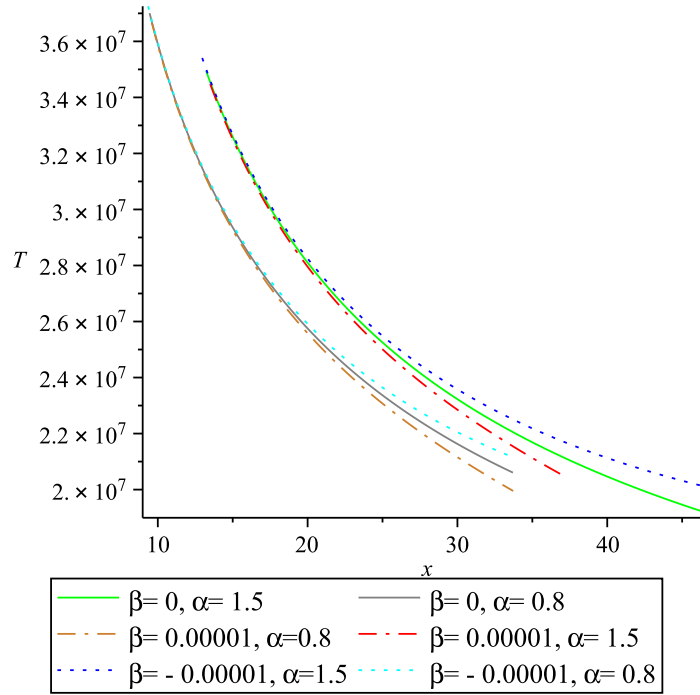


**Figure 10.3:** Temperature for different values of parameters.

This is also true for any other choices of  $\alpha$  as expected. In particular, in the plot of flux for the case when both parameters are zero and correspond to the Schwarzschild solution the intensity is much higher, also closer to the central source. In addition, at smaller radii, for negative quadrupole  $\beta$ , there is a sharper ascent and descent with a higher pick compared to the undistorted and positive  $\beta$  case. However, this may not be a surprise, because also in the case of negative quadrupole of the external matter  $\beta$ , the inner edge of the disc, ISCO, is getting closer to the horizon even very small since the values for quadrupole  $\beta$  are relatively small (see table 7.1), and we expect to have more intense effects at the inner part.

The temperature  $T$  is plotted over distance in Figure 10.3 for different values of  $\alpha$  and  $\beta$ . Again we see the effects of smaller quadrupole is more intense and one expect to have a higher temperature for them. This is worth mentioning that since this is not the surface temperature and we expect this behavior. The pressure  $P$  is plotted over distance in Figure 10.4 for different values of  $\alpha$  and  $\beta$ . We see almost the same pattern as temperature as we expected from the equations. In Figure 10.5 we plotted the viscose stress for the same parameters values. As this function links to the flux in the equation directly we expected to have similar behavior by looking at the equations.



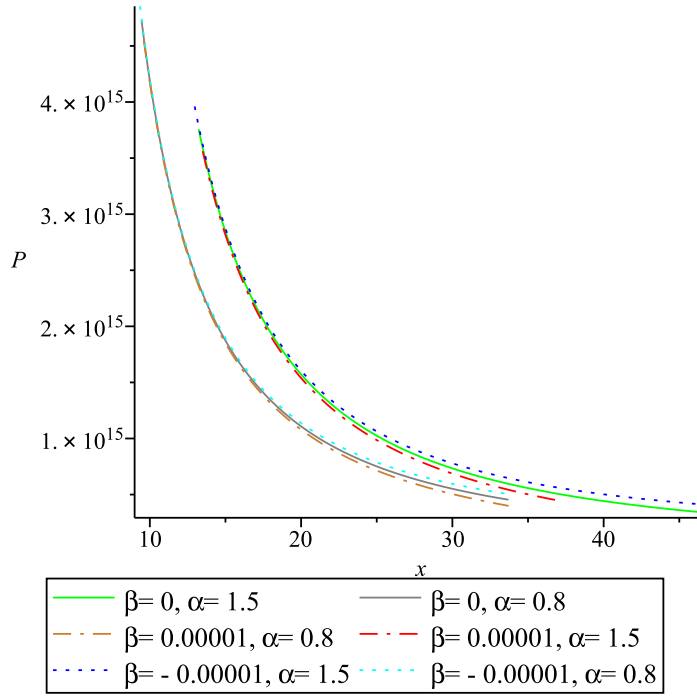


**Figure 10.4:** Pressure  $P$  for different values of parameters.

Figure 10.6 shows the height scale  $h$  of the disc over  $x$  for the same values. In general, the disc gets thicker and gradually becomes thinner after reaching some maximum. Although this thickness change is less manifest for higher quadrupoles  $\beta$ , it is stronger in the case of the lower quadrupole.

The pattern of all quantities repeats for all values; however, the range of change and the amplitude vary. In fact, the valid region is more restricted for the positive quadrupole, as we have seen from the shear rate analysis. Thus, to see the difference between the case of negative quadrupole  $\beta < 0$  and  $\beta = 0$  at larger radii.

In general, we can conclude that the effect of external quadrupole  $\beta$  for a fixed  $\alpha$  at small radii closer to the central source has a rather small impact on the results. The deviations between the case of  $(\beta = 0, \alpha)$  and different choices of the quadrupole  $\beta$  become more clear in larger radii. In addition, in all quantities for a fixed  $\alpha$ , for negative  $\beta$  the amplitude is higher than for  $(\beta = 0, \alpha)$ , on the contrary to the positive  $\beta$  values. In this case, also, the ISCO is closer to the central object; however, because the differences are tiny, we can not see it on plots. However, since the values for quadrupole  $\beta$  are relatively small (see table 7.1), we expect to have more intense effects in the inner part. Besides, it is clearly seen from the plots that as the quadrupole  $\alpha$

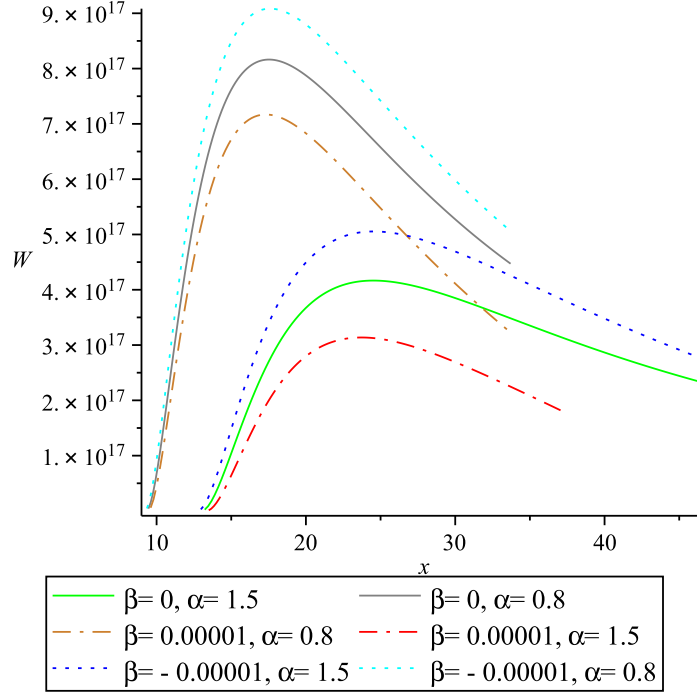


**Figure 10.5:** Viscous stress for different values of parameters.

becomes larger, the effect of these distortions also becomes more significant because we have a wider domain for them, as discussed earlier 7.

### 10.3 Summary and conclusion

In this chapter, we have analyzed the structure of the Thin accretion disc model in the background of the Generalized q-metric described in Chapter 7, and also compared the results with the Schwarzschild black hole. In fact, qualitatively, the results appear to be entirely consistent.

We have derived some physical conditions to determine the upper limit on the valid region depending on quadrupole parameters, as this solution is only valid locally. In general, an analysis shows that the result for a given  $\alpha$ , say  $\alpha_0$ , at small radii close to the ISCO for a non-vanishing external quadrupole  $\beta \neq 0$ , has a small effect on the results. However, the deviations between the undistorted naked singularity ( $\beta = 0, \alpha_0$ ) and different choices of the distortion background, ( $\beta \neq 0, \alpha_0$ ) become stronger for larger radii. Also, as the magnitude of the quadrupole  $|\beta|$  approaches zero, we get a wider valid range, as is expected from the ( $\beta = 0, \alpha$ ) limit for each choice of  $\alpha$ . Furthermore, the pick of the mentioned quantities for ( $\beta < 0, \alpha_0$ )

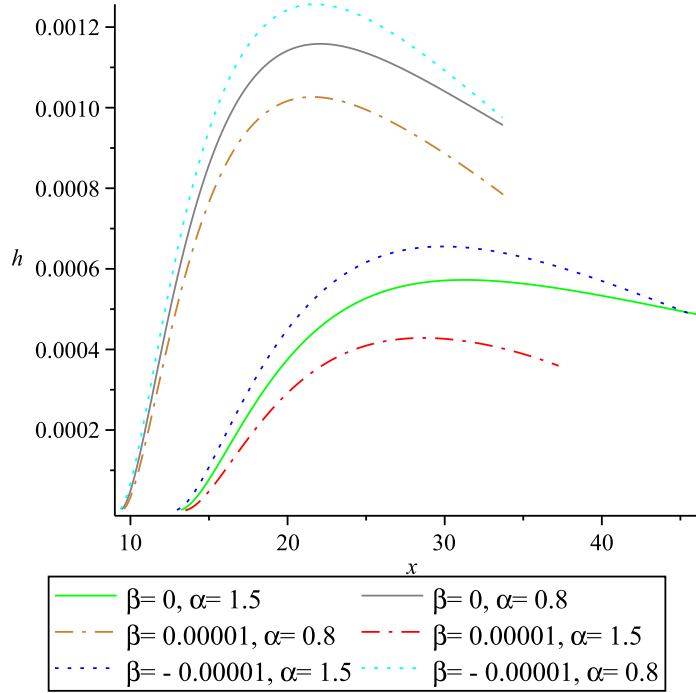


**Figure 10.6:** Height scale of the disc  $h$  for  $\alpha < 0$ ,  $\alpha = 0$  and  $\alpha > 0$ .

is generally higher than the  $(\beta = 0, \alpha_0)$ , and the situation is reversed for  $(\beta > 0, \alpha_0)$ . In addition, the intensity of effects due to distortion background is a monotonically increasing function of  $\alpha$ .

Further, we have shown that the presence of quadrupoles changes the geometric properties of the accretion disc drastically. Thus, the disc structure in the background of a deformed and/or distorted compact object is significantly different and clearly distinguishable from other solutions when trying to fit with the observations. In this respect, a disc around the distorted deformed compact object is much more luminous than one around a regular black hole that is completely distinguishable in observational data. The results of this chapter are presented in [210] and [211].



## CHAPTER 11

# Thick accretion disc model

In this chapter, we discuss various results with focus on the parameters of different metrics, as well as the other parameters of the Thick disc related to the angular momentum distributions and magnetic field. We study their impact on the location and morphology of the equipotential sequences described in Section 2.2.

As mentioned, in this model, the different regions are bounded by the value of the angular momentum at the marginally bound orbit  $\ell_{\text{mb}}$ , and at the marginally stable circular orbit  $\ell_{\text{ms}}$ . Through this thesis, my interest is in the regions where we can construct discs with or without a cusp, i.e.,  $\ell_{\text{ms}} < \ell_0 < \ell_{\text{mb}}$  to use in the future works.

In what follows, in three cases 11.1, 11.2 and 11.4 we consider magnetized version. In addition, the morphology of the solutions seems to have no change for magnetization values higher than  $\beta_c = 10^3$  or lower than  $\beta_c = 10^{-3}$ . These cases can thus be considered as the limiting values, the same also applies in the simulations [212]. Besides, by its definition<sup>1</sup>, the lower  $\beta_c$  corresponds to the stronger magnetic pressure. In this regard, we aim to study the impact of the magnetic pressure on the characteristics of the disc when this is strong in comparison to the gas pressure.

Furthermore, in two cases 11.1 and 11.2 we considered two non-constant angular momentum distributions, apart from the constant one. Moreover, we compared the results with the Schwarzschild case. As a special case, the results are in good agreement with the result in the literature when we limited our solution to the vanishing quadrupole moment.

---

<sup>1</sup>The magnetization parameter is defined as the gas pressure to the magnetic pressure Section 2.2.1. In fact, the interplay between magnetic pressure and the gas pressure is important to magnetohydrodynamics and plasma physics.

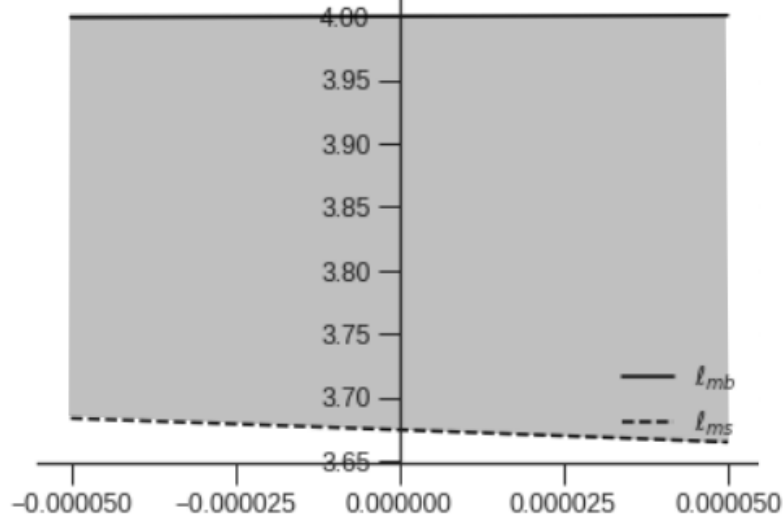


**Figure 11.1:** profiles of  $\ell_{ms}$  and  $\ell_{mb}$  as a function of  $q$ .

## 11.1 Magnetized Thick disc in distorted Schwarzschild

This section presents the magnetized Thick disc model in the background of the distorted Schwarzschild space-time (6.12) where described briefly in Section 6.2. The results showing the effect of the quadrupole parameter of the metric related to the distortion of the black hole combining with a magnetization parameter and different angular momentum distributions. In this section, letter  $q$  presents the quadrupole.

### 11.1.1 Discussion on the constant angular momentum

As mentioned in section 2.2.2, different discs can be constructed upon different choices of the value of  $\ell_0$ . To see how to choose  $\ell_0$  to have a solution for which closed equipotential surfaces can exist we interrogation the variation of  $\ell_{ms}$  and  $\ell_{mb}$  as a function of  $q$  where depicted in Figure 11.1 for  $q \in [-0.0001, 0.0001]$ . We see that the specific angular momentum at the marginally stable orbit is decreasing. Consequently, the area where closed equipotential surfaces are possible increases for higher values of  $q$ . First, we assume specific angular momentum is constant and fixed to be  $\ell(x, y) = \ell_0 = 3.77$  which is compatible with Figure 11.1. Therefore, it allows us to have the solution with a cusp for all values of  $q$ .

Figure 11.2 shows the profile of the maximum rest-mass density and its location in the equatorial plane over  $q$ , for different values of  $\beta_c$ . We see

that for a fixed value of  $q$ , the rest-mass density maximum is a decreasing function, and its location is an increasing function of  $\beta_c$ . Considering the assumptions of MHD, the magnetic field causes the rest-mass density increase in the inner part of the disc as a response to the magnetic pressure, and as a result, its place shifted farther away accordingly. This is compatible with the proceeding literature. Furthermore, for a fixed  $\beta_c$ , the maximum and its location are an increasing function of  $q$ . In fact, the disc has been constructed between the compact object and the mass distribution parameterized by  $q$  in its vicinity. Therefore, as the parameter,  $q$  increases, the effect of this external source is more manifest, and maximum density becomes higher at the radios farther away from the central object and closer to the external source. Then for some proper combination of parameters,  $q$  and  $\beta_c$ , can compensate some of their effects. In Figure 11.3, the location of the rest-mass density maximum and its amplitude are plotted as a function of  $\beta_c$ . The results are compatible with the result of Figure 11.2.

One can construct various disc models with different shapes due to different cusp locations and the centre. We have considered models denoted by the letters A, B, C, D, and E, to show the effect of the quadrupole  $q$ . Also, by subscripts 1, 2, 3 to show the effect of the magnetization parameter  $\beta_c$  on the disc's shape. The parameters of each case are given in Table 11.1. All these solutions are depicted in Figure 11.3.

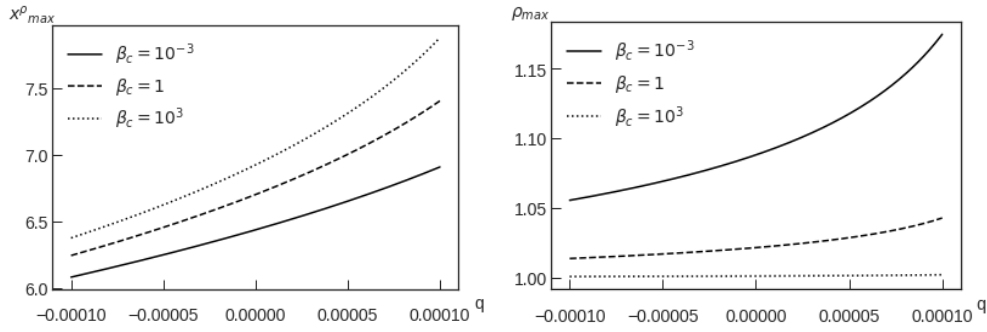


**Figure 11.2:** Amplitude and location of the rest-mass density maximum over  $q$ , for  $\ell(x, y) = \ell_0 = 3.83$ .

In Figure 11.4 we have examined models A, C and E of the Table 11.1. Figure 11.4, shows that  $q$  and  $\beta_c$  both have significant effects on the structure of the Thick disc model. In fact, magnetic pressure does not touch the overall shape of the disc and its radial expansion strongly. However, further analysis shows a slight change occurs in the range of isodensity contours. This is compatible with increasing density toward the inner part of the disc.

On the other hand, the role of  $q$  is more substantial on the shape of the

disc and its place. In fact, as the value of  $q$  increases, the disc has more radially extended and shifted away from the central object. This is also well matched with the result of Figures 11.2 and 11.3.

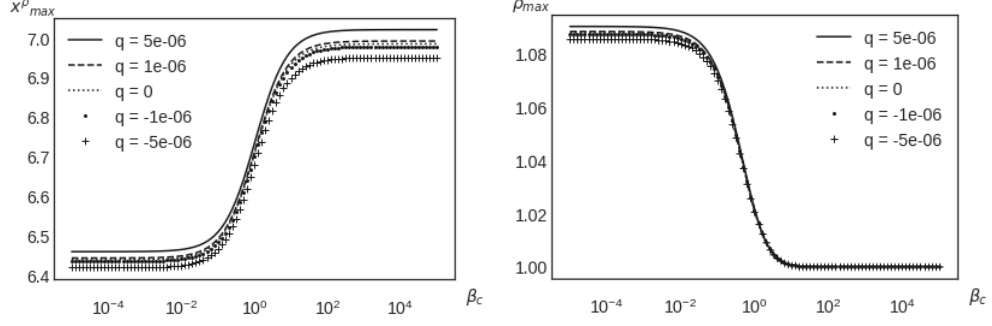
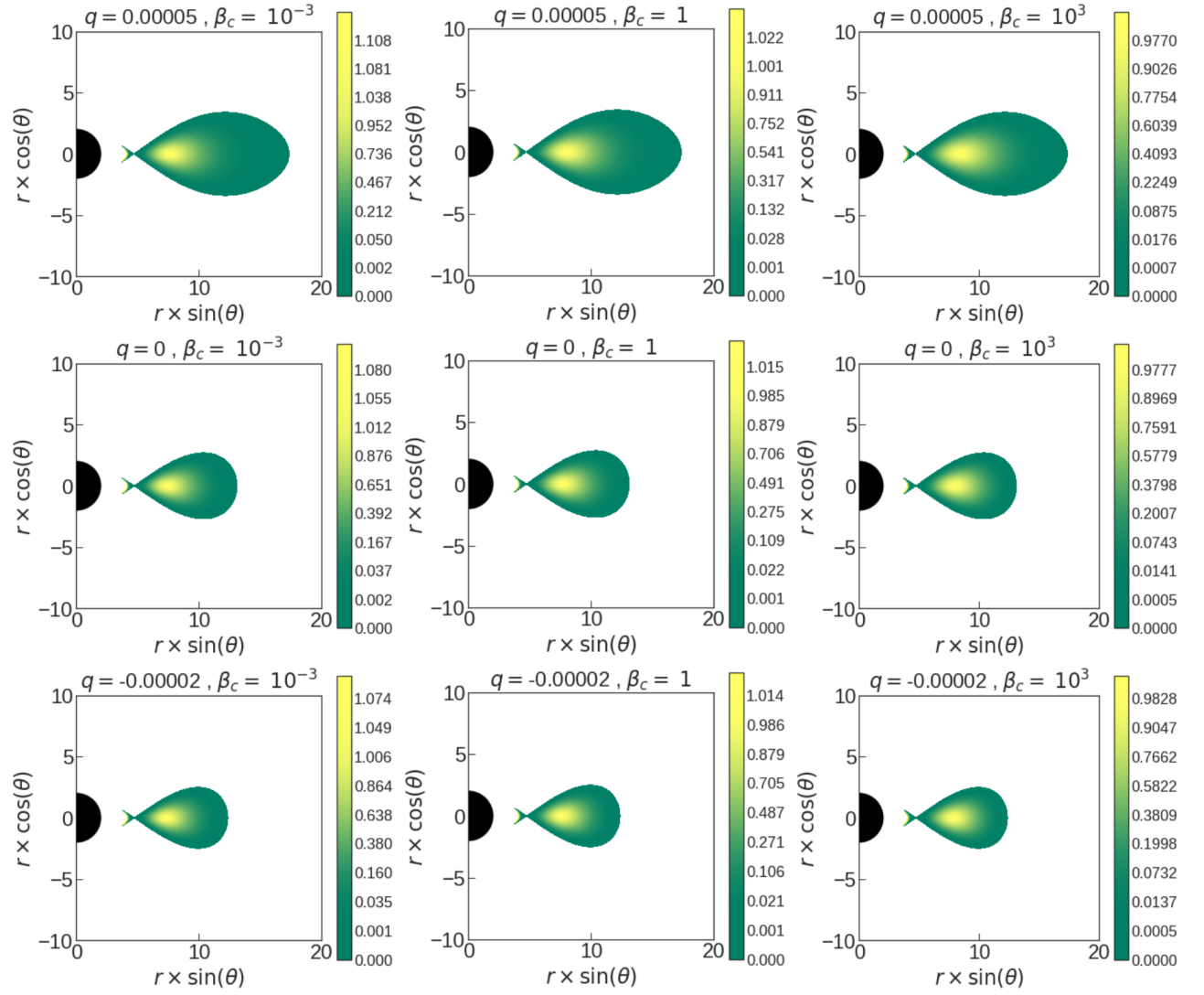


**Figure 11.3:** Amplitude and location of the rest-mass density maximum over  $\beta_c$ , and the five values of  $q$  described in Table 11.1. This is plotted for  $\ell(x, y) = \ell_0 = 3.83$ .

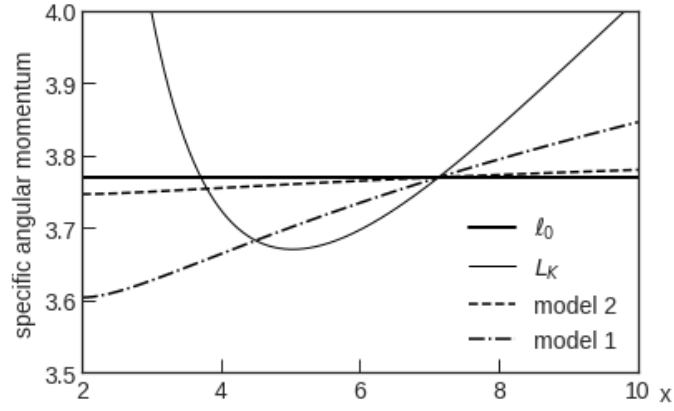
Case	$q$	$x_{\text{in}}$	$x_c$	$x_{\text{max}}^{\text{P}}$	$x_{\text{max}}^{\text{P}_m}$	$\beta_c$
B <sub>1</sub>	0.000001	3.719	6.991	6.439	6.569	$10^{-3}$
B <sub>2</sub>	0.000001	3.719	6.991	6.710	6.849	1
B <sub>3</sub>	0.000001	3.719	6.991	6.990	7.139	$10^3$
B <sub>1</sub>	0.0000001	3.720	6.985	6.440	6.570	$10^{-3}$
B <sub>2</sub>	0.0000001	3.720	6.985	6.700	6.840	1
B <sub>3</sub>	0.0000001	3.720	6.985	6.980	7.130	$10^3$
C <sub>1</sub>	0	3.720	6.984	6.440	6.570	$10^{-3}$
C <sub>2</sub>	0	3.720	6.984	6.700	6.840	1
C <sub>3</sub>	0	3.720	6.984	6.980	7.130	$10^3$
D <sub>1</sub>	-0.0000001	3.720	6.983	6.440	6.570	$10^{-3}$
D <sub>2</sub>	-0.0000001	3.720	6.983	6.700	6.840	1
D <sub>3</sub>	-0.0000001	3.720	6.983	6.980	7.130	$10^3$
D <sub>1</sub>	-0.000001	3.721	6.977	6.430	6.560	$10^{-3}$
D <sub>2</sub>	-0.000001	3.721	6.977	6.700	6.830	1
D <sub>3</sub>	-0.000001	3.721	6.977	6.970	7.120	$10^3$

Table 11.1: Parameters of the considered solutions for a constant specific angular momentum  $\ell_0 = 3.77$ .





**Figure 11.4:** The rest-mass density distribution for constant angular momentum. The models A, C and E of the Table 11.1 are presented in rows. The index 1, 2 and 3 of each model correspond to each column from left to right.



**Figure 11.5:** The models 1, 2 are radial profiles of the specific angular momentum in the equatorial plane with different slopes. The constant specific angular momentum is shown with a thick straight line, which is chosen to be  $\ell(x, y) = \ell_0 = 3.83$ . This profile corresponds to  $q = 0.00002$ .

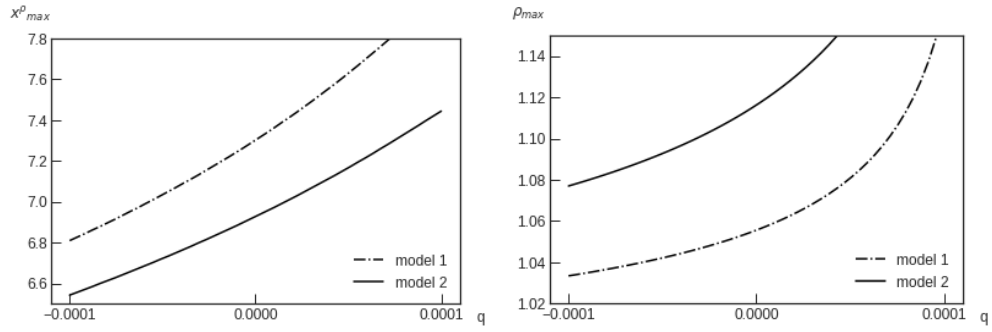


**Figure 11.6:** Amplitude and location of the rest-mass density maximum over  $q$ . The different curves represent different distributions of specific angular momentum depicted in the Figure 11.5.

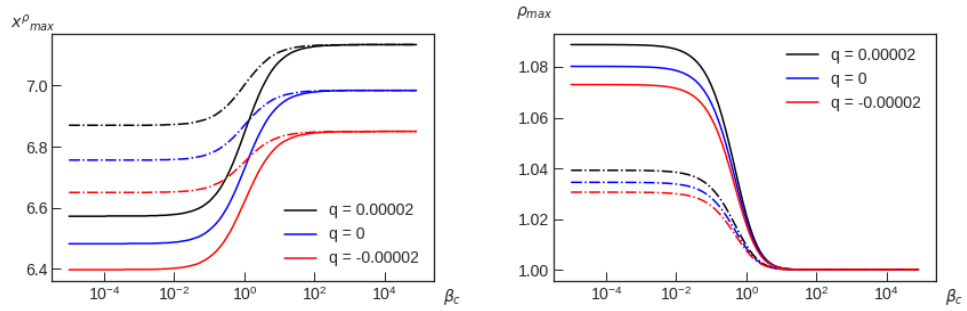


**Figure 11.7:** Amplitude and location of the rest-mass density maximum as a function of  $\beta_c$ . The solid lines correspond to the model 2 and the dot-dashed lines present the model 1.

### 11.1.2 Discussion on the power-law distribution

In this section, we discuss different profiles of  $\ell(x, y)$  following the method described in [53] which is described in Subsection 2.2.2. This method requires choosing a fixed specific angular momentum  $\ell_0$  to fix the centre  $x_c$  and cusp  $x_{\text{cusp}}$ . This procedure proceeds as follows. We keep  $x_c$  fixed and set a new cusp point called  $x'_{\text{cusp}}$ , choosing between  $x_{\text{cusp}}$  and  $x_{\text{ms}}$ . The slope of each profile then depends on the chosen value for  $x'_{\text{cusp}}$ . Therefore, we chose two different values to get two  $\ell(x, y)$  distributions denoted by a numeral index 1 and 2. In Figure 11.5, the profile of the specific angular momentum distribution is plotted for  $q = 0.00002$ .

In addition, as in the previous case,  $x_{\text{cusp}}$  and  $x_c$  vary with quadrupole's value, then it is expected the slope changes also with  $q$ .

In Figures 11.6 and 11.7, we turned on the magnetic field, and we studied the effect of magnetic pressure combines with different distributions of angular momentum presented in Figure 11.5. In Figure 11.6 a global view of the variation of the location and amplitude of the maximum rest-mass density over  $q$  is plotted. In addition, Figure 11.7 shows the maximum rest-mass density profile and its value in the equatorial plane over magnetization parameter for different values of quadrupole and two models. For  $\beta_c$  and  $q$ , the same behaviour as the constant case applies, so we expect the more radially extended disc structure for higher values of  $q$ . Increasing in  $\beta_c$  decreases the rest-mass density maximum and places its location farther away. In addition, an increase in  $q$  has the same impact as  $\beta_c$  on the rest-mass maximum and its location. Besides, these Figures suggest the effect of  $q$  is more intense for model 1, which has a steeper slope, while the impact of  $\beta_c$  is stronger on model 2, which is closer to the Keplerian one. In fact, a further inspection reveals that when  $q$  is higher, the influence of changing in  $\beta_c$  is also greater for all models.

In Figures 11.8 and 11.9 the rest-mass density distribution profiles are explored for a different combination of parameters to clearly see the effect of changing them [213]. Figure 11.8 presents the results for the angular momentum distribution model 2, and for the cases  $G_2$ ,  $H_2$ , and  $J_2$  in Tables 11.2 and 11.3. As we expected from the constant angular momentum case in the previous subsection 11.1.1, magnetic pressure causes the rest of mass density to increase in the inner part of the disc regardless of the type distribution of angular momentum, as also seen in Figure 11.9. Furthermore, the overall shape of the disc depends on the choice of  $q$ . Especially the disc is more radially extended for positive values of  $q$ . Besides, further analysis shows for positive values of  $q$ ; the disc has more balloon shape than negative values.

Figure 11.9 presents the results for the angular momentum distribution

Case	q	$x_{\text{in}}$	$x_{\text{c}}$	$x_{\text{max}}^{\text{P}}$	$x_{\text{max}}^{\text{P}_m}$
F <sub>1</sub>	0.000050	4.5	7.206	7.360	7.469
F <sub>2</sub>	0.000050	3.8	7.206	6.957	7.147
G <sub>1</sub>	0.000020	4.5	7.241	7.162	7.249
G <sub>2</sub>	0.000020	3.8	7.241	6.810	6.971
H <sub>1</sub>	0	4.5	7.353	7.044	7.120
H <sub>2</sub>	0	3.8	7.353	6.719	6.866
I <sub>1</sub>	-0.000015	4.5	7.519	6.961	7.030
I <sub>2</sub>	-0.000015	3.8	7.519	6.655	6.792
J <sub>1</sub>	-0.000020	4.5	7.817	6.934	7.001
J <sub>2</sub>	-0.000020	3.8	7.817	6.634	6.768

Table 11.2: Parameters of the considered solutions for power-law angular momentum distribution. The alphabetical enumeration of the models  $F, G, H, I$  and  $J$  refers to the different values of  $q$  given in Table 11.2. The indexes in each model refer to the different specific angular momentum distributions in Figure 11.5. All the models have  $\beta_c = 10^{-3}$ .

Case	q	$x_{\text{in}}$	$x_{\text{c}}$	$x_{\text{max}}^{\text{P}}$	$x_{\text{max}}^{\text{P}_m}$
F <sub>1</sub>	0.000050	4.5	7.817	7.816	7.939
F <sub>2</sub>	0.000050	3.8	7.817	7.816	8.076
G <sub>1</sub>	0.000020	4.5	7.519	7.518	7.611
G <sub>2</sub>	0.000020	3.8	7.519	7.518	7.720
H <sub>1</sub>	0	4.5	7.353	7.353	7.431
H <sub>2</sub>	0	3.8	7.353	7.352	7.528
I <sub>1</sub>	-0.000015	4.5	7.241	7.241	7.311
I <sub>2</sub>	-0.000015	3.8	7.241	7.240	7.400
J <sub>1</sub>	-0.000020	4.5	7.206	7.205	7.274
J <sub>2</sub>	-0.000020	3.8	7.206	7.205	7.360

Table 11.3: The same cases as table 11.2 for  $\beta_c = 10^3$ .

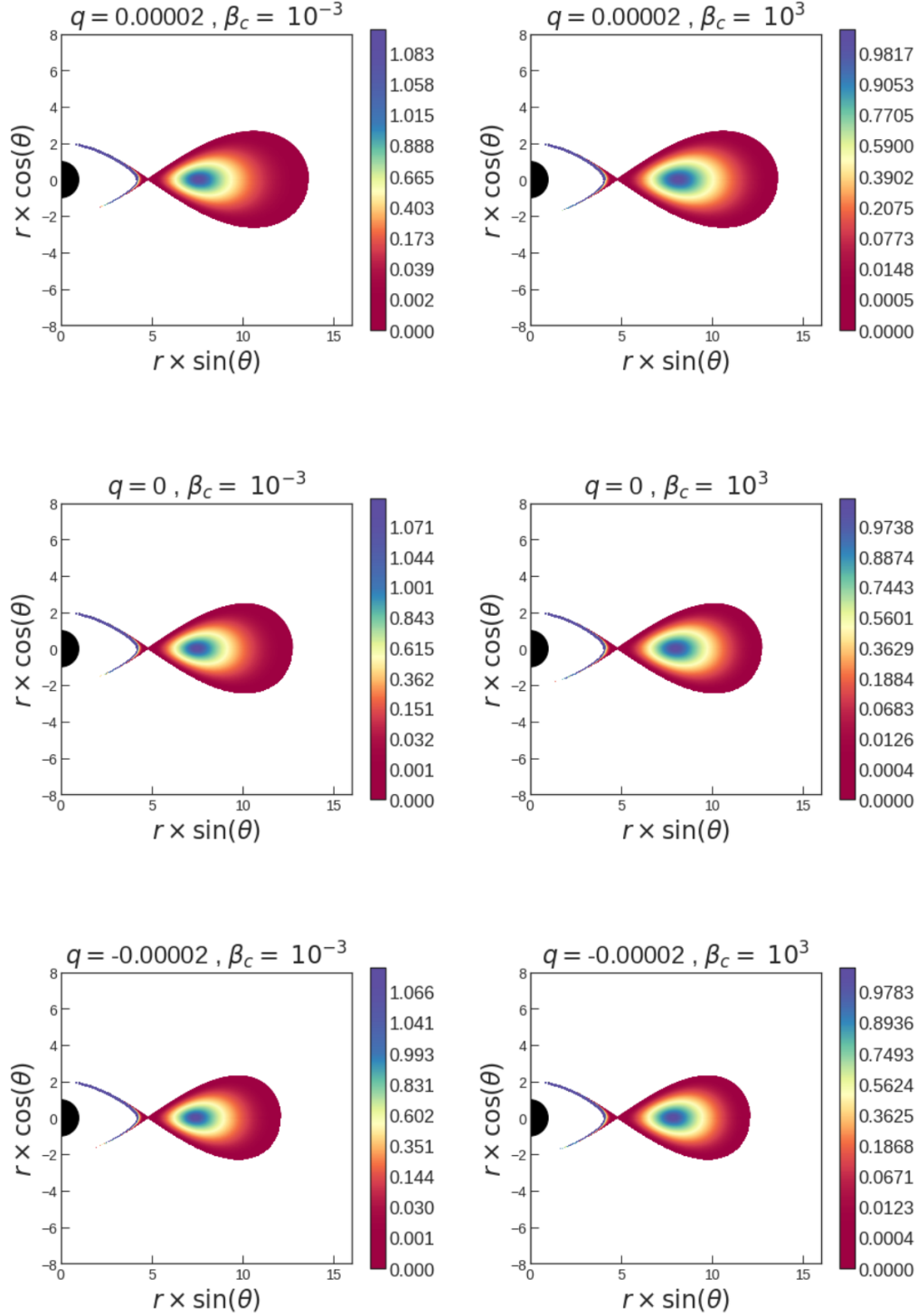


**Figure 11.8:** Map of the rest-mass density distribution for the angular momentum model 2 as described in the Figure 11.5. Each row corresponds to different values of  $q$ , and each column shows different value of  $\beta_c$ .

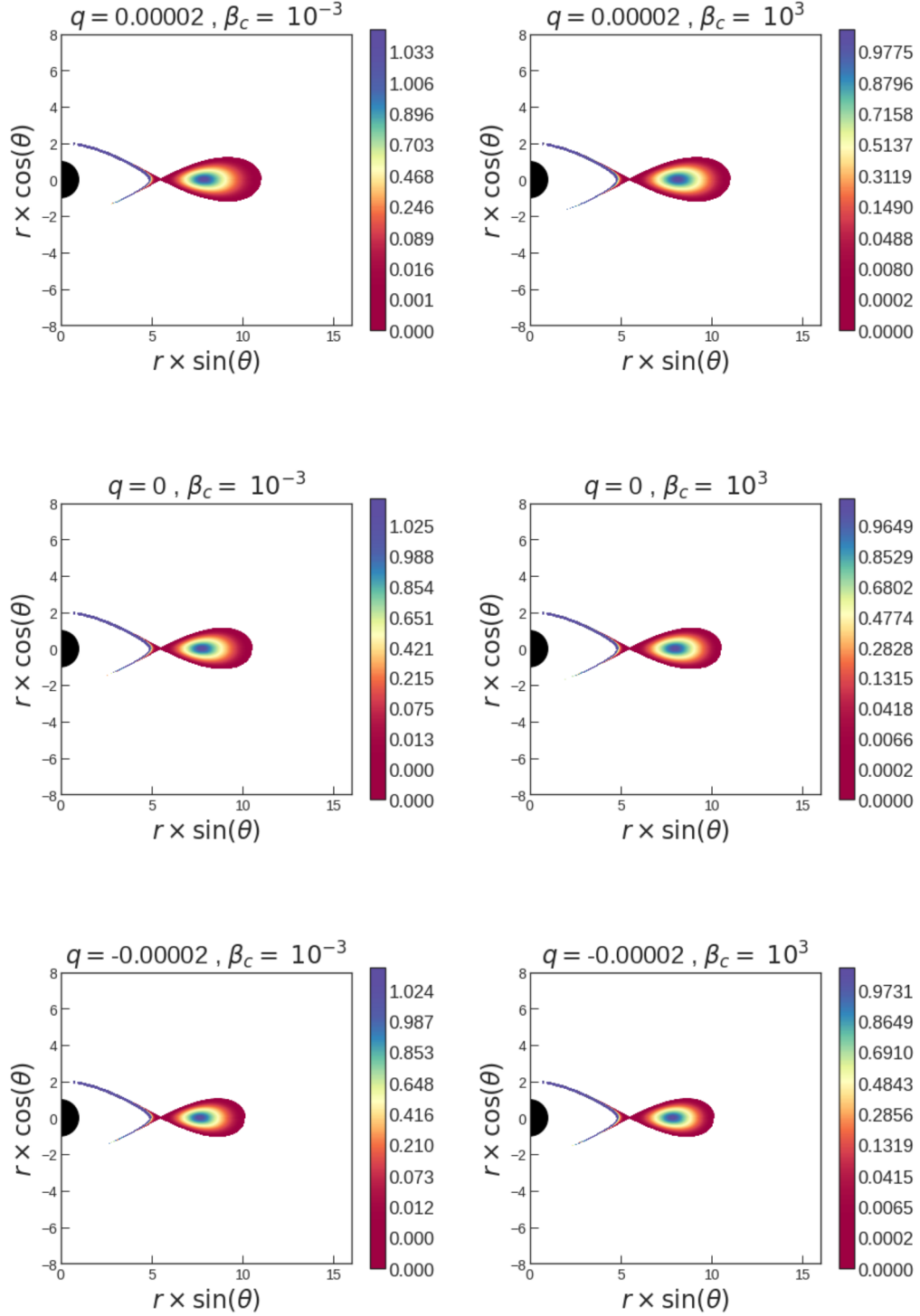


**Figure 11.9:** Map of the rest-mass density distribution for the more steeper angular momentum model 1, as described in the Figure 11.5. Each row corresponds to different values of  $q$ , and each column shows different value of  $\beta_c$ .

model 1, and for the cases  $G_1$ ,  $H_1$ , and  $J_1$  in Tables 11.2 and 11.3. In Figure 11.9 we have the same patterns as in Figure 11.8. However, for the distribution of model 1, we obtain a smaller disc structure in both vertical and radial directions. Since as we have seen in Figure 11.5 the place of  $x_c$  and  $x_{\text{cusp}}$  are closer to each other. In addition, comparing these Figures shows the smallest disc is obtained when the steepest distribution is combined with the largest quadrupole moment. Besides, we can see in each case, as the slope of specific angular momentum becomes steeper, the matter accumulates more in the inner part. Thus steeper the slope, the more centrally the matter distributes. This pattern also reminds the role of the magnetization parameter.

### 11.1.3 Discussion on the trigonometric distribution

In this section, we discuss different profiles of  $\ell(x, y)$  following the method developed in [57] which is described in Subsection 2.2.2. In Figures 11.10 and 11.11, we have discussed the rest-mass density maximum and its place for different angular momentum profiles,  $q$  and  $\beta_c$ . Like previous cases, increasing  $q$  causes an increase in rest-mass density maximum and its location. However, as  $\alpha$  becomes higher for a fixed value of  $q$  and the curve deviates from the constant angular momentum distribution, the intensity in density maximum reduces, and the matter spreads more through the disc. Also, Figure 11.11 shows the sensitivity of each model on  $\beta_c$ . Also, in this case,  $\beta_c$  has a stronger effect on the disc which its angular momentum distribution is closer to the constant one. And as the matter becomes more distributed through the disc caused by a higher value of  $\alpha$ , magnetic pressure also has a weaker effect on the disc.

In Figure 11.12 and 11.13 the panels of rest-mass density distributions presented. The parameters are listed in Tables 11.4 and 11.5. In Figure 11.12 the goal is to study the effect of parameter  $\beta_c$ , and in the first column, we have relatively strong magnetic pressure compare to the second one. However, the model parameters are the same to distinguish the effect of magnetic pressure clearly. Also,  $q$  is set to be fixed. As mentioned before,  $\beta_c$  influences the distribution of mater inside the disc and not on the shape of the disc, in general. However, parameters  $\alpha$  and  $\delta$  have influenced the disc structure strongly. In fact, these two parameters are highly correlated to each other. However, further analysis shows that for a fixed  $\alpha$ , an increase in  $\sigma$  causes the disc becomes thinner, the same for a fixed value of  $\delta$ .

Figure 11.13 explores the effects of different parameters, particularly  $q$ , on the panel of rest-mass density in the presence of relatively strong magnetic pressure. Comparison of columns shows the effect of different values of  $q$  on the models. The parameter  $q$  is responsible for the radial extension of

$\alpha$	$\delta$	q	$x_c$	$x_{\max}^P$	$x_{\max}^{P_m}$
0	0.9	0.00002	9.191	6.663	7.230
0.5	0.5	0.00002	9.191	7.077	7.660
0.5	0.9	0.00002	9.191	7.078	7.662
0	0.9	0	9.476	6.692	7.352
0.5	0.5	0	9.476	7.128	7.746
0.5	0.9	0	9.476	7.130	7.746
0	0.9	-0.00002	9.814	6.751	7.446
0.5	0.5	-0.00002	9.814	7.210	7.858
0.5	0.9	-0.00002	9.814	7.210	7.858

Table 11.4: Parameters of the considered models for non-constant trigonometric specific angular momentum. All the models have  $\beta_c = 10^{-3}$ .

$\alpha$	$\delta$	q	$x_c$	$x_{\max}^P$	$x_{\max}^{P_m}$
0	0.9	0.00002	9.191	9.191	10.017
0.5	0.5	0.00002	9.191	9.190	10.016
0.5	0.9	0.00002	9.191	9.190	9.864
0	0.9	0	9.476	9.476	10.346
0.5	0.5	0	9.476	9.475	10.305
0.5	0.9	0	9.476	9.476	10.209
0	0.9	-0.00002	9.814	9.814	10.722
0.5	0.5	-0.00002	9.814	9.814	11.000
0.5	0.9	-0.00002	9.814	9.814	10.701

Table 11.5: The same cases as Table 11.4 for  $\beta_c = 10^3$ .

the disc as it becomes higher. In addition, a deeper analysis shows q is also responsible for a shift in the radial direction of the disc. In the sense that as the values of q increase, the disc shifts in the outward direction. However, as the values of quadrupole parameters that we chose in our models are minimal, this is not easy to see from the panels. This is also coherent with the shift in the place of the rest-mass density maximum as q increases.

#### 11.1.4 Summary and conclusion

In this section, we investigated the equilibrium sequences of magnetized, non-self-gravitating discs around distorted Schwarzschild black holes 6.2.

We have analyzed these models' properties and their dependency on the magnetization parameter  $\beta_c$ , the quadrupole parameter related to the exter-



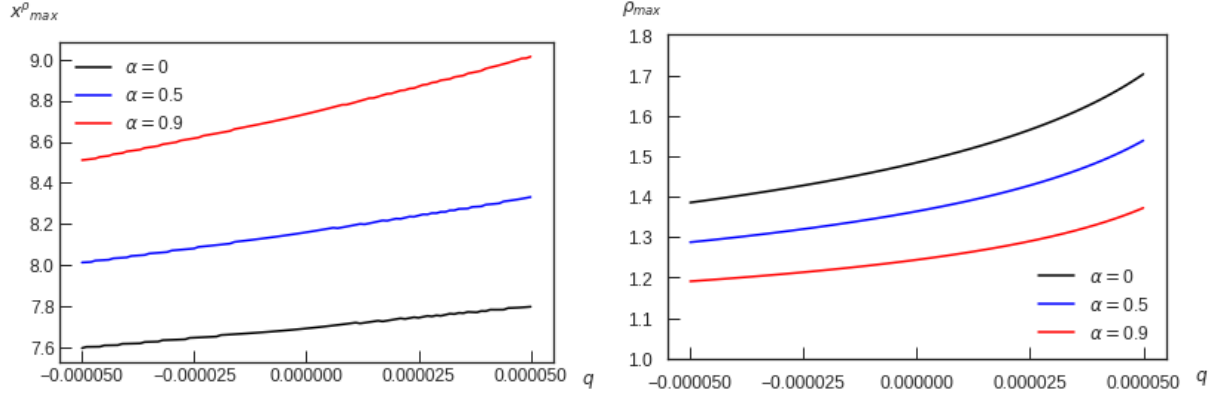


**Figure 11.10:** Amplitude and location of the rest-mass density maximum as a function of  $q$ . The different curves represent different distributions of specific angular momentum.

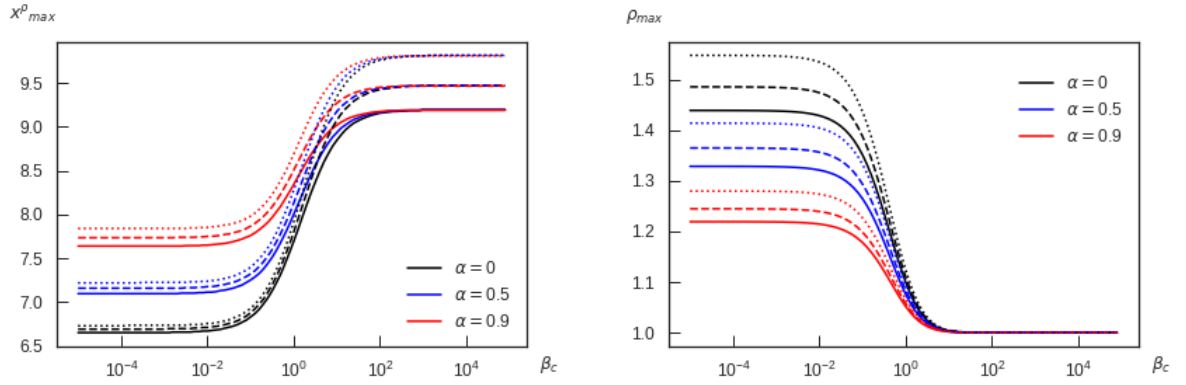


**Figure 11.11:** Amplitude and location of the rest-mass density maximum as a function of  $\beta_c$ , and for different angular momentum profiles. The solid lines correspond to  $q = -0.00002$ . The Schwarzschild case is shown in dashed line. Also,  $q = 0.00002$  is represented in dotted line.

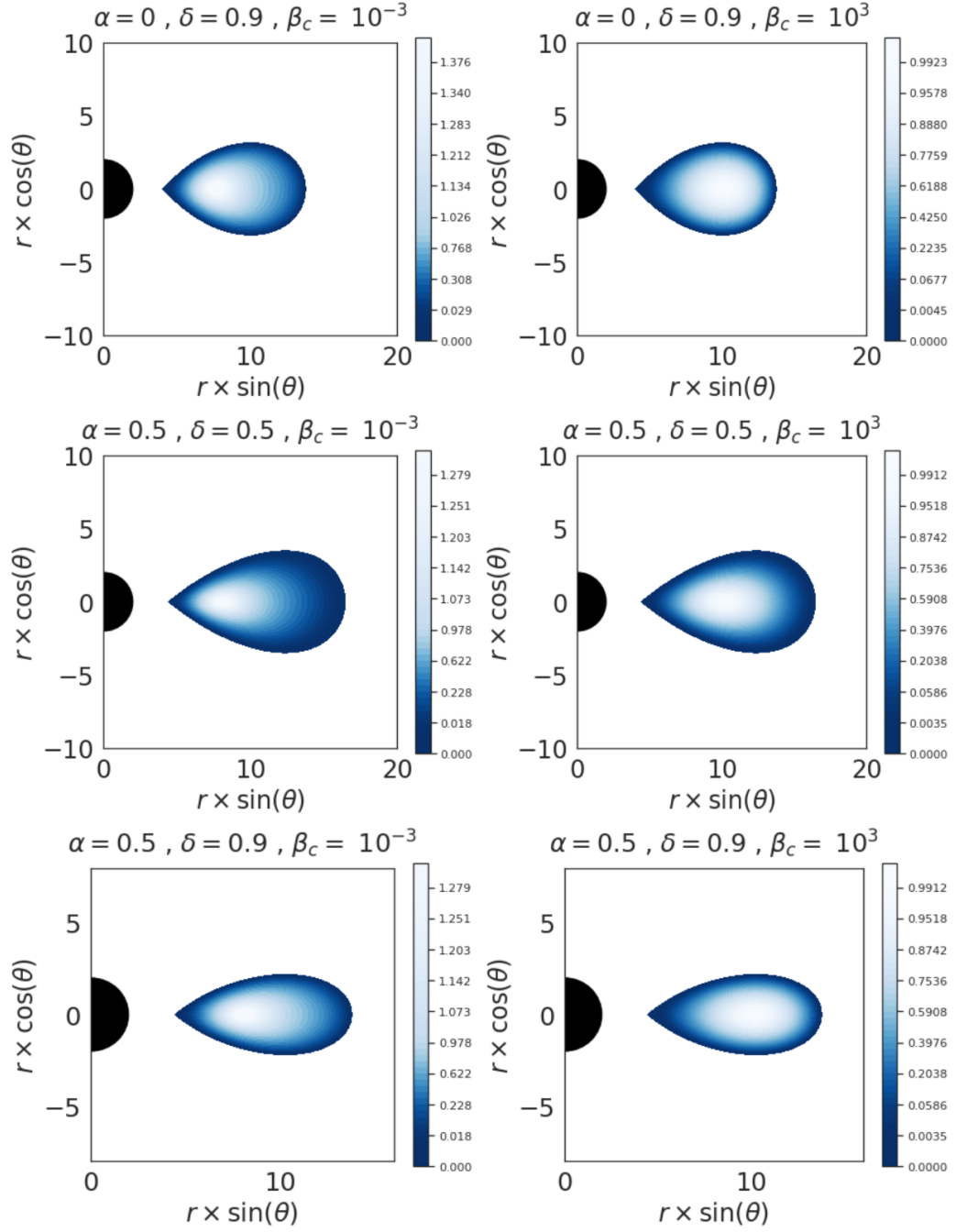


**Figure 11.12:** Effect of the magnetized parameter  $q$  on the rest-mass density distribution. The deformation parameter is fixed to be  $q = -0.00002$ .

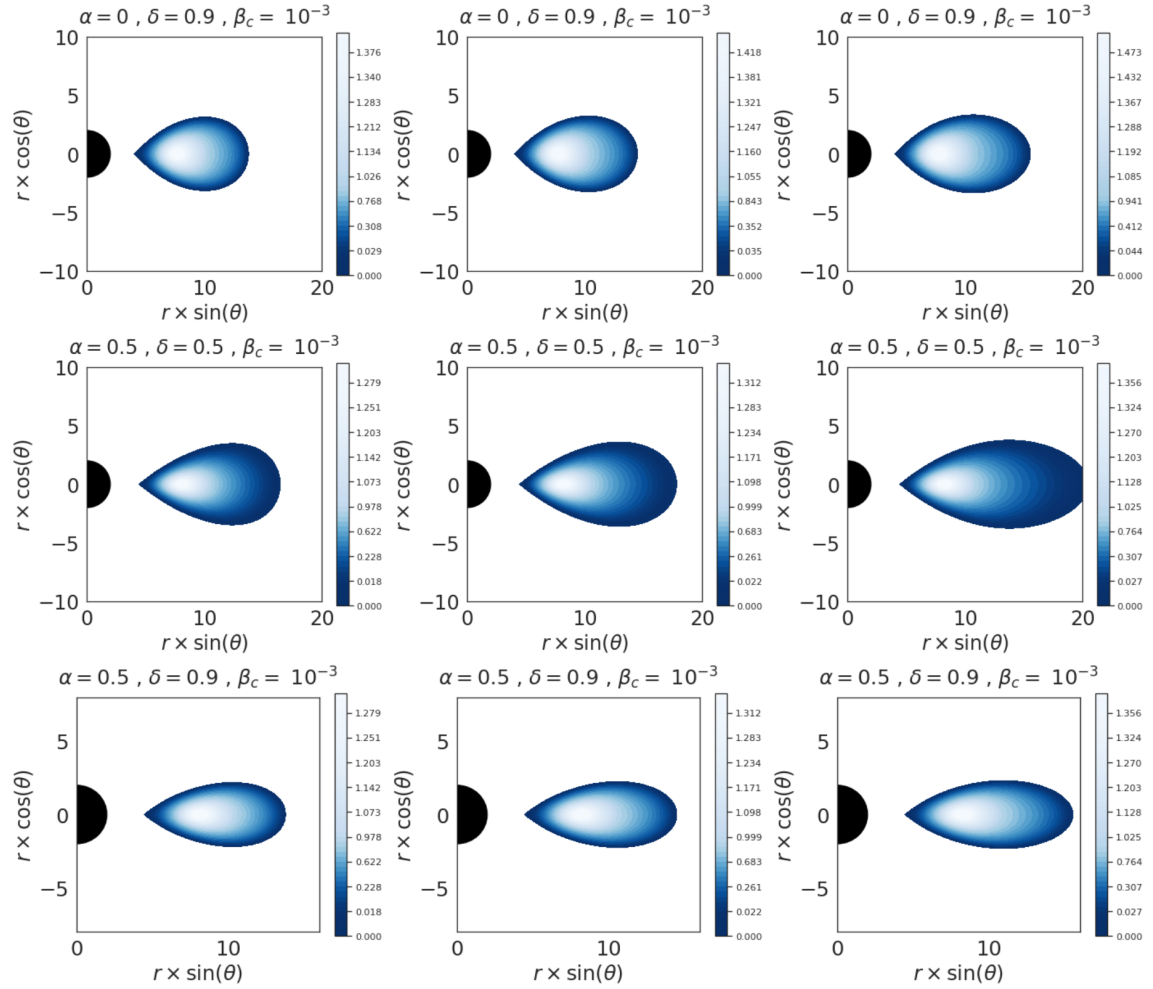


**Figure 11.13:** Effect of the distortion parameter  $q$  on the rest-mass density distribution. The first column is dedicated to  $q = -0.00002$ . The middle column represents the Schwarzschild case  $q = 0$ . The last column shows  $q = 0.00002$ . The magnetization parameter is fixed to be  $\beta_c = 10^{-3}$ .

nal source, and the angular momentum distributions. As a result, the effects of changing parameter  $\beta_c$ , in general, does not change the disc's overall configuration in both constant and non-constant angular momentum distributions. However, the strongest effect of  $\beta_c$  was seen on the rest-mass density in the disc's inner part. Furthermore, a slight change occurs in the range of isodensity contours, which is also compatible with increasing density toward the disc's inner part.

In the one hand, the effect of varying quadrupole moments has changed the disc's geometry and overall shape. In addition, this changes the location of maximum rest-mass density and its value which is compatible with our understanding of the way that external matter manifest their existence. We also traced the fingerprint of different angular momentum distributions on the shape the size of the disc, and the rest-mass density profile.

On the other hand, in the distribution in the power-low form, we obtain the smallest disc is obtained when the steepest distribution is combined with the largest quadrupole moment. Besides, as the slope of specific angular momentum becomes steeper, the matter accumulates more in the inner part. Thus steeper the slope, the more centrally the matter distributes. This pattern also reminds the role of the magnetization parameter. For the triangular distribution like the previous case, increasing  $q$  causes an increase in rest-mass density maximum and its location. However, as  $\alpha$  becomes higher for a fixed value of  $q$  and the curve deviates from the constant angular momentum distribution, the intensity in density maximum reduces, and the matter spreads more through the disc.

Further, the results also compared with the ordinary Schwarzschild solution. It has shown that the results are in good agreement with the mentioned literature. The result of this study presented in [213].

## 11.2 Magnetized Thick disc in Static $q$ -metric

In this Section, we study the magnetized version of the Thick disc model 2.2 in the background of  $q$ -metric (6.18). Here the plots are presented in the  $(x, y)$  coordinates. In this section, letter  $q$  present the quadrupole in the metric.

One of the determinant factors in this model is the condition on the existence of the closed equipotential surfaces, which is the case for having the angular momentum distribution in this range:  $\ell_{ms} < \ell \leq \ell_{mb}$  2.2. In this respect, Figure 11.14 gives us an insight on how the specific angular momentum at the marginally bound orbit  $\ell_{mb}$  and at the marginally stable orbit  $\ell_{ms}$ , behaves as a function of the deformation parameter  $q$  in static

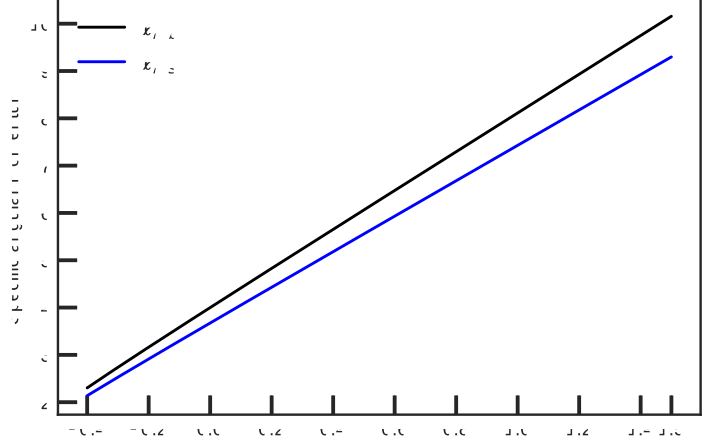


**Figure 11.14:** Variation of  $\ell_{\text{mb}}$  and  $\ell_{\text{ms}}$  as a function of  $q$ , which determines the corresponding area for existence of closed equipotential surfaces.

$q$ -metric. In particular, Figure 11.14 shows that by increasing  $q$ , the area where equipotential surfaces can exist, increases.

### 11.2.1 Discussion on the power-law angular momentum

In this subsection the results are of considering the angular momentum distribution introduced in [53] and briefly described in Section 2.2.2. In this work the construction of the angular momentum profile consists of two steps. First, choosing a fixed  $\ell_0$  specific angular momentum, that fixes the position of the cusp and the centre of the disc. However, as it has shown in Figure 11.14, it is challenging to set a fixed value for  $\ell$ . We have chosen  $\ell_0 = \ell_{\text{mb}}$  for all models. Second, creating a new point called  $x'_{\text{cusp}}$  settled between  $x_{\text{cusp}}$  and  $x_{\text{ms}}$ , as shown in the Figure 11.15. By using this approach, one can build a power-law specific angular momentum distribution. As an example,  $\ell$ -profile in the equatorial plane is given for  $q = 0.8$  in Figure 11.15.

In this work, three different angular momentum profiles built via choosing three different values of  $x'_{\text{cusp}}$ . The profiles are presented via numbers 1, 2 and 3 in Figure 11.15 and they are named by model 1, 2 and 3. Besides, the constant angular momentum distribution  $\ell_0 = \ell_{\text{mb}}$  is also presented for the sake of comparison. In fact, the value of  $x_{\text{cusp}}$ ,  $x'_{\text{cusp}}$  and  $x_c$  depend on  $q$ . As a result, the slope of the three models depends on  $q$  as well. For all the plots in within this angular momentum, the solid line represents the constant angular momentum case, the dashed line the model 3, the dotted line the

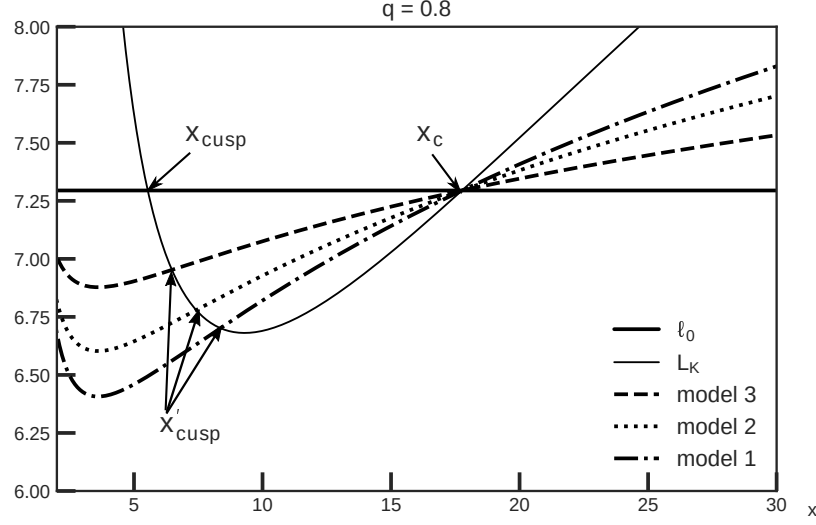


**Figure 11.15:** The curves 1, 2 and 3 are profiles of the specific angular momentum in the equatorial plane with different slopes. The constant specific angular momentum is shown with the solid straight line which is chosen to be  $\ell(x, y) = \ell_0 = \ell_{mb}(q)$ . This profile corresponds to  $q = 0.8$ .

model 2, and the model 1 is represented by the dot-dashed line.

In Figure 11.16 top panels, the location and the amplitude of the rest-mass density maximum as a function of the magnetization parameter have been represented. The bottom panels depicted the location and amplitude of the maximum of the magnetic pressure as a function of the magnetization parameter for the mentioned parameters. As we have different parameters that result depend on, we need to fix other parameters simultaneously to study the effect of one variable precisely.

In fact, for any fixed value of  $q$  and steepness of angular momentum profile, the location of the rest-mass density maximum by decreasing the value of  $\beta_c$  -increasing the magnetic pressure- has been shifted inward. Additionally, when  $\beta_c$  is low, the equidensity surfaces are not coinciding anymore with the equipotential surfaces. Besides, decreasing  $\beta_c$  increases the maximum of the rest-mass density. This causes to push the matter closer to the central object. Thus, the matter concentrates more on the inner part of the disc for any quadrupole value. This effect is coherent with the results in the previous figures and proceeding studies [52, 212]. This pattern repeats for all the profiles of angular momentum distributions. In general, the magnetization parameter has a major effect on how the matter is distributed in the disc compared to its effect on the geometrical structure of the disc that is more clearly seen in Figures 11.19 and 11.20.

For the maximum of the magnetic pressure, we see that for a fixed value of  $q$ , the trend of the curves for the location and the amplitude is following the same path as for the maximum of the rest-mass density. The only difference comes from the fact that the constant value reached by the pressure maximum's location depends on the angular momentum profile. It is worth mentioning that for the four models (constant, profile 1, 2, and 3), the location of the magnetic pressure maximum intersect. This happens at  $x_{max} = x_c$ . Therefore, it does not depend on the angular momentum profile. In fact, this result has been also predicted in [212] for the trigonometric angular momentum profile presented in the next subsection.

An investigation on the different angular momentum profiles shows that the steeper the slope of the profile, the farther is the maximum of the rest-mass density from the central object. In fact, the higher steepness means that we have higher angular momentum at a given fixed place, as expected, leading to lower pressure. Then this is not a surprise that by using a steeper angular momentum profile, one obtains the maximum of the rest-mass density farther away from the central object; while, having a decline in the maximum value of the density. This results in obtaining different shapes and sizes of the disc, which we see in the following Figures. This result is coherent with the fact that the steeper the profile, the closer  $x_{cusp}$  and  $x_c$  to each other, as it has been seen clearly in the Figure 11.15. Further analysis reveal that as the steepness of the angular momentum profile increases, the place of pressure's maximum becomes closer to the center of the disc rather than the cusp point. This is also a reasoned result since as the steepness increase, the distance between  $x_{cusp}$  and  $x_c$  decreases; simultaneously, the place of density's maximum shifted to the outer part of the disc. So, this should become closer to the center of the disc.

Besides, an inspection on the impact of the parameter of geometry, deformation parameter  $q$ , on the disc structure indicates that, the negative values of  $q$  cause the place of the maximum of rest-mass density move inward and its value higher and vice versa for positive values. So, one can conclude that increasing  $q$  tends to make the disc shape thinner and more extended. It is reasonable to think that a prolate shape will enlarge the disc in the vertical direction closer to the inner edge. Also, an oblate form tend to flatten the disc on the equatorial plane. In summary, the effects of steepness and positivity of quadrupole parameters are aligned and opposite to the negativity of quadrupole values and  $\beta_c$ . To have a better insight on how the deformation parameter  $q$  affects the disc structure, the location of the maximum of the rest-mass density (black lines) and the one of the maximum of the magnetic pressure (blue lines) for all models and a fixed chosen value of  $\beta_c$  are shown in Figure 11.16. The corresponding amplitudes are shown in Figure 11.18,

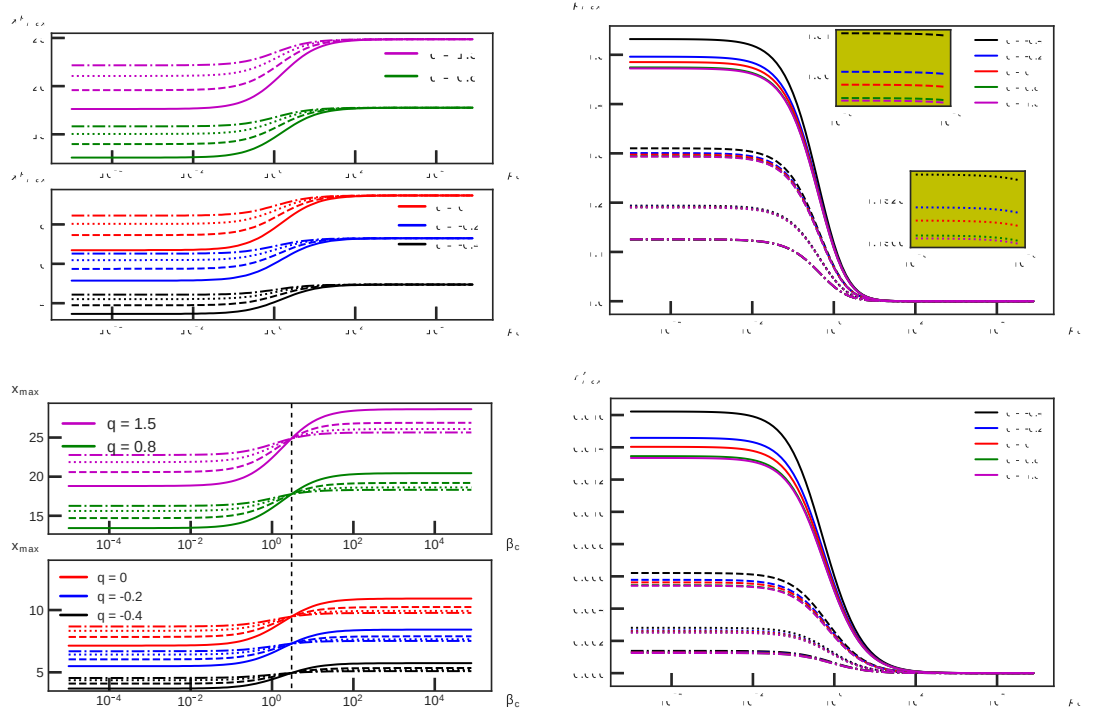


**Figure 11.16:** Top panels: Variation of the location and amplitude of the rest-mass density maximum in the equatorial plane as a function of  $\beta_c$ , for distribution profiles described in Figure 11.15. Bottom panels: Same description for the magnetic pressure maximum.

at the left for the maximum of the rest-mass density and at the right for the maximum of the pressure maximum. The Figure 11.17 also confirms the results obtained in the Figure 11.16.

Figures 11.19 and 11.20 show the general structure of the disc. In Figure 11.19 we have investigated the impact of the deformation parameter  $q$  and the effect of different slopes of angular momentum profiles for a fixed value of  $\beta_c$  which corresponds to a stronger magnetic pressure in the models. As seen, the deformation parameter has a minor effect on the overall shape of the disc. In fact, this is more relevant for the radial extension.

Figure 11.20 shows how the rest-mass density distribution is changing with the magnetization parameter and with the steepness of the angular momentum profile for a fixed negative value of  $q = -0.4$ . We note that the total pressure distribution follows the same behavior on all the panels as the rest-mass density. The main point here is that, as expected, by increasing  $\beta_c$ , the maximum of the rest-mass density tends to coincide with the maximum of the total pressure. Besides, as expected from the analysis of the Figure



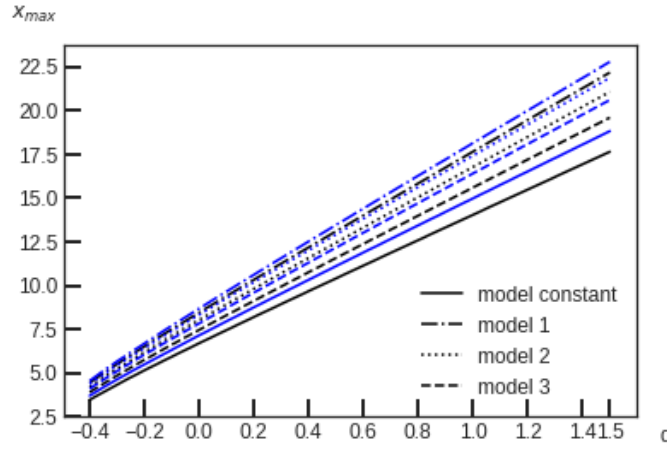


**Figure 11.17:** Variation of the location of the rest-mass density maximum (black lines), and the magnetic pressure maximum (blue lines), in the equatorial plane as a function of  $q$ , for distribution profiles described in Figure 11.15. The magnetization parameter is set to be  $\beta_c = 10^{-3}$ .

11.16, the impact of  $\beta_c$  decreases on the disc structure by increasing the steepness of the angular momentum profile, as is seen by comparing all rows in a column.

### 11.2.2 Discussion of the trigonometric angular momentum

In this subsection we describe the results of considering the angular momentum distribution presented in [57] and described in Section 2.2.2. In this case, different angular momentum profiles are given by different combinations of the parameters. In fact, the angular momentum distribution is constructed in such a way that for all pairs of  $(\alpha, \delta)$ , the center of the torus places at the same location.

In Figure 11.21, we have discussed the location of the positions for  $x_{\text{cusp}}$  and  $x_c$  as a function of different profiles and different quadrupole values  $q$ . In fact, the dashed line  $x_c$  does not change by changing the profile; however, it is expected to vary with  $q$ . On the contrary,  $x_{\text{cusp}}$  is not fixed and changes with different profiles. Furthermore, both  $x_{\text{cusp}}$  and  $x_c$  are increasing functions of  $q$ . Thus, we expect that in the profiles for where the area between  $x_{\text{cusp}}$  and  $x_c$  shrinks, the size of the discs becomes smaller. Namely, for larger quadrupole values we have a more extended disc, where this result is coherent with the one given by the power-law angular momentum. In fact, in this case, the parameter  $q$  plays the opposite role of steepness in the power-law distribution in the sense that as it increases, the distance between  $x_{\text{cusp}}$  and

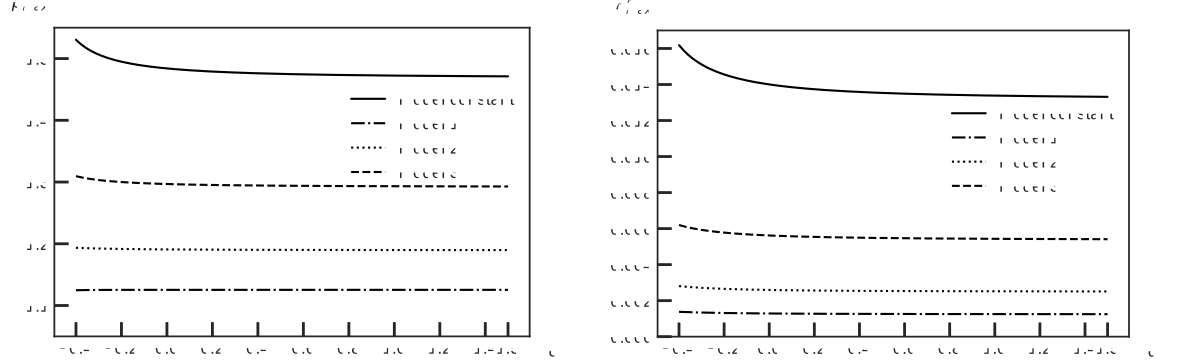


**Figure 11.18:** Variation of the amplitude of the rest-mass density maximum (left panel), and the magnetic pressure maximum (right panel), in the equatorial plane as a function of  $q$ , for distribution profiles described in Figure 11.15. The magnetization parameter is set to be  $\beta_c = 10^{-3}$ .

$x_c$  grows. Therefore, we expect that the density maximum shifted from the cusp point, as  $q$  increases. Besides, in Figure 11.21 for any fixed value of  $q$ , by increasing  $\alpha$ , the cusp point becomes closer to the disc center, and again the area between them shrinks, this may result in having a more shrinked disc structure for larger values of  $\alpha$ . However, one should keep in mind that in this profile,  $\delta$  also affects the disc structure, and one can not only predict the shape and properties of the disc by considering  $\alpha$  alone.

As shown in Figure 11.22, we have focused on three different angular momentum profiles. An investigation on the effect of  $\beta_c$  on the disc properties shows that, as the same as the previous model -the power-law angular momentum- for any fixed value of  $q$  and angular momentum profile, the location of the maximum moves inward by decreasing  $\beta_c$ , equivalently by increasing magnetic pressure; however, the strength of its effect in this case is different. Indeed, for any chosen value of  $q$ , the corresponding curves of different models coincide when  $\beta_c$  is very high. Again, when  $\beta_c$  is low, the equipotential surfaces are not coinciding with the equidensity surfaces. This effect is in agreement with the results of the previous studies [52, 212]. This is also coherent with the results found in the previous Figures. Furthermore, in this model, the location of the maximum is also an increasing function of the parameter  $\alpha$ , on the contrary to its value. One can see the effect of increasing the value of  $\alpha$  is aligned with an increase in the steepness of angular profile in power-law profile. And again the maximum of density is obtained for the constant case.

In fact, for small values of  $\beta_c$  the effect of changing the profile of angular momentum has the weaker effects on the displacement of maximum density

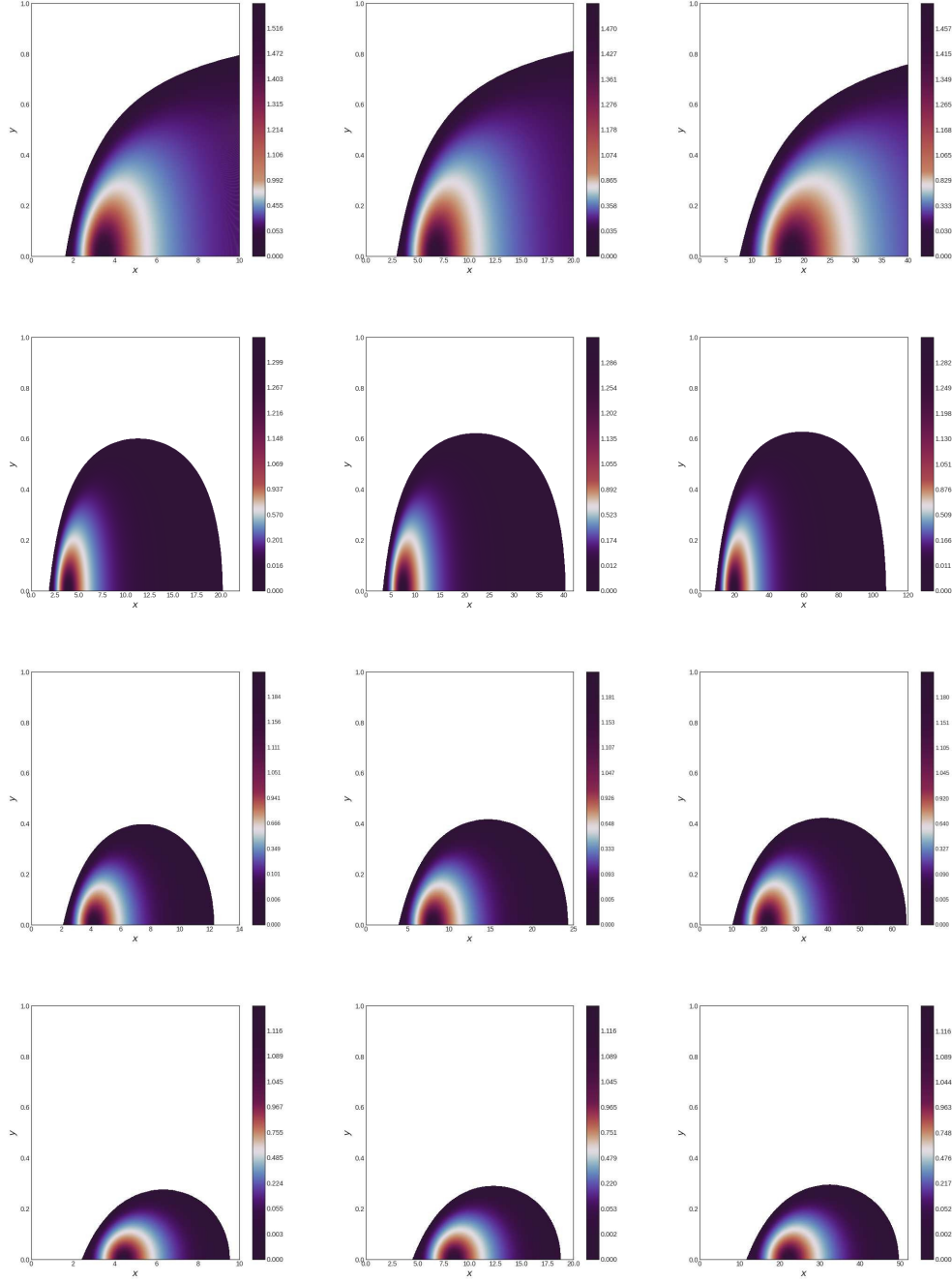


**Figure 11.19:** Map of the rest-mass density. From the left to the right the value of  $q$  varies. The column at the left shows  $q = -0.4$ , at the centre  $q = 0$  and, at the right represents  $q = 1.5$ . Also, rows correspond to different distributions of the specific angular momentum. First row shows the constant specific angular momentum, the second row model 3, the third row model 2, and the last one shows model 1. The magnetization parameter is set to be  $\beta_c = 10^{-3}$  in all maps.

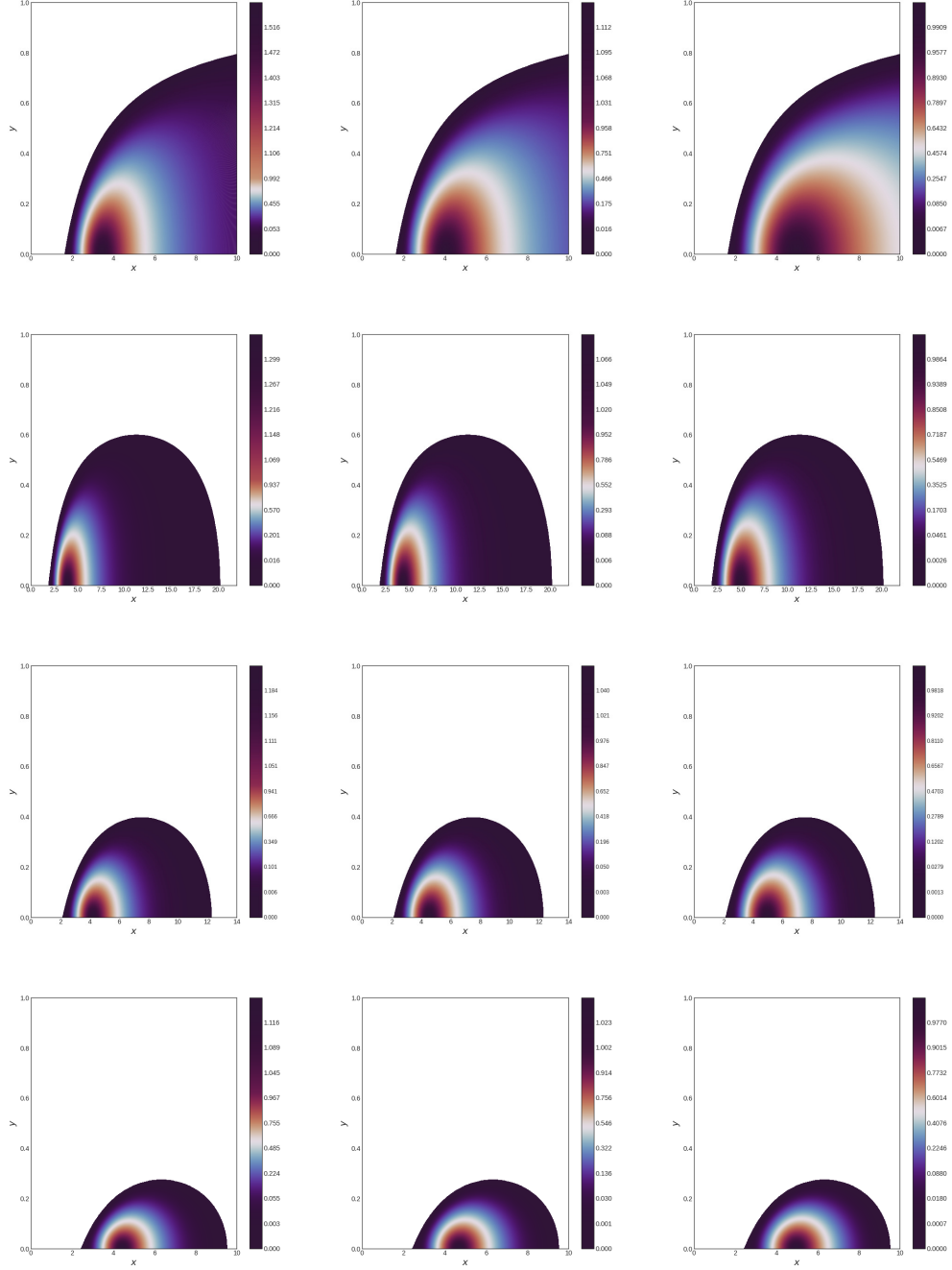


**Figure 11.20:** Map of the rest-mass density distribution for  $q = -0.4$ . From the left to the right, the magnetization parameter varies. The first column corresponds to  $\beta_c = 10^{-3}$ , second to  $\beta_c = 1$  and third to  $\beta_c = 10^3$ . Also, the distribution of the specific angular momentum varies in rows. First row represents the constant specific angular momentum, the second row model 3, the third row model 2, and the last row shows model 1.

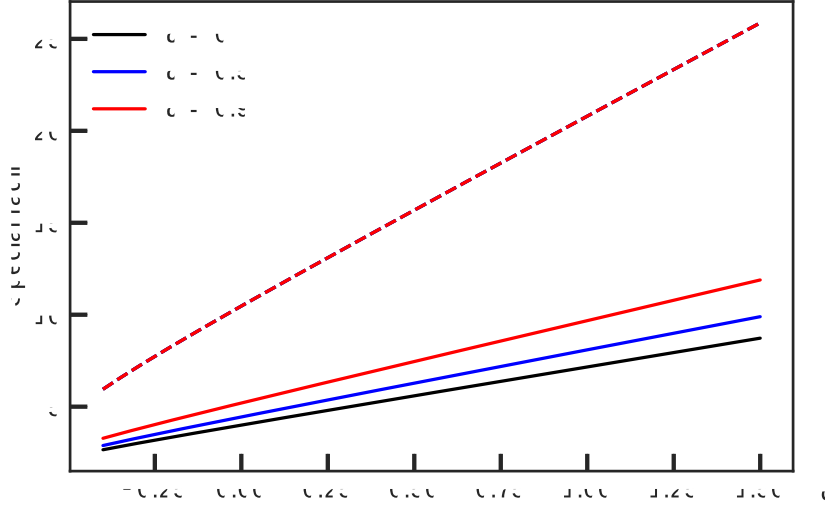


**Figure 11.21:** Variation of the location of the cusp (solid lines), and the location of the centre (dashed line), as a function of  $q$  for the different distribution of specific angular momentum.

and its position, in comparison to changing the value of quadrupole. However, a deeper inspection shows that the strength of the impact of  $\beta_c$  depends on both parameters  $q$  and  $\alpha$  as seen in the Figure 11.22. As for larger values of  $q$  and  $\alpha$ , the impact of changing in  $\beta_c$  is tenser. Besides, for any fixed value of  $\beta_c$  but not large, the parameter  $\alpha$  is not also independent of  $q$ . As one can see in the Figure 11.22 the higher  $q$ ,  $\alpha$  has a higher impact on the disc properties.

Further, the solutions with this angular momentum ansatz and two panels of the rest-mass density are presented in Figures 11.23 and 11.24. As it has been shown also in the power-low case, the higher the magnetization, the more accumulated the rest-mass density distribution in the inner part of the disc. In the Figure, it is important to mention that the rows 1 and 4 have the same parameter  $\alpha = 0$ , which means they have the same location and amplitude of the rest-mass density maximum and total pressure. The same discussion applies to rows 3 and 5, which they have shared the parameter  $\alpha = 0.9$ . In fact, an analysis shows that the  $\alpha$  parameter is more responsible for the vertical direction of the disc in the way that as much as we increase  $\alpha$  we have a less vertically extended disc. While, parameter  $\delta$  effects on both the radial and the vertical extension of the disc. Besides, it has an effect on the distribution of equidensity surfaces in general. However, the analysis on

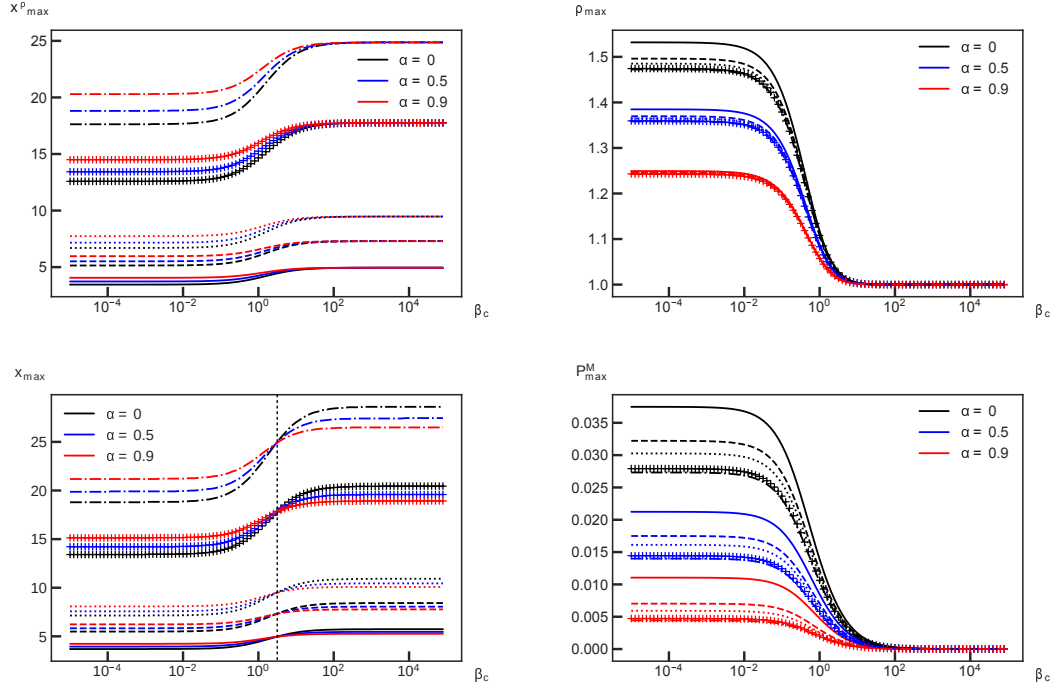


**Figure 11.22:** Top panels: Variation of the location and amplitude of the rest-mass density maximum as a function of  $\beta_c$ , for three models of angular momentum profiles and five values of  $q$ . In this plot  $q = -0.4$  and  $q = -0.2$  are depicted in solid line and dashed line,  $q = 0$  is shown in the dotted line,  $q = 0.8$  and  $q = 1.5$  are represented in crossed and dot-dashed lines respectively. Bottom panels: same description but for the maximum of the magnetic pressure.

how  $\delta$  affects the structure of the disc is in correlation with  $\alpha$  that one can not study this contribution independently.

In Figure 11.24 we have explored the effect of the deformation parameter  $q$  on the structure of the disc with considering the variation of angular momentum distributions. In this case we have set magnetization parameter to be  $\beta_c = 10^{-3}$  corresponding to a strong magnetic field. Each column presents a chosen value of  $q$ . It starts with a negative value  $q = -0.4$  at the left, then  $q = 0$ , and a positive value  $q = 1.5$  at the right. Also, the variation of the angular momentum is in the same as in the Figure 11.23. In comparison to the Figure 11.23, one can say that the deformed parameter  $q$  is more responsible for a shift in the radial direction of the disc. In addition, this is also responsible for radial extension of the disc in the same manner.

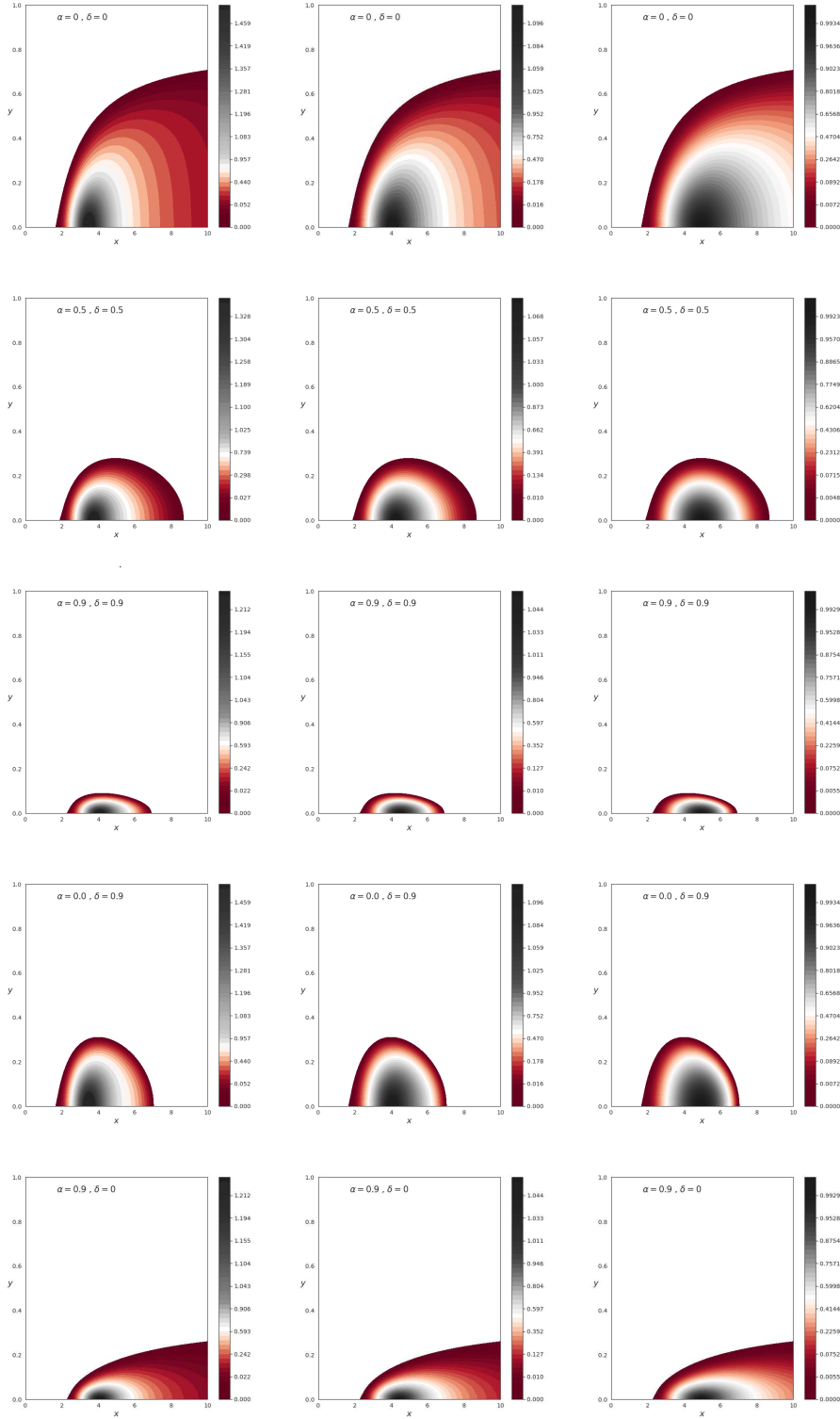


**Figure 11.23:** Map of the rest-mass density distribution for  $q = -0.4$ . From the left to the right, the magnetization parameter varies, namely  $10^{-3}$ ,  $1$  and  $10^3$  respectively. In rows the power index  $\alpha$  and  $\delta$  is changing. We have chosen these following pairs  $(\alpha = \delta = 0)$ ,  $(\alpha = \delta = 0.5)$ ,  $(\alpha = \delta = 0.9)$ ,  $(\alpha = 0, \delta = 0.9)$ ,  $(\alpha = 0.9, \delta = 0)$  from the top to the bottom.

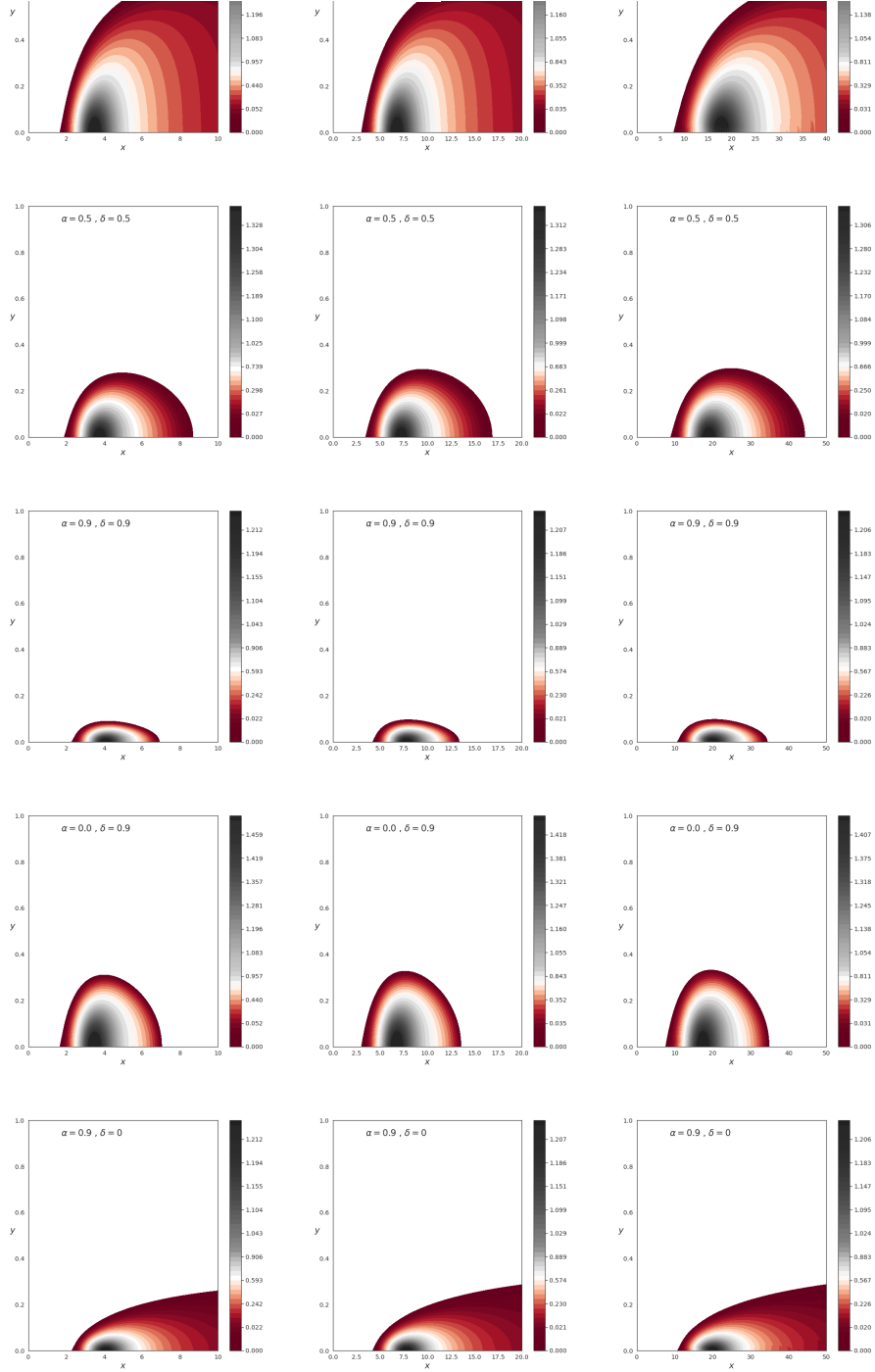


**Figure 11.24:** Map of the rest-mass density distribution. From the left to the right, the parameter  $q$  varies. The column at the left shows  $q = -0.4$ , the middle  $q = 0$  and the right represents  $q = 1.5$ . In rows the power index  $\alpha$  and  $\delta$  is changing. We have chosen these following pairs with the following pairs  $(\alpha = \delta = 0)$ ,  $(\alpha = \delta = 0.5)$ ,  $(\alpha = \delta = 0.9)$ ,  $(\alpha = 0, \delta = 0.9)$ ,  $(\alpha = 0.9, \delta = 0)$  from the top to the bottom. Also, the magnetization parameter is set to be  $\beta_c = 10^{-3}$ .



### 11.2.3 Summary and conclusion

In this section, we explored the magnetized Thick disc model around a deformed compact object up to the quadrupole,  $q$ -metric, which is briefly explained in Section 6.3.

In the case of the power-law distribution described in Subsection 2.2.2, we have shown that steeper angular momentum causes the disc to be more shrunk. Moreover, increasing in the steepness of the angular momentum profile, decreases the amplitude of the rest-mass density and pushes away the location of its maximum. Besides, in the case of trigonometric distribution profile, we have shown that the pair  $(\alpha, \delta)$  affect strongly on the overall configuration of the disc.

In addition, the parameter  $q$  is more responsible for a shift of the whole disc, also its radial extension. Namely, the bigger we choose  $q$ , the more extended disc we have and the disc is more pushed outward from the central object. Furthermore, a slightly prolate shape of the central object- which is related to the negative values of  $q$ - shows a tendency to enlarge the disc in the vertical direction. However, a slightly oblate shape which is associated with the positive values of  $q$  tends to flatten the disc in the equatorial plane. However, as the values of quadrupole parameters that we chose in our models are minimal, this is not easy to see from the panels. For example, in the oblate case, We can think the matter tends to spread more through the disc as we have seen the area between the cusp point and the center of the disc is greater, and the disc is more diluted comparing to the prolate case. This is also coherent with decreasing the amplitude of the rest-mass density maximum and the total pressure maximum.

In addition, the magnetization parameter has more impact on the distribution of matter in the disc and its properties, rather than on the geometrical structure of the discs. This result is coherent with the results of the previous studies [52, 212]. Further, for larger values of  $q$  and  $\alpha$ , the impact of changing in  $\beta_c$  is tenser. Besides, for any fixed value of  $\beta_c$  but not large, the parameter  $\alpha$  is not also independent of  $q$ . As one can see in the Figure 11.22 the higher  $q$ ,  $\alpha$  has a higher impact on the disc properties.

More importantly, the parameters of angular momentum, quadrupole and the magnetization parameter can neutralized their effect for some proper combination, which can have a great consequence in the model outcome to interpret the astrophysical observational data when considering different backgrounds. The result of this study is presented in [214].

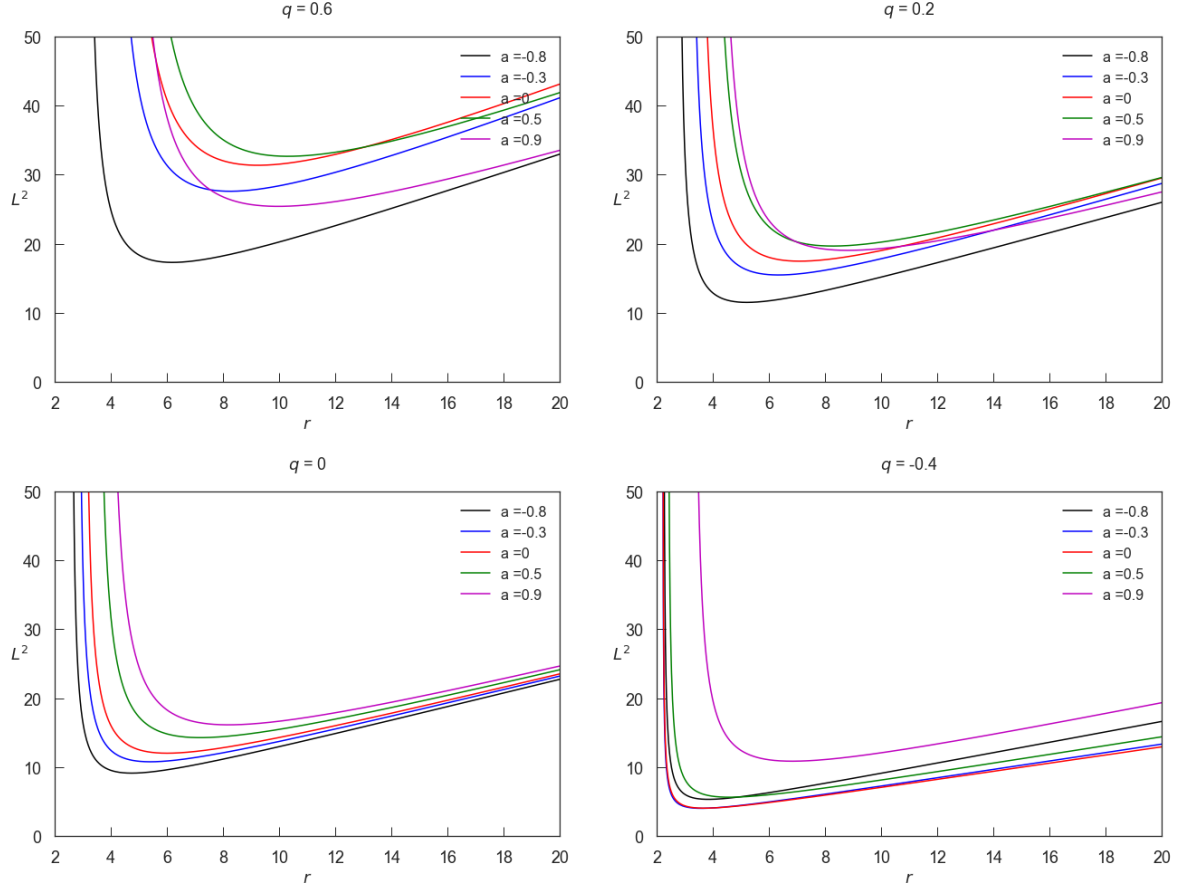


**Figure 11.25:** Plots of  $\ell^2$  for Stationary q-metric, for different values of  $q$  and  $a$ .

### 11.3 Thick disc in Stationary q-metric

In this section, we construct the non-magnetized relativistic tori described in Section 2.2 in the background of the stationary q-metric where presented in Sections 6.4 and 9. In this study, we focus on a constant angular momentum distribution.

#### 11.3.1 Discussion on the constant angular momentum

First of all, Figure 11.25 shows the plots of  $\ell^2$  for different values of  $q$  and  $a$ . This can be seen clearly that depend on the different values of  $q$  and  $a$  the place of minimum of  $\ell^2$  changes. However, for smaller  $q$ s they happen to be more closer to each other (see  $q = -0.4$ ) while as  $q$  increases the different cases start to have more distant from each other (see  $q = 0.6$ ). In particular, we notice that for  $q > 0$  the smallest negative value of  $a$  is corresponds

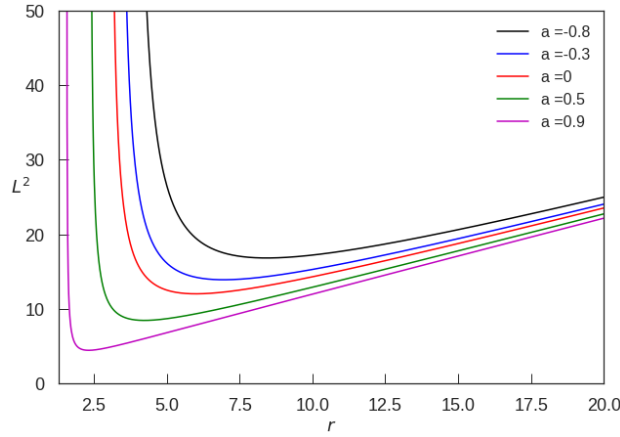


**Figure 11.26:** Plots of  $\ell^2$  for Kerr space-time, for different values of  $a$ .

to the smallest minimum in  $\ell^2$  which is also closer to the central source (see for example in plots  $a = -0.8$ ). Besides, the situation is reversed for higher positive values of  $a$ . Therefore, one may conclude that the places and the amplitudes of minimums are increasing function of  $a$ . However, when  $q < 0$  the situation is complex and we can not state a general outcome. For a comparison  $\ell^2$  in the Kerr background is plotted in 11.26. The most important difference, in the contrary with the Stationary  $q$ -metric, is here the places and the amplitudes of minimums are a decreasing function of  $a$ . In spite of this fact, the general patterns is more similar to the static  $q$ -metric, where  $a = 0$ . It seems the static  $q$ -metric more closely can mimic the general properties of Kerr solution at least in the vicinity of the central object; however, there exist significant differences in details.

The radius of the center in terms of  $a$  for different values of  $q$  is shown in Figure 11.27. In the left plot, we see that  $r_c$  is an increasing function of  $a$  and  $q$ . Thus, for any fixed value of  $q$ , for larger values of  $a$  the disc can be constructed farther away from the central object and the same for a fixed value of  $a$  and an increase in  $q$ . In addition, the plots of  $r_c$  as a function of  $a$  have maximum for the positive  $q$ s and minimum for the negative  $q$ s. Therefore, for positive values by an continuously increase in  $a$ , the disc configuration shifted from the central source and then come closer. It could be either an interesting behavior of this space-time, or some signal to discard larger positive values of  $q$ . This pattern again is indicated in the right plot in Figure 11.27. In fact, this needs to have a deeper analysis on the physical properties of the background metric which was not focus of this work and could be a future work.

The right plot in Figure 11.27 shows the angular momentum profiles at

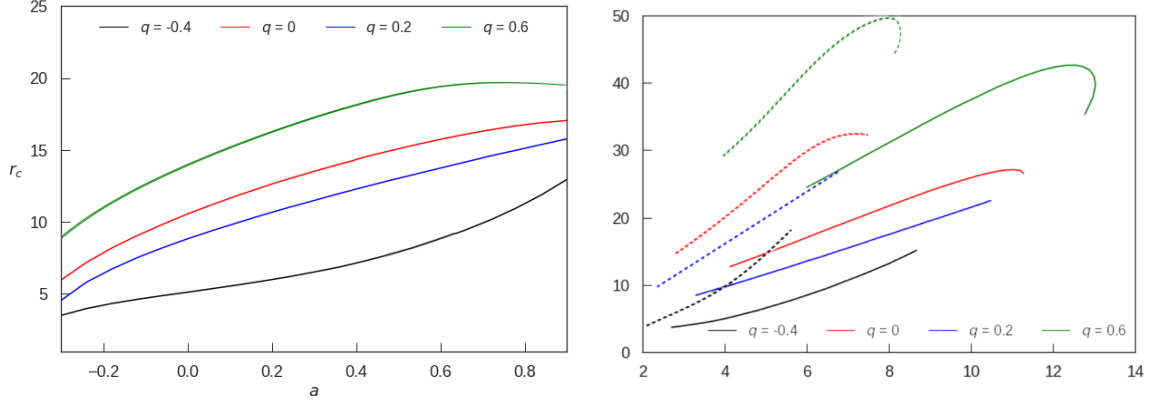


**Figure 11.27:** Left: The Variation of the position of the center of the disc as a function of  $a$  and  $\ell_0 = (\ell_{mb}^2 + \ell_{ms}^2)/2$ . Right: The variation of  $\ell_{mb}^2$  (dashed line) and  $\ell_{ms}^2$  (thick line) as a function of  $r_{mb}(a)$  and  $r_{ms}(a)$ , respectively.

the marginally stable and marginally bound orbits [209]. In fact, these angular momentum profiles have the same behavior as  $r_c$  with respect to the parameter  $a$ . However, these are increasing functions as  $q$ , as we see, for example, the highest profile of angular momentum happens for  $q = 0.6$ . In addition, the area between these two profiles are also an increasing function, where it leads to having a wider area where closed equipotential surfaces exist. As mentioned, the chosen angular momentum distribution should be within this area to have closed equipotential surfaces. To have a consistent approach for different values of parameters we set the constant angular momentum to  $\ell_0^2 = \frac{1}{2}(\ell_{mb}^2 + \ell_{ms}^2)$  for all different set of parameters that we considered to calculate  $W$  equation (2.45) in this case (see Section 2.2).

$$W(r, \theta) = \frac{1}{2} \ln \left| \frac{g_{t\phi}^2 - g_{tt}g_{\phi\phi}}{g_{\phi\phi} + 2\ell_0 g_{t\phi} + \ell_0^2 g_{tt}} \right|. \quad (11.1)$$

In addition, an analysis on the location of the maximum of the rest mass density in the equatorial plane shows that increasing  $q$  or  $a$  only shifts the position of maximum of rest mass density farther away from the central object which is consistent with the result in Figure 11.27.

To study the influence of the parameters  $q$  and  $a$  on the morphology of the equipotential surfaces, in Figure 11.28 the structure of the disc is plotted for the chosen values that we studied earlier. In the second column, we chose  $a = 0$  to have the static  $q$ -metric 11.2 and compare with the stationary case, as well as Schwarzschild case specifying as  $a = 0 = q$ . In this Figure, a comparison among the different rows tells us about the role of quadrupole  $q$

for any chosen  $a$ , while a contrast among the columns shows the influence of parameter  $a$  on the model for any chosen value of  $q$ . Clearly, one can see that by increasing the value of  $a$ , the position of the disc shifts away from the central object. Besides in this case, we have a more radially extended disc structure. Thus, both parameters have the same effect on the disc structure. However, a deeper analysis reveals that the growth rate caused by increasing  $a$  is higher than by an increase in  $q$ . For the case  $a = 0$ , the result is in the good agreement with the results found in Section 11.2 for a constant angular momentum case [214].

### 11.3.2 Summary and conclusion

In conclusion, in this section, we investigated the Thick disc structure in the background of the stationary  $q$ -metric to reveal more physical properties of this space-time through the study of the shape and properties of equipotential surfaces in this model. In addition, we also compare the result with the static  $q$ -metric and Schwarzschild solution.

In general, we conclude that for higher values of  $q$  and  $a$  we have the larger Thick disc configuration which is also constructed farther away from the central object with more radially extension. In particular, the size and position of the disc with respect to the central source, are a monotonically increasing function of both parameters  $a$  and  $q$ . In addition, the plots of  $\ell^2$  behave entirely different from the Kerr space-time which make it distinguishable easily in analysis of observational data. The results of this study are presented in [209].

## 11.4 Magnetized Thick disc in C-metric

In this section, we analyzed the impact of the different parameters of the spinning charged C-metric described in Section 6.5 on the morphology of the equipotential surfaces of the Thick disc model 2.2 with constant angular momentum.

### 11.4.1 Von Zeipel radius

Before we start to investigate the construction of the Thick disc model, we briefly discuss the modified Von Zeipel radius or radius of gyration [50]. This radius determines surfaces of constant  $\mathcal{R}$ , which for an axisymmetric and the stationary metric is defined as

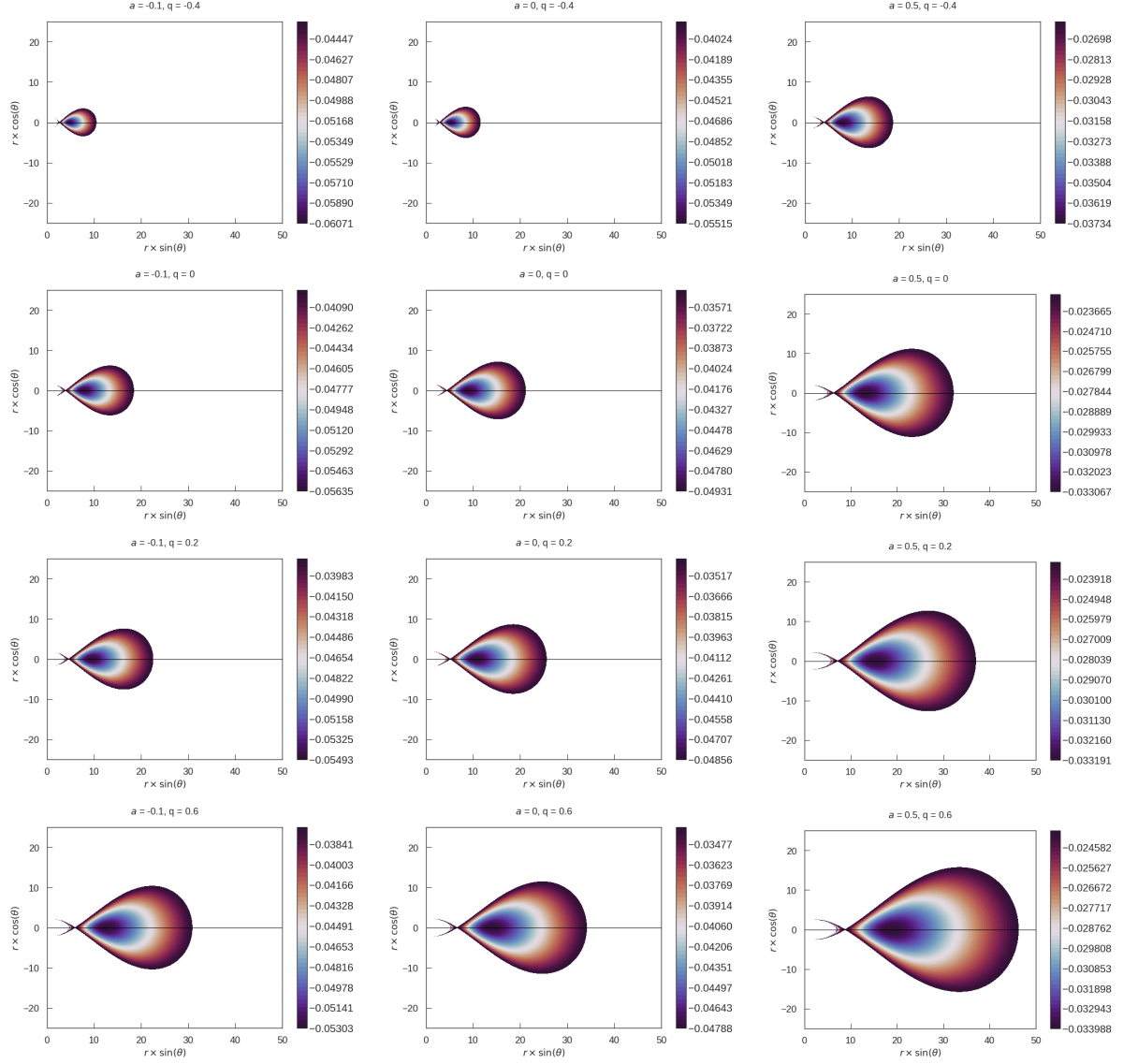


**Figure 11.28:** Thick disc configurations for various values of  $a$  (vertical direction) and  $q$  (horizontal direction). All along the plots,  $\ell_0 = (\ell_{mb}^2 + \ell_{ms}^2)/2$ , with the  $\ell_{mb}^2$  and  $\ell_{ms}^2$  values associated to  $a$  and  $q$ .

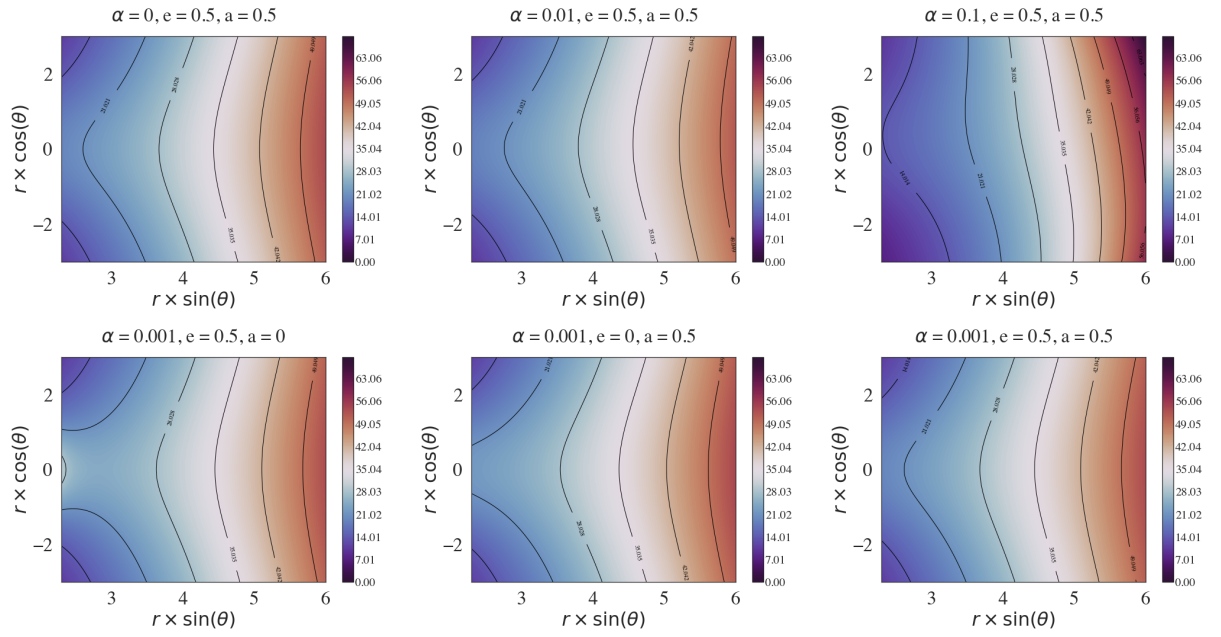


**Figure 11.29:** Von Zeipel cylinders with respect to the stationary observers. The plots show poloidal sections across the constant  $R$  surfaces, where the circular time-like motion of the fluid is possible. Colours correspond to different values of the radius, as listed on the colour-bar to the right of each panel. Selected contours are indicated with black lines.

$$\mathcal{R} = \frac{g_{\varphi\varphi}^2}{g_{t\varphi}^2 - g_{tt}g_{\varphi\varphi}}, \quad (11.2)$$

with respect to the stationary observers, and known as von Zeipel cylinders [215, 216]. In fact, this radius helps to analyze circular particle motion and provides an intuitive image of them in this space-time. Besides, this radius is related to the inertial forces. In this concept using von Zeipel theorem, we can conclude that for a constant angular momentum distribution, the surface of constant  $\mathcal{R}$  and constant  $\Omega$  coincide. In Figure 11.29, we see the effect of parameters on this radius for different sets of  $\alpha$ ,  $e$  and  $a$  in this space-time.

#### 11.4.2 Discussion on the constant angular momentum

In the part, we examine the possibility of having solutions for this disc's model rely on the variation of the parameters. To have a better insight on the role of acceleration parameter, first we focus on the non-spinning case.

Figure 11.30 shows the regions where we may have a disc in the non-spinning charged set-up.

In the panel, the intersection of the dashed curve with the white and the dark-blue areas show the possible places for choosing the centre of the disc, and the cusp point, respectively. As we see the acceleration parameter  $\alpha$  plays a crucial role in the existence of solutions. As a result, as  $\alpha$  even slightly increases, almost the possibility of having solutions decreases dramatically. Therefore, we can build this disc's model only for relatively small acceleration. On the other hand, the charge parameter  $e$  has an imperceptible impact, and positively contributes to having solutions. Especially, the charge's effect manifests clearly when  $\alpha$  is relatively large. For example, with a comparison in the second row for relatively large  $\alpha$  and vanishing  $e$ , we do not have a solution while by increasing  $e$ , we obtain solutions.

This panel 11.30 also shows that the distance between the center and the cusp point changes as an monotonic decreasing function of  $\alpha$ . This leads to the larger disc structure for smaller rotation parameters  $a$ . In conclusion, as  $\alpha$  increases with a moderate rate the disc structure become smaller and finally, it will be vanished. Besides, the deeper analysis of the panel manifests the possibility of the existence of two cusps for some choices of parameters.

In Figure 11.31, by using Figure 11.30, we choose a solution possessing an inner cusp, a centre and an outer cusp to construct the largest possible model. Here, clearly can be seen for vanishing rotation in the first column, there is a possibility of having an inner cusp and an outer cusp specified by the red curves. In addition, by increasing charge, the closed equipotential surfaces also become larger, as predicted by Figure 11.30. Furthermore, by



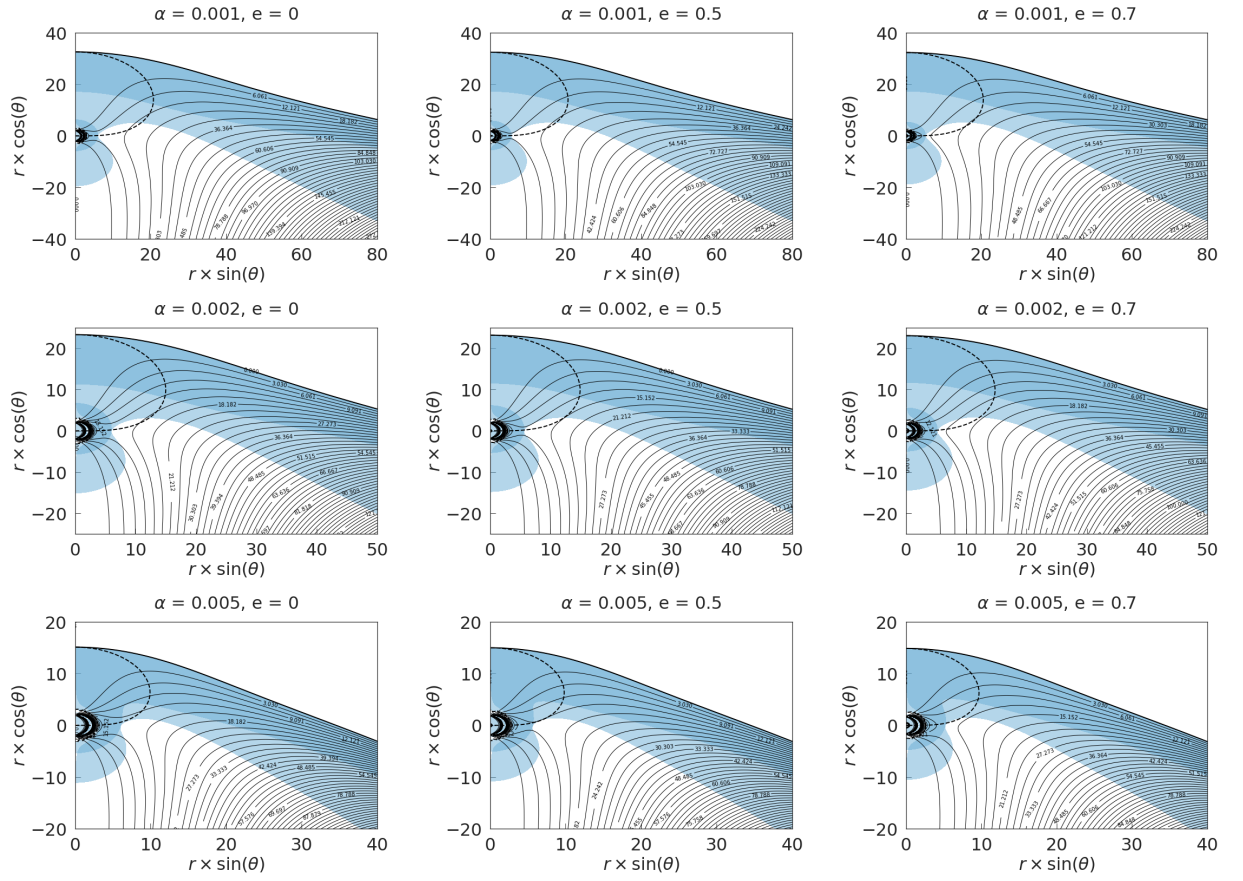


**Figure 11.30:** Possible region for having the Thick disc solution. The dashed curves shows when  $\partial_r W = 0$  and  $\partial_\theta W = 0$ . The dark blue regions shows area where the condition for a maximum of  $W(r, \theta)$  are fulfilled. The white area depicts where the condition for a minimum of  $W(r, \theta)$  are fulfilled.

comparing the first and second columns we can see the impact of the rotation parameter  $a$ . In general, the deepest analysis reveals the effect of the rotation parameter  $a$  on having solutions is not strong compared to  $\alpha$  as we see in Figure 11.30, but stronger than the effect of the charge parameter  $e$ . In fact, parameter  $a$ , like  $\alpha$ , has a negative effect on having solutions, and for relatively higher acceleration and rotation parameters we do not find any disc structure, unless we add a relatively high charge as far as it is possible. Moreover, the possibility of having the inner cusp is strongly reduced, while increasing the possibility of the outer cusp, in fact, leads matter to flow outwards.

Besides, the distance between the center and the cusp point is an monotonic increasing function of  $e$ , while it is a monotonic decreasing function of  $a$ . Therefore, the larger disc structure for bigger charge values  $e$  and smaller rotation parameters  $a$  is predicted. In other words, on the contrary to  $e$ , by increasing  $a$  and  $\alpha$ , the centre and the cusp's locations approach one another, and gradually we lose solutions.

In addition, by increasing  $\alpha$  and  $e$ , we obtain closed equipotential surfaces where more oriented concerning the horizontal axis. Of course the effect of  $\alpha$  is more decisive than  $e$  in this behavior; namely, as  $\alpha$  even slightly increases the disc deviate from the horizontal axis noticeably.

In Figures 11.32, we examine the effect of the magnetization parameter  $\beta_c$  and the dependency of the disc structure and its orientation on the parameter  $e$  in the vicinity of the compact object for a fixed value of acceleration parameter  $\alpha$  and vanishing rotation. In the first column we chose high magnetized model, and in the second row relatively high charged one. In fact, comparing columns shows that the magnetization parameter does not influence the disc's geometry; however, it changes the distribution of matter inside the disc and shifts the location of the rest-mass density maximum which is pointed out as the dashed lines in Figure 11.32. In addition, comparing rows show that we have a larger oriented disc for larger values of  $e$ . Moreover, the matter is more concentrated in the inner part of the disc, as was predicted in the previous Figures 11.30 and 11.31.

In Figures 11.33 and 11.34 we focus more on the impact of only one parameter  $\alpha$  and  $a$  on the disc structure, respectively. Figure 11.33 presents the profound impact of  $\alpha$  on the geometry and orientation of the disc for a fixed value of  $e$  and magnetization parameters. In fact, according to the last row of Figure 11.30, the possibility of having solutions for larger  $\alpha$  could be depend on having large values for  $e$ , so the effect of higher  $\alpha$  on the disc could be neutralized only partially with the higher charge values.

Figure 11.34 shows the dependency of the disc structure on the parameter  $a$  in the presence of the rotation. As expected, increasing  $a$  change the

disc size and the distribution of matter inside the disc. Furthermore, we do not have an inner cusp for any value of rotation parameters. In addition, increasing  $\alpha$  and  $a$  shifts the disc farther away from the compact object, contrary to an increase in  $e$ .

### 11.4.3 Summary and conclusion

In this section, we have analyzed the influence of the magnetization parameter  $\beta_c$ , and the C-metric parameters on the structure of the magnetized Thick disc model. In one hand, we have shown that changing magnetization parameter  $\beta_c$  has a noticeable effect on the location and amplitude of the rest-mass density maximum, also distributing the matter inside the disc. The effect of the magnetization parameter is in complete agreement with previous studies using this model e.g [52]. Furthermore, in this case, the range of isodensity contours increases, which is compatible with the increase of rest-mass density in the inner part of the disc. Indeed, this result remains valid for any chosen value of other parameters.

On the other hand, we have seen that acceleration parameter play a crucial role on the existence and behavior of the solutions in this set-up. It means, we can have the Thick disc model only for relatively small values of  $\alpha$ , and by increasing  $\alpha$ , the disc structure becomes smaller and more oriented concerning the horizontal axis and gradually vanishes. Besides, higher values of  $\alpha$  shifts the disc farther away from the black hole. Additionally,  $a$  has a similar effect but weaker on the structure; by increasing  $a$ , the disc becomes thinner and smaller and more oriented concerning the horizontal axis until it vanishes completely. On the contrary to these two parameters, an increase in  $e$  increases the disc size and possibility of having solutions.

In addition, we have seen that  $e$  changes the distribution of matter inside the disc in the opposite way of  $\alpha$  and  $a$ . Besides, increasing  $\alpha$  and  $a$  shifts the disc farther from the compact object, contrary to an increase in  $e$ . However, we should emphasize that the strength of the parameters are not the same; among these three parameters,  $\alpha$  has a stronger and  $e$  has the weaker effect on the disc structure, in comparison. In general, impact of charge parameter is the inverse of  $\alpha$  and  $a$  in any aspects regarding the disc properties. As the final point, it is worth mentioning that because of the asymmetry with respect to the equatorial plane, the accretion discs in this space-time, in general, are likely to be unstable even to axis-symmetric instabilities, which is the subject of the following work. The results of this Section are presented in [217].

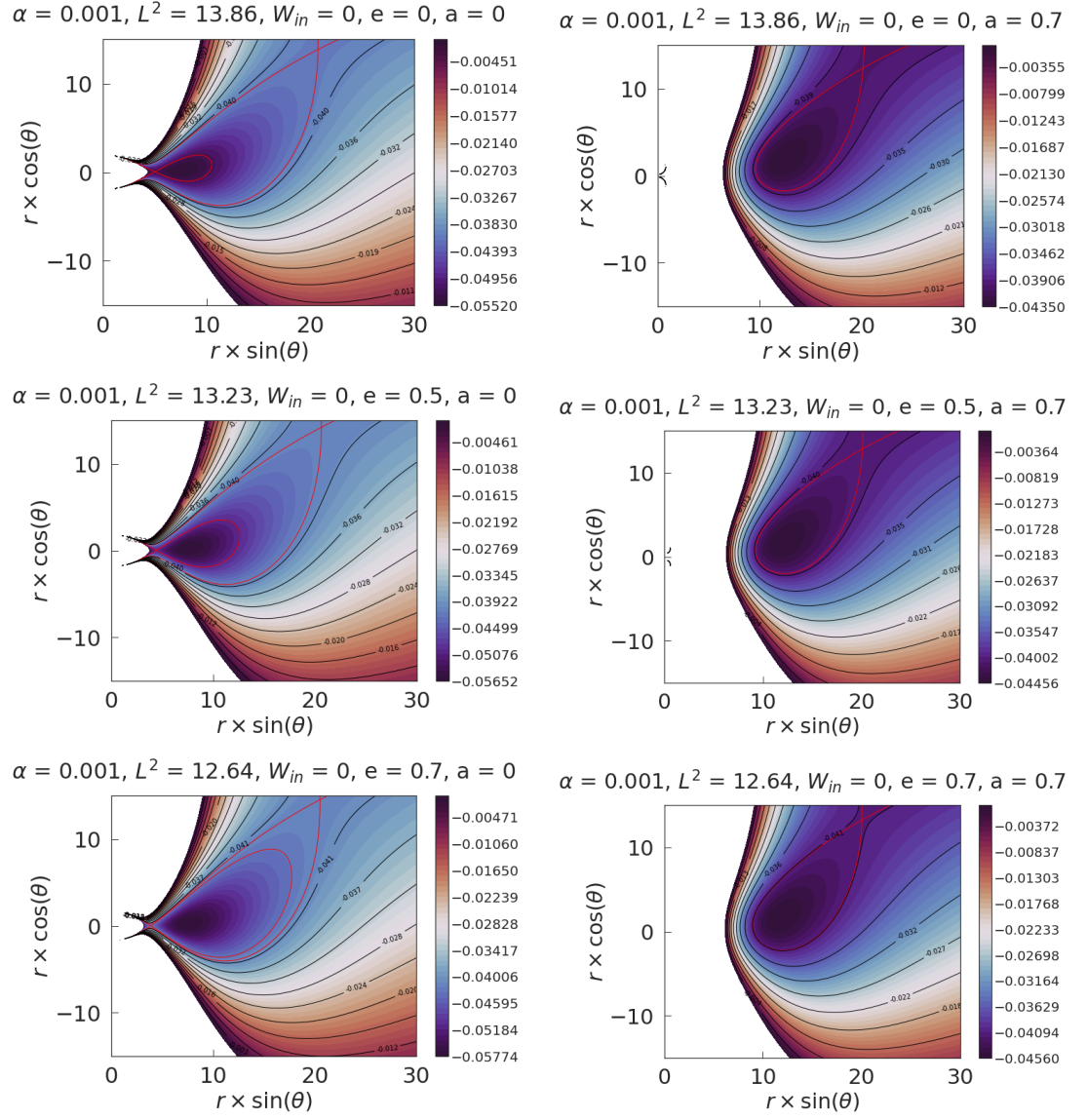


**Figure 11.31:** Contour map of the equipotential surfaces. The red lines show the equipotential corresponding to the inner and outer cusps.

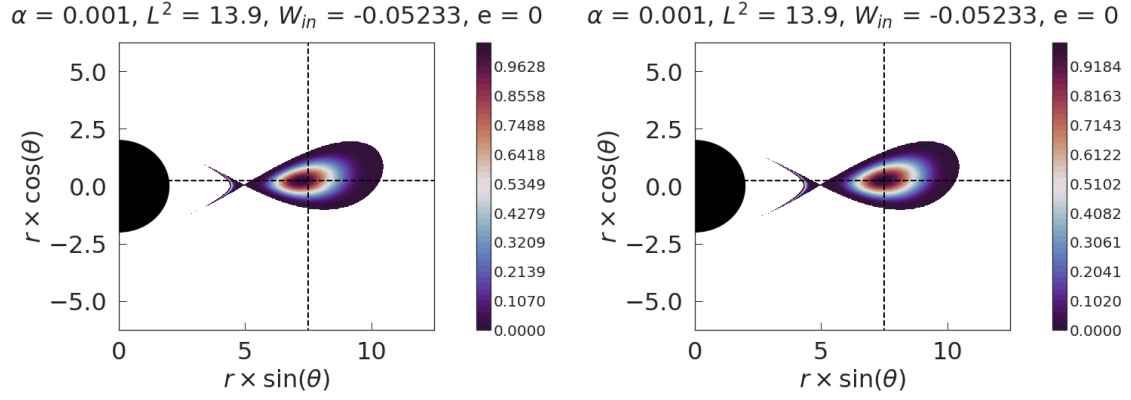


**Figure 11.32:** Contour map of the rest-mass density of magnetized disc. The dashed lines point the center of the disc located at  $r_c = 7.5$ . The first plot shows highly magnetized disc and the second one low magnetized.

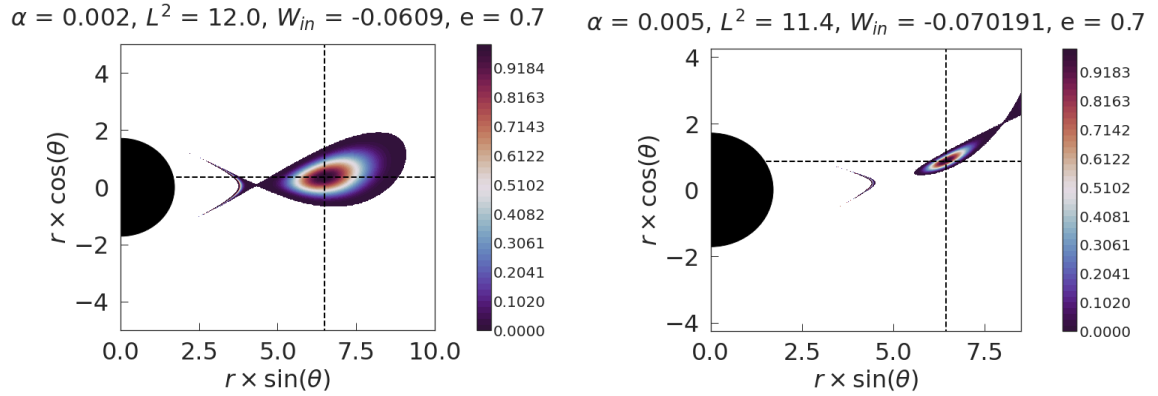


**Figure 11.33:** Contour map of the rest-mass density of magnetized highly disc. The dashed lines point the center of the disc located at  $r_c = 6.5$ .

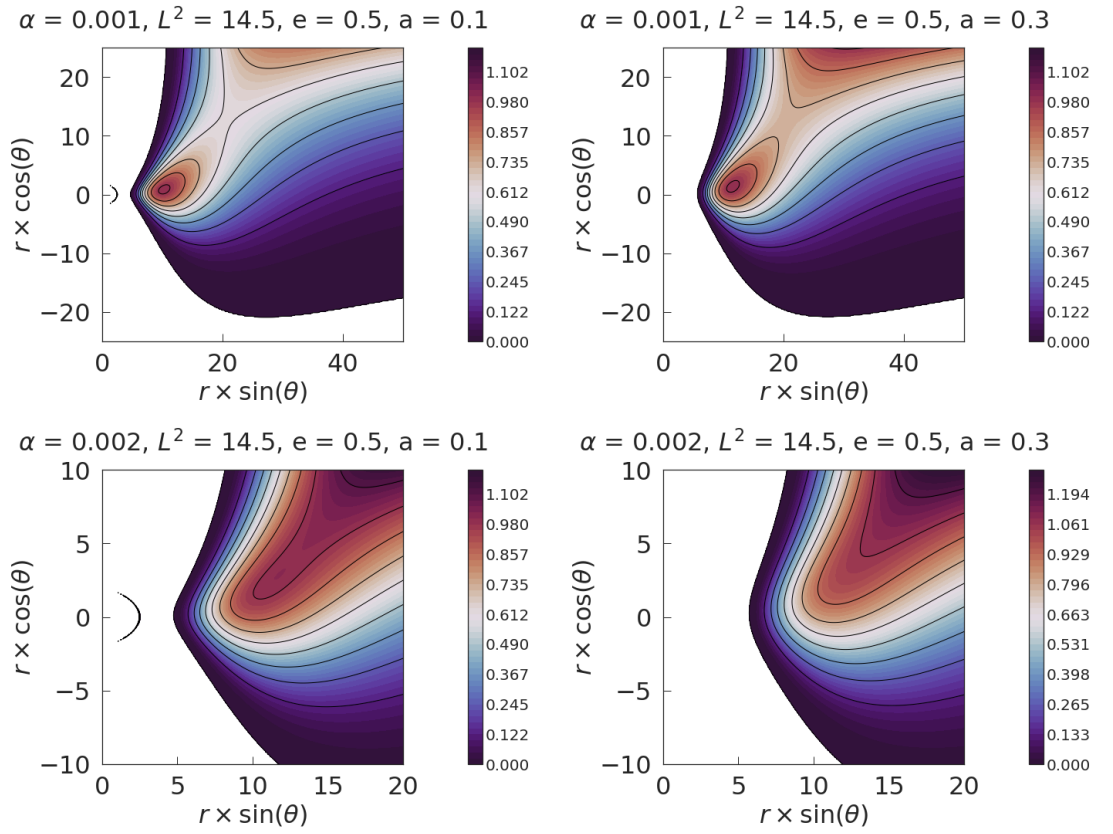


**Figure 11.34:** Contour map of the rest-mass density for various spin values. The dashed lines point the center of the disc. Those solution have the same parameters ( $\alpha, L$  and  $e$ ) of the non-rotating solution given at the bottom left of the Figure 11.32.

## QPOs in Generalized q-metric in the uniform magnetic field

As mentioned in Chapter 3, circular and quasi-circular orbits seem to be crucial in the study of accretion process and in particular HF QPOs, since in these processes, a variety of oscillatory motions are expected. In this regard, in the study of the relativistic accretion disc, three frequencies are relevant: the Keplerian orbital frequency  $\nu_K = \frac{\Omega}{2\pi}$ , radial frequency  $\nu_x = \frac{\omega_x}{2\pi}$  and the vertical frequency  $\nu_y = \frac{\omega_y}{2\pi}$  where the resonance among these frequencies can be a source of quasi-periodic oscillations that leads to chaotic and quasi-periodic variability in X-ray fluxes observations in many observations.

Furthermore, an external magnetic field at a large distance in a finite region can be approximated as a uniform magnetic field [218, 81]. Such a large-scale magnetic field could be initiated during the early phases of the expansion of the Universe [219, 220, 221, 222, 223]. Further, a compact object near the equatorial plane of a magnetar can be approximated to be in a uniform magnetic field if the magnetar is at a distance large enough [224, 82]. In fact, the motion in a gravitational field and in the presence of an external electromagnetic field was explored in a large variety of studies e.g. [225, 226, 227] among many more.

In this chapter we aim to investigate them in the background of the Generalized q-metric with and without an asymptotically uniform magnetic field. In addition, in the last section we examine the ability of this set-up to fit to the observational data and compare with some results in the Kerr metric.

## 12.1 Epicyclic frequencies and stability of circular motion

These mentioned fundamental frequencies related to the circular motion, in equatorial plane of the Schwarzschild metric, in spheroidal coordinates, are given by

$$\omega_y^2 = \Omega^2 = \frac{1}{(x+1)^3}, \quad (12.1)$$

$$\omega_x^2 = \frac{1}{(x+1)^3} \left( 1 - \frac{6}{x+1} \right). \quad (12.2)$$

The vertical and keplerian frequencies are always positive; however, it is not the case for radial frequency. Therefore, the stable circular orbits are located at radial distances larger than the location of the ISCO at  $x = 5$  in these coordinates. Further, for the Schwarzschild metric, we have  $\omega_x^2 < \omega_y^2 = \Omega^2$ . Interestingly, in contrast to Newtonian geometry, bounded quasi-elliptic orbits can also exist, meaning the trajectories relevant to a perturbed stable circular test particle may not be elliptic but exhibit a periapsis shift, which is often called the effect of relativistic precession [228].

In what follows, we investigate the stability of circular motion in the presence of the asymptotically homogeneous magnetic field in the background of Generalized q-metric with two quadrupoles (see chapter 7). In this regard, seminal papers [73, 74] studied the existence and stability of circular non-geodesic equatorial orbits, and derived Keplerian and epicyclic orbital frequencies in Kerr(-Newman) geometry. In this chapter, we extend the result to this space-time. Of course, if parameters of the metric vanish, the axial and radial oscillations frequencies are the same as their result for non-rotating case.

The equation of motion for a particle with mass  $m$  and electric charge  $e$  is the geodesic equation with force in its right-hand side takes this standard form

$$\frac{d^2 x^\mu}{ds^2} + \Gamma_{\nu\rho}^\mu \frac{dx^\nu}{ds} \frac{dx^\rho}{ds} = \frac{q}{m} F_\eta^\mu \frac{dx^\eta}{ds} \quad (12.3)$$

In the equatorial plane we have  $x = x_0$  and  $y = 0$ , and replace all necessary Christoffel symbols on the left-hand side using equations (7.19). For substitute the right hand side we utilized (7.48) and (7.49).

To describe the more general class of orbits in the equatorial plane slightly deviated from the circular ones, we can use the perturbation approach and consider a slightly perturbed orbit  $x'^\mu = x^\mu + \xi^\mu$  from the original one  $x^\mu$ .



By substituting this relation into equation (12.3) and consider only terms up to linear order in  $\xi^\mu$ , we obtain

$$\frac{d^2 \xi^\mu}{dt^2} + 2\gamma^\mu_\eta \frac{d\xi^\eta}{dt} + \xi^\eta \partial_\eta U^\mu = \frac{q}{mu^0} f^\mu, \quad (12.4)$$

and

$$\gamma^\mu_\eta = \left[ 2\Gamma^\mu_{\eta\delta} u^\delta (u^0)^{-1} - \frac{q}{mu^0} F^\mu_\eta \right]_{y=0}, \quad (12.5)$$

$$U^\mu = \left[ \gamma^\mu_\eta u^\eta (u^0)^{-1} - \frac{q}{mu^0} F^\mu_\eta u^\eta (u^0)^{-1} \right]_{y=0}, \quad (12.6)$$

where the 4-velocity for the circular orbits in the equatorial plane is  $u^\mu = u^0(1, 0, 0, \Omega)$  and the external force as  $f^\mu_\nu u^\nu (u^0)^{-1}$  [74]. Then the integration of equation (12.4) for the  $t$  and  $\phi$  components leads to

$$\frac{d\xi^\eta}{dt} + \gamma^\eta_\nu \xi^\nu = \frac{q}{mu^0} \int f^\eta dt, \quad (12.7)$$

$$\frac{d^2 \xi^x}{dt^2} + \omega_x^2 \xi^x = \frac{q}{mu^0} \left( f^x - \gamma^x_\eta \int f^\eta dt \right), \quad (12.8)$$

$$\frac{d^2 \xi^y}{dt^2} + \omega_y^2 \xi^y = \frac{q}{mu^0} f^y. \quad (12.9)$$

where here  $\eta$  can be taken  $t$ , or  $\phi$ , and

$$\begin{aligned} \omega_x^2 &= \partial_x U^x - \gamma^x_\eta \gamma^\eta_x, \\ \omega_y^2 &= \partial_y U^y. \end{aligned} \quad (12.10)$$

This system of equations describes radial phase and vertical oscillations of the charged particle around the circular orbits<sup>1</sup>. The positive sign of the squared frequencies (12.10) determines the stability of circular orbits; otherwise, even a minimal perturbation can make a strong deviation from the unperturbed orbit. In the absence of the external force, these equations describe the free radial phase and vertical oscillations of particles around the circular orbits.

The corresponding frequencies (12.10) in the background of a distorted, deformed compact object with vanishing magnetic field are obtained as

$$\begin{aligned} w_x^2 &= A_x \Omega^2, \\ w_y^2 &= A_y \Omega^2, \end{aligned} \quad (12.11)$$

---

<sup>1</sup>For an alternative definition of the epicyclic harmonic motion, see [140].

where

$$A_x = \frac{e^{-2\hat{\gamma}}(1 - 1/x^2)^{-\alpha(2+\alpha)}}{(x^2 - 1)} \left[ 2(2S - x)(S - x) - \frac{(x^2 - 1)}{S}(1 + \alpha + 2\beta x^3) \right], \quad (12.12)$$

$$A_y = \frac{e^{-2\hat{\gamma}}(1 - 1/x^2)^{-\alpha(2+\alpha)}}{S}(1 + \alpha + 2\beta x^3), \quad (12.13)$$

where  $S$  is given by

$$S := 1 + \alpha + \beta x - \beta x^3. \quad (12.14)$$

Note that these frequencies are measured regarding the proper time of a comoving observer. Nevertheless, in the presence of magnetic field, this is not possible to write these equations as some coefficients of  $\Omega$ . The vertical frequency is obtained as

$$w_y^2 = e^{-2\hat{\gamma}} \left( \frac{x^2 - 1}{x^2} \right)^{-\alpha(2+\alpha)} \left[ \Omega^2 \frac{x f_1(x, \beta) + S}{S} + (1 + f_1(x, \beta)) \Omega \omega_B \right]. \quad (12.15)$$

And radial frequency is given by

$$w_x^2 = \frac{\Omega^2 e^{-2\hat{\gamma}}(1 - 1/x^2)^{-\alpha(2+\alpha)}}{x(1 - x^2)} \left[ g_1(x, \beta, \alpha) \frac{x - S}{S} + g_2(x, \beta, \alpha) \right] + \frac{e^{-2\hat{\gamma}}(1 - 1/x^2)^{-\alpha(2+\alpha)}}{x(1 - x^2)} \left[ -\omega_B^2 x (S - x)^2 + \Omega \omega_B g_2(x, \beta, \alpha) \right], \quad (12.16)$$

where

$$f_1(x, \beta) = \beta(-1 + 3x^2), \quad (12.17)$$

$$g_1(x, \beta, \alpha) = 2\alpha^3 + \alpha^2 (6 - 2\beta x (-1 + x^2)) + 2\alpha (2 + x (x + \beta (-1 + x^2) (-4 + \beta x (-1 + x^2)))) + x (2x - \beta (-1 + x^2) (5 + x (-x + 2\beta (-1 + x^2) (-3 + \beta x (-1 + x^2))))) , \quad (12.18)$$

and

$$\begin{aligned}
g_2(x, \beta, \alpha) = & 2\alpha^3 - 4x(1 + \alpha + (-1 + \beta)x - \beta x^3)^2 \\
& - 2\alpha^2(-3 + x - \beta x + \beta x^3) \\
& + 2\alpha(2 + x(-2 + \beta(-1 + x^2)(-4 + \beta x(-1 + x^2)))) - x(-1 + x^2) \\
& \times (-1 + \beta(5 + x(-4 - 3x + 2\beta(-1 + x^2)(-3 + x - \beta x + \beta x^3)))) .
\end{aligned} \tag{12.19}$$

In Figure 12.1 and 12.2 we see the locations of maxima of these frequencies  $\omega_x$  and  $\omega_y$ . For any choice of parameters, the radial frequency's extrema must be located above the marginally stable orbit. The extrema are dependent on the choice of parameters for the vertical frequency, but these are always a monotonic function of distance  $x$ .

Figures 12.3 and 12.4 are depicted for the study of the existence and the stability of timelike orbits with respect to vertical or radial oscillations. On these Figures, the red line and the blue line correspond to  $w_x^2 = 0$  and  $w_y^2 = 0$ , respectively. The dark-green region bounded by those two blue and red lines represents the area where both are positive  $w_x^2 > 0$  and  $w_y^2 > 0$ , which is the condition to have stability with respect to vertical and radial oscillations. Note that above the red line, where we have  $w_x^2 < 0$  and  $w_y^2 > 0$ , orbits are stable with respect to vertical oscillations but unstable to the radial one. And on the contrary, below the blue line, where  $w_x^2 > 0$  and  $w_y^2 < 0$ , the orbits are stable with respect to radial oscillations and unstable with respect to the vertical one. We analyze these Figures by exploring the existence of the timelike circular orbit for different parameters. In fact, the region of existence is clearly affected by the three parameters. In the  $(x, \beta)$ -plane in Figure 12.5, we see that switching  $\alpha$  from negative to positive values tends to shrink the light-green region, on the contrary to an increase in  $\beta$ . The effect of the magnetic parameter is not monotonic; namely, by decreasing  $Q$  from positive to zero, the region is reduced in the vertical direction, but when  $Q$  becomes negative, and we continue to decrease that parameter, the region extends again.

Let's focus now on the stability region (dark-green area). As for the existing area, all three parameters also have influence on the region of stability but with different strengths. We can note that switching  $\beta$  negative to positive values makes the area of stability shrink (see Figure 12.4). The opposite effect is visible when switching  $\alpha$  from negative to positive (see Figure 12.5). However, the region of stability hardly changes with the parameter  $Q$ . It starts to shrink when  $Q$  decreases and continues by being pushed away from the central mass and then completely disappear for the negative values. This is due to the fact that, on the  $(x, \beta)$ -plane, the blue curve comes up, and the red one comes down, so the dark-green region shrinks, and at the end does

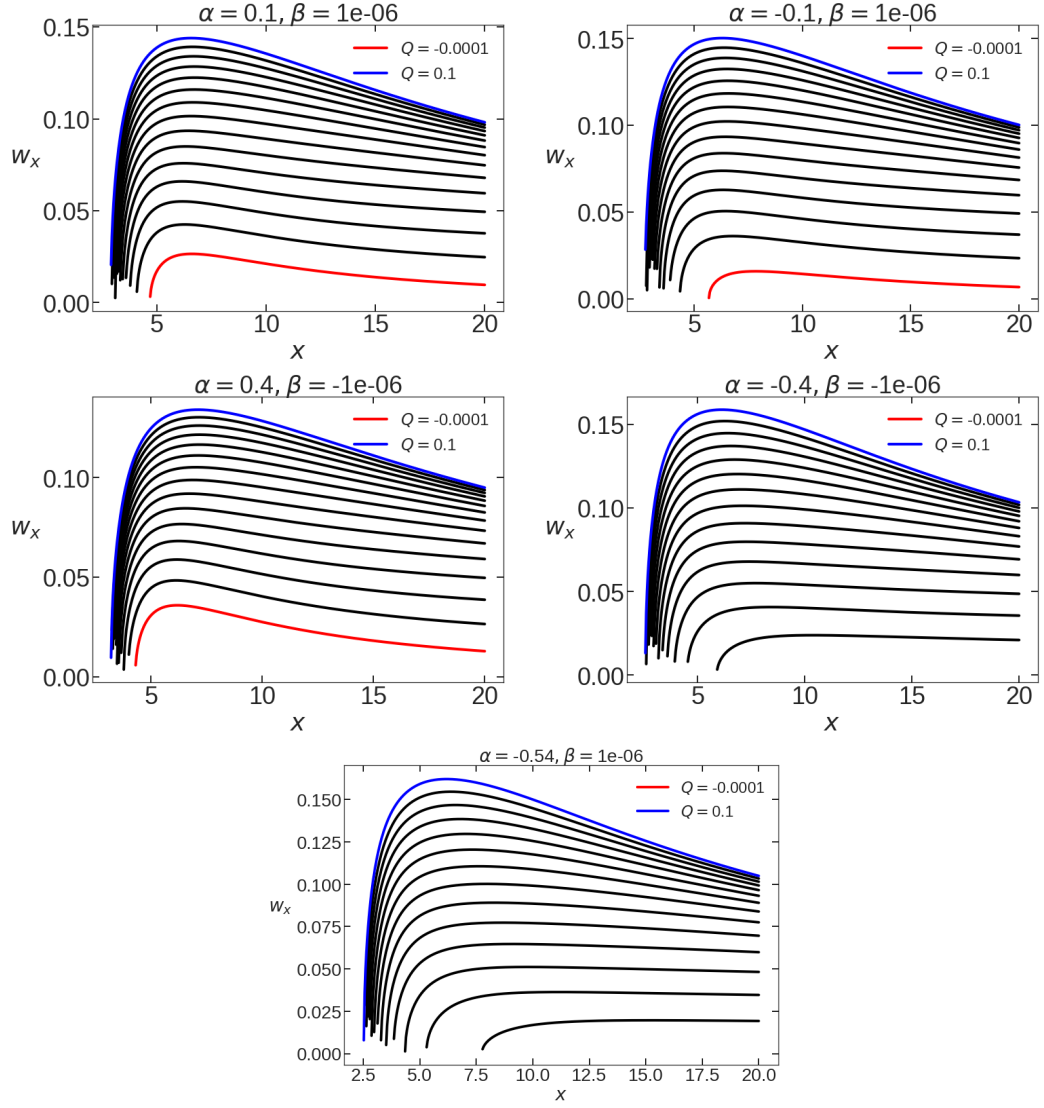


**Figure 12.1:** The radial epicyclic frequency  $w_x$  is plotted with respect to  $x$  for four different pairs of  $(\alpha, \beta)$ . On each plot, different values of  $Q$  are used from  $Q = -0.0001$  to  $Q = 0.1$ . The blue curve corresponds to  $Q = 0.1$  and the red curve to  $Q = -0.0001$ . When the red curve ( $Q = -0.0001$ ) is not appearing, it means for these pair, the radial epicyclic frequency is not real.

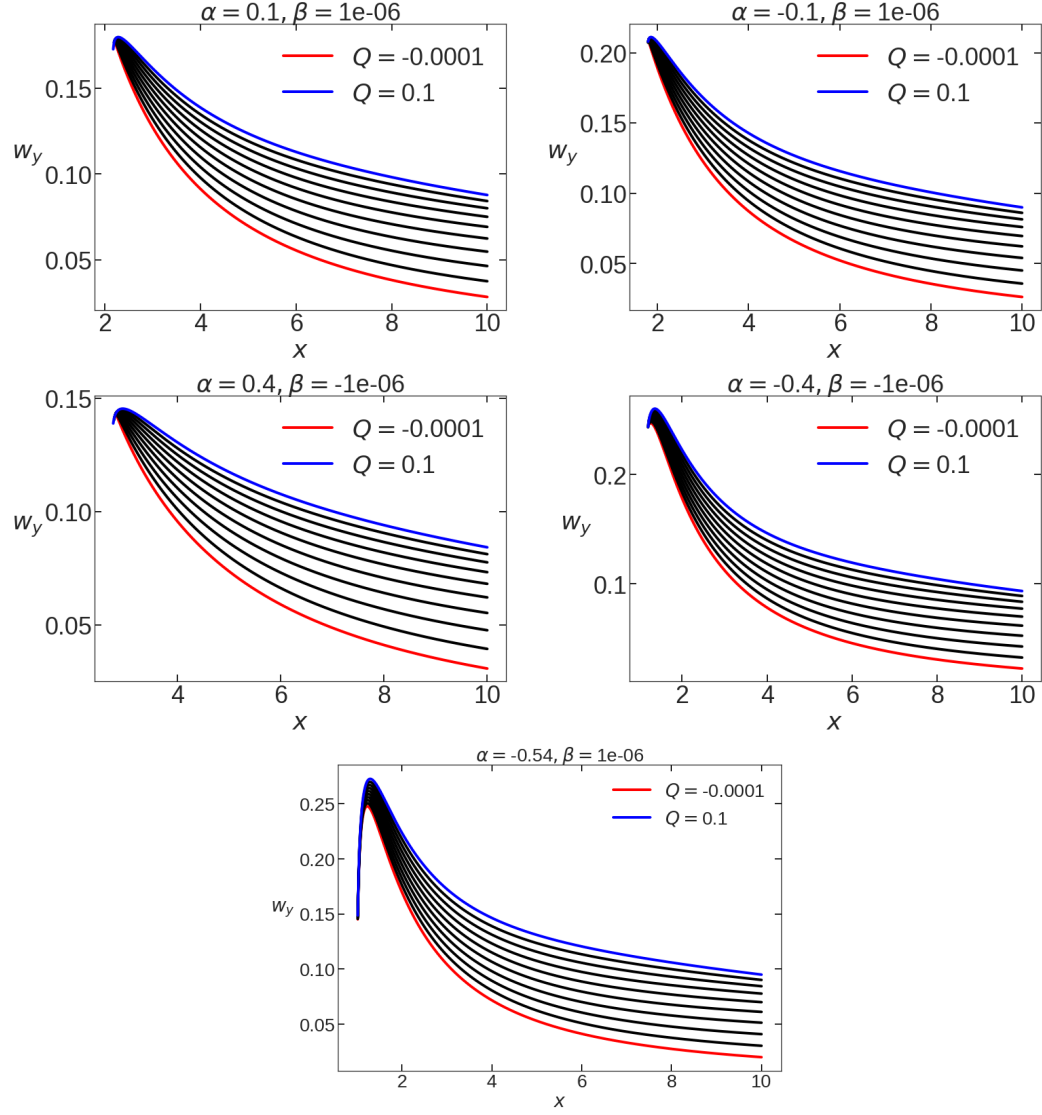


**Figure 12.2:** The vertical epicyclic frequency  $w_y$  is plotted with respect to  $x$  for four different pairs of  $(\alpha, \beta)$ . On each plot, different values of  $Q$  are used from  $Q = -0.0001$  to  $Q = 0.1$ . The blue curve corresponds to  $Q = 0.1$  and the red curve to  $Q = -0.0001$ .

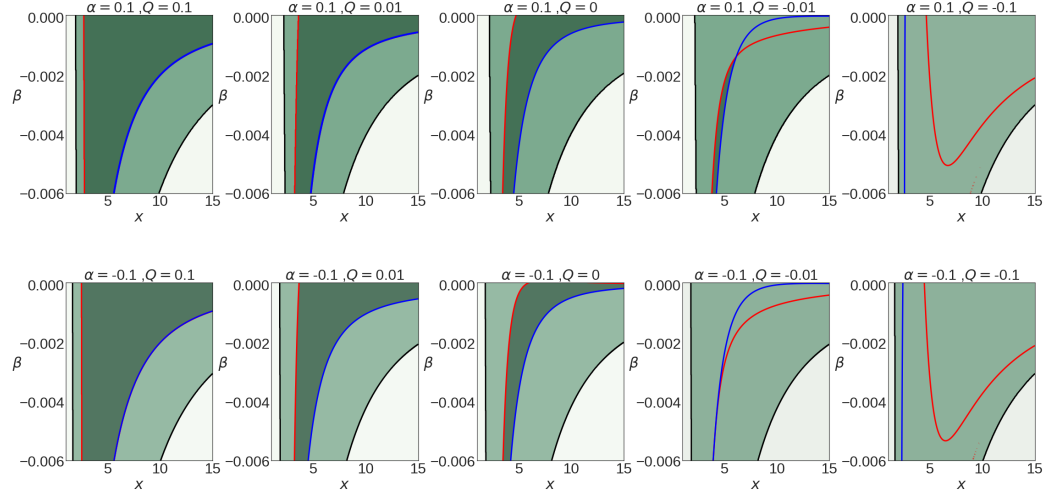


**Figure 12.3:** Stability of the timelike circular orbits of a charged particle in the  $(x, \beta)$ -plane. Timelike circular orbits can exist in the green light area. The blue curve represents  $w_y^2 = 0$  and the red one  $w_x^2 = 0$ . Timelike orbits are stable with respect to vertical and radial perturbations in the region where  $w_x^2 > 0$  and  $w_y^2 > 0$ . This area is depicted by the green-gray region, which combined the conditions of existence and the condition of stability,  $w_x^2 > 0$  and  $w_y^2 > 0$ . The analysis is done for two positive values of  $Q$ , two negatives values of  $Q$ , and the unmagnetized case  $Q = 0$ . Also, we have examined opposite signs of the deformation parameter  $\alpha$ .

not exist anymore. For larger negative values, a branch from above comes back in the physical range but keeps staying below the blue curve. On the  $(x, \alpha)$ - plane, this is due to the fact that the red curve goes up and then goes out from the physical range. This situation is mainly what is happening for negatives values of  $Q$ . A small area remains for values of the magnetic parameter close to zero  $Q = -0.01$ . In this case, it means there is no stable orbit in any direction in the chosen physical range.

## 12.2 Different possibilities

In Figures 12.5 and 12.6, different relations between the frequencies have been plotted [229]. Similar to Figures 12.3 and 12.4 the red and the blue curves are representing  $w_x^2 = 0$  and  $w_y^2 = 0$ , respectively. Besides, The orange line shows  $w_y^2 = \Omega^2$ , which leads to the hatched line region  $w_y^2 > \Omega^2$ . Also,  $w_x^2 = \Omega^2$  corresponds to the pink line related to the dark-green area where  $w_x^2 > \Omega^2$ . Furthermore,  $w_x^2 = w_y^2$  is shown by the yellow line. The corresponding region  $w_x^2 > w_y^2$  is presented in the hatched dotted line. By analyzing both Figures together, we can order the frequencies as a function of the magnetic parameter  $Q$ . We see that for  $Q \geq 0$ , the order's behavior will depend on two

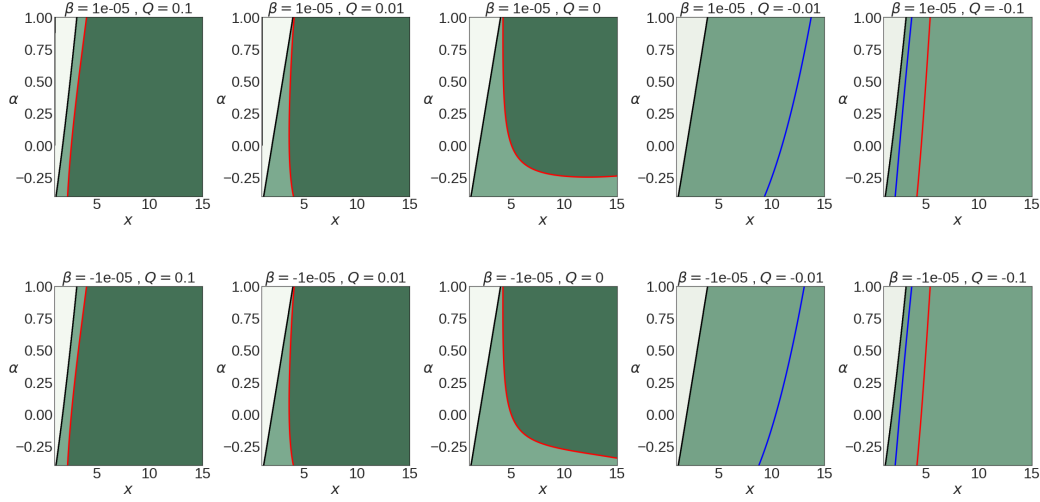


**Figure 12.4:** Stability of the timelike circular orbits in the  $(x, \beta)$ -plane. Timelike circular orbits exist in the green light area. The blue curve represents  $w_y^2 = 0$  and the red one  $w_x^2 = 0$ . Timelike orbits are stable with respect to vertical and radial perturbations in the region where  $w_x^2 > 0$  and  $w_y^2 > 0$ . The analysis has done for two positive values of  $Q$ , two negatives values of  $Q$ , also for the unmagnetized case  $Q = 0$ . Besides, we have examined opposite signs of the deformation parameter  $\alpha$ .

crossing points. One when the orange line crossed the red line and another one when the orange, pink and yellow all are crossing.

For small values of  $\beta$ , the order is pretty steady (see plots with  $Q \geq 0$  on the left in Figure 12.6). However, by increasing  $\beta$ , the crossing points appear, then the behaviour of ordering becomes more complicated (see plots with  $Q \geq 0$  on the left in Figure 12.5). For instance, using the second plot of the first row of Figure 12.5 in the stable region; namely, between the red and blue lines, the frequencies are ordered as follow:

- (i) Inside the hatched region (above the orange line) where  $\beta$  is close to zero, and for positive or negative  $\alpha$ :
  - (a) from the red line to the pink one:  $w_x^2 < \Omega^2 < w_y^2$ ,
  - (b) from the pink line to the yellow one:  $\Omega^2 < w_x^2 < w_y^2$ ,
  - (c) above the yellow line:  $\Omega^2 < w_y^2 < w_x^2$ .
- (ii) Outside the hatched region (below the orange line), where  $\beta$  has larger negative values, for any value of  $\alpha$ , the order of the frequencies is different,
  - (a) from the red line to the yellow one:  $w_x^2 < w_y^2 < \Omega^2$ ,

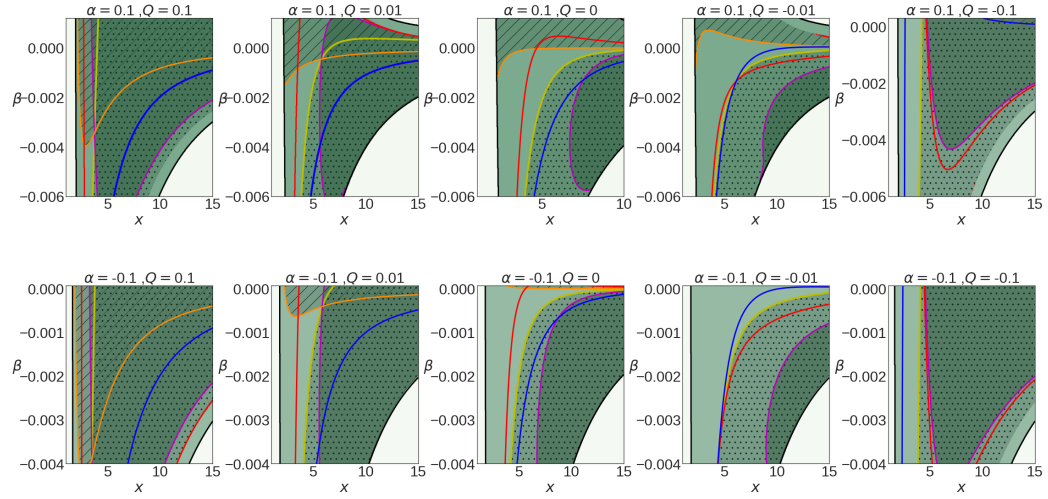


**Figure 12.5:** Order of the different epicyclic frequencies in the  $(x, \beta)$ -plane. Timelike circular orbits can exist in the green light area. The blue curve represents  $w_y^2 = 0$  and the red one  $w_x^2 = 0$ . The pink, orange and yellow depicts  $w_x^2 = \Omega^2$ ,  $w_y^2 = \Omega^2$  and  $w_x^2 = w_y^2$ , respectively. The green-gray area shows the region where  $w_x^2 > \Omega^2$ . The hatched line region represents the area where  $w_y^2 > \Omega^2$ . Also, the hatched dotted area is where  $w_x^2 > w_y^2$ . The analysis has done for different values of  $Q$ . Besides, two different values of the deformation parameter  $\alpha$  has been tested.

- (b) from the yellow line to the pink one:  $w_y^2 < w_x^2 < \Omega^2$ ,
- (c) and above the pink line:  $w_y^2 < \Omega^2 < w_x^2$ .

About negative values of  $Q$ , the order's distribution is different; however, the analysis is simple because the region of stability is strongly reduced. In this Figure, the only stable region appears for the positive value of  $\alpha$  and the case  $Q = -0.01$  (the fourth plot of the top line in Figure 12.6). In this small stable region (dark-green region in the corresponding plot in Figure 12.4), the order is as follow:

- (i) from the red to the yellow line (small extended vertically region):  $w_x^2 < w_y^2 < \Omega^2$ ,
- (ii) from the yellow line to the blue one:  $w_y^2 < w_x^2 < \Omega^2$ .

To sum up, increasing  $Q$  makes the region of specific order larger and creates new regions where the order of the frequencies is different.



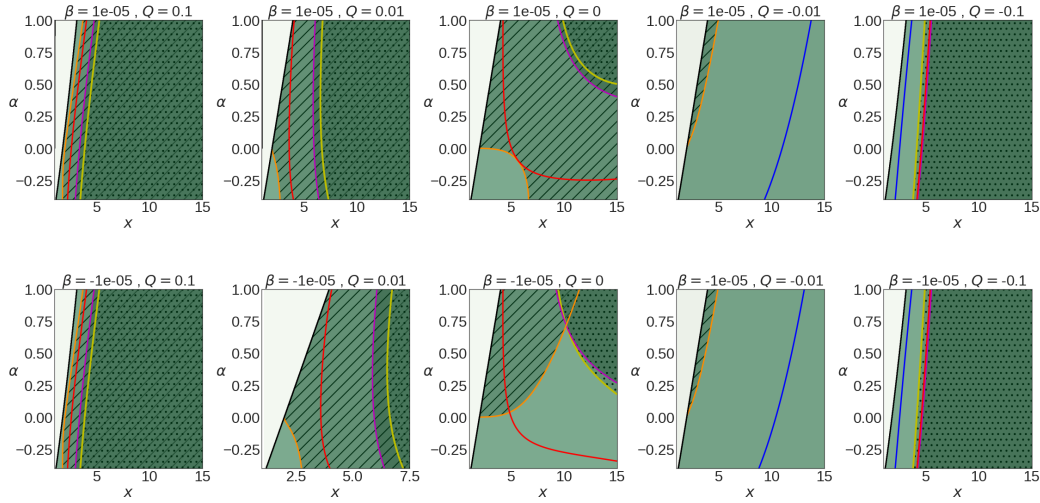


**Figure 12.6:** Order of the different epicyclic frequencies in the  $(x, \alpha)$ -plane. Timelike circular orbits exist in the green light area. The blue curve represents  $w_y^2 = 0$  and the red one  $w_x^2 = 0$ . The pink, orange and yellow depicts  $w_x^2 = \Omega^2$ ,  $w_y^2 = \Omega^2$  and  $w_x^2 = w_y^2$ , respectively. The green-gray area shows the region where  $w_x^2 > \Omega^2$ . The hatched line region represents the area where  $w_y^2 > \Omega^2$ . Finally, the hatched dotted area is where  $w_x^2 > w_y^2$ . The analysis has done for different signs of  $Q$ . In addition, two different values of the deformation parameter  $\beta$  has been tested.

## 12.3 Comparison with the observations

The results of fitting the charged particle oscillation frequencies to the observed frequencies of three microquasars XTE 1550-564, GRS 1915+105, and GRO 1655-40 is presented in Figures 12.7 and 12.8 presented in Table 12.1. Indeed significant spin is expected in astrophysical black holes at all scales, and it is important to develop the model that encode spin also, which is in progress. However, this results show for some chosen parameters of the model the fitting can be done even for the fast rotating microquasar GRS 1915+105.

The observed values of the twin HF QPO frequencies for this three sources show  $\nu_U : \nu_L = 3 : 2$  ratio [66, 230]. In Figure 12.7 the resonance model EP is fixed and we try to find the best fitting with exercising different parameters of the model; the deformation, the distortion and the magnetic parameter.

In Figure 12.7 each plot corresponds to different values of the distorted parameter  $\beta$ , and the line styles present various deformation parameter  $\alpha$ . Finally, the magnetic parameter is given by the different colors. Interestingly a direct inspection of the various combinations of the parameters shows the crossing of the data line and could fit with the data. Although the fitting

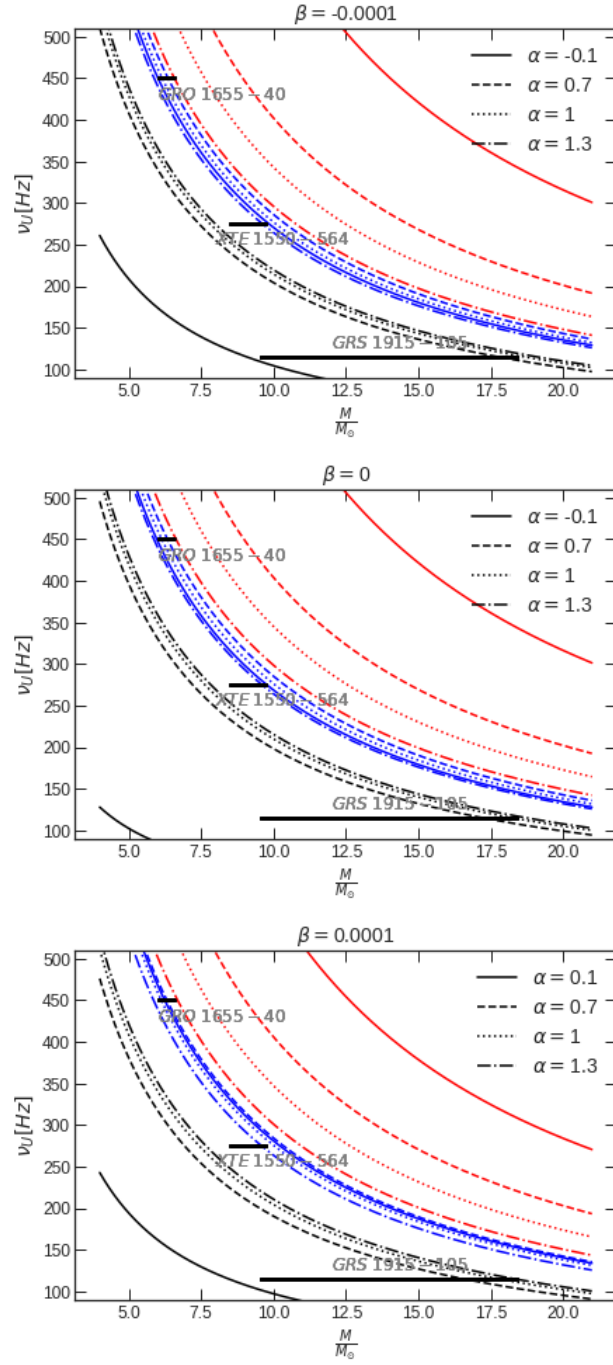


**Figure 12.7:** The upper oscillation frequency  $\nu_U$  at the resonance radius 3 : 2 is presented for various combinations of the studied parameters for the EP model. The magnetic parameter vary with the color's lines. The black lines depict  $Q = 0$  (unmagnetized case). The blue lines show  $Q = 0.01$  and the red lines present  $Q = 0.1$ . The upper frequency is compared to the mass-limits obtained from observations of three mentioned microquasars.

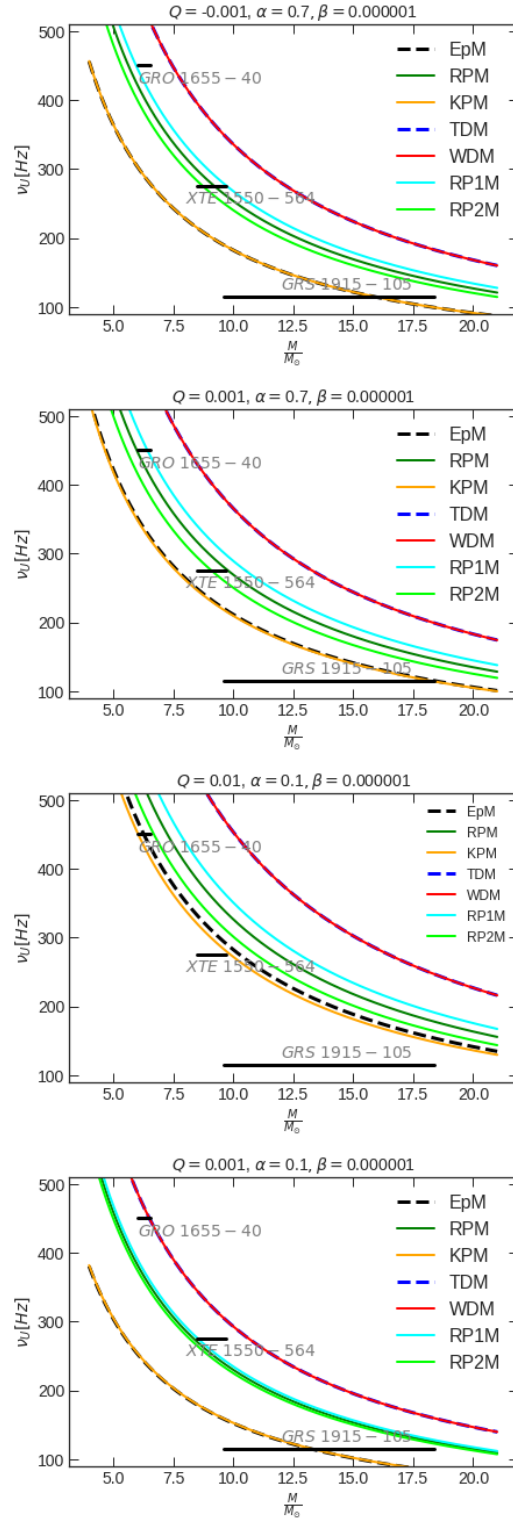


**Figure 12.8:** The upper oscillation frequencies for the models presented in the Table 3.1 are compared to the mass-limits obtained from observations of three microquasars for various set of parameters.

Table 12.1: Observed twin HF QPO data for the three micro-quasars, based on measurements independent of the HF QPO measurements given by the spectral continuum fitting.

Source	GRO 1655-40	XTE 1550-564	GRS 1915+105
$\nu_U$	447 — 453	273 — 279	165 — 171
$\nu_L$	295 — 305	179 — 189	108 — 118
$\frac{M}{M_\odot}$	6.03 — 6.57	8.5 — 9.7	9.6 — 18.4
$a$	0.65 — 0.75	0.29 — 0.52	0.98 — 1

totally depends on the combination of parameters, we still can expect to have a better fitting for choosing a larger  $\alpha$  in the combination.

In Figure 12.8 we have analyzed the fitting of different models presented in Section 3.3.2. In fact, we note that although different sets of parameters can fit the data, even for the fast-rotating source as GRS 1915+105 and GRO 1655–40, we focus on this fitting in the case of relatively slowly rotating XTE 1550-564 source which is more compatible with our set up. As Figure 12.8 suggests, for chosen parameters  $Q$ ,  $\alpha$ , and  $\beta$ ; the best fit almost corresponds to RP2, RP, and RP1 models in low spin cases. For a high spin source Kp and Ep models seems to be the best fit. It is worth comparing this result with the behavior of these models in Kerr space-time [106]. In general, it appears that a non-zero magnetic field facilitates the fitting procedure. As a result, we find that WD and TD almost have similar behavior. The same is true for Ep and Kp, while RP1, RP2, and RP may deviate from each other depending on the magnetic field and deformation parameter  $\alpha$ . These results are almost compatible with the result in Kerr space-time, where spin plays a similar role to  $\alpha$  [106]. More precisely, by increasing  $\alpha$  the deviation between RP’s models increases. In this way, studying these three models and the deviations from each other may play an important role to recognize the oblateness of the source from observational data. However, a deeper analysis shows that we can note that almost for  $\alpha \in [0.1, 0.9]$  one can have a better fitting to observations.

Further analysis reveals that the curves take their minimum at different radius depending on the choice of parameters. We see that in all cases, almost the positive and negative values of  $\beta$  take their maximum at the same radius; however, further investigation indicates that this radius is smaller for negative values of this parameter. Also, the maximums in all curves in the desirable domain depend on the ratio; for example, we see that as this ratio becomes larger, the maximum happens in smaller radius. This means that the resonance is not monotonic after some distance from the central object,

depending on the combination of parameters in this background.

## 12.4 Summary and conclusion

In this chapter, we studied the dynamics of test charged particles in the presents of a uniform magnetic field, also discussed the case of vanishing magnetic field. Further, we have examined different QPOs models considered in [106] in the vicinity of a deformed compact object up to the quadrupole 7. We have shown that the effect of parameters on the radial and vertical frequencies around a stable equatorial orbit is significant and different ordering can arise in comrasion to the Schwarzschild and Kerr solutions. In addition, the resonant phenomena of the radial and vertical oscillations at their frequency ratio 3 : 2 depending on chosen parameters, and can be well related to the observed frequencies of the HF QPOs 3 : 2 in the microquasars GRS 1915 + 105, XTE 1550 – 564, GRO 1655 – 40. In particular, different combinations can fit link to different observed effects.

This is worth mentioning that in this deformed and distorted background, with different combinations of quadorpole parameters  $\alpha$ ,  $\beta$  and charge  $Q$ , it is possible to have other ratios which can be relevant in other observed data like in other frequencies observed in the microquasar GRS 1915 + 105, see for example [231].

Importantly, the result of fit into data showed the Generalized q-metric and q-metric can imitate some effects produced by the Kerr space-times reflected in the QPOs. In fact, the quadrupole parameter in these metrics related to the central source, for some range of values, can play the role of spin in the Kerr black hole perfectly. The results of this chapter are presented in [232, 229].



## Oscillations of tori in the background of Generalized q-metric

As mentioned earlier, the radial epicyclic frequency in an accretion disc around compact objects may serve to interpret the observed QPOs phenomenon in different models. However, to have a more accurate model, one needs to pay attention to the problems in using the expression of the radial epicyclic frequency obtained in a test particle and investigate it in a perfect fluid case. The approach employed here is considered by Rezzolla et al. for Schwarzschild, and Kerr space-times [115, 116]. However, instead of power-law angular momentum distribution, here the trigonometric description for angular momentum is used where introduced in Section 2.2.2.

In this chapter, we intend to employ the local perturbation analysis for Thick disc model oscillation when the perturbations of the space-time are neglected via a local approach. This approach is briefly explained in Section 3.4. Nevertheless, since their domains are quite different, there is no difficulty in recognizing them. In the next section, we briefly discuss the Thick disc model in this background; then, in the second section, we study the radial epicyclic frequency.

### 13.1 The Thick disc model

Before start studying the epicyclic frequency, without going into the details we present the Thick disc model in this background briefly. To be convenient we state the metric again here

$$\begin{aligned}
ds^2 = & - \left( \frac{x-1}{x+1} \right)^{(1+\alpha)} e^{2\hat{\psi}} dt^2 + M^2(x^2-1) e^{-2\hat{\psi}} \\
& \left( \frac{x+1}{x-1} \right)^{(1+\alpha)} \left[ \left( \frac{x^2-1}{x^2-y^2} \right)^{\alpha(2+p)} e^{2\hat{\gamma}} \right. \\
& \left. \left( \frac{dx^2}{x^2-1} + \frac{dy^2}{1-y^2} \right) + (1-y^2) d\phi^2 \right], \tag{13.1}
\end{aligned}$$

where

$$\begin{aligned}
\hat{\psi} = & -\frac{\beta}{2} [-3x^2y^2 + x^2 + y^2 - 1], \\
\hat{\gamma} = & -2x\beta(1+\alpha)(1-y^2) \\
& + \frac{\beta^2}{4}(x^2-1)(1-y^2)(-9x^2y^2 + x^2 + y^2 - 1). \tag{13.2}
\end{aligned}$$

Figure 13.1 shows the map of relativistic tori with constant angular momentum  $\ell_{\text{cons.}} = (\ell_{\text{ms}} + \ell_{\text{mb}})/2$  for different parameters  $\alpha$  and  $\beta$ . I should emphasize that the place of  $\ell_{\text{ms}}$  and  $\ell_{\text{mb}}$  also depends on quadrupoles  $\alpha$  and  $\beta$ . As we expected from what we have seen so far, for negative  $\alpha$  parameters the disc is closer to the central object than for positive  $\alpha$ s. In particular, for both positive values of  $\alpha$  and  $\beta$  we have a more radially extended disc. In fact, when both are positive the disc configuration is farther away from the central object and the external matter has more chance to reveal its influence. However, the impact of distortion parameter  $\beta$  is less than  $\alpha$  for the chosen values. Note that to have a good comparison with literature we plot all Figures in the  $(r, \theta)$  plane which is obtained easily by a simple transformation (6.10).

In Figure 13.2 we investigate the disc configuration for a non-constant angular momentum as it is needed to have the non-vanishing radial epicyclic frequency. We write this angular momentum distribution again to be easier to follow

$$\ell(r, \theta) = \begin{cases} \ell_0 \left( \frac{\ell_{\text{K}(r)}}{\ell_0} \right)^\gamma \sin^{2\delta}, & r \geq r_{\text{ms}}, \\ \ell_0 (\zeta)^{-\gamma} \sin^{2\delta}, & r < r_{\text{ms}}, \end{cases} \tag{13.3}$$

where  $\ell_0 = \zeta \ell_{\text{K}}(r_{\text{ms}})$ , and  $\ell_{\text{K}}$  is the Keplerian angular momentum in the equatorial plane, and



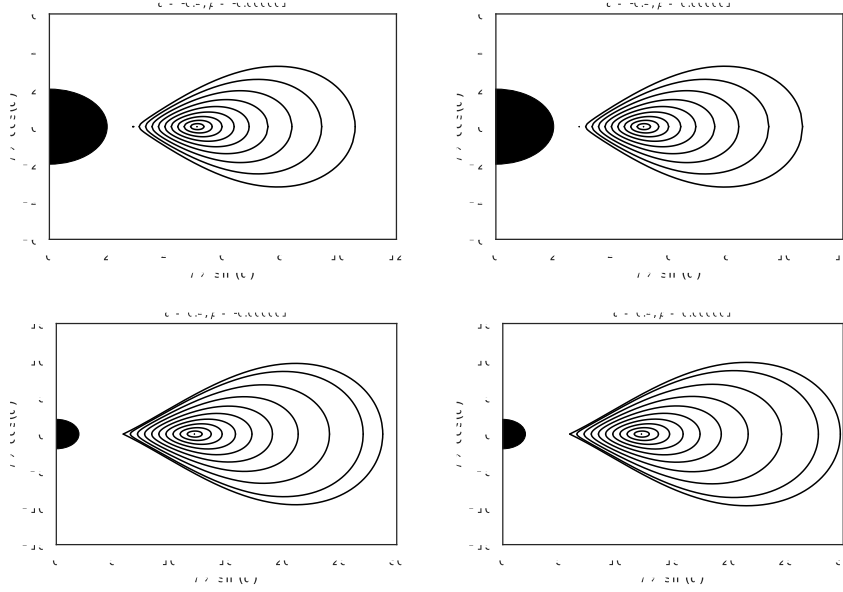


**Figure 13.1:** Equipotential surfaces for tori with a constant angular momentum distribution for various values of combination of  $\alpha$  and  $\beta$  in  $(r, \theta)$  coordinates.

$$0 \leq \gamma \leq 1, \quad -1 \leq \delta \leq 1, \quad -1 \leq \zeta \leq \frac{\ell_K(x_{mb})}{\ell_K(x_{ms})}. \quad (13.4)$$

As we have already seen for q-metric 11.2 and distorted Schwarzschild solution 11.1 these parameters in this distribution have a strong correlation with each other. However, for each fixed pair of  $(\gamma, \delta)$  we can see the play of metric parameters  $\alpha$  and  $\beta$  in each row. In this Figure, the same values are chosen as for quadrupoles as in Figure 13.1 to see the effect of angular momentum distribution clearly. The impact of different combinations of  $(\gamma, \delta)$  is seen in columns. We see that choosing the angular momentum profile has a strong effect on the shape and size of the disc. As we chose higher values for these pairs the disc configuration become smaller. However, the interplay between these two quadrupole parameters, is similar to the previous case.

## 13.2 Radial epicyclic frequency

Following the same steps for the Schwarzschild and Kerr solutions, in mentioned papers described in Section 3.4, one can obtain the radial epicyclic frequency of a perfect fluid disc in a Generalized q-metric space-time without writing the expressions of the perturbed equations and dispersion relation,

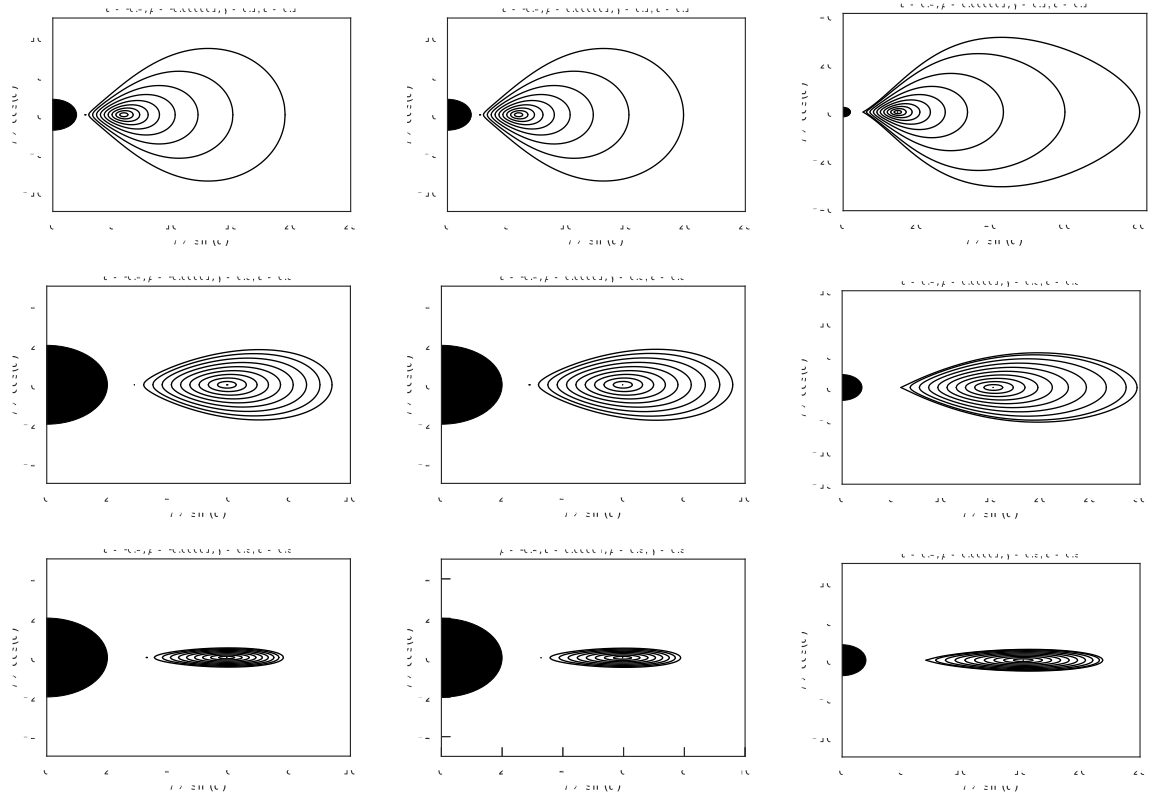


**Figure 13.2:** Equipotential surfaces for tori with the non-constant angular momentum distribution (2.50) for different parameters in combinations with quadrupole parameters  $\alpha$  and  $\beta$ .

due to their complexity the  $\kappa_r$  squared in this background is obtained as follows

$$\kappa_r^2 = \frac{2e^{\beta(x^2-1)+2\psi-2\lambda} \left(\frac{x+1}{x-1}\right)^\alpha \Omega V (-2\Omega V + (x^2-1)\partial_x \Omega)}{F}, \quad (13.5)$$

where

$$V = 1 + \alpha + (\beta - 1)x - \beta x^3 + (x^2 - 1)\partial_x \psi \quad (13.6)$$

$$F = (x^2 - 1) \left( -e^{2\psi} + e^{\beta(x^2-1)} (x+1)^2 \left(\frac{x+1}{x-1}\right)^\alpha \Omega^2 \right),$$

$$\psi(x) = \left(\frac{1+\alpha}{2}\right) \ln \frac{x-1}{x+1} + \hat{\psi}, \quad (13.7)$$

$$\lambda(x) = \left(\frac{1+\alpha}{2}\right) \ln \frac{x+1}{x-1} + \left(\frac{\alpha(2+\alpha)}{2}\right) \ln \frac{x^2-1}{x^2} - \hat{\psi} + \hat{\gamma}. \quad (13.8)$$

In Figure 13.3 we see the plot of  $\kappa_r$  for different values of  $\alpha$  and Schwarzschild case, with  $\gamma = 0.1$  in the angular momentum distribution (13.3). First of all, in calculation of the epicyclic radial frequency because of vertically integration, we are interested in a neighborhood of equatorial plane; therefore parameter  $\delta$  in the angular momentum distribution equation (13.3) plays no role. However, we have its contribution in the disc configuration. In this Figure, the blue curve represents the  $\kappa_r$  for a test particle with a Keplerian angular momentum. The red line is  $\kappa_r$  for a perfect fluid disc. We see that for all values of the deformation parameter  $\alpha$  the radial epicyclic frequency for a test particle is higher than for a perfect fluid. However, by increasing  $\gamma$  these the red curves goes closer to the blue one by the definition of this angular momentum. As it is stated before, we are interested in prograde orbits which for this the maximum of the frequency is outside of the ISCO ( $r_{ms}$ ) as mentioned earlier in Chapter 3.4. Of course, the place of ISCO is dependent on quadrupole moments. We see that for  $\alpha < 0$  the maximum is higher than for  $\alpha > 0$ , also it is closer to the central object. In general, the amplitude and its position are monotonically decreasing functions of  $\alpha$ .

Figure 13.4 shows the radial epicyclic frequency for different parameters of  $\alpha$ ,  $\beta$ , also  $\gamma$  in angular momentum (13.3). In this Figure, the line styles present the values of  $\alpha$  and colors represent different values of the distortion parameter  $\beta$ . We see that for any fixed value of  $\alpha$  the curve corresponds to a positive value of  $\beta$  is below  $\beta = 0$ , and the one related to  $\beta < 0$  is upper. Furthermore, there is an interesting fact about positive quadrupole  $\beta$ . When

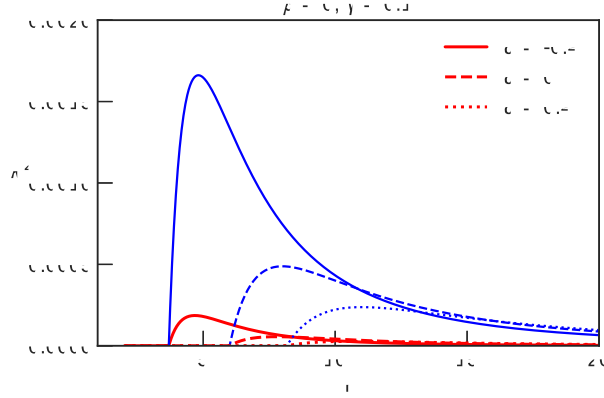


**Figure 13.3:** Left plot: In red  $\kappa_r$  is depicted for a perfect fluid with the angular momentum (13.3)( $\gamma = 0.1$ ). In blue,  $\kappa_r$  is depicted for a test particle with respect to  $r$ . The vertical dashed line corresponds to the radius of the marginally stable orbit.

$\beta$  is positive the radial epicyclic frequency terminates much faster regardless of sign of  $\alpha$ . It is worth mentioning that as we saw before 7, the place of ISCO also depends on the value of  $\beta$ ; however, since their values are very small the main contribution to determine its position comes from  $\alpha$  and on the plots, we can not see the differences. In general, we see the same behavior for  $\kappa_r$  both for  $\alpha$  and  $\beta$  regarding amplitude and its position. Additionally, the larger parameter  $\beta$  has more influence on the area  $r > \text{ISCO}$  with its definition (13.3) that we also see in Figure 13.4.

### 13.3 Summary and conclusion

In this chapter, we studied the radial epicyclic frequency of the Thick disc for a perfect fluid. As was mentioned before in an effort to have a better fitting of the data to the analytical models of QPOs, one way is to consider a perfect fluid frequency rather than a test particle. In this regard, we derived the  $\kappa_r$  for the Generalized q-metric and investigated the influences of the metric quadrupoles. In addition, the impact of chosen angular momentum distribution parameters on the disc configuration and  $\kappa_r$  in this background was investigated. In general, for higher quadrupoles,  $\kappa_r$  can have a lower amplitude where is placed also farther away from the central object. Indeed, this result is consistent with other results from different parts of this study that was stated so far. The results also compare with a test particle extensively are submitted to the journal.

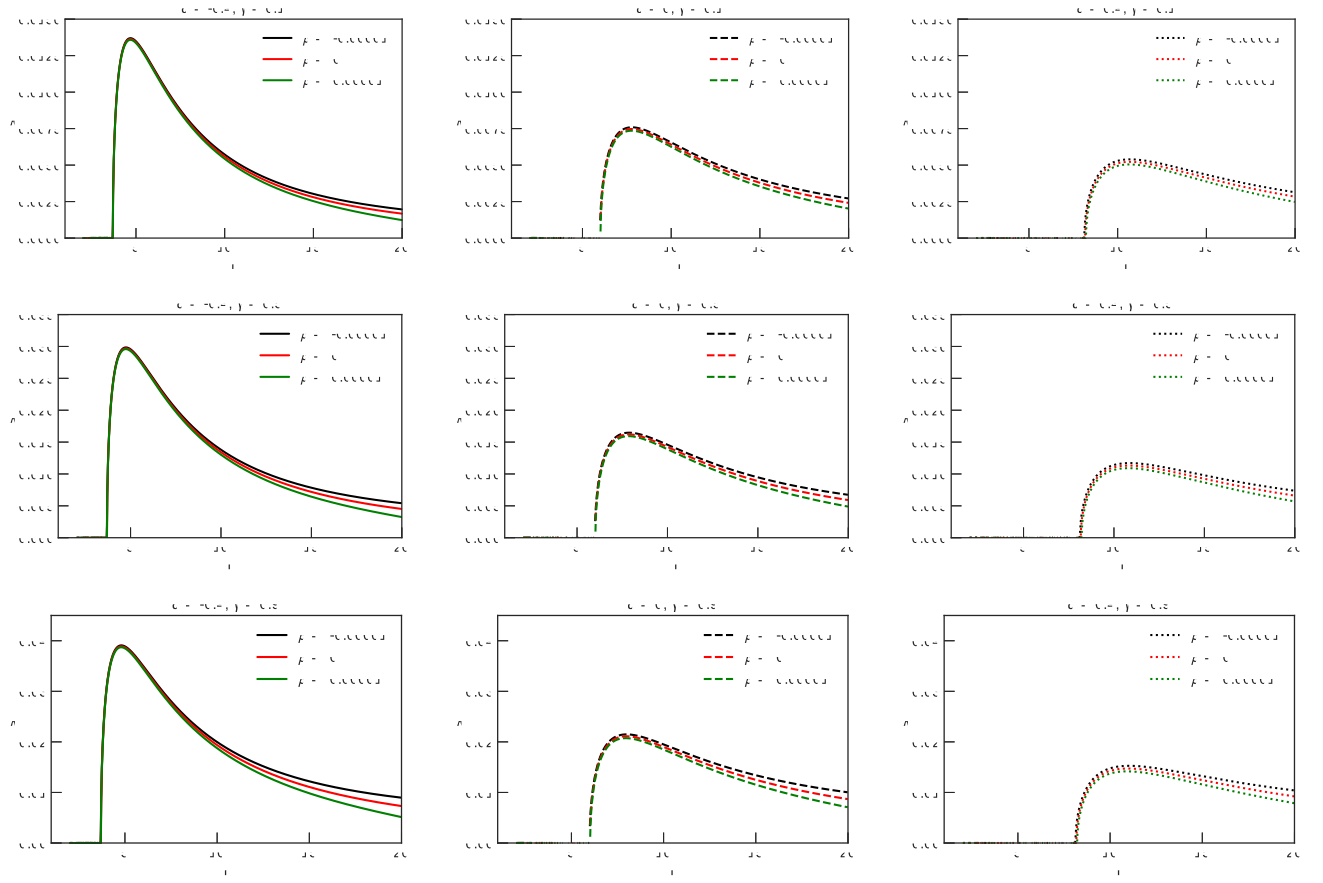


**Figure 13.4:**  $\kappa_r$  with respect to  $r$  for a perfect fluid with a non-constant angular momentum (13.3), and for different combination of  $\beta$ ,  $\alpha$  and  $\gamma$ . The solid lines presents  $\alpha = -0.4$ , the dashed lines  $\alpha = 0$ , and the dotted one is  $\alpha = 0.4$ .



## Shadow in the presence of cold plasma in the background of q-metric

In this chapter, we analytically analyze the influence of the cold plasma on the shadow in the q-metric background. The structure is briefly explained in Chapter 4. We present the result in the prolate spheroidal coordinates. In fact, the non-vanishing quadrupole moment will give rise to some deviation from the spherical symmetry; however in this work, to start with, we employ the condition  $y = 0$  and choose relatively small quadrupoles. Under these assumptions, we consider the metric to be spherically symmetric as the first step in studying shadow in this background.

### 14.1 Photon sphere

From Chapter 4, to have the equation of the photon sphere (4.9) first we should derive  $h^2(x)$  via equation (4.6). In this space-time this function reads as

$$h^2(x) = M^2(x^2 - 1) \left( \frac{x+1}{x-1} \right)^{1+q} \left[ \left( \frac{x+1}{x-1} \right)^{1+q} - \frac{\omega_p^2}{p_t^2} \right], \quad (14.1)$$

so the equation of the photon sphere (4.9) becomes

$$\left( \frac{x+1}{x-1} \right)^{1+q} [x_{ph} - 2(1+q)] - \frac{\omega_p^2}{p_t^2} [x_{ph} - (1+q)] - (x^2 - 1) \frac{\omega_p \omega'_p}{p_t^2} = 0, \quad (14.2)$$

where for  $q = 0$  and Schwarzschild-like coordinates this is reduced to photon sphere for Schwarzschild solution for a special choice of  $\omega_p$  [233]. Besides, for

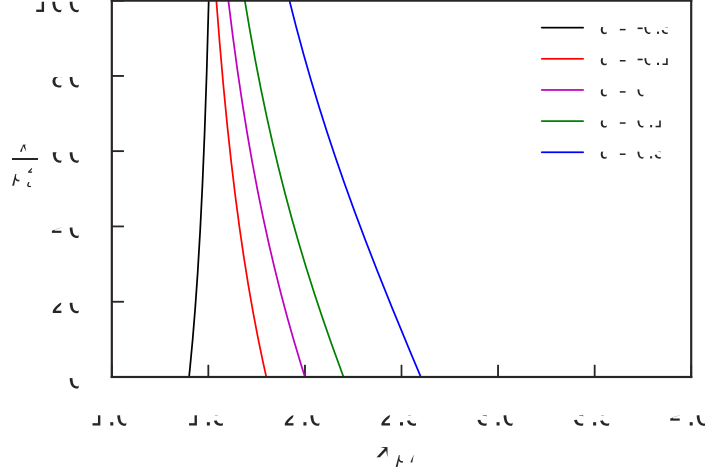


**Figure 14.1:** The photon sphere for the different values of  $q$ , and  $\frac{k}{p_t^2} = 1$ , and for  $\omega^2 \propto (x+1)^{-3}$ .

$\omega_p = 0$  we recover  $x_{ph} = 2$  or equivalently  $r_{ph} = 3M$ . If we choose  $w_p$  as a special power-law [233]

$$\omega_p^2 = \frac{k}{(x+1)^3}, \quad (14.3)$$

by substituting in equation (14.2) we obtain

$$\left(\frac{x+1}{x-1}\right)^{1+q} [x_{ph} - 2(1+q)] - \frac{k}{p_t^2(x_{ph}+1)^3} [x_{ph} - (1+q)] + \frac{3k}{2p_t^2} \frac{(x_{ph}-1)}{(x_{ph}+1)^3} = 0. \quad (14.4)$$

In Figure 14.1 we see the photon sphere for different chosen values of parameter  $q$  for this chose of  $\omega_p^2 \propto (x+1)^{-3}$ . We see that in all cases, plasma has a negative effect on the place of the photon sphere. However, a further investigation shows that by choosing  $q = -0.25$ , one can neutralise the effect of plasma on the photon sphere. As a consequence, also by having a smaller value of  $q < -0.25$ , the impact of plasma on the size of the photon sphere will reverse. Nevertheless, one should keep in mind that we don not want to go very far from zero to have a valid approximation of the spherical symmetric set-up. Additionally, for any fixed parameter related to plasma (i.e. fixed  $\frac{k}{p_t^2}$ ) we see by increasing  $q$  the place of photon sphere goes farther from the central object. We saw such a behavior also in the place of ISCO



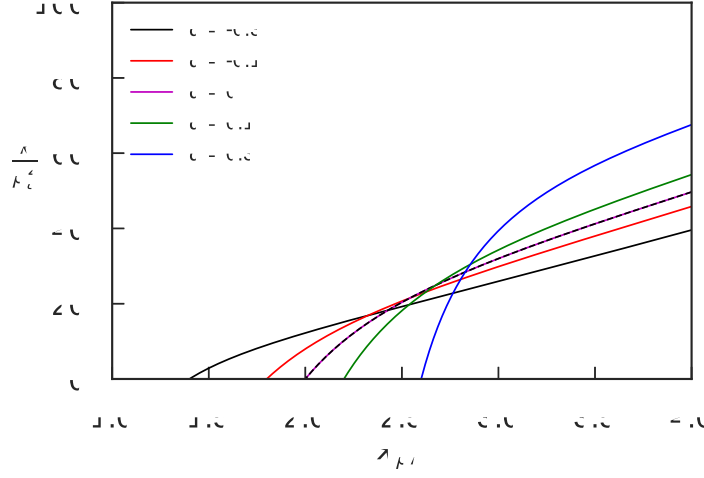


**Figure 14.2:** The photon sphere for the different values of  $q$ , and  $\frac{k_z}{p_t^2} = 1$  and for  $\omega^2 \propto (x+1)^{-3/2}$ .

in Chapter 7.3. However, the impact of plasma can be totally different for different powers of  $(x+1)$  (smaller or larger than  $-2$ ). For example, Figure 14.2 shows the place of photon sphere for when we have  $\omega_p^2 \propto (x+1)^{-3/2}$ . Even it can totally change the effect of quadrupole as we see in Figure 14.2. In the following section, we analyze the radius of shadow in this set-up.

## 14.2 Radius of Shadow in the low density plasma

As mentioned in Chapter 4, in this set-up the boundary of the shadow (4.18) by assuming  $\omega_p \ll \omega$  is given by

$$\sin^2 \alpha_{bd} = \frac{(x_{ph}^2 - 1) \left( \frac{x_{ph}+1}{x_{ph}-1} \right)^{(1+q)} \left( \frac{x_O-1}{x_O+1} \right)^{(1+q)}}{(x_O^2 - 1) \left( \frac{x_O+1}{x_O-1} \right)^{(1+q)} \left( \frac{x_{ph}-1}{x_{ph}+1} \right)^{(1+q)}} \left[ 1 - \left( \frac{1+2q}{3+2q} \right)^{(1+q)} \left( \frac{\omega_p^2(2+2q)}{p_t^2} \right) + \left( \frac{x_O-1}{x_O+1} \right)^{(1+q)} \left( \frac{\omega_p^2(x_O)}{p_t^2} \right) \right]. \quad (14.5)$$

Therefore, one can investigate the revelation of the plasma impact by calculating  $x_O$  from

$$\left( \frac{1+2q}{3+2q} \right)^{(1+q)} \left( \frac{\omega_p^2(2+2q)}{p_t^2} \right) - \left( \frac{x_O-1}{x_O+1} \right)^{(1+q)} \left( \frac{\omega_p^2(x_O)}{p_t^2} \right) = 0. \quad (14.6)$$

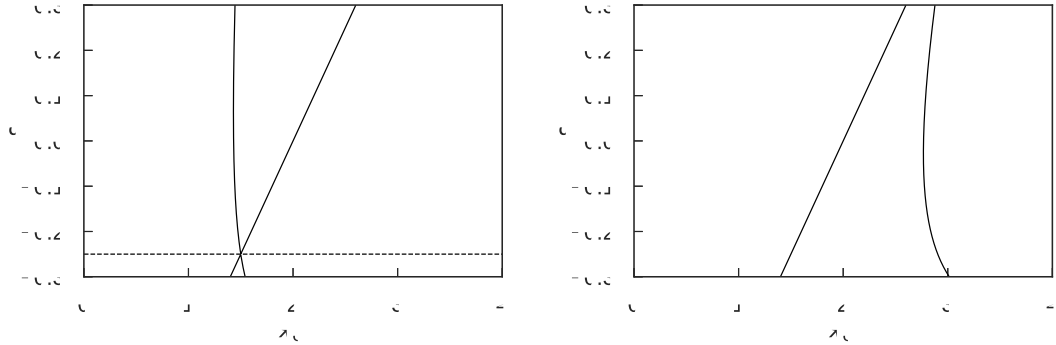


**Figure 14.3:** Variation of  $x_O$  with respect to  $q$ . Left plot:  $\omega_p^2 \propto (x+1)^{-3}$ . The dashed line correspond to  $q = -0.25$ . Right plot:  $\omega_p^2 \propto (x+1)^{-3/2}$

By choosing again  $\omega_p$  as equation (14.3) we obtain

$$\left(\frac{1+2q}{3+2q}\right)^{(1+q)} \left(\frac{k}{p_t^2(2+2q)^3}\right) - \left(\frac{x_O-1}{x_O+1}\right)^{(1+q)} \left(\frac{k^2}{p_t^2(x_O)^3}\right) = 0. \quad (14.7)$$

For  $q = 0$  it gives  $x_O \simeq 1.999$ . However, in Figure 14.3 we see the variation of  $x_O$  with respect to  $q$ . In fact, for a homogeneous plasma, there is a unique photon sphere for any choice of  $q$ . However, in general, there is not necessarily a unique photon sphere in each case. Nevertheless, determining shadow is more relevant to the outermost photon sphere.

Figure 14.4 shows the dependency of size of shadow on the frequency of plasma  $\omega_p$  in the Schwarzschild background. Of course, the place of  $x_O$  in each case when the effect manifests calculated with respect to related  $\omega_p$  from equation (14.7). Figure 14.5 and 14.6 investigate the dependency of the shadow radius on  $\frac{k}{p_t^2}$  for different quadrupoles  $q$  and different observers. For chosen values of  $q$ , we see that the radius of the shadow is a decreasing function of the distance of the observer from the source. Further, it turns out that for any  $q \geq 0$ , the radius of shadow for any fixed observers is smaller in the presence of plasma compared to the vanishing case. In particular, for larger  $q$ , we have a smaller radius for each fixed observer. On the contrary, for  $q \leq 0$  for closer observers to the central object, we have a larger shadow radius which increases by increasing  $|q|$ . In addition, considering different power of distance in  $\omega_p$  cause different behavior in the size of shadow; nevertheless, in general, we have a reduction in size for a distant observer.

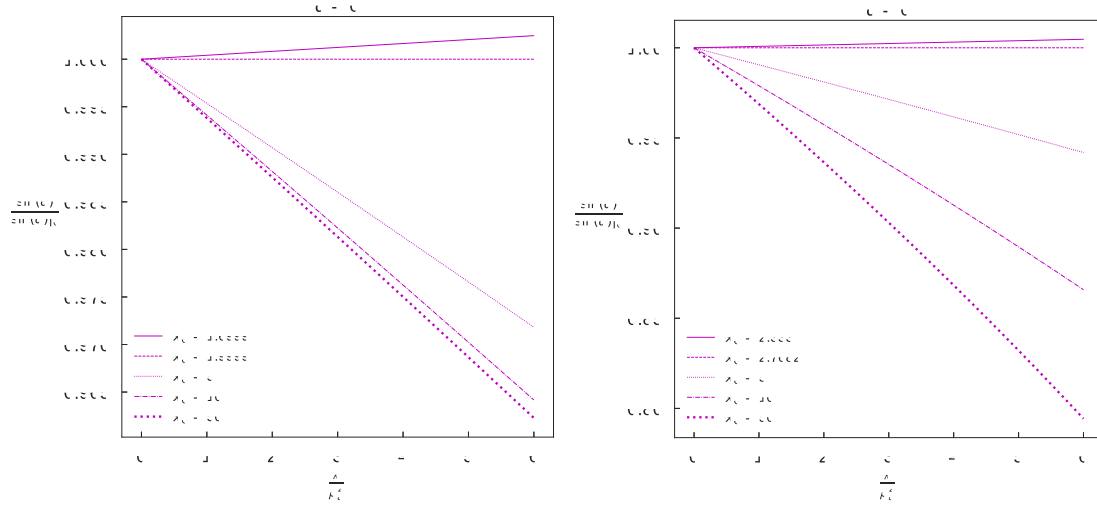


**Figure 14.4:** Variation of  $\frac{\sin \alpha}{\sin \alpha|_0}$  with respect to  $\frac{k}{p_t^2}$  for various values of  $x_O$  for the Schwarzschild case  $q = 0$ , in the left plot  $\omega_p \propto (x+1)^{3/2}$ , in the right one  $\omega_p \propto (x+1)^{3/4}$ .

### 14.3 Summary and conclusion

In this chapter, we studied the photon sphere and the size of shadow in the background of q-metric, as the first step approximation. We have seen the influence of plasma as well as the metric parameter on the place of the photon sphere. In general, this depends highly on the chosen profile of plasma frequency and may result in an increase or decrease in the photon sphere as well as its position. The size of the shadow also depends on the quadrupole values and the plasma frequency can change. However, for a distant observer in all cases, we see a reduction in the size. The second step of this study is considering the axisymmetric space-time in a more general set-up that is in preprint.

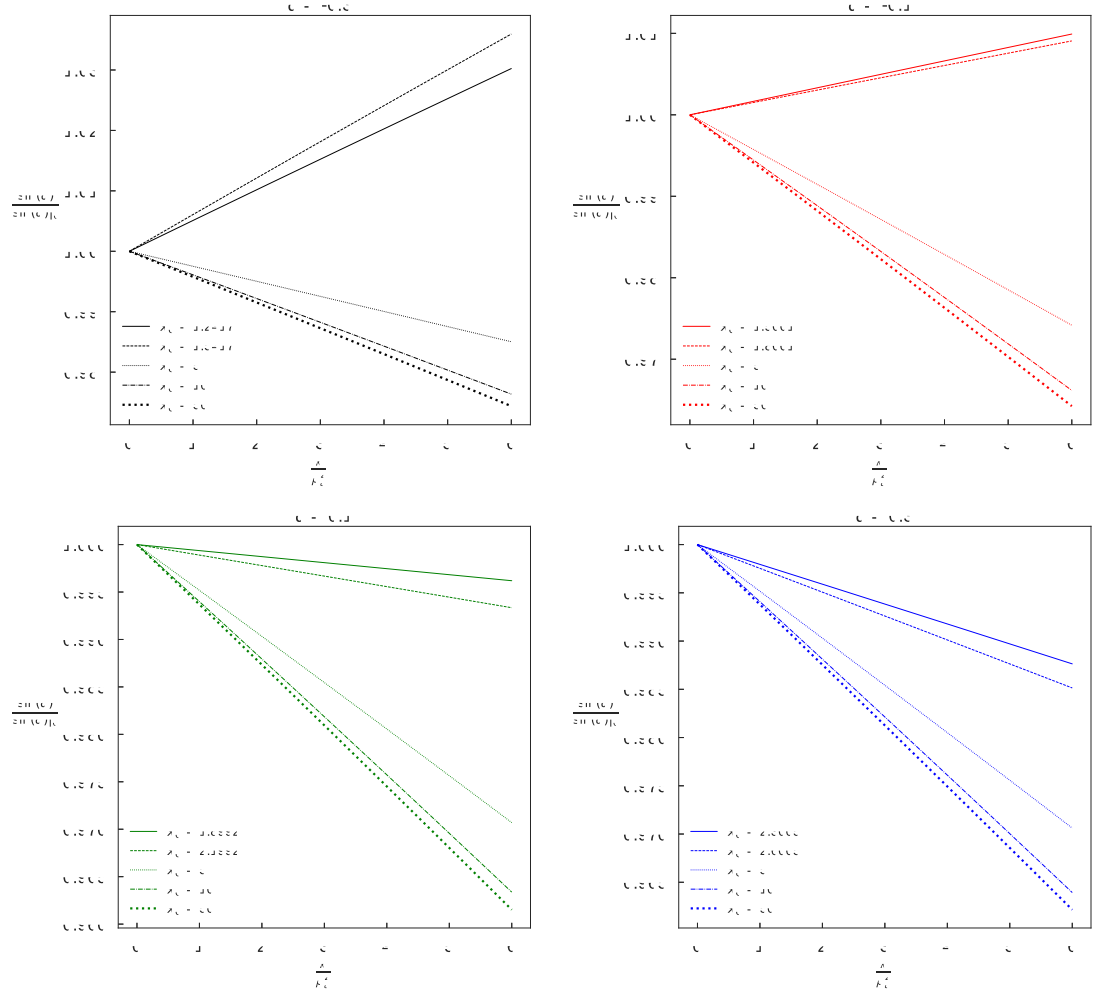


**Figure 14.5:** Variation of  $\frac{\sin \alpha}{\sin \alpha|_0}$  with respect to  $\frac{k}{k_t^2}$  for various values of  $q$  and  $x_O$  for  $\omega_p \propto (x+1)^{3/2}$ .

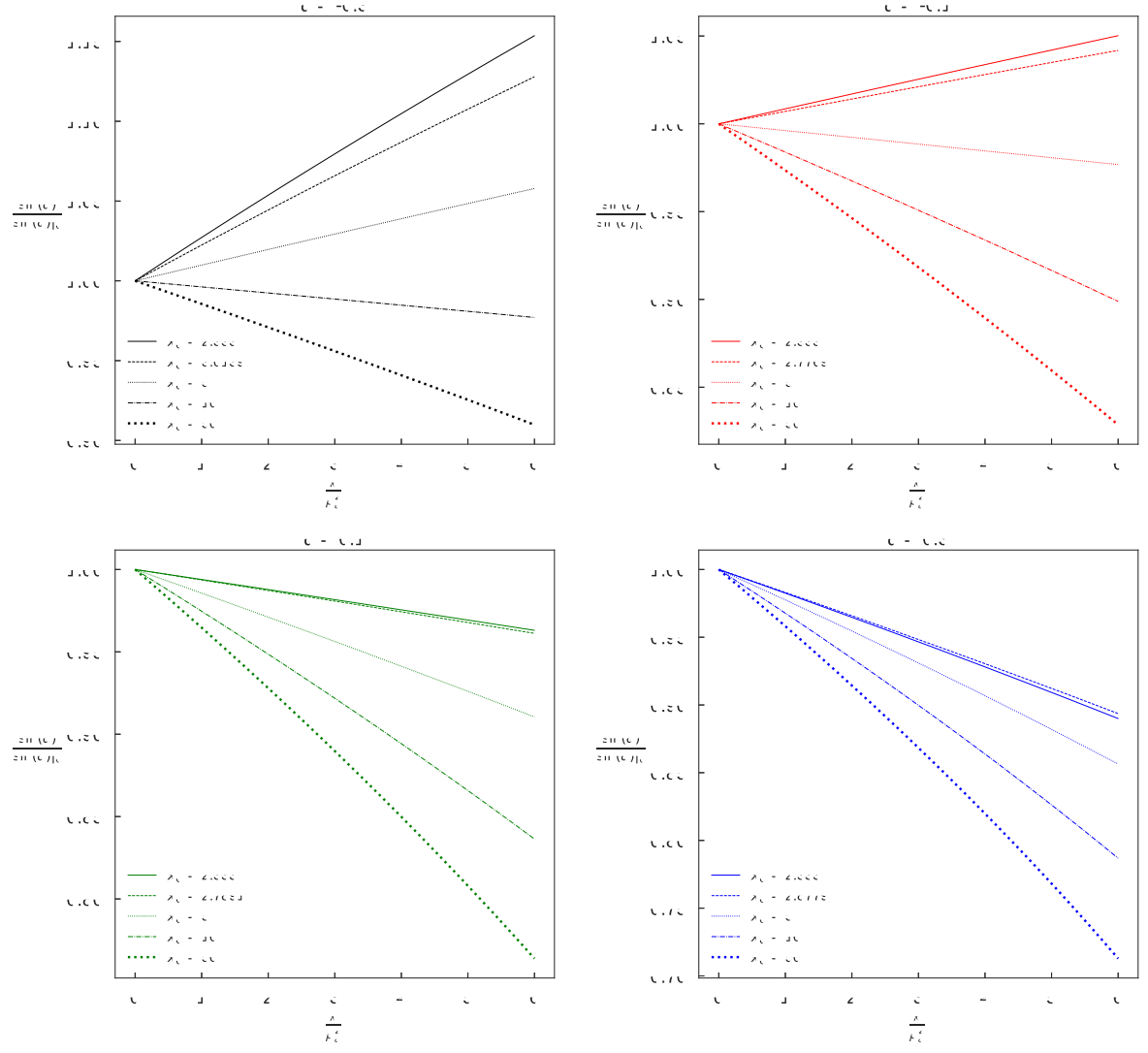


**Figure 14.6:** Variation of  $\sin \alpha / \sin \alpha|_0$  with respect to  $k/p_t^2$  for various values of  $q$  and  $x_O \propto (x+1)^{3/4}$ .



## Stability analysis of circular geodesics in Generalized q-metric

We discuss dynamical system stability analysis in Chapter 5. Now in this chapter, we apply the linear and non-linear stability analysis in the circular geodesics of Generalized q-metric 7 in the equatorial plane, to investigate the behavior of the geodesics in this metric.

### 15.1 Existence of equilibrium points

To apply the stability analysis of the associated system of ordinary differential equations to this metric we proceed as follows. The Lagrangian associated to this metric reads as

$$\mathcal{L} = \frac{1}{2} \left( - \left( \frac{x-1}{x+1} \right)^{(1+\alpha)} e^{2\hat{\psi}} \dot{t}^2 + (x^2-1) e^{-2\hat{\psi}} \left( \frac{x+1}{x-1} \right)^{(1+\alpha)} \right. \\ \left. \left[ \left( \frac{x^2-1}{x^2-y^2} \right)^{\alpha(2+\alpha)} e^{2\hat{\gamma}} \left( \frac{\dot{x}^2}{x^2-1} + \frac{\dot{y}^2}{1-y^2} \right) + (1-y^2) \dot{\phi}^2 \right] \right), \quad (15.1)$$

where "over-dot" is derivative with respect to the affine parameter  $\eta$ . Moreover, the conserved energy and angular momentum per unit mass are obtained as follows

$$E = \frac{\partial \mathcal{L}}{\partial \dot{t}} = - \left( \frac{x-1}{x+1} \right)^{(1+\alpha)} e^{2\hat{\psi}} \dot{t}, \\ L = \frac{\partial \mathcal{L}}{\partial \dot{\phi}} = (x^2-1)(1-y^2) \left( \frac{x+1}{x-1} \right)^{(1+\alpha)} e^{-2\hat{\psi}} \dot{\phi}. \quad (15.2)$$

We carry out the stability analysis for the circular geodesics in the equatorial plane and in the metric and Lagrangian (15.1) we substitute  $y = 0$ . By replacing  $E$  and  $L$  into the Lagrangian and solving the geodesic equation  $\mathcal{L} = \epsilon$ , for  $\dot{x}^2$  we obtain

$$\dot{x}^2 = \frac{\left(\frac{x-1}{x+1}\right)^{(1+\alpha)} e^{2\hat{\psi}} (x^2 - 1) \epsilon - L^2 \left(\frac{x-1}{x+1}\right)^{2(1+\alpha)} e^{4\hat{\psi}} + E^2 (x^2 - 1)}{(x^2 - 1) \left(\frac{x^2-1}{x^2}\right)^{\alpha(2+\alpha)} e^{2\hat{\gamma}}} \\ := 2h(x). \quad (15.3)$$

Where for simplicity we defined the new variable  $X^2 := (x^2 - 1)$ . The right-hand side is only a function of  $x$  and we can note it by  $2h$ , where factor 2 is just a convention to have nicer forms of equations. Thus we find an equation where the left-hand side is derivative of  $x$  and the right-hand side is a differentiable function of  $x$ . In the next section, we proceed to investigate the existence of fixed points or equilibrium points of this differential equation.

Derivation of equation (15.3) with respect to the affine parameter gives the geodesic equation as

$$\ddot{x} = h'(x), \quad (15.4)$$

where "prime" is the derivative with respect to  $x$ . This equation easily can be separated as two first-order ODE in the two-dimension phase space

$$\begin{cases} \dot{x} = p, \\ \dot{p} = h', \end{cases} \quad (15.5)$$

where  $p$  is the inverse of  $\phi$  component of the metric times  $p_x$  conjugate momentum of  $x$  given by  $\frac{\partial \mathcal{L}}{\partial \dot{x}}$ .

These two equations construct a system in the phase space which is spanned by  $(x, p)$ . Mixing phase space is a necessary condition for the relaxation of a non equilibrium state to equilibrium. By definition, the fixed points of this system  $(x^*, p^*)$  is obtained by asking the right-hand side of equations (15.5) vanish

$$p = 0, \quad \text{and} \quad h' = 0, \quad (15.6)$$

or equivalently

$$\dot{x}(x^*, p^*) = 0, \quad \text{and} \quad \dot{p}(x^*, p^*) = 0, \quad (15.7)$$



where obviously for our desired system  $p^* = 0$ . In order to obtain physical restriction, in this part, we work with the set of equations (15.7). To have an easier expression we play with  $\dot{p}_x$  as

$$\begin{aligned} 0 = \dot{p}_x^* &= \frac{d}{d\eta} \left( \frac{\partial \mathcal{L}}{\partial \dot{x}} \right) = \dot{x} \frac{d}{dx} (g_{\phi\phi} \dot{x}) \\ &= \frac{1}{2g_{\phi\phi}} \frac{d}{dx} (g_{\phi\phi}^2 \dot{x}^2), \end{aligned} \quad (15.8)$$

where in the first line we used the chain rule. Now, if we replace  $g_{\phi\phi}$  metric component and  $\dot{x}$  from (15.3), at the fixed points we obtain

$$\dot{p}_x = 0 \quad \equiv \quad h' = 0 \quad \equiv \quad h_N' = 0, \quad \text{at} \quad x = x^*, \quad (15.9)$$

and  $h_N$  is the nominator of  $h$ , and

$$h_N' = \left( \frac{x^* - 1}{x^* + 1} \right)^{(1+\alpha)} (\xi + x) e^{2\hat{\psi}} \epsilon - 2 \left( \frac{x^* - 1}{x^* + 1} \right)^{2(1+\alpha)} \xi \frac{L^2}{x^2 - 1} e^{4\hat{\psi}} + x E^2, \quad (15.10)$$

where for simplicity we use  $\xi := 1 + \alpha + \hat{\psi}_{,x}(x^{*2} - 1)$  which appears frequently. Therefore, solving these two equations  $\dot{x} = 0$  and  $h_N' = 0$  is equivalent to solve this following matrix equation

$$\begin{pmatrix} x^{*2} - 1 & -e^{4\hat{\psi}} \left( \frac{x^* - 1}{x^* + 1} \right)^{2(1+\alpha)} \\ x^*(x^{*2} - 1) & -2e^{4\hat{\psi}} \left( \frac{x^* - 1}{x^* + 1} \right)^{2(1+\alpha)} \xi \end{pmatrix} \begin{pmatrix} E^2 \\ L^2 \end{pmatrix} = -\epsilon \begin{pmatrix} (x^{*2} - 1) \left( \frac{x^* - 1}{x^* + 1} \right)^{(1+\alpha)} e^{2\hat{\psi}} \\ \left( \frac{x^* - 1}{x^* + 1} \right)^{(1+\alpha)} e^{2\hat{\psi}} (x^{*2} - 1)(x^* + \xi) \end{pmatrix}. \quad (15.11)$$

This system of equations has a unique solution if and only if the determinant of the coefficients be non zero, therefore we need to exclude

$$x^* - 2\xi = 0. \quad (15.12)$$

To solve the system of equations (15.11), first we choose  $\epsilon = -1$  and study the (massive) particle geodesics, then replace  $\epsilon = 0$  to study the photon geodesics.

### 15.1.1 For time-like geodesics

In this case, we obtain the following solutions for  $E^2$  and  $L^2$

$$E^2 = \frac{\left(\frac{x^*-1}{x^*+1}\right)^{(1+\alpha)} e^{2\hat{\psi}}(x^* - \xi)}{x^* - 2\xi}, \quad (15.13)$$

$$L^2 = \frac{\left(\frac{x^*+1}{x^*-1}\right)^{(1+\alpha)} e^{-2\hat{\psi}}\xi(x^{*2} - 1)}{x^* - 2\xi}. \quad (15.14)$$

Indeed, to have a physically reasonable solution the right-hand side of this set of solutions should be positive. Therefore, by analyzing the existing solutions for the entire system, we obtain conditions that violate the entire system. If one of these conditions satisfies then there exists no solution for  $E^2$  and  $L^2$

$$\begin{aligned} 1. \quad & x^* - 2\xi \leq 0, \\ 2. \quad & \xi < 0, \\ 3. \quad & x^* - \xi < 0. \end{aligned} \quad (15.15)$$

However, the first condition already leads to the third condition. Thus, in conclusion, we have these conditions to not have a solution for the system

$$\begin{aligned} 1. \quad & x^* - 2\xi \leq 0, \\ 2. \quad & \xi < 0. \end{aligned} \quad (15.16)$$

Note that the entire system should have a solution. For example, in all these cases  $E^2$  has a solution but not  $L^2$ . To be able to go further we consider function  $\hat{\psi}$  and  $\hat{\gamma}$  up to the quadrupole and in the equatorial plane ( $y = 0$ ). Since we are interested to find the restriction on the domain of  $\beta$ , we write the conditions (15.16) in terms of  $\beta$  as

$$\begin{aligned} 1. \quad & \beta \leq \frac{-x^* + 2(1 + \alpha)}{2x^*(x^{*2} - 1)}, \\ 2. \quad & \beta > \frac{1 + \alpha}{x^*(x^{*2} - 1)}. \end{aligned} \quad (15.17)$$

Thus, this system of equations admit fixed point for

$$\frac{-x^* + 2(1 + \alpha)}{2x^*(x^{*2} - 1)} < \beta \leq \frac{1 + \alpha}{x^*(x^{*2} - 1)}. \quad (15.18)$$

However, for the equality which is equivalent to vanishing  $\xi$ , we have  $L^2 = 0$ . This situation happens only when  $\beta \neq 0$  and presents the effect of the external source. Obviously, the domain of  $\beta$  depends on the chosen value for  $\alpha \in (-1, \infty)$ .

### Case1: q-metric

If we restrict our self in the case of q-metric; namely  $\hat{\psi} = 0$ , for timelike geodesics, the first condition in (15.17) is relevant, since  $\xi = 1 + \alpha > 0$ . Thus, the condition to have the fixed points is equivalent to having this restriction on  $\alpha$

$$\alpha < \frac{x^*}{2} - 1. \quad (15.19)$$

Therefore, the minimum valid domain of  $\alpha$  where we always have a fixed point is  $\alpha \in (-1, -\frac{1}{2})$  and as far as we go farther from the central object this domain increases.

### Case2: Distorted Schwarzschild

For studying the distorted Schwarzschild solution by replacing  $\alpha = 0$  we have

$$\frac{-x^* + 2}{2x^*(x^{*2} - 1)} < \beta \leq \frac{1}{x^*(x^{*2} - 1)}. \quad (15.20)$$

Therefore, for positive and negative values of  $\beta$  we can have fixed points. However, the domain of  $\beta$  for any chosen value of  $x^*$  is more restricted than for  $\alpha$ .

#### 15.1.2 For light-like geodesics

To investigate the existence of an equilibrium point for the photon geodesics, we fix  $\epsilon = 0$ . Hence, the condition (15.7) equivalent to have

$$1. \quad \frac{E^2}{L^2} = \frac{e^{4\hat{\psi}}}{(x^* + 1)^2} \left( \frac{x^* - 1}{x^* + 1} \right)^{(2\alpha+1)}, \quad (15.21)$$

$$2. \quad x^* - 2\xi = 0. \quad (15.22)$$

The right-hand side of the first equation is positive and for some combination of parameters has a solution. The second condition states that the system

does not have a unique solution for  $E^2$  and  $L^2$ . This condition for the existence of fixed point for lightlike geodesics considering (15.17) is equivalent to have  $\beta = \frac{x^* - 2(1+\alpha)}{2x^*(x^{*2}-1)}$ .

### Case1: q-metric

In this case, for lightlike geodesics, for any chosen value of  $\alpha \in (-1, \infty)$ , the relation  $\alpha = \frac{x^*}{2} - 1$  leading to have equilibrium points. However, also here the system does not admit a unique solution.

### Case2: Distorted Schwarzschild

Similar to the first case, for any chosen value of  $\beta$ , one can obtain fixed points via  $\beta = \frac{x^* - 2}{2x^*(x^{*2}-1)}$ , while there is no unique solution.

## 15.2 Lyapunov linear Stability

In this section, we start with the system (15.5). The vector field mentioned earlier in Section 5 associated with this system is given by

$$f(x, p) = (p, h'(x)), \quad (15.23)$$

where  $f : \mathbb{R}^+ \times \mathbb{R} \rightarrow \mathbb{R}^2$ . The Jacobian matrix (5.3) of  $f$  at the equilibrium point  $(x^*, 0)$  for the mentioned system (15.5) is obtained as

$$A = \begin{pmatrix} 0 & 1 \\ h''(x^*) & 0 \end{pmatrix}. \quad (15.24)$$

From the characteristic equation (5.5) for this matrix we obtain

$$\lambda_{\pm} = \pm \sqrt{h''_N(x^*)}. \quad (15.25)$$

Thus, depending on the sign of  $h''(x)$  at  $x = x^*$  we can find the stability nature of the equilibrium point. Besides, in our case, the sign of  $h''(x^*)$  is the same as the sign of  $h''_N(x^*)$ . To see its physical meaning, let's assume a perturbation  $\delta$  around the fixed point as

$$x(t) = x^* + \delta(t), \quad (15.26)$$

So, at  $x(t)$  we have

$$\begin{aligned}
 \dot{\delta}(t) &= \dot{x}(t) \\
 &= f(x, 0) \\
 &= f(x^* + \delta, 0) \\
 &= f(x^*, 0) + \delta f'(x^*, 0) + \frac{\delta^2}{2} f''(x^*, 0) + \dots \quad . \quad (15.27)
 \end{aligned}$$

Since we are interested in linear stability analysis, we only look up to the first derivative, and by definition of the fixed points the first term in (15.27) vanishes, then

$$\begin{aligned}
 \dot{\delta} &= \delta f'(x^*, 0) \\
 &= \delta h''(x^*). \quad (15.28)
 \end{aligned}$$

Thus

$$\delta(t) = e^{ah''(x)}, \quad (15.29)$$

where  $a$  is some constant. This means if  $h''(x^*) > 0$  then trajectories are diverging since the perturbation grows exponentially. If  $h''(x^*) < 0$  trajectories are converging since the perturbation decays exponentially.

Therefore, for any chosen values for the metric parameters, we need to compute the sign of  $h''$  at the zeros of  $h'$  to see the behavior of the corresponding geodesics.

### 15.3 Jacobi nonlinear stability

To study the Jacobi analysis we rewrite the equation (15.4) in this form

$$\ddot{x} + 2\left(-\frac{1}{2}h'\right) = 0. \quad (15.30)$$

Besides, we can state the  $G^1$  term in the equation (5.7) as

$$G^1 = -\frac{1}{2}h'. \quad (15.31)$$

In addition, the Berwald connection and coefficient of a nonlinear connection associated with this system respectively obtain as

$$N_1^1 = \frac{\partial G^1}{\partial p} = 0 \quad , \quad G_{11}^1 = \frac{\partial N_1^1}{\partial p} = 0. \quad (15.32)$$

Then second KCC invariant  $P_1^1$  at the equilibrium points of our system  $(x^*, 0)$  is given by

$$\begin{aligned} P_1^1(x^*, 0) &= -2 \frac{\partial G^1}{\partial x} - 2G^1 G_{11}^1 + p \frac{\partial N_1^1}{\partial x} + N_1^1 N_1^1, \\ &= -2 \frac{\partial G^1}{\partial x}, \\ &= h''. \end{aligned} \quad (15.33)$$

Therefore, we have an equilibrium point that is Jacobi stable if  $h'' < 0$ . Hence, if  $h''$  at the roots of  $h'$  is negative we have Jacob stability for any chosen pair of  $(\alpha, \beta)$  in the metric.

There is a subtle point here worth mentioning that aside from the same having equal, there is a difference in meaning: Let us point out that the stability in the Jacobi sense refers to a linear stability type of the trajectories in the curved space endowed with a nonlinear connection and a curvature tensor, as described above. Here the role of the usual partial derivative is played by the covariant derivative along with the flow. This obviously leads to the difference in the meaning of linear stability and Jacobi stability.

## 15.4 Kolmogorov entropy

The test particle motion expected to be chaotic even in the equatorial plane for some combinations of parameters  $\alpha$  and  $\beta$ , since a perturbation in the gravitational or the electromagnetic field generally leads to chaos. As a first systematic study toward this issue the Kolmogorov entropy was explored that has link to this feature.

As we stated before in Section 5.3 the Kolmogorov-Sinai entropy is equal to the sum of the positive Lyapunov exponents (5.16). Therefore in our system for the fixed points and any pair of  $(\alpha, \beta)$  we have at most one positive  $\lambda$  (15.25)

$$h_{ks} = \lambda_+ > 0. \quad (15.34)$$

Therefore, just the sign of the positive exponent of the system for fixed parameters reveals the chaotic behavior of the corresponding trajectory.

## 15.5 Summary and conclusion

In this chapter, we have studied the stability of timelike and null circular geodesics in the background of Generalized q-metric on the equatorial plane using Lyapunov stability and the Jacobi stability analysis. Mainly, We have analyzed the effect of the metric parameter in the region of stable circular orbit by using effective potential and phase portrait analysis. The linear stability analysis is performed by the linearization of the dynamical system via the Jacobian matrix of a non-linear system at the equilibrium point. In addition, we study the Kolmogorov entropy in this setup. This entropy links to the chaos, which is one of the most important ideas for understanding various non-linear phenomena in nature. We try to find some conditions that is interpreted as the chaotic behavior of the solution. However, all the above criteria depend on the values of both quadrupoles in the metric and by choosing them and using the results of this part, one can recognize the corresponding solutions. However, a more complete description of this stability analysis regarding also non-geodesics trajectories is in the preparation by the author.





# Part III

## Epilogue



## CHAPTER 16

### Summary

One of the main aims of this study was to have a comprehensible analysis of different aspects of space-times containing a quadrupole or acceleration parameter on the astrophysical systems and compare them with Schwarzschild and Kerr black holes with analytical and semi-analytical methods. In addition, the construction of a metric describing a non-isolated deformed object having q-metric as a seed, via considering the external mass distribution was of the main goals.

Upon these aims, this thesis is composed of two main parts. In part one, the necessary material for this research was presented in Chapters 2-6. Part two presented the new results and contribution of the author to the literature. This part contains 9 chapters, each of them dealing with different aspects of these aims.

Chapter 7 presented the construction of a new generalization of the static q-metric via considering the external distribution of matter characterized by multipole moments as planned, which is one of the most significant results in this thesis. Besides, based on an analytical approach which provides a systematic study, this chapter discussed extensively the impact of the external fields up to the quadrupole on the circular geodesics and the interplay of these two quadrupoles in the place of the Innermost Stable Circular Orbit, ISCO. In addition, the circular geodesics and the place of the ISCO as a function of the quadrupole parameter were also revisited in the q-metric, with the considered approach in the second part of this investigation. Aside from its simplicity, the results agree with the studies in previous literature. Chapter 15 also revealed the stability nature of the geodesics of Generalized q-metric and their chaos behavior. However, because this calculation is very complicated, we restrict our attention up to the quadrupoles. This also required to specify values of both quadrupole moments to use the final results.

However, presenting the external source leads to having a bound orbit for light-like geodesics on the equatorial plane, this is the case in the Generalized q-metric and distorted Schwarzschild solution. The key point is that this bound orbit's existence directly is reflected in the having negative quadrupole in the external matter distributions. In fact, most of our information about the astrophysical environment is obtained from electromagnetic radiation and consequently by studying the null geodesics; therefore, this result is of great implications in studying some astrophysical phenomena like the shadow.

Further, Chapter 9 illustrated the effect of rotation in the q-metric. The goal of this study was to examine the similarity of the rotation parameter in this metric with the Kerr solution. The Thick accretion disc model was investigated in Chapter 11 to evaluate its importance even more. However, the result of this part was more than it was planned.

In the line of this research's goals, Chapters 8, 10, 11, 12 and 13 provided a big picture to understanding the role of parameters of the metric in association with astrophysical systems. To do so, the impacts of the parameters of considered space-times were examined. In the Thin disc model, the properties are distinguishable with the Schwarzschild solution, but in the inner part of the disc, they are similar to the Kerr metric with different spin parameters. Interestingly, in the extensive study on the quasi-periodic oscillations and the Thick accretion discs with non-constant angular momentum distributions, this has been seen that a proper combination of the angular momentum parameters, magnetization parameters, and value chosen for the quadrupole can drain away their effects on the disc configuration, also on the distribution of material inside the disc. In fact, this can be of great consequence in the application to the astrophysical systems as well as to the numerical simulation. Since these configurations are indistinguishable from the standard space-times of Schwarzschild and Kerr, therefore, can act as black hole mimickers.

Chapter 14 showed the differences between the photon sphere position and radius of shadow in q-metric and the Schwarzschild space-time. In this study was considered that the space-time was filled with cold plasma. The results show the clear differences in these two metrics, for different choices of plasma frequency. Chapter 11 also provided an understanding of the acceleration parameter in C-metric, in combination with charge, rotation and magnetization parameters via constructing the morphology of the equilibrium configuration of the Thick discs, which was one of the goals of the present study.

In general, for some parameters range we obtain the quantities values that correspond to Schwarzschild or Kerr solutions. Therefore, among other results, one can conclude that if we evaluate the central compact object

properties without having tested the Schwarzschild or Kerr hypothesis first, then these measurements might be misleading and may be related to some black hole mimickers. Thus, more studies and researches on these objects is worthwhile to continue.

The possible future works are presented in the outlook.



## Outlook

The work accomplished in this thesis opened a variety of research areas and applications mostly in general relativity and astrophysics that can be continued for future in the several interesting passes including:

### **Astrophysical Observable**

- Predict the existence of possible various types of astrophysical observations with searching for the probable outcomes of considering different values of quadrupole that mathematically allowed. In addition, compare the analytical results with the ambiguous high-energy astronomy observational data. This research line is under investigation by author and colleagues.
- Determine an upper bound on the mean efficiency parameter using the Generalized q-metric solution in this thesis. In fact, the energy radiated by a compact object as a consequence of the accretion process is related to the mass rate and efficiency parameter. However, accurate estimate of mass rate is typically very problematic and model dependent. It is instead possible to determine the mean efficiency parameter of active galactic nuclei. In this analytical set-up, one can find upper bound on this efficiency in terms of quadrupoles that can be very much better fit to the observational data related to calculating this efficiency.
- Investigate how the different types of plasma, and magnetic fields surrounding the objects describing with the considered metric, especially containing quadrupoles, interact with each other and have impact on the properties of shadow in these backgrounds (this is also related to the extension of the Generalized q-metric.).

- Study the periodicity of the particle trajectories, where it can reveal the observables associated to the trajectory of the metric (this is also related to the extension of the Generalized q-metric.).
- Explore the variabilities in high frequency quasi-periodic oscillations associated with discoseismic oscillation modes of the accretion disc. There are models that relate these variabilities in HF QPOs to general relativistic effects. In these models, with no magnetic field, the inertial oscillations, g-modes, can be self-trapped in the inner region of the disc. While a weak magnetic field even can modify or destroy the self-trapping zone of these g-modes [234, 235]. Therefore, it seems reasonable to consider the effect of the deformation parameter on this self-trapping zone and compare with data. An interesting preliminary investigation reveals that as  $\alpha$  even increases slightly, this self-trapping zone of g-mode changes. Indeed, this critical result needs further consideration (this is also related to the extension of the Generalized q-metric.).

### Numerical simulations

- Use these discussed analytical settings in this research as the initial conditions for the numerical simulations of accretion discs and corresponding gravitational wave templates, and test their ability to account for observable constraints of astrophysical systems simulations.

### Analytical Accretion Disc Models

- Develop a new analytical accretion disc model to include chaotic behavior of trajectories to have a more realistic and still analytic model to study the link to the observational data with more accuracy and freedom. Since, this may offer a better insight into the physical mechanisms of the accretion discs like dissipation processes and stability. In particular, to clarify which processes dominate its evolution and what are the applicable ranges of model parameters capable to fit into observational data. The results in the last chapter was the first attempt to accomplish this goal and more in progress.
- Study the instability in space-times with quadrupole and see the impact of quadrupole on the instability puzzle of the Thin accretion discs.



### Extension of the Generalized q-metric

- Considering the Generalized q-metric is valid locally, it seems reasonable to use an approach like the perturbation matching calculation to describe the external universe [236], which may be the next stage of this study.
- This metric can be seen as the first step toward considering the self-gravity of the disc, which is the one of main plan for extending this work. In this line of research, considering the external distribution of matter was the starting point to model the effect of outer part of the disc on the inner part. Of course, real models will be inaccurate due to incomplete knowledge of the underlying physics, or perhaps a desire for simplicity.
- Considering quadrupoles may facilitate the study on heating the outer region by inner part that normally is neglected in the assumptions of models.

### Multipole Moments

- Applying this approach of considering distribution of matter characterizing first only with quadrupoles to other theories of gravity, and study the quadrupolar structure of the underlying gravitational field.
- Finding another way of defining multipoles, where be applicable in the setting of neutron stars tidal deformations to interpret the universal relations among special multipole moments.

### Observational and analytical Applications of the C-metric

- Study the recoil velocity, or the natal kick reaching values up to 5000 km/s where possibly left behind after a binary black hole merger, via the C-metric as the first semi-analytical step to provide enough initial acceleration. This phenomenon has important implications for gravitational wave, black hole formation, and in general testing general relativity.
- Analyzing the axis-symmetric instabilities in the family of C-metric and regarding accretion discs, probably starting with the standard version without charge and rotation, because of the existence of conical deficit the accretion discs in this space-time are likely to be unstable.

To sum up, it is expected that future works in this field to be guided more by astrophysics questions and observations and other areas where strong-field gravitational theory applies.

## Bibliography

- [1] Serena Repetto, Melvyn B. Davies, and Steinn Sigurdsson. Investigating stellar-mass black hole kicks. *MNRAS*, 425(4):2799–2809, October 2012.
- [2] Fintan D. Ryan. Gravitational waves from the inspiral of a compact object into a massive, axisymmetric body with arbitrary multipole moments. *Phys. Rev. D*, 52(10):5707–5718, 1995.
- [3] José P. S. Lemos and Oleg B. Zaslavskii. Black hole mimickers: Regular versus singular behavior. *Phys. Rev. D*, 78:024040, Jul 2008.
- [4] Rajibul Shaikh, Prashant Kocherlakota, Ramesh Narayan, and Pankaj S. Joshi. Shadows of spherically symmetric black holes and naked singularities. *MNRAS*, 482(1):52–64, January 2019.
- [5] M. A. Abramowicz, W. Kluźniak, and J. P. Lasota. No observational proof of the black-hole event-horizon. *Astron Astroph*, 396:L31–L34, December 2002.
- [6] N. Afshordi and B. Paczyński. Geometrically Thin Disk Accreting into a Black Hole. *Astrophys.*, 592(1):354–367, Jul 2003.
- [7] M. van der Klis. Millisecond Oscillations in X-ray Binaries. *Annu. Rev. Astron. Astrophys.*, 38:717–760, 2000.
- [8] Jeffrey E. McClintock and Ronald A. Remillard. *Black hole binaries*, volume 39, pages 157–213. Oxford, 2006.
- [9] Adam R. Ingram and Sara E. Motta. A review of quasi-periodic oscillations from black hole x-ray binaries: Observation and theory. *New Astronomy Reviews*, 85:101524, 2019.
- [10] N. I. Shakura and R. A. Sunyaev. Black holes in binary systems. Observational appearance. *Astron Astroph*, 24:337–355, 1973.

- [11] J. M. Bardeen, W. H. Press, and S. A. Teukolsky. Rotating Black Holes: Locally Nonrotating Frames, Energy Extraction, and Scalar Synchrotron Radiation. *Astrophys.*, 178:347–370, December 1972.
- [12] I. D. Novikov and K. S. Thorne. Astrophysics of black holes. In C. Dewitt and B. S. Dewitt, editors, *Black Holes (Les Astres Occlus)*, pages 343–450, 1973.
- [13] D. Lynden-Bell and J. E. Pringle. The evolution of viscous discs and the origin of the nebular variables. *MNRAS*, 168:603–637, Sep 1974.
- [14] Omer M. Blaes and Steven A. Balbus. Local Shear Instabilities in Weakly Ionized, Weakly Magnetized Disks. *Astrophys.*, 421:163, Jan 1994.
- [15] Banibrata Mukhopadhyay, Niayesh Afshordi, and Ramesh Narayan. Hydrodynamic turbulence in accretion disks. 2005.
- [16] Kazunori Kohri, Ken Ohsuga, and Ramesh Narayan. Multidimensional treatment of photon emission from accretion discs around black holes. *MNRAS*, 381(3):1267–1274, Nov 2007.
- [17] Feng Yuan and Ramesh Narayan. Hot accretion flows around black holes, Aug 2014.
- [18] Jeffrey E. McClintock, Rebecca Shafee, Ramesh Narayan, Ronald A. Remillard, Shane W. Davis, and Li-Xin Li. The Spin of the Near-Extreme Kerr Black Hole GRS 1915+105. *Astrophys.*, 652(1):518–539, Nov 2006.
- [19] Rebecca Shafee, Ramesh Narayan, and Jeffrey E. McClintock. Viscous Torque and Dissipation in the Inner Regions of a Thin Accretion Disk: Implications for Measuring Black Hole Spin. *Astrophys.*, 676(1):549–561, Mar 2008.
- [20] Robert F. Penna, Jonathan C. McKinney, Ramesh Narayan, Alexander Tchekhovskoy, Rebecca Shafee, and Jeffrey E. McClintock. Simulations of magnetized discs around black holes: effects of black hole spin, disc thickness and magnetic field geometry. *MNRAS*, 408(2):752–782, Oct 2010.
- [21] Steven A. Balbus and John F. Hawley. A Powerful Local Shear Instability in Weakly Magnetized Disks. I. Linear Analysis. *Astrophys.*, 376:214, July 1991.

- [22] Steven A. Balbus and John F. Hawley. A Powerful Local Shear Instability in Weakly Magnetized Disks. IV. Nonaxisymmetric Perturbations. *Astrophys.*, 400:610–621, Dec 1992.
- [23] Steven A. Balbus and John F. Hawley. Instability, turbulence, and enhanced transport in accretion disks. *Rev. Mod. Phys.*, 70:1–53, Jan 1998.
- [24] O. M. Blaes. *Physics Fundamentals of Luminous Accretion Disks Around Black Holes*. 2002.
- [25] Marek Abramowicz, Axel Brandenburg, and Jean-Pierre Lasota. The dependence of the viscosity in accretion discs on the shear/vorticity ratio. *MNRAS*, 281:L21, Jul 1996.
- [26] Martin E. Pessah, Chi Kwan Chan, and Dimitrios Psaltis. The fundamental difference between shear  $\alpha$  viscosity and turbulent magnetorotational stresses. *Monthly Notices of the Royal Astronomical Society*, 383(2):683–690, 1 2008.
- [27] Robert F. Penna, Aleksander Sadowski, Akshay K. Kulkarni, and Ramesh Narayan. The Shakura-Sunyaev viscosity prescription with variable  $\alpha(r)$ . *Monthly Notices of the Royal Astronomical Society*, 428(3):2255–2274, 11 2012.
- [28] J. H. Krolik. Magnetized Accretion inside the Marginally Stable Orbit around a Black Hole. *ApJ*, 515(2):L73–L76, Apr 1999.
- [29] Charles F. Gammie. Efficiency of Magnetized Thin Accretion Disks in the Kerr Metric. *ApJ*, 522(1):L57–L60, September 1999.
- [30] Steven A. Balbus. The general relativistic thin disc evolution equation. *Monthly Notices of the Royal Astronomical Society*, 471(4):4832–4838, Aug 2017.
- [31] Akshay K. Kulkarni, Robert F. Penna, Roman V. Shcherbakov, James F. Steiner, Ramesh Narayan, Aleksander Sadowski, Yucong Zhu, Jeffrey E. McClintock, Shane W. Davis, and Jonathan C. McKinney. Measuring black hole spin by the continuum-fitting method: effect of deviations from the Novikov-Thorne disc model. *MNRAS*, 414(2):1183–1194, Jun 2011.
- [32] Abraham Loeb, Ramesh Narayan, and John C. Raymond. Does the Mass Accretion Rate Depend on the Radius of the Accreting Star? *ApJ*, 547(2):L151–L154, February 2001.

- [33] D. N. Page and K. S. Thorne. Disk-Accretion onto a Black Hole. Time-Averaged Structure of Accretion Disk. *Astrophys.*, 191:499–506, July 1974.
- [34] G. Compère and R. Oliveri. Self-similar accretion in thin discs around near-extremal black holes. *MNRAS*, 468:4351–4361, July 2017.
- [35] M. A. Abramowicz, A. Lanza, and M. J. Percival. Accretion Disks around Kerr Black Holes: Vertical Equilibrium Revisited. *Astrophys.*, 479:179–183, April 1997.
- [36] M. A. Abramowicz. Theory of Level Surfaces Inside Relativistic: Rotating Stars. II. *Acta Astron*, 24:45, January 1974.
- [37] M. Kozłowski, M. Jaroszynski, and M. A. Abramowicz. The analytic theory of fluid disks orbiting the Kerr black hole. *Astron Astroph*, 63(1-2):209–220, February 1978.
- [38] M. Jaroszynski, M. A. Abramowicz, and B. Paczynski. Supercritical accretion disks around black holes. *Acta Astron*, 30(1):1–34, January 1980.
- [39] B. Paczyński and P. J. Wiita. Thick accretion disks and supercritical luminosities. *Astron Astroph*, 500:203–211, August 1980.
- [40] M. A. Abramowicz, M. Calvani, and L. Nobili. Thick accretion disks with super-Eddington luminosities. *Astrophys.*, 242:772–788, December 1980.
- [41] M. A. Abramowicz. Innermost parts of accretion disks are thermally and secularly stable. *Nature*, 294(5838):235–236, November 1981.
- [42] B. Paczynski. Thick Accretion Disks around Black Holes (Karl-Schwarzschild-Vorlesung 1981). *Mitteilungen der Astronomischen Gesellschaft Hamburg*, 57:27, January 1982.
- [43] B. Paczynski and M. A. Abramowicz. A model of a thick disk with equatorial accretion. *Astrophys.*, 253:897–907, February 1982.
- [44] Yuichiro Sekiguchi, Kenta Kiuchi, Koutarou Kyutoku, and Masaru Shibata. Gravitational waves and neutrino emission from the merger of binary neutron stars. *Phys. Rev. Lett.*, 107:051102, Jul 2011.
- [45] Joshua A. Faber and Frederic A. Rasio. Binary Neutron Star Mergers. *Living Reviews in Relativity*, 15(1):8, July 2012.

- [46] Masaru Shibata and Keisuke Taniguchi. Coalescence of Black Hole-Neutron Star Binaries. *Living Reviews in Relativity*, 14(1):6, December 2011.
- [47] Luca Baiotti and Luciano Rezzolla. Binary neutron star mergers: a review of Einstein’s richest laboratory. *Reports on Progress in Physics*, 80(9):096901, September 2017.
- [48] M. Abramowicz, M. Jaroszynski, and M. Sikora. Relativistic, accreting disks. *Astron Astroph*, 63:221–224, February 1978.
- [49] Marek A. Abramowicz and P. Chris Fragile. Foundations of black hole accretion disk theory. *Living Reviews in Relativity*, 16(1):1, Jan 2013.
- [50] H. von Zeipel. The radiative equilibrium of a rotating system of gaseous masses. *MNRAS*, 84:665–683, June 1924.
- [51] O. Zanotti and D. Pugliese. Von Zeipel’s theorem for a magnetized circular flow around a compact object. *General Relativity and Gravitation*, 47:44, April 2015.
- [52] S. S. Komissarov. Magnetized tori around kerr black holes: analytic solutions with a toroidal magnetic field. *Monthly Notices of the Royal Astronomical Society*, 368(3):993–1000, Apr 2006.
- [53] Maciek Wielgus, P. Chris Fragile, Ziming Wang, and Julia Wilson. Local stability of strongly magnetized black hole tori. *MNRAS*, 447(4):3593–3601, March 2015.
- [54] W. G. Dixon. *Special relativity: the foundation of macroscopic physics*. Oxford Univ. Press, 1978.
- [55] Angelo Marcello Anile. *Relativistic fluids and magneto-fluids : with applications in astrophysics and plasma physics*. Oxford Univ. Press, 1989.
- [56] Rika Okada, Jun Fukue, and Ryoji Matsumoto. A model of astrophysical tori with magnetic fields. *PASJ*, 41(1):133–140, January 1989.
- [57] Lei Qian, M. A. Abramowicz, P. C. Fragile, J. Horák, M. Machida, and O. Straub. The Polish doughnuts revisited. I. The angular momentum distribution and equipressure surfaces. *Astron Astroph*, 498(2):471–477, May 2009.

- [58] Adam Ingram and Sara Motta. A review of quasi-periodic oscillations from black hole X-ray binaries: observation and theory. *arXiv e-prints*, page arXiv:2001.08758, January 2020.
- [59] Gupta, Alok C., Tripathi, Ashutosh, Wiita, Paul J., Gu, Minfeng, Bambi, Cosimo, and Ho, Luis C. Possible 1 hour quasi-periodic oscillation in narrow-line seyfert 1 galaxy mcg-06-30-15. *A&A*, 616:L6, 2018.
- [60] J. P. Halpern, K. M. Leighly, and H. L. Marshall. An Extreme Ultraviolet Explorer Atlas of Seyfert Galaxy Light Curves: Search for Periodicity. *Astrophys.*, 585(2):665–676, March 2003.
- [61] Marek Gierliński, Matthew Middleton, Martin Ward, and Chris Done. A periodicity of  $\sim 1$  hour in X-ray emission from the active galaxy RE J1034+396. *Nature*, 455(7211):369–371, September 2008.
- [62] Dacheng Lin, Jimmy A. Irwin, Olivier Godet, Natalie A. Webb, and Didier Barret. A  $\sim 3.8$  hr Periodicity from an Ultraviolet Active Galactic Nucleus Candidate. *ApJ*, 776(1):L10, October 2013.
- [63] W. N. Alston, M. L. Parker, J. Markevičiūtė, A. C. Fabian, M. Middleton, A. Lohfink, E. Kara, and C. Pinto. Discovery of an  $\sim 2$ -h high-frequency X-ray QPO and iron K $\alpha$  reverberation in the active galaxy MS 2254.9-3712. *MNRAS*, 449(1):467–476, May 2015.
- [64] Krista Lynne Smith, Richard F. Mushotzky, Patricia T. Boyd, and Robert V. Wagoner. Evidence for an Optical Low-frequency Quasi-periodic Oscillation in the Kepler Light Curve of an Active Galaxy. *ApJ*, 860(1):L10, June 2018.
- [65] P. Zhang, J. Z. Yan, and Q. Z. Liu. Two Quasi-periodic Oscillations in ESO 113-G010. *Acta Astronomica Sinica*, 61(1):2, January 2020.
- [66] Ronald A. Remillard and Jeffrey E. McClintock. X-Ray Properties of Black-Hole Binaries. *Annu. Rev. Astron. Astrophys.*, 44(1):49–92, September 2006.
- [67] T. M. Belloni, A. Sanna, and M. Méndez. High-frequency quasi-periodic oscillations in black hole binaries. *MNRAS*, 426(3):1701–1709, November 2012.
- [68] S. E. Motta. Quasi periodic oscillations in black hole binaries. *Astronomische Nachrichten*, 337(4-5):398, May 2016.



- [69] Tomaso M Belloni, Dipankar Bhattacharya, Pietro Caccese, Varun Bhalerao, Santosh Vadawale, and J S Yadav. A variable-frequency HFQPO in GRS 1915+105 as observed with AstroSat. *Monthly Notices of the Royal Astronomical Society*, 489(1):1037–1043, 08 2019.
- [70] Xin-Lin Zhou, Weimin Yuan, Hai-Wu Pan, and Zhu Liu. Universal Scaling of the 3:2 Twin-peak Quasi-periodic Oscillation Frequencies With Black Hole Mass and Spin Revisited. *ApJ*, 798(1):L5, January 2015.
- [71] Luigi Stella and Mario Vietri. Lense-Thirring Precession and Quasi-periodic Oscillations in Low-Mass X-Ray Binaries. *ApJ*, 492(1):L59–L62, January 1998.
- [72] Luigi Stella and Mario Vietri. khz quasiperiodic oscillations in low-mass x-ray binaries as probes of general relativity in the strong-field regime. *Phys. Rev. Lett.*, 82:17–20, Jan 1999.
- [73] A. N. Aliev and D. V. Galtsov. Radiation from relativistic particles in nongeodesic motion in a strong gravitational field. *General Relativity and Gravitation*, 13(10):899–912, October 1981.
- [74] A. N. Aliev, D. V. Galtsov, and V. I. Petukhov. Negative Absorption Near a Magnetized Black-Hole - Black-Hole Masers. *Astrophys. Space Sci.*, 124(1):137–157, 1986.
- [75] A. N. Aliev and Valeri P. Frolov. Five-dimensional rotating black hole in a uniform magnetic field: The gyromagnetic ratio. *Phys. Rev. D*, 69(8):084022, April 2004.
- [76] Gabriel Török, Pavel Bakala, Eva Šrámková, Zdeněk Stuchlík, and Martin Urbanec. On Mass Constraints Implied by the Relativistic Precession Model of Twin-peak Quasi-periodic Oscillations in Circinus X-1. *Astrophys.*, 714(1):748–757, May 2010.
- [77] Pavel Bakala, Eva Šrámková, Zdeněk Stuchlík, and Gabriel Török. On magnetic-field-induced non-geodesic corrections to relativistic orbital and epicyclic frequencies. *Classical and Quantum Gravity*, 27(4):045001, February 2010.
- [78] Gabriel Török, Pavel Bakala, Eva Šrámková, Zdeněk Stuchlík, Martin Urbanec, and Kateřina Goluchová. Mass-Angular-momentum Relations Implied by Models of Twin Peak Quasi-periodic Oscillations. *Astrophys.*, 760(2):138, December 2012.

- [79] Andres F. Gutierrez-Ruiz, Cesar A. Valenzuela-Toledo, and Leonardo A. Pachon. Innermost Stable Circular Orbits and Epicyclic Frequencies Around a Magnetized Neutron Star. *arXiv e-prints*, page arXiv:1309.6396, September 2013.
- [80] Bushra Majeed, Mubasher Jamil, and Saqib Hussain. Particle Dynamics Around Weakly Magnetized Reissner-Nordström Black Hole. *arXiv e-prints*, page arXiv:1411.4811, November 2014.
- [81] Martin Kološ, Zdeněk Stuchlík, and Arman Tursunov. Quasi-harmonic oscillatory motion of charged particles around a Schwarzschild black hole immersed in a uniform magnetic field. *Classical and Quantum Gravity*, 32(16):165009, August 2015.
- [82] Zdeněk Stuchlík and Martin Kološ. Acceleration of the charged particles due to chaotic scattering in the combined black hole gravitational field and asymptotically uniform magnetic field. *European Physical Journal C*, 76:32, January 2016.
- [83] Mustapha Azreg-Aïnou. Vacuum and nonvacuum black holes in a uniform magnetic field. *European Physical Journal C*, 76(7):414, July 2016.
- [84] Bobur Turimov, Bobir Toshmatov, Bobomurat Ahmedov, and Zdeněk Stuchlík. Quasinormal modes of magnetized black hole. *Phys. Rev. D*, 100(8):084038, October 2019.
- [85] Ahmadjon Abdujabbarov, Javlon Rayimbaev, Farruh Atamurotov, and Bobomurat Ahmedov. Magnetized Particle Motion in  $\gamma$ -Spacetime in a Magnetic Field. *Galaxies*, 8(4):76, October 2020.
- [86] Miao Yi and Xin Wu. Dynamics of charged particles around a magnetically deformed Schwarzschild black hole. *Phys. Scr.*, 95(8):085008, August 2020.
- [87] Gabriel Török, Andrea Kotrlová, Monika Matuszková, Kateřina Klimovičová, Debora Lančová, Gabriela Urbancová, and Eva Šrámková. Simple analytic formula relating the mass and spin of accreting compact objects to their rapid x-ray variability. *The Astrophysical Journal*, 929(1):28, apr 2022.
- [88] D. Barret, W. Kluźniak, J. F. Olive, S. Paltani, and G. K. Skinner. On the high coherence of kHz quasi-periodic oscillations. *MNRAS*, 357(4):1288–1294, March 2005.

- [89] Didier Barret, Jean-Francois Olive, and M. Coleman Miller. The coherence of kilohertz quasi-periodic oscillations in the X-rays from accreting neutron stars. *MNRAS*, 370(3):1140–1146, August 2006.
- [90] M. A. Abramowicz and W. Kluźniak. A precise determination of black hole spin in GRO J1655-40. *Astron Astroph*, 374:L19–L20, August 2001.
- [91] Wlodek Kluźniak and Marek Artur Abramowicz. Strong-Field Gravity and Orbital Resonance in Black Holes and Neutron Stars — kHz Quasi-Periodic Oscillations (QPO). *Acta Physica Polonica B*, 32(11):3605, November 2001.
- [92] Robert V. Wagoner, Alexander S. Silbergleit, and Manuel Ortega-Rodríguez. “Stable” Quasi-periodic Oscillations and Black Hole Properties from Diskoseismology. *ApJ*, 559(1):L25–L28, September 2001.
- [93] Shoji Kato. Basic Properties of Thin-Disk Oscillations <sup>1</sup>. *PASJ*, 53(1):1–24, February 2001.
- [94] L. Rezzolla, S'i. Yoshida, T. J. Maccarone, and O. Zanotti. A new simple model for high-frequency quasi-periodic oscillations in black hole candidates. *MNRAS*, 344(3):L37–L41, September 2003.
- [95] Robert V. Wagoner. Diskoseismology and QPOs Confront Black Hole Spin. *ApJ*, 752(2):L18, June 2012.
- [96] Z. Stuchlík, A. Kotrlová, and G. Török. Multi-resonance orbital model of high-frequency quasi-periodic oscillations: possible high-precision determination of black hole and neutron star spin. *Astron Astroph*, 552:A10, April 2013.
- [97] Marcio G. B. de Avellar, Oliver Porth, Ziri Younsi, and Luciano Rezzolla. Kilohertz QPOs in low-mass X-ray binaries as oscillation modes of tori around neutron stars - I. *MNRAS*, 474(3):3967–3975, March 2018.
- [98] Bhupendra Mishra, Wlodek Kluźniak, and P. Chris Fragile. Relativistic, axisymmetric, viscous, radiation hydrodynamic simulations of geometrically thin discs. II. Disc variability. *MNRAS*, 497(1):1066–1079, September 2020.
- [99] Shoji Kato and Mami Machida. A possible origin of kilohertz quasi-periodic oscillations in low-mass X-ray binaries. *PASJ*, 72(3):38, June 2020.

- [100] G. Török, K. Goluchová, J. Horák, E. Šrámková, M. Urbanec, T. Pecháček, and P. Bakala. Twin peak quasi-periodic oscillations as signature of oscillating cusp torus. *MNRAS*, 457(1):L19–L23, March 2016.
- [101] A. Kotrlová, E. Šrámková, G. Török, K. Goluchová, J. Horák, O. Straub, D. Lančová, Z. Stuchlík, and M. A. Abramowicz. Models of high-frequency quasi-periodic oscillations and black hole spin estimates in Galactic microquasars. *Astron Astroph*, 643:A31, November 2020.
- [102] G. Török, M. A. Abramowicz, W. Kluźniak, and Z. Stuchlík. The orbital resonance model for twin peak kHz quasi periodic oscillations in microquasars. *Astron Astroph*, 436(1):1–8, June 2005.
- [103] W. Macke. L. d. landau and e. m. lifshitz mechanics. vol. 1 of: Course of theoretical physics. 165 s. m. 55 abb. oxford/london/paris 1960. pergamon press ltd. preis geb. 40 s. net. *ZAMM - Journal of Applied Mathematics and Mechanics / Zeitschrift für Angewandte Mathematik und Mechanik*, 41(9):392–392, 1961.
- [104] James F. Steiner, Jeffrey E. McClintock, Ronald A. Remillard, Ramesh Narayan, and Lijun Gou. Measuring Black Hole Spin Via the X-Ray Continuum-Fitting Method: Beyond the Thermal Dominant State. *ApJ*, 701(2):L83–L86, August 2009.
- [105] Jiří Horák. General aspects of nonlinear resonance 3:2 in QPO context. In *RAGtime 4/5: Workshops on black holes and neutron stars*, pages 91–110, December 2004.
- [106] G. Török, A. Kotrlová, E. Šrámková, and Z. Stuchlík. Confronting the models of 3:2 quasiperiodic oscillations with the rapid spin of the microquasar GRS 1915+105. *Astron Astroph*, 531:A59, July 2011.
- [107] A. Kotrlová, E. Šrámková, G. Török, Z. Stuchlík, and K. Goluchová. Super-spinning compact objects and models of high-frequency quasi-periodic oscillations observed in Galactic microquasars. II. Forced resonances. *Astron Astroph*, 607:A69, November 2017.
- [108] Martin Kološ, Arman Tursunov, and Zdeněk Stuchlík. Possible signature of the magnetic fields related to quasi-periodic oscillations observed in microquasars. *European Physical Journal C*, 77(12):860, December 2017.

- [109] Luigi Stella and Mario Vietri. Strong Field Gravity and Quasi-Periodic Oscillations from Low-Mass X-Ray Binaries. In Vahe G. Gurzadyan, Robert T. Jantzen, and Remo Ruffini, editors, *The Ninth Marcel Grossmann Meeting*, pages 426–437, December 2002.
- [110] A. Čadež, M. Calvani, and U. Kostić. On the tidal evolution of the orbits of low-mass satellites around black holes. *Astron Astroph*, 487(2):527–532, August 2008.
- [111] U. Kostić, A. Čadež, M. Calvani, and A. Gomboc. Tidal effects on small bodies by massive black holes. *Astron Astroph*, 496(2):307–315, March 2009.
- [112] Shoji Kato. Resonant Excitation of Disk Oscillations by Warps: A Model of kHz QPOs. *PASJ*, 56:905–922, October 2004.
- [113] M. A. Abramowicz, M. Calvani, and L. Nobili. Runaway instability in accretion disks orbiting black holes. *Nature*, 302(5909):597–599, April 1983.
- [114] Olindo Zanotti, Luciano Rezzolla, and José A. Font. Quasi-periodic accretion and gravitational waves from oscillating ‘toroidal neutron stars’ around a Schwarzschild black hole. *Monthly Notices of the Royal Astronomical Society*, 341(3):832–848, 05 2003.
- [115] Luciano Rezzolla, Shin’ichirou Yoshida, and Olindo Zanotti. Oscillations of vertically integrated relativistic tori – I. Axisymmetric modes in a Schwarzschild space-time. *Monthly Notices of the Royal Astronomical Society*, 344(3):978–992, 09 2003.
- [116] Pedro J. Montero, Luciano Rezzolla, and Shin’ichirou Yoshida. Oscillations of vertically integrated relativistic tori - II. Axisymmetric modes in a Kerr space-time. *MNRAS*, 354(4):1040–1052, November 2004.
- [117] Atsuo T. Okazaki, Shoji Kato, and Jun Fukue. Global trapped oscillations of relativistic accretion disks. *PASJ*, 39:457–473, January 1987.
- [118] F. H. Shu. *The physics of astrophysics. Volume II: Gas dynamics*. 1992.
- [119] W. Kluźniak, M. A. Abramowicz, S. Kato, W. H. Lee, and N. Stergioulas. Nonlinear Resonance in the Accretion Disk of a Millisecond Pulsar. *ApJ*, 603(2):L89–L92, March 2004.
- [120] S. Kato and J. Fukue. Trapped Radial Oscillations of Gaseous Disks around a Black Hole. *PASJ*, 32:377, January 1980.

- [121] Event Horizon Telescope Collaboration and et.al. First M87 Event Horizon Telescope Results. I. The Shadow of the Supermassive Black Hole. *ApJ*, 875(1):L1, April 2019.
- [122] Event Horizon Telescope Collaboration and et.al. First M87 Event Horizon Telescope Results. II. Array and Instrumentation. *ApJ*, 875(1):L2, April 2019.
- [123] Event Horizon Telescope Collaboration and et.al. First M87 Event Horizon Telescope Results. III. Data Processing and Calibration. *ApJ*, 875(1):L3, April 2019.
- [124] Event Horizon Telescope Collaboration and et.al. First M87 Event Horizon Telescope Results. IV. Imaging the Central Supermassive Black Hole. *ApJ*, 875(1):L4, April 2019.
- [125] Event Horizon Telescope Collaboration and et.al. First M87 Event Horizon Telescope Results. V. Physical Origin of the Asymmetric Ring. *ApJ*, 875(1):L5, April 2019.
- [126] Event Horizon Telescope Collaboration and et.al. First M87 Event Horizon Telescope Results. VI. The Shadow and Mass of the Central Black Hole. *ApJ*, 875(1):L6, April 2019.
- [127] Event Horizon Telescope Collaboration and et.al. First M87 Event Horizon Telescope Results. VII. Polarization of the Ring. *ApJ*, 910(1):L12, March 2021.
- [128] Event Horizon Telescope Collaboration and et.al. First M87 Event Horizon Telescope Results. VIII. Magnetic Field Structure near The Event Horizon. *ApJ*, 910(1):L13, March 2021.
- [129] Feryal Özel, Dimitrios Psaltis, and Ramesh Narayan. Hybrid Thermal-Nonthermal Synchrotron Emission from Hot Accretion Flows. *Astrophys.*, 541(1):234–249, September 2000.
- [130] Oliver James, Eugénie von Tunzelmann, Paul Franklin, and Kip S. Thorne. Gravitational lensing by spinning black holes in astrophysics, and in the movie *Interstellar*. *Classical and Quantum Gravity*, 32(6):065001, March 2015.
- [131] Volker Perlick, Oleg Yu. Tsupko, and Gennady S. Bisnovatyi-Kogan. Influence of a plasma on the shadow of a spherically symmetric black hole. *Phys. Rev. D*, 92(10):104031, November 2015.

- [132] Audrey Trova Shokoufe Faraji. Shadow in the presence of plasma in the background of q-metric. *submitted*, 2022.
- [133] Edited by B. Fiedler. *Handbook of Dynamical Systems*. Elsevier, 2002.
- [134] S.V. Sabau. Some remarks on jacobi stability. *Nonlinear Analysis: Theory, Methods and Applications*, 63(5):e143–e153, 2005. Invited Talks from the Fourth World Congress of Nonlinear Analysts (WCNA 2004).
- [135] Luis Barreira. *Metric Entropy and Topological Entropy*. Springer Berlin Heidelberg, Berlin, Heidelberg, 2012.
- [136] J. P. Eckmann and D. Ruelle. Ergodic theory of chaos and strange attractors. *Rev. Mod. Phys.*, 57:617–656, Jul 1985.
- [137] Y. B. Pesin. characteristic Lyapunov exponents and smooth ergodic theory. *Russian Mathematical Surveys*, 1977.
- [138] Vito Latora and Michel Baranger. Kolmogorov-sinai entropy rate versus physical entropy. *Phys. Rev. Lett.*, 82:520–523, Jan 1999.
- [139] Paolo Allegrini, Jack F. Douglas, and Sharon C. Glotzer. Dynamic entropy as a measure of caging and persistent particle motion in supercooled liquids. *Phys. Rev. E*, 60:5714–5724, Nov 1999.
- [140] R. M. Wald. *General relativity*. 1984.
- [141] Robert Geroch. A method for generating solutions of einstein’s equations. *Journal of Mathematical Physics*, 12(6):918–924, 1971.
- [142] Hermann Weyl. Zur gravitationstheorie. *Annalen der Physik*, 359(18):117–145, 1917.
- [143] G. Erez and N. Rosen. The gravitational field of a particle possessing a multipole moment. *Bull. Research Council Israel*, Vol: Sect. F.8, 9 1959.
- [144] Hernando Quevedo. General static axisymmetric solution of einstein’s vacuum field equations in prolate spheroidal coordinates. *Phys. Rev. D*, 39:2904–2911, May 1989.
- [145] S Chandrasekhar. *The mathematical theory of black holes*. Oxford classic texts in the physical sciences. Oxford Univ. Press, Oxford, 2002.

- [146] A. G. Doroshkevich, Y. B. Zel'dovich, and I. D. Novikov. Gravitational Collapse of Non-Symmetric and Rotating Bodies. *Zhurnal Eksperimentalnoi i Teoreticheskoi Fiziki*, 4:170, December 1965.
- [147] R. Geroch and J. B. Hartle. Distorted black holes. *Journal of Mathematical Physics*, 23:680–692, 1982.
- [148] Nora Bretón, Tatiana E. Denisova, and Vladimir S. Manko. A Kerr black hole in the external gravitational field. *Physics Letters A*, 230:7–11, Feb 1997.
- [149] David M. Zipoy. Topology of some spheroidal metrics. *Journal of Mathematical Physics*, 7(6):1137–1143, 1966.
- [150] B. H. Voorhees. Static axially symmetric gravitational fields. *Phys. Rev. D*, 2:2119–2122, Nov 1970.
- [151] Hernando Quevedo. Mass quadrupole as a source of naked singularities. *International Journal of Modern Physics D*, 20(10):1779–1787, 2011.
- [152] Ts. I. Gutsunayev, Ts. I. Gutsunaev, and V. S. Manko. On the gravitational field of a mass possessing a multipole moment. *General Relativity and Gravitation*, 17(11):1025–1027, November 1985.
- [153] V S Manko. On the description of the external field of a static deformed mass. *Classical and Quantum Gravity*, 7(9):L209–L211, sep 1990.
- [154] J. L. Hernández-Pastora and J. Martín. Monopole-quadrupole static axisymmetric solutions of Einstein field equations. *General Relativity and Gravitation*, 26(9):877–907, September 1994.
- [155] Hernando Quevedo. Exterior and interior metrics with quadrupole moment. *Gen. Rel. Grav.*, 43:1141–1152, 2011.
- [156] R. Geroch. Multipole Moments. II. Curved Space. *Journal of Mathematical Physics*, 11:2580–2588, August 1970.
- [157] K. Boshkayev, E. Gasperín, A. C. Gutiérrez-Piñeres, H. Quevedo, and S. Toktarbay. Motion of test particles in the field of a naked singularity. *Phys. Rev. D*, 93:024024, Jan 2016.
- [158] K. A. Boshkayev, H. Quevedo, M. S. Abutalip, Zh. A. Kalymova, and Sh. S. Suleymanova. Geodesics in the field of a rotating deformed gravitational source. *International Journal of Modern Physics A*, 31(02n03):1641006, 2016.



- [159] H. Quevedo. Multipole Moments in General Relativity Static and Stationary Vacuum Solutions. *Fortschritte der Physik*, 38:733–840, 1990.
- [160] Francisco Frutos-Alfaro and Michael Soffel. On relativistic multipole moments of stationary space-times. *Royal Society open science*, 5(7):180640, 2018.
- [161] Robert Geroch. Multipole moments. i. flat space. *Journal of Mathematical Physics*, 11(6):1955–1961, 1970.
- [162] R. O. Hansen. Multipole moments of stationary space-times. *Journal of Mathematical Physics*, 15(1):46–52, 1974.
- [163] T. Levi-Civita. *Ds2 einsteiniani in campi newtoniani. 7. Il sottocaso B2: soluzioni oblique : nota del socio T. Levi-Civita.* 1918.
- [164] E. T. Newman and L. A. Tamburino. New approach to einstein’s empty space field equations. *Journal of Mathematical Physics*, 2(5):667–674, 1961.
- [165] I. Robinson and A. Trautman. Some Spherical Gravitational Waves in General Relativity. *Proceedings of the Royal Society of London Series A*, 265(1323):463–473, February 1962.
- [166] Jurgen Ehlers and Wolfgang Kundt. Exact solutions of the gravitational field equations. 1962.
- [167] William Kinnersley and Martin Walker. Uniformly accelerating charged mass in general relativity. *Phys. Rev. D*, 2:1359–1370, Oct 1970.
- [168] J.F Plebanski and M Demianski. Rotating, charged, and uniformly accelerating mass in general relativity. *Annals of Physics*, 98(1):98–127, 1976.
- [169] Kenneth Hong and Edward Teo. A new form of the C-metric. *Classical and Quantum Gravity*, 20(14):3269–3277, July 2003.
- [170] Kenneth Hong and Edward Teo. A new form of the rotating C-metric. *Classical and Quantum Gravity*, 22(1):109–117, January 2005.
- [171] Mukunda Aryal, L. H. Ford, and Alexander Vilenkin. Cosmic strings and black holes. *Phys. Rev. D*, 34:2263–2266, Oct 1986.
- [172] F. J. Ernst. Black holes in a magnetic universe. *Journal of Mathematical Physics*, 17(1):54–56, 1976.

- [173] Andrey A. Shoom, Cole Walsh, and Ivan Booth. Geodesic motion around a distorted static black hole. *Physical Review D*, 93(6), Mar 2016.
- [174] Jutta Kunz, Petya Nedkova, and Stoytcho Yazadjiev. Magnetized black holes in an external gravitational field. *Phys. Rev. D*, 96:024017, Jul 2017.
- [175] Patricio S. Letelier. Stability of circular orbits of particles moving around black holes surrounded by axially symmetric structures. *Phys. Rev. D*, 68:104002, Nov 2003.
- [176] Javier Ramos-Caro, Juan F. Pedraza, and Patricio S. Letelier. Motion around a monopole + ring system – i. stability of equatorial circular orbits versus regularity of three-dimensional motion. *Monthly Notices of the Royal Astronomical Society*, 414(4):3105–3116, 2011.
- [177] Bruno Boisseau and Patricio S. Letelier. Relativistic multipoles and the advance of the perihelia. *General Relativity and Gravitation*, 34(7):1077–1096, Jul 2002.
- [178] Framsol López-Suspes and Guillermo A. González. Equatorial circular orbits of neutral test particles in weyl spacetimes. *Brazilian Journal of Physics*, 44(4):385–397, Aug 2014.
- [179] O. Semerák. Circular orbits in stationary axisymmetric spacetimes. *General Relativity and Gravitation*, 30(8):1203–1215, Aug 1998.
- [180] Patricio S Letelier. On the gravitational field of static and stationary axial symmetric bodies with multi-polar structure. *Classical and Quantum Gravity*, 16(4):1207–1213, jan 1999.
- [181] Eduardo Guéron and Patricio S. Letelier. Chaotic motion around prolate deformed bodies. *Phys. Rev. E*, 63:035201, Feb 2001.
- [182] Eduardo Guéron and Patricio S. Letelier. Geodesic chaos around quadrupolar deformed centers of attraction. *Phys. Rev. E*, 66:046611, Oct 2002.
- [183] M. Žáček and Oldrich Semerak. Gravitating discs around a schwarzschild black hole ii. *Czechoslovak Journal of Physics*, 52:19–27, 01 2002.

- [184] Milton Abramowitz. *Handbook of Mathematical Functions, With Formulas, Graphs, and Mathematical Tables*,. Dover Publications, Inc., New York, NY, USA, 1974.
- [185] Robert M. Wald. Black hole in a uniform magnetic field. *Phys. Rev. D*, 10:1680–1685, Sep 1974.
- [186] M. Yu. Piotrovich, N. A. Silant’ev, Yu. N. Gnedin, and T. M. Natsvlishvili. Magnetic fields and quasi-periodic oscillations of black hole radiation. *Astrophysical Bulletin*, 66(3):320–324, July 2011.
- [187] Shokoufe Faraji. Circular Geodesics in a New Generalization of q-Metric. *Universe*, 8(3):195, March 2022.
- [188] Máximo Bañados, Joseph Silk, and Stephen M. West. Kerr Black Holes as Particle Accelerators to Arbitrarily High Energy. *Phys. Rev. L*, 103(11):111102, September 2009.
- [189] T. Piran, J. Shaham, and J. Katz. High Efficiency of the Penrose Mechanism for Particle Collisions. *ApJ*, 196:L107, March 1975.
- [190] Tsvi Piran and Jacob Shaham. Upper bounds on collisional penrose processes near rotating black-hole horizons. *Phys. Rev. D*, 16:1615–1635, Sep 1977.
- [191] T. Piran and J. Shaham. Production of gamma-ray bursts near rapid rotating accreting black holes. *Astrophys.*, 214:268–299, May 1977.
- [192] Tomohiro Harada and Masashi Kimura. Collision of two general geodesic particles around a Kerr black hole. *Phys. Rev. D*, 83(8):084041, April 2011.
- [193] Oleg B. Zaslavskii. Ultra-high energy collisions of nonequatorial geodesic particles near dirty black holes. *Journal of High Energy Physics*, 2012:32, December 2012.
- [194] Chang-Qing Liu. Collision of Two General Geodesic Particles around a Kerr—Newman Black Hole. *Chinese Physics Letters*, 30(10):100401, October 2013.
- [195] Oleg B. Zaslavskii. Acceleration of particles as a universal property of rotating black holes. *Phys. Rev. D*, 82(8):083004, October 2010.

- [196] Shao-Wen Wei, Yu-Xiao Liu, Heng Guo, and Chun-E. Fu. Charged spinning black holes as particle accelerators. *Phys. Rev. D*, 82(10):103005, November 2010.
- [197] O. B. Zaslavskii. Acceleration of particles by nonrotating charged black holes? *Soviet Journal of Experimental and Theoretical Physics Letters*, 92(9):571–574, November 2010.
- [198] Tomohiro Harada, Hiroya Nemoto, and Umpei Miyamoto. Upper limits of particle emission from high-energy collision and reaction near a maximally rotating Kerr black hole. *Phys. Rev. D*, 86(2):024027, July 2012.
- [199] Michał Bejger, Tsvi Piran, Marek Abramowicz, and Frida Håkanson. Collisional Penrose Process near the Horizon of Extreme Kerr Black Holes. *Phys. Rev. L*, 109(12):121101, September 2012.
- [200] Filip Hejda and Jiří Bičák. Kinematic restrictions on particle collisions near extremal black holes: A unified picture. *Phys. Rev. D*, 95(8):084055, April 2017.
- [201] Ayesha Zakria and Qurat-ul-Ain Satti. Black Holes and White Holes as Particle Accelerators. *arXiv e-prints*, page arXiv:1807.01621, July 2018.
- [202] Jeremy D. Schnittman. The collisional Penrose process. *General Relativity and Gravitation*, 50(6):77, June 2018.
- [203] F. Hejda, J. Bičák, and O. B. Zaslavskii. Extraction of energy from an extremal rotating electrovacuum black hole: Particle collisions along the axis of symmetry. *Phys. Rev. D*, 100(6):064041, September 2019.
- [204] Filip Hejda, José P. S. Lemos, and Oleg B. Zaslavskii. Extraction of energy from an extremal rotating electrovacuum black hole: Particle collisions in the equatorial plane. *Phys. Rev. D*, 105(2):024014, January 2022.
- [205] Valeri P. Frolov and Andrey A. Shoom. Motion of charged particles near a weakly magnetized Schwarzschild black hole. *Phys. Rev. D*, 82(8):084034, October 2010.
- [206] Frederick J. Ernst. New formulation of the axially symmetric gravitational field problem. *Phys. Rev.*, 167:1175–1178, Mar 1968.

- [207] C. Hoenselaers and W. Dietz. *Solutions of Einstein's Equations: Techniques and Results*. Springer, Berlin, 1984.
- [208] S. Toktarbay and H. Quevedo. A stationary q-metric. *Gravitation and Cosmology*, 20(4):252–254, October 2014.
- [209] Shokoufe Faraji, Audrey Trova, and Hernando Quevedo. Relativistic equilibrium fluid configurations around rotating deformed compact objects. *arXiv e-prints*, page arXiv:2205.03842, May 2022.
- [210] Shokoufe Faraji and Eva Hackmann. Thin accretion disk around the distorted schwarzschild black hole. *Phys. Rev. D*, 101:023002, Jan 2020.
- [211] Audrey Trova Shokoufe Faraji. Properties of the thin accretion disc is the background of a distorted deformed compact object. *submitted*, 2022.
- [212] Sergio Gimeno-Soler and José A. Font. Magnetised Polish doughnuts revisited. *Astron Astroph*, 607:A68, November 2017.
- [213] Shokoufe Faraji and Audrey Trova. Effect of an external mass distribution on the magnetized accretion disk. *Phys. Rev. D*, 104:083006, Oct 2021.
- [214] S. Faraji and A. Trova. Magnetised tori in the background of a deformed compact object. *Astron Astroph*, 654:A100, October 2021.
- [215] M. A. Abramowicz, J. C. Miller, and Z. Stuchlík. Concept of radius of gyration in general relativity. *Phys. Rev. D*, 47:1440–1447, Feb 1993.
- [216] Sandip K. Chakrabarti. Von Zeipel surfaces. II - A catalogue. *MNRAS*, 250:7–13, May 1991.
- [217] Shokoufe Faraji, Audrey Trova, and Vladimir Karas. Magnetized relativistic accretion disk around a spinning, electrically charged, accelerating black hole: Case of the  $c$  metric. *Phys. Rev. D*, 105:103017, May 2022.
- [218] Robert M. Wald. Black hole in a uniform magnetic field. *Phys. Rev. D*, 10(6):1680–1685, September 1974.
- [219] Bharat Ratra. Cosmological “Seed” Magnetic Field from Inflation. *ApJ*, 391:L1, May 1992.

- [220] D. Grasso and H. R. Rubinstein. Magnetic fields in the early Universe. *Phys. Rep.*, 348(3):163–266, July 2001.
- [221] Andrii Neronov and Ievgen Vovk. Evidence for Strong Extragalactic Magnetic Fields from Fermi Observations of TeV Blazars. *Science*, 328(5974):73, April 2010.
- [222] Rajeev Kumar Jain and Martin S. Sloth. Consistency relation for cosmic magnetic fields. *Phys. Rev. D*, 86(12):123528, December 2012.
- [223] Ruth Durrer and Andrii Neronov. Cosmological magnetic fields: their generation, evolution and observation. *Astron Astroph*, 21:62, June 2013.
- [224] Jiří Kovář, Petr Slaný, Claudio Cremaschini, Zdeněk Stuchlík, Vladimír Karas, and Audrey Trova. Electrically charged matter in rigid rotation around magnetized black hole. *Phys. Rev. D*, 90(4):044029, August 2014.
- [225] Jiří Kovář, Zdeněk Stuchlík, and Vladimír Karas. Off-equatorial orbits in strong gravitational fields near compact objects. *Classical and Quantum Gravity*, 25(9):095011, May 2008.
- [226] O. Kopáček, V. Karas, J. Kovář, and Z. Stuchlík. Transition from Regular to Chaotic Circulation in Magnetized Coronae near Compact Objects. *Astrophys.*, 722(2):1240–1259, October 2010.
- [227] J. Kovář, O. Kopáček, V. Karas, and Z. Stuchlík. Off-equatorial orbits in strong gravitational fields near compact objects—II: halo motion around magnetic compact stars and magnetized black holes. *Classical and Quantum Gravity*, 27(13):135006, July 2010.
- [228] L. Stella and M. Vietri. Quasi-Periodic Oscillations from Low-Mass X-ray Binaries and Strong Field Gravity. In Riccardo Giacconi, Salvatore Serio, and Luigi Stella, editors, *X-ray Astronomy 2000*, volume 234 of *Astronomical Society of the Pacific Conference Series*, page 213, January 2001.
- [229] S. Faraji and A. Trova. Dynamics of charged particles and quasi-periodic oscillations in the vicinity of a distorted, deformed compact object embedded in a uniform magnetic field. *MNRAS*, 513(3):3399–3413, July 2022.

- [230] Rebecca Shafee, Jeffrey E. McClintock, Ramesh Narayan, Shane W. Davis, Li-Xin Li, and Ronald A. Remillard. Estimating the Spin of Stellar-Mass Black Holes by Spectral Fitting of the X-Ray Continuum. *ApJ*, 636(2):L113–L116, January 2006.
- [231] Pawel Lachowicz, Bozena Czerny, and Marek A. Abramowicz. Wavelet analysis of MCG-6-30-15 and NGC 4051: a possible discovery of QPOs in 2:1 and 3:2 resonance. *arXiv e-prints*, pages astro-ph/0607594, July 2006.
- [232] Shokoufe Faraji and Audrey Trova. Quasi-periodic oscillatory motion of particles orbiting a distorted, deformed compact object. *Universe*, 7(11), 2021.
- [233] Adam Rogers. Frequency-dependent effects of gravitational lensing within plasma. *MNRAS*, 451(1):17–25, July 2015.
- [234] Wen Fu and Dong Lai. Effects of Magnetic Fields on the Diskoseismic Modes of Accreting Black Holes. *Astrophys.*, 690(2):1386–1392, January 2009.
- [235] Janosz W. Dewberry, Henrik N. Latter, Gordon I. Ogilvie, and Sebastien Fromang. HFQPOs and discoseismic mode excitation in eccentric, relativistic discs. II. Magnetohydrodynamic simulations. *MNRAS*, 497(1):451–465, September 2020.
- [236] Eric Poisson. Retarded coordinates based at a world line and the motion of a small black hole in an external universe. *Phys. Rev. D*, 69:084007, Apr 2004.